

## Setting Africa's rainfall straight

### A warping approach to position and timing errors in rainfall estimates

le Coz, C.M.L.

**DOI**

[10.4233/uuid:811faec9-9688-4f60-829e-3b073fc6fe59](https://doi.org/10.4233/uuid:811faec9-9688-4f60-829e-3b073fc6fe59)

**Publication date**

2021

**Document Version**

Final published version

**Citation (APA)**

le Coz, C. M. L. (2021). *Setting Africa's rainfall straight: A warping approach to position and timing errors in rainfall estimates*. [Dissertation (TU Delft), Delft University of Technology].  
<https://doi.org/10.4233/uuid:811faec9-9688-4f60-829e-3b073fc6fe59>

**Important note**

To cite this publication, please use the final published version (if applicable).  
Please check the document version above.

**Copyright**

Other than for strictly personal use, it is not permitted to download, forward or distribute the text or part of it, without the consent of the author(s) and/or copyright holder(s), unless the work is under an open content license such as Creative Commons.

**Takedown policy**

Please contact us and provide details if you believe this document breaches copyrights.  
We will remove access to the work immediately and investigate your claim.

# **SETTING AFRICA'S RAINFALL STRAIGHT**

A WARPING APPROACH TO POSITION AND TIMING ERRORS IN  
RAINFALL ESTIMATES



# **SETTING AFRICA'S RAINFALL STRAIGHT**

**A WARPING APPROACH TO POSITION AND TIMING ERRORS IN  
RAINFALL ESTIMATES**

## **Dissertation**

for the purpose of obtaining the degree of doctor  
at Delft University of Technology,  
by the authority of the Rector Magnificus, Prof. dr. ir. T. H. J. van der Hagen,  
chair of the Board for Doctorates  
to be defended publicly on Thursday 17 June at 15:00 o'clock

by

**Camille Marie-Jeanne Laurence LE COZ**

Master of Science in Applied Mathematics, Delft University of Technology, the  
Netherlands,  
born in Sèvres, France.

This dissertation has been approved by the promotor.

promotor: Prof.dr.ir. N.C. van de Giesen

promotor: Prof.dr.ir. A.W. Heemink

Composition of the doctoral committee:

Rector Magnificus,	chairperson
Prof.dr.ir. N.C. van de Giesen,	Delft University of Technology, promotor
Prof.dr.ir. A.W. Heemink,	Delft University of Technology, promotor

*Independent members:*

Prof.dr.ir. R. Uijlenhoet	Delft University of Technology
Prof.dr.ir. H.J. Russchenberg	Delft University of Technology
Prof.dr. C. Ichoku	Howard University
Dr.ir. J.A.E. ten Veldhuis	Delft University of Technology

*Other members:*

Prof.dr.ir. M. Verlaan	Delft University of Technology, Deltares
------------------------	--



*Keywords:* African rainfall, precipitation estimation, field displacement, warping

*Printed by:* Ipskamp Printing

*Front & Back:* Camille Le Coz

Copyright © 2021 by C. Le Coz

ISBN 978-94-6421-387-4

An electronic version of this dissertation is available at  
<http://repository.tudelft.nl/>.

# CONTENTS

<b>Summary</b>	<b>ix</b>
<b>Résumé</b>	<b>xi</b>
<b>1 Introduction</b>	<b>1</b>
References . . . . .	5
<b>2 Comparison of rainfall products over sub-Saharan Africa</b>	<b>9</b>
2.1 Introduction . . . . .	10
2.2 Reanalysis and models . . . . .	13
2.2.1 Global Circulation Models (GCMs) . . . . .	13
2.2.2 Reanalyses . . . . .	16
2.2.3 Dynamic downscaling . . . . .	18
2.3 Satellite-based products . . . . .	20
2.3.1 Satellite-based rainfall estimates . . . . .	20
2.3.2 Regional vs global . . . . .	21
2.3.3 Gauges data in satellite-based products . . . . .	21
2.4 Gauge-only products . . . . .	25
2.4.1 Factors influencing the performance of gauge-only products . . . . .	25
2.4.2 Gauge-only versus satellite-based products . . . . .	26
2.5 Discussion . . . . .	28
2.5.1 Factors influencing the performance. . . . .	28
2.5.2 Use cases. . . . .	31
2.6 Conclusion . . . . .	35
<b>Appendix</b> . . . . .	<b>37</b>
2.A Satellite-based products - description and performance . . . . .	37
2.A.1 Climate Anomaly Monitoring System - Outgoing longwave radiation Precipitation Index (CAMS-OPI) . . . . .	37
2.A.2 Global Precipitation Climatology Project (GPCP) - Satellite and Gauge (SG) . . . . .	37
2.A.3 CPC Merged Analysis of Precipitation (CMAP) . . . . .	38
2.A.4 Global Precipitation Climatology Project (GPCP)-1DD . . . . .	41
2.A.5 CPC Morphing Technique (CMORPH) . . . . .	44
2.A.6 Tropical Rainfall Measuring Mission (TRMM) Multi-satellite Pre- cipitation Analysis (TMPA) . . . . .	45
2.A.7 Precipitation Estimation from Remote Sensing Information using Artificial Neural Network (PERSIANN) . . . . .	49
2.A.8 Rainfall Estimate version 2 (RFE2) . . . . .	53
2.A.9 Africa Rainfall Climatology version 2 (ARC2) . . . . .	54

2.A.10	Global Satellite Mapping of Precipitation (GSMaP)	56
2.A.11	Climate Hazards Group InfraRed Precipitation (CHIRP) with Station data (CHIRPS)	58
2.A.12	Tropical Applications of Meteorology using SATellite data and ground based observations (TAMSAT) African Rainfall Climatology And Time-series (TARCAT)	58
<b>List of acronyms</b>		<b>63</b>
References		66
<b>3</b>	<b>Correcting position error in precipitation estimates using image warping</b>	<b>77</b>
3.1	Introduction	78
3.2	Methodology	79
3.2.1	Definitions	80
3.2.2	Automatic registration	80
3.2.3	Extension to space-time data	84
3.3	Synthetic cases	86
3.3.1	Study cases	86
3.3.2	Results	87
3.3.3	Sensitivity	95
3.4	Southern Ghana case	102
3.4.1	Study case	102
3.4.2	Results	105
3.5	Discussion	111
3.6	Conclusion	113
3.7	Future work	114
<b>Appendix</b>		<b>117</b>
3.A	Optimization Step of the Automatic Registration Algorithm	117
3.A.1	Constraints	117
3.A.2	Minimization Method	117
3.B	Extra results from the synthetic case	118
3.C	Extra results from the southern Ghana case	122
References		127
<b>4</b>	<b>Correcting timing error in precipitation estimates using image warping</b>	<b>131</b>
4.1	Introduction	132
4.2	Methodology	133
4.2.1	Definitions	133
4.2.2	Automatic registration	133
4.2.3	Extension to space-time data	135
4.2.4	Work-flow	137
4.3	Synthetic case	137
4.3.1	Study case	137
4.3.2	Results	138
4.3.3	Sensitivity	143

4.4	Southern Ghana case . . . . .	157
4.4.1	Study case . . . . .	157
4.4.2	Results . . . . .	160
4.5	Discussion . . . . .	167
4.6	Conclusion . . . . .	170
4.7	Future work . . . . .	171
	<b>Appendix</b> . . . . .	<b>173</b>
4.A	TAHMO stations . . . . .	173
4.B	Mappings from the synthetic case . . . . .	173
4.C	Warped fields from the synthetic case . . . . .	176
4.D	Warped fields from the southern Ghana case . . . . .	178
	References . . . . .	181
<b>5</b>	<b>Conclusions and recommendations</b>	<b>183</b>
5.1	Conclusions. . . . .	184
5.1.1	State of the art of rainfall estimates over sub-Saharan Africa . . . . .	184
5.1.2	Space warping as a way to gauge-adjust satellite-based estimates with respect to position . . . . .	184
5.1.3	Time warping as a way to gauge-adjust satellite-based estimates with respect to timing . . . . .	185
5.1.4	General conclusions on warping . . . . .	186
5.2	Recommendations . . . . .	187
5.2.1	Spatial and time warping. . . . .	187
5.2.2	High-resolution weather simulation for sub-Saharan Africa on the World Community Grid . . . . .	190
	References . . . . .	191
	<b>Acknowledgements</b>	<b>193</b>
	<b>Curriculum Vitae</b>	<b>195</b>
	<b>List of Publications</b>	<b>197</b>





# SUMMARY

There is an increasing number of rainfall products available over Africa and globally. Rainfall has considerable socio-economic impacts in sub-Saharan Africa, and the sparse gauge and radar networks make such estimates particularly valuable. They are used in many important applications such as drought/flood forecasting, water management or climate monitoring. The choice of which one to use has a significant influence on the output and performance of such applications. The large number of available rainfall products makes it difficult to select the “best” one for one’s need.

Among the rainfall products, there is an increasing number of satellite-based estimates with ever finer resolution. They are particularly valuable in Africa where the gauge network is not dense enough to represent the high variability of the rainfall during the monsoon season. However, there are substantial differences between them. Rainfall events are moving systems which can be described by their positions and timings beside of their intensity. A position or timing error will also lead to mismatches in the rainfall occurrence or intensity. This is especially true for localized rainfall events such as the convective rainstorms occurring during the rainy season in sub-Saharan Africa. However, rainfall is mainly evaluated with respect to its intensity or occurrence, while position and timing errors are rarely studied.

This led us to the following research questions:

- What is the state of the art of rainfall products in sub-Saharan Africa?
- How can we correct the position and timing errors in rainfall estimates?

Because of the large number of rainfall estimates available, it is not always possible to evaluate them all to find the one that best fits one’s application. Many inter-comparison and validation studies are available. However, they cover different parts of Africa, focus on different rainfall characteristics and use different reference data and metrics. In Chapter 2, we perform a systematic review of such studies in order to identify the strengths and limitations of the many rainfall products available for Africa. We consider three types of rainfall estimates: the gauge-only products, the satellite-based ones and the reanalyses. In addition to the global rainfall products, we also include three regional ones that have been specifically developed for Africa: the African Rainfall Climatology version 2 (ARC2), the Rainfall Estimate version 2 (RFE2) and the TAMSAT African Rainfall Climatology And Timeseries (TARCAT). When using rainfall products, one has to keep in mind several factors influencing their performance, such as the gauge density, the orography or the rainfall regime. Their performance is also linked to the way the estimates are derived from the various measurements. To make them easier to compare, we present the algorithms of the most used products as flowcharts with uniform notation. In the end, the most important consideration when choosing a rainfall product is the intended application. Thus, we discuss seven use-cases and their requirements as well

as corresponding recommendations. This review is meant as a guide to help users make informed decisions about which rainfall product to use.

Many satellite-based estimates use gauge data for bias correction. In general, bias adjustment methods are focusing on the intensity error and are not explicitly correcting possible position errors. In Chapter 3, we investigate the use of a warping method to gauge-adjust satellite-based estimates with respect to the position instead of the intensity. Warping is a field deformation method that transforms an image, or in our case a rainfall field, into another one, by applying a spatial mapping on the coordinates. The mapping is derived by an automatic registration method that only needs the two fields as input (i.e. the one to be corrected and the “true” rainfall). It does not require any manual selection of rain features. The spatial warping method was applied to two case studies. The first case uses synthetic rainfall events represented by ellipses, and allows us to evaluate the accuracy and the sensitivity of the method when the “true” rainfall is known. The second case is a rainfall event in southern Ghana during the monsoon season of 2018. It is used to assess the potential of the method when applied to real noisy data. We use the gauge data from the Trans-African Hydro-Meteorological Observatory (TAHMO) network to correct IMERG-Late (Integrated Multi-Satellite Retrievals for GPM) estimates. The results show that the position can be corrected while preserving the higher spatial variability of the satellite-based estimates. Moreover, by correcting the position error, the continuous statistics and the timing error are also improved.

In Chapter 4, the warping method is adapted to work on time-series instead of rainfall fields. The goal is to use this time warping to correct timing errors. We use the same two case studies as for the spatial warping to allow for a better comparison of the two methods. For both cases, the time warping decreases significantly the timing error and by extension improves the continuous statistics. It has, however, a more limited impact on the position error.

More cases would be needed to fully examine the sensitivity and limits of the spatial and time warping methods. However, these two cases show that they both have potential. Their main limitation comes from the automatic registration that needs the two input fields or time series to be similar enough in order to perform properly. Here, we consider the corrections of the position and of the timing separately. In a later step, they could be merged in order to correct both at the same time and fully take into account the relations between the spatial and time dimensions. One of the main challenges of such a step will be the computational cost which increases exponentially with the number of variables. For some applications, the position and timing of rainfall is as important as its intensity. The warping methods could be applied to the rainfall estimates to correct them before using them in such applications. They could also be used on types of rainfall estimates other than satellite-based ones. For example, they could be applied on numerical weather prediction for the data assimilation of rainfall.

# RÉSUMÉ

Il y a un nombre croissant d'estimations de précipitation disponibles pour l'Afrique. Ces estimations sont particulièrement intéressantes en Afrique sub-Saharienne où la pluie a un impact socio-économique considérable tandis que le nombre de stations aux sol reste limité. Ces estimations sont utilisées dans beaucoup d'applications essentielles telles que les prévisions d'inondations et de sécheresses, la gestion des ressources en eaux ou le suivis des changements climatiques. Les estimations de pluie influencent significativement les résultats et performances de telles applications. Le choix d'une estimation de pluie est donc crucial. Sélectionner la « meilleure » estimation pour ses besoins est rendu difficile par le grand nombre de choix possibles.

Parmi les estimations de pluie disponibles, il y a un nombre croissant d'estimations basées sur des observations satellitaires (alias produits satellitaires de pluie) avec des résolutions de plus en plus élevées. Ces estimations sont particulièrement intéressantes en Afrique où les réseaux de stations météorologiques ne sont pas assez denses pour représenter la forte variabilité pluviométrique durant la saison des pluies. Il y a des différences substantielles entre les différentes estimations de pluie. Celles-ci s'observent non seulement au niveau de l'intensité ou de la quantité de pluie, mais aussi au niveau de son occurrence. Puisque les événements pluviométriques sont des systèmes en mouvement, une partie de ces différences peut être expliquée par des erreurs de position ou de timing. Cela est particulièrement vrai pour les événements localisés tels que les précipitations convectives qui caractérisent la saison des pluies en Afrique sub-Saharienne.

Ceci nous a conduit aux questions de recherches suivantes:

- Quel est l'état des lieux des estimations de pluie en Afrique sub-Saharienne?
- Comment peut on corriger les erreurs de position et de timing dans les estimations de pluie?

A cause du grand nombre d'estimations de pluie disponibles, il n'est pas toujours possible de toutes les évaluer pour trouver celle qui convient le mieux à une application donnée. Beaucoup d'études de comparaison et de validation ont déjà été réalisées. Cependant, elles couvrent différentes régions d'Afrique, se concentrent sur différentes caractéristiques de la pluie et utilisent différentes données de référence. Dans le Chapitre 2, nous effectuons une évaluation systématique de ces études afin d'identifier les forces et faiblesses des nombreuses estimations de pluie disponibles pour l'Afrique. Nous considérons trois types d'estimations: celles n'utilisant que des données de stations météorologiques, celles utilisant des données satellitaires et celles provenant de réanalyses météorologiques. En plus des estimations globales (i.e. disponible pour tout le globe), nous incluons aussi trois estimations régionales qui ont été spécifiquement développées pour l'Afrique: ARC2 (African Rainfall Climatology version 2), RFE2 (Rainfall Estimate version 2) et TARCAT (TAMSAT African Rainfall Climatology And Timeserie).

Il y a plusieurs facteurs communs aux trois types d'estimations qui peuvent influencer leurs performances, tels que la densité des réseaux au sol, l'orographie ou le type de précipitations. Leurs performances sont aussi liées à la manière dont les estimations sont dérivées des différentes sources de données (ex.: au sol, satellitaire, model numérique). Pour permettre de les comparer plus facilement, nous avons représenté les algorithmes des produits satellitaires les plus utilisés par des organigrammes avec des notations unifiées. En fin de compte, la plus importante considération pour choisir une estimation de pluie est l'application à laquelle elle est destinée. Par conséquent, nous discutons sept cas d'utilisation et leurs exigences en terme d'estimations de pluie. Cette synthèse est conçue comme un guide pour aider les utilisateurs à prendre des décisions informées à propos de quelle estimation utiliser.

Beaucoup de produits satellitaires de pluie utilisent des données au sol pour corriger les biais. En général, les méthodes de correction de biais se concentrent sur les erreurs d'intensité et ne corrigent pas explicitement de possible erreurs de positions. Dans le Chapitre 3, nous examinons l'utilisation d'une méthode de morphing pour corriger ces estimations par rapport à la position des événements de pluie au lieu de leur intensité. Le morphing est une méthode de traitement des images qui transforme une image, ou dans notre cas un champ pluviométrique, en une autre en appliquant une transformation spatiale sur les coordonnées. Cette transformation est obtenue par une méthode automatique qui a seulement besoin de deux champs pluviométriques comme entrées (i.e. le champ à corriger et celui venant de données au sol qui est pris comme référence). Elle ne nécessite aucune sélection manuelle. Le morphing a été appliqué à deux études de cas. Le premier cas utilise des événements de pluie synthétiques qui sont représentés par des ellipses. Il nous permet d'évaluer la performance et la sensibilité de la méthode quand pluie "réelle" est connue. Le second cas correspond à un événement pluvieux dans le sud du Ghana pendant la saison des pluies 2018. Ce cas est utilisé pour évaluer le potentiel de la méthode quand elle est appliquée à des données réelles de pluie. Nous avons utilisé les stations météorologiques du réseau TAHMO (Trans-African Hydro-Meteorological Observatory) pour corriger les estimations de pluie de IMERG-Late (Integrated Multi-Satellite Retrievals for GPM). Les résultats montrent que la position peut être corrigée tout en conservant la plus grande variabilité spatiale de l'estimation satellitaire. De plus, en corrigeant l'erreur de position, l'erreur de timing et les indicateurs statistiques ont aussi été améliorés.

Dans le Chapitre 4, la méthode de correction par morphing est adaptée pour fonctionner avec des séries de données pluviométriques au lieu de champs en 2D. Le but est d'utiliser un morphing temporel pour corriger les erreurs de timing. Nous utilisons les deux mêmes études de cas que précédemment pour le morphing spatial pour permettre une meilleure comparaison des deux méthodes. Dans les deux études de cas, le morphing temporel réduit fortement les erreurs de timing, et par extension améliore les indicateurs statistiques. Cette méthode a cependant un impact plus limité sur les erreurs de position.

Plus d'études de cas seraient nécessaires pour examiner pleinement la sensibilité et les limites des méthodes de morphing spatial et temporel. Cependant, ces deux cas montrent que les deux méthodes ont un potentiel intéressant. Leur principale limitation est dû à la méthode automatique utilisée pour trouver la transformation. Elle nécessite

en effet que les deux champs ou séries pluviométriques soient suffisamment semblables pour fonctionner correctement. Dans le cadre de cette thèse, nous avons considéré séparément la correction de la position et celle du timing des évènements pluvieux. Dans une prochaine étape, ces deux corrections pourraient être combinées pour pleinement prendre en compte les relations entre les dimensions spatiales et temporelle. Un des principaux défis d'une telle étape sera le coût des calculs qui augmente exponentiellement avec le nombre de variables. Pour certaines applications, la position et le timing d'un évènement pluvieux est aussi important que son intensité. Les méthodes de morphing pourraient être appliquées aux estimations de pluie pour les corriger avant de les utiliser dans ces applications. Ces méthodes pourraient aussi être appliquées à d'autres types d'estimations que celles basées sur des données satellitaires. Par exemple, elles pourraient être appliquées sur des prédictions météorologiques numériques pour l'assimilation de données de précipitations.



# 1

## INTRODUCTION

*Rien ne prédit mieux le beau temps que la pluie.*

French proverb



## BACKGROUND

Precipitation is an important part of the hydrological cycle. As such, precipitation data is needed for many applications such as flood and drought monitoring, power generation, or water management in general. It is also very important for agriculture in sub-Saharan Africa where 95% of the agriculture is rain-fed (Food and Organization (2016)), making farmers vulnerable to climate change and extreme weather (c.f. Figs 1.1 and 1.2). Rainfall forecasts can help them make informed decisions about when or what to plant, while data of the recent past are needed for crop insurance (e.g. in case of drought). Data of the (recent) past are also used for irrigation scheduling, reservoir management and large scale flood detection and prediction. Longer data records are very useful in climate research to study precipitation trends. In general, it is difficult to overestimate the social and economic importance of rainfall information in Africa.



Figure 1.1: A farmer who lost her field of tomatoes because of a lack of rainfall in northern Ghana (Photo by Monica Estebanez Camarena).



Figure 1.2: Flooded field in Madagascar at the beginning of the rainy season.

In sub-Saharan Africa, most of the rainfall is produced by convective systems (e.g., [Dezfuli et al., 2017](#)). In West Africa, 60% of the total annual rainfall is generated by mesoscale convective systems, and more than 90% in the Sahel ([Abiodun 2003](#)). Rainfall is difficult to estimate because of its high temporal and spatial variability ([Sivakumar and Hatfield, 1990](#); [Le Barbé et al., 2002](#)). This is especially true for convective rainstorms which can be very localized in time and space. In sub-Saharan Africa, the relatively small number of ground-based measurements is an additional challenge. Gauges are the most direct way of measuring rainfall. However, in sub-Saharan Africa, the gauge networks are not dense enough to represent accurately such rainfall events. Gauge observations are sparse there, and their number has been decreasing over the last decades. Similarly, the amount of data from ground-radar is limited, and they only cover an infinitesimal part of the continent. Another challenge in sub-Saharan Africa, and in the Tropics in general, is the lower performance of numerical weather models (and reanalysis) compared to the mid-latitudes ([Haiden et al., 2012](#); [Ebert et al., 2007](#)). In general, their performance in terms of precipitation is decreasing when the rainfall regime tends toward convection ([Ebert et al., 2007](#)).

Rainfall is mainly evaluated with respect to its intensity. However, rainfall events are moving coherent systems, thus they can also be described with respect to their timing,

position and shape. Position errors have been taken into account in the field of forecast verification with methods such as the SAL (Structure Amplitude Location, [Wernli et al. \(2008\)](#)), the MODE (Method for Object-based Diagnostic Evaluation, [Davis et al. \(2006\)](#)), and neighbourhood methods ([Ebert, 2008](#)), to name just a few. These methods are rarely used for the evaluation of rainfall estimates other than forecasts from Numerical Weather Prediction (NWP) models, even though the position of a rainfall event can be as important as its intensity. This is true especially for some applications such as hydrological modelling or data assimilation in a numerical model. Position and timing errors are not completely distinct. For example, from the point of view of a gauge, a spatial shift can be seen as a delay in the timeseries. Nevertheless, timing errors received little attention regarding the evaluation of rainfall estimates. Timing errors were more studied in the field of hydrological modelling ([Ball, 1994](#); [Singh, 1997](#); [Máca and Torfs, 2009](#)). The reason being that the temporal pattern of the rainfall events can have a significant impact on the outputs of hydrological models.

There are different types of precipitation data available. We mentioned above the gauge measurements and the numerical models, but there is also an increasing number of satellite-based rainfall estimates available (see Chapter 2). They are covering large areas, and are representing convective rainfall better than NWP models. Most of them are merging rainfall estimates derived from different instruments and sensors. Some are also using data from gauges or NWP models. Estimates can be merged in different ways. Estimates covering different areas can be stitched together to cover a larger domain. If they are covering the same area, the “best” estimate can be selected or they can be combined together, for example with a weighted average. One estimate can also be used to calibrate another one. In general, the merging is done with respect to the rainfall intensity. An exception are CMORPH (CPC morphing technique, [Joyce et al. \(2004\)](#)) and IMERG ([Huffman et al., 2018](#)). In CMORPH, motion vectors are derived from one type of estimates and applied to a second one to obtain a higher temporal resolution while keeping the better accuracy of the second estimate.

Many satellite-based estimates use gauge data for bias correction and/or merge them. Both bias correction and merging are generally done with respect to the intensity. There are different bias correction methods. The multiplicative adjustment method consists of computing the ratio of the gauge-based to the satellite-based estimates averaged over an area, and then multiplying the satellite-based estimate by the ratio. The additive adjustment is similar, instead of the ratio, the difference between the (averaged) gauge-based and the (averaged) satellite-based estimates is computed and then added to the satellite-based estimate. Sometimes, these two methods are combined ([Huffman et al., 1997, 2007](#)). The Probability Density Function (PDF) matching is another type of bias correction method (e.g. in [Xie et al. \(2017\)](#)). Pairs of gauge- and satellite-based estimates are used locally to build Cumulative Density Function (CDF) tables. The bias is removed by assuming that at a given percentage point, the precipitation intensity should be the same in the CDF table for satellite estimates as in the CDF table from gauge data. Merging is usually done by using a weighted average. There are some exceptions, such as ARC2 (African Rainfall Climatology Version 2) and RFE2 which are using the blending method from [Reynolds \(1988\)](#): the rainfall intensity is determined by the gauge data (where available), while the shape of the rainfall events is defined by the satellite-based

estimate.

Field deformation methods form a category of spatial verification methods based on the distortion of a forecast field to make it as similar as possible to a target or observation field (Gilleland *et al.*, 2009). These methods are particularly interesting because they produce a spatial mapping (that is a field of distortion vectors). This mapping can be used to quantify the error between the two fields, but can also be applied to the forecast field to correct it. Therefore, field deformation methods are also used in the framework of data assimilation (e.g. in Hoffman and Grassotti (1996); Nehrkorn *et al.* (2014); Brewster (2003); Ravela *et al.* (2007)). Mandel *et al.* (2010) described a framework based on such methods to assimilate radar precipitation data into a NWP model, but they did not implement it or apply it to rainfall data. We will refer to this field deformation method as warping hereafter. We will explore the application of warping for the correction of other type of rainfall estimates. In particular, we want to use gauge data that is non-gridded as opposed to the gridded fields used in the above mentioned studies. We are focusing on the gauge-adjustment of satellite-based estimates. The goal is to gauge-adjust them with respect to the position and to the timing of the rainfall events, instead of the usual bias adjustment of the intensity.

## RESEARCH QUESTIONS

Rainfall data is essential for many applications, and at the same time there is an increasing number of rainfall products available. This large large choice of products makes it difficult to select the best one for a specific application. In a large inter-comparison study, Sun *et al.* (2018) examined the discrepancies between 30 global rainfall data set at different time-scales. They found large differences in northern Africa (among other regions). This means that the choice of a precipitation product can have a large impact on one's application. This makes the choice of a rainfall product more critical, and led us to the following research question:

- What is the state of the art of rainfall products over Africa?

To answer this question, we performed a systematic review of existing inter-comparison and validation studies to identify the strengths and limitations of the different rainfall products, including the regional ones that have been specifically developed for Africa. From this review, we noticed that most of the validations were done with respect to the rainfall intensity or occurrence. However, rainfall can also be considered from the perspective of rainfall events. Rainfall events can be described by their position and timing (beside their intensity). A position or timing error will result in an occurrence or intensity mismatch. Thus, an important question is to what extent the discrepancies between the rainfall estimates can be explained by position and timing errors, and if they can be corrected. Many satellite-based estimates use gauge data for bias adjustment or to merge it with a prior estimate. That is, they use gauge data to adjust the intensity of the estimate. Thus, we investigate a method to gauge-adjust estimates with respect to the position or timing information instead of the intensity.

- What is the best way to use warping to correct position errors in rainfall estimates?
- What is the best way to use warping to correct timing errors in rainfall estimates?

## THESIS OUTLINE

This thesis consists of five chapters including this introduction chapter. Chapters 2 to 4 try to answer the research questions.

Chapter 2 reviews the different types of rainfall products and their performance over sub-Saharan Africa. It includes three types of products: numerical models and reanalysis, satellite-based products, and gauge-only products. After discussing the various factors influencing their performance, recommendations are given about which products to use depending on the applications. This chapter also includes the description of the algorithm of the most used satellite-based estimates, showing how they are merging/using the different types of data.

Chapter 3 investigates the possibility to use gauge measurements to correct a rainfall estimate with respect to the position of the event. We adapted an image warping method originally designed for data assimilation (Mandel *et al.*, 2010; Beezley and Mandel, 2008). Three approaches with different assumptions about the time dimension are evaluated.

Since rainfall events are moving systems, the temporal and spatial dimension are related. A position error can sometimes be seen as a timing error, and vice-versa. Chapter 4 focuses on the time dimension, and explores the potential of warping to correct timing errors. The previous image warping method is adapted to 1D data (timeseries). Three warping approaches are considered, each with a different assumption on the spatial connection between the timeseries.

The final chapter synthesizes the main findings of this thesis, before discussing possible improvements and future work.

## REFERENCES

- Food and A. Organization, eds., *The State of Food and Agriculture 2016: Climate Change, Agriculture and Food Security* (FAO, 2016) p. 173.
- A. K. Dezfuli, C. M. Ichoku, K. I. Mohr, and G. J. Huffman, *Precipitation characteristics in West and East Africa from satellite and in situ observations*, *Journal of Hydrometeorology* **18**, 1799 (2017).
- B. J. Abiodun, *Numerical Modelling of Mesoscale convective systems over West Africa*, Ph.D. thesis, Federal University of Technology, Akure, Nigeria (2003).
- M. V. K. Sivakumar and J. L. Hatfield, *Spatial variability of rainfall at an experimental station in Niger, West Africa*, *Theoretical and Applied Climatology* **42**, 33 (1990).
- L. Le Barbé, T. Lebel, and D. Tapsoba, *Rainfall variability in West Africa during the years 1950–90*, *Journal of Climate* **15**, 187 (2002).
- T. Haiden, M. J. Rodwell, D. S. Richardson, A. Okagaki, T. Robinson, and T. Hewson, *Intercomparison of global model precipitation forecast skill in 2010/11 using the SEEPS score*, *Monthly Weather Review* **140**, 2720 (2012).
- E. E. Ebert, J. E. Janowiak, and C. Kidd, *Comparison of near-real-time precipitation estimates from satellite observations and numerical models*, *Bulletin of the American Meteorological Society* **88**, 47 (2007).

- H. Wernli, M. Paulat, M. Hagen, and C. Frei, *SAL—a novel quality measure for the verification of quantitative precipitation forecasts*, *Monthly Weather Review* **136**, 4470 (2008).
- C. Davis, B. Brown, and R. Bullock, *Object-based verification of precipitation forecasts. part i: Methodology and application to mesoscale rain areas*, *Monthly Weather Review* **134**, 1772 (2006).
- E. E. Ebert, *Fuzzy verification of high-resolution gridded forecasts: a review and proposed framework*, *Meteorological Applications* **15**, 51 (2008).
- J. E. Ball, *The influence of storm temporal patterns on catchment response*, *Journal of Hydrology* **158**, 285 (1994).
- V. P. Singh, *Effect of spatial and temporal variability in rainfall and watershed characteristics on stream flow hydrograph*, *Hydrological Processes* **11**, 1649 (1997).
- P. Máca and P. Torfs, *The influence of temporal rainfall distribution in the flood runoff modelling*, *Soil and Water Research* **4**, S102 (2009).
- R. J. Joyce, J. E. Janowiak, P. A. Arkin, and P. Xie, *CMORPH: A method that produces global precipitation estimates from passive microwave and infrared data at high spatial and temporal resolution*, *Journal of Hydrometeorology* **5**, 487 (2004).
- G. J. Huffman, D. T. Bolvin, D. Braithwaite, K. Hsu, R. Joyce, C. Kidd, E. J. Nelkin, S. Sorooshian, J. Tan, and P. Xie, *NASA Global Precipitation Measurement (GPM) Integrated Multi-satellite Retrievals for GPM (IMERG)*, Algorithm Theoretical Basis Document Version 5.2 (NASA GSFC, Greenbelt, MD 20771, USA, 2018) [Available online at [https://pmm.nasa.gov/sites/default/files/document\\_files/IMERG\\_ATBD\\_V5.2\\_0.pdf](https://pmm.nasa.gov/sites/default/files/document_files/IMERG_ATBD_V5.2_0.pdf)].
- G. J. Huffman, R. F. Adler, P. Arkin, A. Chang, R. Ferraro, A. Gruber, J. Janowiak, A. McNab, B. Rudolf, and U. Schneider, *The Global Precipitation Climatology Project (GPCP) combined precipitation dataset*, *Bulletin of the American Meteorological Society* **78**, 5 (1997).
- G. J. Huffman, D. T. Bolvin, E. J. Nelkin, D. B. Wolff, R. F. Adler, G. Gu, Y. Hong, K. P. Bowman, and E. F. Stocker, *The TRMM Multisatellite Precipitation Analysis (TMPA): Quasi-global, multiyear, combined-sensor precipitation estimates at fine scales*, *Journal of Hydrometeorology* **8**, 38 (2007).
- P. Xie, R. Joyce, S. Wu, S.-H. Yoo, Y. Yarosh, F. Sun, and R. Lin, *Reprocessed, bias-corrected CMORPH global high-resolution precipitation estimates from 1998*, *Journal of Hydrometeorology* **18**, 1617 (2017).
- R. W. Reynolds, *A real-time global sea surface temperature analysis*, *Journal of Climate* **1**, 75 (1988).
- E. Gilleland, D. Ahijevych, B. G. Brown, B. Casati, and E. E. Ebert, *Intercomparison of spatial forecast verification methods*, *Weather and Forecasting* **24**, 1416 (2009).

- R. N. Hoffman and C. Grassotti, *A technique for assimilating SSM/I observations of marine atmospheric storms: Tests with ECMWF analyses*, *Journal of Applied Meteorology* **35**, 1177 (1996).
- T. Nehr Korn, B. Woods, T. Auligné, and R. N. Hoffman, *Application of feature calibration and alignment to high-resolution analysis: Examples using observations sensitive to cloud and water vapor*, *Monthly Weather Review* **142**, 686 (2014).
- K. A. Brewster, *Phase-correcting data assimilation and application to storm-scale numerical weather prediction. Part I: Method description and simulation testing*, *Monthly Weather Review* **131**, 480 (2003).
- S. Ravela, K. Emanuel, and D. McLaughlin, *Data assimilation by field alignment*, *Physica D: Nonlinear Phenomena* **230**, 127 (2007), data Assimilation.
- J. Mandel, J. D. Beezley, K. Eben, P. Jirus, V. Y. Kondratenko, and J. Resler, *Data assimilation by morphing fast fourier transform ensemble Kalman filter for precipitation forecasts using radar images*, (2010) UCD/CCM Report 289.
- Q. Sun, C. Miao, Q. Duan, H. Ashouri, S. Sorooshian, and K.-L. Hsu, *A review of global precipitation data sets: Data sources, estimation, and intercomparisons*, *Reviews of Geophysics* **56**, 79 (2018).
- J. D. Beezley and J. Mandel, *Morphing ensemble Kalman filters*, *Tellus A* **60**, 131 (2008).



# 2

## COMPARISON OF RAINFALL PRODUCTS OVER SUB-SAHARA AFRICA

*A cloudy sky doesn't always cry rain.*

African proverb

*Choosing the most adapted rainfall product for one's specific application is important because of the impact it has on the performance. This choice is made difficult by the increasing number of rainfall products available. Here, we perform a systematic review of previous works evaluating or comparing rainfall products in order to understand the strengths and limitations of such products. This chapter is meant as a guide through the numerous rainfall products available over Africa, and the factors influencing their performance. Its goal is to help the reader make informed decisions about which products serve their specific purpose best.*

*We focus on sub-Saharan Africa because of the considerable socio-economic impacts of rainfall there. Moreover, the low density of the gauge and radar networks makes the rainfall products particularly valuable.*

---

This chapter is based on:

**C. Le Coz**, and N. van de Giesen, *Comparison of Rainfall Products over Sub-Saharan Africa*, [Journal of Hydrometeorology](#) **21**, 553–596 (2020).



## 2.1. INTRODUCTION

Knowledge about precipitation is very important in sub-Saharan Africa, since 95% of the agriculture there is rain-fed (Food and Organization, 2016), making farmers vulnerable to climate change and extreme weather. Rainfall is a difficult variable to estimate accurately due to its large spatial variability. Even more so in Africa, since rainfall there is mainly generated by convective rainstorms, which can be very localized in time and space.

There are different types of precipitation data available in Africa. In-situ measurements from gauges can be accurate, but reporting weather stations are especially sparse over Africa. Their number is often under the minimum recommended by World Meteorological Organization (WMO), and has been decreasing. The national meteorological agencies are often underfunded, and so cannot maintain or upgrade their station network, for example some manual stations might still work but are not reporting to the global systems such as Global Telecommunication System (GTS). Another possible source of data is satellite estimation. They are covering large area, but are more indirect. They derive precipitation rates from other measurements such as cloud properties (e.g. cloud top temperature and radiation scattering by ice particles). There also have been efforts to use lightning observations (Xu *et al.*, 2013, 2014), or satellite soil moisture data (Brocca *et al.*, 2013, 2014). A third possibility are precipitation fields from numerical weather models. They can be used to estimate both past (reanalysis) and future (forecast) precipitation, or to better understand the mechanism of the monsoon. They can cover the entire globe for long periods or focus on a region with high temporal and spatial resolution. These three different sources of data have different advantages and limitations. Rainfall products can be based on one or several sources to combine the advantages and cancel out limitations.

Different global rainfall products are available at different spatial and temporal scales. Some regional rainfall products have been developed and calibrated especially for Africa or a specific region. These various products use very different approaches to derive rainfall estimates. They can be divided into three categories: 1) Reanalyses, based on a numerical weather prediction models and on data assimilation, 2) Gauge-only products, derived only from gauge data, and 3) Satellite-based products, based only or partially on satellite data. Most of the latter ones use gauges for calibration or bias adjustment and a few (e.g. CMAP<sup>1</sup> and CHIRPS<sup>2</sup>) also use data from models. Tables 2.1, 2.2 and 2.3 give a comprehensive list of rainfall products available over Africa for these three categories respectively. The algorithms of the most used satellite-based products are described in appendix B, along with a review of their performances over Africa from various evaluation studies.

All these products differ in various ways. They have different advantages and weaknesses. Moreover, precipitation data are used for different purposes, such as hydrological applications, climatology studies, flood or drought early warning systems or water management and planning. Depending on the application, the relevant characteristics are not the same. For instance, for drought monitoring one is interested in the good representation of small rainfall amounts (Maidment *et al.*, 2014), while for climatology,

<sup>1</sup>CPC Merged Analysis of Precipitation.

<sup>2</sup>Climate Hazards Group InfraRed Precipitation (CHIRP) with Station data.

Table 2.1: Non-exhaustive list of reanalysis available over Africa, ordered by increasing spatial resolution then by temporal resolution. (RT=Real-Time)

Name	Data input	Spatial coverage	Temporal coverage	Spatial resolution	Temporal resolution	Latency	Reference
<b>R1</b>	Reanalysis	Global	Jan 1948 - present	$2.5^\circ \times 2.5^\circ$	6-hourly	updated monthly	Kalnay <i>et al.</i> (1996)
<b>R2</b>	Reanalysis	Global	Jan 1979 - present	$2.5^\circ \times 2.5^\circ$	6-hourly	updated monthly	Kanamitsu <i>et al.</i> (2002)
<b>JRA-25</b>	Reanalysis	Global	Jan 1979 - Feb 2014	T106 ( $\sim 120\text{km}$ or $\sim 1.125^\circ$ )	6-hourly, monthly	-	Onogi <i>et al.</i> (2007)
<b>ERA-Interim</b>	Reanalysis	Global	Jan 1979 - present <sup>a</sup>	T255 ( $\sim 0.703^\circ \times \sim 0.702^\circ$ )	3-hourly, monthly	2 month (updated monthly)	Dee <i>et al.</i> (2011)
<b>MERRA</b>	Reanalysis	Global	Jan 1979 - Feb 2016	$0.5^\circ \times 0.66^\circ$	3-hourly, monthly	-	Rienecker <i>et al.</i> (2011)
<b>MERRA-2</b>	Reanalysis	Global	Jan 1980 - present	$0.5^\circ \times 0.625^\circ$	3-hourly, monthly	2-3 weeks (updated monthly)	Gelaro <i>et al.</i> (2017)
<b>JRA-55</b>	Reanalysis	Global	Dec 1957 - present	TL319 ( $\sim 55\text{km}$ or $\sim 0.56^\circ$ )	3-hourly, monthly	updated monthly	Kobayashi <i>et al.</i> (2015)
<b>CFSR</b>	Reanalysis	Global	Jan 1979 - Dec 2010	T382 ( $\sim 38\text{km}$ or $\sim 0.313^\circ$ )	6-hourly, monthly	-	Saha <i>et al.</i> (2010)
<b>ERA-5</b>	Reanalysis	Global	Jan 1979 <sup>b</sup> - present	TL639 ( $\sim 31\text{km}$ or $\sim 0.28125^\circ$ )	hourly, monthly	2/3 month (5 days for RT version)	Hersbach <i>et al.</i> (2018)
<b>CFSv2</b>	Reanalysis	Global	Jan 2011 - present	T574 ( $\sim 0.205^\circ$ )	6-hourly, monthly	updated daily	Saha <i>et al.</i> (2014)

<sup>a</sup> will end in August 2019, and be replaced by ERA-5.

<sup>b</sup> will be extended back to 1950.

consistency of the product's performance in time is more important, e.g. no changes in the bias due to a new input data. In a recent review, [Sun \*et al.\* \(2018\)](#) described 30 datasets (including gauge-based, satellite-related and reanalysis data), and examined the discrepancies between them at different timescales. They found large differences in northern Africa (among other regions). This means that the choice of a precipitation product can have a large impact on one's application. It is difficult to know which rainfall product, among the many existing ones, is the best to use according to the region of interest and the application considered, but also to know why and to which extent it is reliable. It is important to compare them with each other and be aware of their advantages, their limits and their relative performances.

The International Precipitation Working Group ([IPWG](#)) is supporting the intercomparison of rainfall products (<http://www.isac.cnr.it/~ipwg/>). They are maintaining a list of publicly available, quasi-operational, and quasi-global products, and are conducting some verification/validation over selected regions (Australia, Europe, Japan, South Africa, South America and US) against ground-based radar and gauge networks. So far, they have not yet conducted any validation/comparison project over sub-Saharan Africa. The [IPWG](#) only takes into account the satellite- and gauge-products, they do not compare them with precipitation estimates derived from numerical weather prediction models or reanalysis. Several model inter-comparison projects with focus on Africa (or West Africa) as well as a (global) reanalysis inter-comparison project exist (see section 2.2). They take into account not only precipitation but also other atmospheric variables.

Many inter-comparisons and validations studies of rainfall estimates have been done at a global and regional scale, as implied by the number of articles cited in the remainder of the article. One of the most comprehensive evaluation has been done by [Beck \*et al.\* \(2017a\)](#), who compared 22 rainfall products at a global scale. However, regional studies, even when using less products, are also very relevant. Global studies have access to less in-situ measurements in sub-Saharan Africa than in other regions such as Europe or America, while regional ones often used additional gauge data from national meteorological agencies or other organizations (see, for example, the reference data used in the global study of [Beck \*et al.\* \(2017a\)](#) and the one used in the regional comparison of [Dinku \*et al.\* \(2007\)](#)). Moreover, regional rainfall products (such as [TARCAT<sup>3</sup>](#) or [RFE2<sup>4</sup>](#)) are not included in global inter-comparisons. A literature review of inter-comparison and validation works has already been done by [Maggioni \*et al.\* \(2016\)](#). They focused on seven global satellite-based products. In this paper, we focus on performance of rainfall products in sub-Sahara Africa and include more products, especially regional ones. In addition, we include rainfall estimates obtained from numerical models and from gauge-only products. The main target audience are scientists and decision makers who need rainfall products for a specific application and do not necessarily want to acquire in-depth knowledge of all products available.

In this paper, we review rainfall products and their performance over sub-Saharan Africa in existing literature. We first look at three types of precipitation estimates: those from models and reanalysis (Section 2.2), satellite-based ones (Section 2.3), and those

<sup>3</sup>Tropical Applications of Meteorology using SATellite data and ground based observations (TAMSAT) African Rainfall Climatology And Timeseries.

<sup>4</sup>Rainfall Estimate version 2

based on gauges data only (Section 2.4). The factors influencing the performance of these products are then discussed in Section 2.5.2.5.1. Finally, Section 2.5.2.5.2 focuses on seven use-cases and their requirements in terms of rainfall data. Some recommendations are given with respect to these applications. The algorithm of a rainfall products is also important in order to understand what to expect from the product; its performance is linked to its algorithm. The main addition of the present review to the extensive literature is that we guide the reader to the best product for a specific application and that we do this by explaining the underlying algorithm with their specific strengths and weaknesses. In the appendix B, the algorithms of the most used products are shown using a uniform structure, making them easy to compare.

## 2.2. REANALYSIS AND MODELS

The uncertainties of a reanalysis depend on the uncertainties of the numerical model and the uncertainties of the observations it uses. However, rainfall is difficult to simulate accurately with numerical models, since it results from a complex interaction of the different model physics. Thus, we will first look at precipitation estimates in global models before moving to reanalyses and then to dynamical downscaling. Another possible way of downscaling global reanalysis to smaller scales is to use a statistical model instead of a numerical one. This method is called statistical downscaling, and has been applied to African rainfall as well (Nikulin *et al.*, 2018; Gebrechorkos *et al.*, 2019). However, in contrast to dynamic downscaling, it has not been the object of an extensive validation or inter-comparison project. The reason why statistically downscaled datasets are less evaluated is that they are downscaled using the very observations needed for such evaluation. One would expect that, in general, statistically downscaled datasets already outperform dynamically downscaled datasets regarding statistics, although Nikulin *et al.* (2018) did not see this in their comparison between four dynamically and two statistically downscaled datasets. Statistical downscaling falls outside the scope of this review, and thus will not be treated in the remainder of the article.

### 2.2.1. GLOBAL CIRCULATION MODELS (GCMs)

Xue *et al.* (2010) and Hourdin *et al.* (2010) evaluated the ability of several GCMs (along regional models and other datasets) to represent the West African monsoon. They showed that GCMs, when they used specified Sea Surface Temperature (SST), reproduce reasonably the main features of the West African monsoon, such as the migration of the Inter Tropical Convergence Zone. However, large discrepancies remained between the GCMs and the other datasets. A possible reason of the GCMs limitations could be their coarse resolution. However, Cr  tat *et al.* (2014) showed that a model with higher resolution is not necessarily better at representing daily intense events. Both Hourdin *et al.* (2010) and Cr  tat *et al.* (2014) pointed out the model's physics, and more specifically the convection parameterization, as an important factor influencing the GCM's performance.

Intercomparison studies (Haiden *et al.* (2012), Ebert *et al.* (2007)) at a global scale have shown that GCMs have poorer forecast skill in the Tropics than the extra-Tropics. They explained that lower performance in the Tropics by the difficulty of GCMs to predict convective precipitation. In general, the skill of models decreases when rainfall tends to

Table 2.2: Non-exhaustive list of satellite-based rainfall products available over Africa or African regions, ordered by increasing spatial resolution then by temporal resolution (italic=reanalysis product, bold=gauge-only product). The input data only used indirectly are put between parenthesis. IR=Thermal InfraRed, PMW=Passive MicroWave, sat-radar=satellite radar, RT=Real-Time.

Name	Data input	Spatial coverage	Temporal coverage	Spatial resolution	Temporal resolution	Latency	Reference
<b>CAMS-OP1</b>	gauges, IR	global	Jan 1979 - present	$2.5^\circ \times 2.5^\circ$	monthly	~5 days	Janowiak and Xie (1999)
<b>GPCP-SG</b>	IR, PMW, gauges	Global	Jan 1979 - present	$2.5^\circ \times 2.5^\circ$	monthly	~3 month	Huffman and Bolvin (2013); Adler <i>et al.</i> (2018)
<b>CMAP</b>	IR, PMW, gauges (RT in enhanced version)	Global	Jan 1979 - present	$2.5^\circ \times 2.5^\circ$	pentad <sup>a</sup> , monthly	irregular	Xie and Arkin (1996, 1997)
<b>GPCP-pentad</b>	GPCP-SG, CMAP	Global	Jan 1979 - Dec 2017	$2.5^\circ \times 2.5^\circ$	pentad	-	Xie <i>et al.</i> (2003)
<b>GPCP-IDD</b>	IR, PMW, GPCP-SG	Global	Oct 1996 - present	$1.0^\circ \times 1.0^\circ$	daily	~3 month	Huffman <i>et al.</i> (2001); Adler <i>et al.</i> (2017)
<b>SM2RAIN</b>	sat-radar ERA5 (gauges)	Land (global)	Jan 2007 - Dec 2018	$12.5km \times 12.5km$	daily	irregularly	Brocca <i>et al.</i> (2019)
<b>TM2P3-3B43</b>	IR, PMW, sat-radar, gauges	50S-50N	Jan 1998 - present	$0.25^\circ \times 0.25^\circ$	monthly	~2 month	Huffman <i>et al.</i> (2007); Huffman and Bolvin (2018)
<b>PERSIANN-CDR</b>	IR, GPCPv2.2 (PMW)	60S-60N	Jan 1983 - (delayed) present	$0.25^\circ \times 0.25^\circ$	daily, monthly	varying	Hsu <i>et al.</i> (2014); Ashouri <i>et al.</i> (2015)
<b>CMORPH v0.X</b>	IR, PMW, gauges	60S-60N	Dec 2002 - present	$8km \times 8km, 0.25^\circ \times 0.25^\circ$	half-hourly, 3 hourly	~18 hours	Joyce <i>et al.</i> (2004)
<b>CMORPH v1.0 (CRT)</b>	IR, PMW, gauges	60S-60N	Jan 1998 - Nov 2018	$8km \times 8km, 0.25^\circ \times 0.25^\circ$	half-hourly, 3 hourly	-	Xie <i>et al.</i> (2017)
<b>TM2P3-3B42</b>	IR, PMW, sat-radar, gauges	50S-50N	Jan 1998 - mid 2019	$0.25^\circ \times 0.25^\circ$	3 hourly	~2 month (8 hours for the RT version starting Mar 2000)	Huffman <i>et al.</i> (2007); Huffman and Bolvin (2018)

<sup>a</sup>end in December 2017.

Table 2.2: (continued)

Name	Data input	Spatial coverage	Temporal coverage	Spatial resolution	Temporal resolution	Latency	Reference
<b>PERSIANN</b>	IR, PMW	60S-60N	Mar 2000 - present	$0.25^\circ \times 0.25^\circ$	hourly	~ 2 days	Sorooshian <i>et al.</i> (2000); Hsu and Sorooshian (2008)
<b>ARC2</b>	IR, gauges	20W-55E-40S-40N	Jan 1983 - present	$0.1^\circ \times 0.1^\circ$	daily	~ 13 hours	Novella and Thiaw (2013)
<b>RFE2</b>	IR, PMW, gauges, other rain-fall products	20W-55E-40S-40N	Jan 2001 - present	$0.1^\circ \times 0.1^\circ$	daily	~ 13 hours	Xie and Arkin (1996); NOAA, CPC (2001)
<b>MSWEP v2.0</b>		global	Jan 1979 - Oct 2017	$0.1^\circ \times 0.1^\circ$	3 hourly	irregularly	Beck <i>et al.</i> (2017b, 2019)
<b>GSMaP standard</b>	IR, MWP (sat-radar, model)	60S-60N	Mar 2000 - present	$0.1^\circ \times 0.1^\circ$	hourly	3 days (4 hours for RT version starting Oct 2008)	Ushio <i>et al.</i> (2009); Aonashi <i>et al.</i> (2009)
<b>GSMaP-gauge</b>	IR, MWP, gauges (sat-radar, model)	60S-60N	Mar 2000 - present	$0.1^\circ \times 0.1^\circ$	hourly	3 days (4 hours for the RT version starting Jan 2017)	Mega <i>et al.</i> (2014)
<b>IMERG - early &amp; late</b>	IR, PMW, sat-radar, gauges	60S-60N	Mar 2014 - present	$0.1^\circ \times 0.1^\circ$	half-hourly	~ 4-12 hours	Huffman <i>et al.</i> (2018)
<b>IMERG - final</b>	IR, PMW, sat-radar, gauges	60S-60N	Jun 2014 - present	$0.1^\circ \times 0.1^\circ$	half-hourly	~ 2.5 month	Huffman <i>et al.</i> (2018)
<b>CHIRPS</b>	IR, TMPA3B42, gauges, CFSv2, CHP-clim	50S-50N	Jan 1981 - present	$0.05^\circ \times 0.05^\circ$ $0.25^\circ \times 0.25^\circ$	daily, pentad	3 weeks after end of month (rapid version 2 days after end of pentad)	Funk <i>et al.</i> (2014, 2015a)
<b>PERSIANN-CCS</b>	IR (PMW)	60S-60N	Jan 2003 - present	$0.04^\circ \times 0.04^\circ$	hourly	~ 1 hour	Hong <i>et al.</i> (2004)
<b>TARCAT</b>	IR (gauges)	Africa (land)	Jan 1983 - present	$0.0375^\circ \times 0.0375^\circ$ ~ 4km	daily, pentad	~ 2 days after end of pentad	Maidment <i>et al.</i> (2014); Tamavsky <i>et al.</i> (2014); Maidment <i>et al.</i> (2017)

convective regime.

### 2.2.2. REANALYSES

There is no regional reanalysis for Africa, however several global reanalysis are produced. A list of such reanalysis is given in Table 2.1 (see articles in reference column for detailed descriptions). An overview of the different reanalyses, including the observations used in the analysis, can be found in [Fujiwara et al. \(2017\)](#).

Global reanalyses are based on global models and thus suffer from the same short-coming as [GCMs](#) despite improvements due to assimilation of observations. Like [GCMs](#), reanalyses have lower performance in the Tropics. [Bosilovich et al. \(2008\)](#) showed that the performance in reproducing precipitation of four well-known reanalyses (namely [R1](#)<sup>5</sup>, [R2](#)<sup>6</sup>, [ERA-40](#)<sup>7</sup> and [JRA-25](#)<sup>8</sup>) was lower over South America and Africa compared to other regions, especially during the boreal summer, corresponding to the monsoon season. They gave two reasons for the poorer performance over the tropics, the difficulty to parameterize the land-atmosphere interaction and the difficult retrieval of satellite observation due to the cloudy conditions. Since conventional observations (ground-stations, radiosonde, aircraft,...) were sparse over South America and Africa, the effects were more visible over these regions.

As for the [GCMs](#), reanalyses are generally outperformed by satellite-based rainfall estimates ([Maidment et al., 2013](#); [Funk and Verdin, 2003](#); [Koutsouris et al., 2016](#)), with some exceptions in sparsely gauged area ([Thiemig et al., 2012](#); [Worqlul et al., 2014](#)). The main results of these studies, with respect to reanalyses, are summarized in Table 2.4. [Funk and Verdin \(2003\)](#) explained the lower skill of reanalyses by the limitation of [GCMs](#), such as the coarse grid and the physics, and by the few moisture-related observations used in the data assimilation. It has to be noted that, since this study, new reanalyses have been created and that they incorporate more moisture-related observations. For example, ERA-Interim assimilates rain-affected satellite radiance which were not used in ERA-40 ([Dee et al., 2011](#)). Most reanalyses do not assimilate precipitation observations directly. However, [MERRA](#)<sup>9</sup> assimilates satellite rain rates over the oceans, but with a low weight, so they have a weak impact on the analysis ([Rienecker et al. \(2011\)](#)). The very recent reanalysis [ERA-5](#)<sup>10</sup> uses precipitation data from satellite and ground-based radar ([Hennermann, 2019](#)). [MERRA2](#)<sup>11</sup> and [CFSR](#)<sup>12</sup> also use precipitation data for the forcing of the land surface model ([Saha et al., 2010](#); [Bosilovich et al., 2015](#)).

The most recent reanalyses have in general better performance than the older ones, due to improvement in both the model and the assimilation system ([Bosilovich et al., 2008](#); [Kim and Alexander, 2013](#)). However, this is not always the case everywhere and at all times ([Bosilovich et al., 2008](#); [Koutsouris et al., 2016](#); [Nkiaka et al., 2017](#)). Even more

<sup>5</sup>NCEP/NCAR Reanalysis

<sup>6</sup>NCEP/DOE Reanalysis

<sup>7</sup>European Centre for Medium-Range Weather Forecasts(ECMWF) ReAnalysis - 40

<sup>8</sup>Japanese Meteorological Agency (JMA) ReAnalysis - 25

<sup>9</sup>Modern-ERA Retrospective Analysis for Research and Applications

<sup>10</sup>European Centre for Medium-Range Weather Forecasts (ECMWF) ReAnalysis - 5

<sup>11</sup>Modern-ERA Retrospective Analysis for Research and Applications, version 2

<sup>12</sup>Climate Forecast System Reanalysis

Table 2.3: Non-exhaustive list of gauge-only rainfall products available over Africa or African regions, ordered by increasing spatial resolution then by temporal resolution.

Name	Data input	Spatial coverage	Temporal coverage	Spatial resolution	Temporal resolution	Latency	Reference
GPCC - first guess	Gauges	Land (global)	Jan 2009 (Aug 2004) - present	$1.0^\circ \times 1.0^\circ$	daily (monthly)	5 days	Schneider <i>et al.</i> (2014)
GPCC - monitoring	Gauges	Land (global)	Jan 1982 - present	$1.0^\circ \times 1.0^\circ$ $2.5^\circ \times 2.5^\circ$	monthly	2 month	Schneider <i>et al.</i> (2014)
GPCC-FDR	Gauges	Land (global)	Jan 1891 - Dec 2016	$0.25^\circ \times 0.25^\circ$ $0.5^\circ \times 0.5^\circ$ $1.0^\circ \times 1.0^\circ$ $2.5^\circ \times 2.5^\circ$	monthly	irregularly	Schneider <i>et al.</i> (2014)
GPCC-FDD	Gauges	Land (global)	Jan 1982 - Dec 2016	$1.0^\circ \times 1.0^\circ$	daily	irregularly	Schneider <i>et al.</i> (2014)
CRU TS	Gauges	Land (global excl. Antarctica)	Jan 1901 - Dec 2018	$0.5^\circ \times 0.5^\circ$	monthly	irregularly	Harris <i>et al.</i> (2014)
University of Delaware PREC/L	Gauges	Land (global)	Jan 1900 - Dec 2017	$0.5^\circ \times 0.5^\circ$	monthly	irregularly	Matsura and Willmott (2015)
CPC Unified	Gauges	Land (global)	Jan 1948 - present	$0.5^\circ \times 0.5^\circ$ $1.0^\circ \times 1.0^\circ$ $2.5^\circ \times 2.5^\circ$ $0.5^\circ \times 0.5^\circ$	monthly	1 week (except $0.5^\circ$ data)	Chen <i>et al.</i> (2002)
			Jan 1979 - present	$0.5^\circ \times 0.5^\circ$	daily	1-2 day(s)	Xie <i>et al.</i> (2007); Chen <i>et al.</i> (2008)



recent reanalyses are available, such as [MERRA2](#), [JRA-55](#)<sup>13</sup> and [CFSv2](#)<sup>14</sup>. However, no comparison of their performance for precipitation has been found in literature yet. The Stratosphere-troposphere Processes And their Role in Climate ([SPARC](#)) Reanalysis Intercomparison Project ([S-RIP](#)) is comparing reanalyses, including the most recent ones, and will publish a report (planned for October 2019). This inter-comparison project is described in [Fujiwara et al. \(2017\)](#), and more information is available on the [S-RIP](#) website <http://S-RIP.ees.hokudai.ac.jp>.

### 2.2.3. DYNAMIC DOWNSCALING

Running continuously a [GCM](#) at a fine resolution would be too computationally expensive, thus a possible solution is to dynamically downscale with a Regional Climate Model ([RCM](#)). A lot of attention has been given to regional downscaling the last decades and several projects have applied [RCMs](#) to obtain an ensemble of multi-model climate projections. Over West Africa, such projects include the [ENSEMBLES](#)-based Predictions of Climate Changes and Their Impacts ([ENSEMBLES](#))- African Monsoon Multi-disciplinary Analyses ([AMMA](#)), the West African Monsoon Modeling and Evaluation project ([WAMME](#)) model intercomparison study ([Xue et al., 2010](#); [Druyvan et al., 2010](#)) and, more recently, the Coordinated Regional climate Downscaling Experiment ([CORDEX](#)) that has a study region over all Africa. The [AMMA](#)-Model Intercomparison Project ([AMMA-MIP](#), [Hourdin et al. \(2010\)](#)) has compared the ability of different models (both [GCM](#)s and [RCMs](#)) to reproduce the West African Monsoon ([WAM](#)). Other studies comparing [RCMs](#) over Africa or West Africa include [Sylla et al. \(2013\)](#) and [Cr  tat et al. \(2014\)](#). They all agree on the added-value of [RCMs](#) compared to [GCMs](#).

The [RCMs](#) are able to reproduce more realistically the features of the monsoon (such as the interannual variability, the annual cycle or the spatial patterns) than the [GCMs](#) and reanalyses. This shows the importance of regional forcing. The higher resolution of [RCMs](#) improves the simulation in several ways. It allows a better representation of the orography, an important regional forcing, which improves the simulation of orographic rainfall ([Druyvan et al. \(2010\)](#)). It also improves the representation of land-surface properties (such as land-cover) that play an important role in the [WAM](#) ([Sylla et al., 2013](#); [Paeth et al., 2011](#)). However, [RCMs](#), with horizontal resolution around 50km, still have difficulties in reproducing both the phase and the intensity of the diurnal cycle ([Nikulin et al., 2012](#)). An explanation could be the choice of the convection scheme to which the diurnal cycle is sensitive.

The outputs of the [RCMs](#) are influenced by the data (usually a reanalysis or a [GCM](#)) used for the initial and boundary forcing ([Druyvan et al., 2010](#); [Druyvan and Fulakeza, 2013](#)). However, [RCMs](#) driven by the same reanalysis can have very different accuracies with bias varying considerably in space and time ([Druyvan et al., 2010](#); [Sylla et al., 2013](#); [Paeth et al., 2011](#); [Nikulin et al., 2012](#)). These differences highlight the importance of the dynamics and physics of each model. An advantage of [RCMs](#) compared to [GCMs](#) is that they give the possibility to choose physics more adapted to the region, and not to the entire globe. [GCMs](#) cover the entire globe and so have to represent a large variety of climates. On the contrary, [RCMs](#) focus on a smaller region, and so can choose physics

<sup>13</sup>Japanese Meteorological Agency (JMA) ReAnalysis - 55

<sup>14</sup>Climate Forecast System version 2

Table 2.4: Reanalysis performance over Africa in literature.

Region	<a href="#">Koutsouris et al. (2016)</a>	<a href="#">Maidment et al. (2013)</a>	<a href="#">Funk and Verdin (2003)</a>	<a href="#">Thiemig et al. (2012)</a>	<a href="#">Worqlul et al. (2014)</a>
	Kilombero Valley (Tanzania)	Uganda	Western Kenya	4 African river basins (Zambezi, Volta, Shabelle and Baro-Akobo)	Lake Tana basin (Ethiopia)
<b>Reanalysis</b>	CFSR, ERA-Interim, MERRA	ERA-40, ERA-Interim	NCEP/NCAR R1	ERA-Interim	CFSR
<b>Other rainfall products</b>	CMORPH, CRU, GPCC, UDEL	RFE2, GPCP-1DD, TAM-SAT	RFE1	CMORPH, GPROF, GSMaP	TMPA3B42, MPEG
<b>'Truth'</b>	TMPA3B42	27 gauges from the Ugandan Met Service	134 gauges	205 gauges	38 gauges from the NMA
<b>Method</b>	Correlation, RMSE, bias, NS efficiency; scatter plots	Bias, RMSE, coefficient of determination, scatter plot, spatial pattern, seasonal cycle	Scatter plot; coefficient of regression; bias; time series	- Point-to-pixel: highest rainfall timing and quantity, number of rainy day - Sub-catchment scale: bias, correlation, Nash coefficient, Q-Q plot - Basin scale: annual average, standard deviation	Coefficient of determination, RMSE, bias
<b>Resolution</b>	$0.25^\circ \times 0.25^\circ$ , monthly	$0.5^\circ \times 0.5^\circ$ , dekad	$0.1^\circ \times 0.1^\circ$ , dekad	Point-to-pixel, $0.1^\circ \times 0.1^\circ$ , and subcatchment scale from daily to seasonal	Point-to-pixel and areal (river basin) daily
<b>Time period</b>	1998-2010	(February-June) 2001-2005	(March-May) 1996-1998	2003-2006	2010
<b>Results</b>	- Reanalysis have a good temporal correlation, but poor spatial statistics (especially CFSR). - GPCC generally has the best performance	- The three satellite-based products outperform the two reanalysis. - ERA-Interim tends to overestimate. - ERA-40 tends to underestimate.	- RFE outperforms the NCEP/NCAR R1 reanalysis	- ERA-Interim overestimates number of rainy day. - ERA-Interim overestimates light precipitation and underestimates. - RFE2 and TMPA3B42 have the best performance, GPROF and GSMaP the worst, and ERA-Interim is in between	- CFSR better performance than TMPA3B42. - MPEG best performance. - TMPA3B42 poor performance (attributed to the orography and the absence of gauges in this area)

parameterizations better suited for the particular climate of this region.

A review of RCM applications in West Africa can be found in Sylla *et al.* (2013) and a review of regional downscaling is given in Paeth *et al.* (2011).

## 2

## 2.3. SATELLITE-BASED PRODUCTS

### 2.3.1. SATELLITE-BASED RAINFALL ESTIMATES

The satellite-based products are based on data from different sensors and satellites. They can also include other data sources, such as ground-radar, gauge network or forecast from model or reanalysis. A list of satellite-based rainfall products, including the type of input they are using, is given in Table 2.2.

Satellites retrieve different types of observations from various sensors such as visible, infrared (IR), passive micro-wave (PMW) and radar measurements. IR measurements are used in many rainfall products. They have the advantage of being frequent and of covering large areas. However, precipitation is estimated through its relationship to Cloud Top Temperature (CTT) derived from thermal IR. This relationship is indirect and varies within and between rain events (Kidd and Levizzani, 2011; Kidd and Huffman, 2011). On the other hand, PMW measurements are less frequent (PMW sensors are only present on low-Earth orbiting satellites) but the relation to precipitation is more direct. PMW-based precipitation estimates are generally more accurate than IR-based ones, but have difficulties over snow-covered and desert areas (Kidd and Levizzani, 2011; Kidd and Huffman, 2011). Satellite-radar measurements for precipitation retrieval are limited: only the Tropical Rainfall Measuring Mission (TRMM), the Global Precipitation Measurement (GPM) and the CloudSat missions have a radar specifically designed to retrieve precipitation (Kidd and Levizzani, 2011; Kidd and Huffman, 2011). A rainfall product can combine different types of measurement to take advantage of their strengths and overcome their weaknesses. For example, many products combine IR measurements with the more accurate but less frequent PMW observations. TMPA<sup>15</sup> and IMERG<sup>16</sup> are the products using the most different types of measurements as input data: IR, PMW, satellite-radar and gauges. They are the only ones using satellite-radar as input (CMORPH<sup>17</sup> uses ground-radar over USA for adjustment), while CMAP and CHIRPS are the only ones using data from numerical models.

Other products with a very different approach include SM2RAIN<sup>18</sup> and MSWEP<sup>19</sup>. SM2RAIN is based on soil moisture observations from satellites and ground measurements. It inverts the soil water balance equation to obtain precipitation estimates. MSWEP does not use satellite measurements directly, instead it is based on other rainfall dataset (e.g. CMORPH, ERA-Interim, GPCC-FDR, ...). A longterm mean precipitation (from CHPclim<sup>20</sup>) is downscaled using precipitation anomalies obtained by a weighted average of different reanalyses, gauge and satellite products. Its goal is to take advantage of the strengths of different types of rainfall products.

<sup>15</sup>TRMM Multi-satellite Precipitation Analysis

<sup>16</sup>Integrated Multi-satellite Retrievals for GPM

<sup>17</sup>CPC Morphing technique

<sup>18</sup>Soil Moisture to Rainfall

<sup>19</sup>Multi-Source Weighted-Ensemble Precipitation

<sup>20</sup>Climate Hazards Group's Precipitation Climatology (Funk *et al.*, 2015b)

Satellite-based products differ by the data (different types of measurement coming from different satellites/sensors) used as input and by their algorithms deriving the final precipitation estimates. As a consequence, the error of a satellite-based product is partially due to the error in the retrieval algorithm (i.e. estimating precipitation from the sensors measurements), and partially due to the merging algorithm, (i.e. combining the different estimates in the final precipitation estimate).

### 2.3.2. REGIONAL VS GLOBAL

There exist several regional rainfall products especially developed for and only covering Africa. They have been compared to global products in various studies for different regions of Africa. Their results are summarized in Table 2.5.

The performance of the regional products and their advantages with respect to the global products vary from region to region. Over the Sahel, both **RFE2** and **TARCAT** are performing well in rainfall detection and in estimating rainfall amounts, at least as well as the global products (*Jobard et al., 2011; Pierre et al., 2011; Novella and Thiaw, 2010; Dinku et al., 2015*). However, over Burkina Faso, which is part of the Sahel, **TARCAT** has been shown to have very poor performance by *Dembélé and Zwart (2016)*, while **RFE2** and **ARC2** were outperforming **TMPA**. *Gosset et al. (2013)* showed that regional products (**RFE2**, **EPSAT**<sup>21</sup>) tend to underestimate rainfall amounts while global and especially near-real time ones overestimate it over the South of West Africa. Over East Africa, regional products do not perform as well, and **TMPA** and **CMORPH** tend to show the best performances. **RFE2** has particularly poor performance over Ethiopia despite some skill for rainfall detection. It is outperformed by most of the global products over this region (*Dinku et al., 2007, 2008a, 2011a*). Over Ethiopia, **TARCAT** still shows some agreement with gauge data despite underestimating (*Dinku et al., 2007*). Over Uganda, **TARCAT** has a similar performance as **CMORPH** and **TMPA**, while **ARC2** outperform **RFE2** (*Asadullah et al., 2008; Diem et al., 2014*). In general, over a large part of East Africa, **TARCAT** and **RFE2** have relatively similar and reasonable performances. They outperform some global products (e.g. **PERSIANN**<sup>22</sup> and **GSMaP**<sup>23</sup>) while they are outperformed by others such as **TMPA3B42** (*Cattani et al., 2016*).

Regional products show very good result and perform as well as or better than the most used global products. However, it can not be concluded that the regional products outperform global ones as a general rule. For example, the algorithm of **RFE2** is not suitable for regions with complicated orography such as Ethiopia. More information about the algorithms and the performance of the regional products is given in Appendices B.2.A.8 (for **RFE2**), B.2.A.9 (for **ARC2**) and B.2.A.12 (for **TARCAT**).

### 2.3.3. GAUGES DATA IN SATELLITE-BASED PRODUCTS

Satellite-based rainfall products can also use data other than satellite data in their algorithms. For instance **CMORPH** uses ground-radar data to adjust the cloud motion vec-

<sup>21</sup> Estimation of Precipitation by SATEllites

<sup>22</sup> Precipitation Estimation from Remotely Sensed Information using Artificial Neural Networks

<sup>23</sup> Global Satellite Mapping of Precipitation

Table 2.5: Regional and global satellite-based products performance over Africa in literature.

Region	Jobard <i>et al.</i> (2011)	Pierre <i>et al.</i> (2011)	Novella and Thiaw (2010)	Dembélé and Zwart (2016)	Gosset <i>et al.</i> (2013)	Dinku <i>et al.</i> (2015)
Regional rainfall products	EPSAT-SG, RFE2	TARCAT, RFE2	RFE2, ARC, TARCAT	ARC2, RFE2, TARCAT	RFE2, EPSAT-SG	EAO-RFE, RFE2, TARCAT
Global rainfall products	GSMaP, TMPA3B42, CMORPH, RT, GPI	GPCP-1DD, PERSIANN, CMORPH, TMPA3B42	TMPA3B42-RT, CMORPH, CPC Unified	CHIRPS, CDR, TMPA3B43	PERSIANN, CMORPH, TMPA3B42-RT, GSMaP, GPCP-1DD, TMPA3B42	CMORPH, TMPA3B42
Truth	570 gauges (AGRHYMET)	3 gauge networks: CLASS (~600), AGRHYMET (~250) and SYNOP (~80)	133 gauges (gridded in three different way)	9 gauges	2 high resolution network from the AMMA-CATCH Observing system	400 stations (Ethiopia) + 30 stations (Sudan) + 200 stations (AGRHYMET)
Method	Scatter plot, distribution, bias, WRMSE, $R_2$ , efficiency, spatial distribution of bias and RMSE	Linear regression statistics, MAE, spatial structure, daily occurrence, dry spell distribution, impact on vegetation modeling	POD, POFD, HK, OR, correlation, RMSE, bias, precision performance	Correlation, ME, bias, RMSE, NS efficiency, POD, FAR, scatter plot, distribution	Mean, std., coef. of variation, bias, $R_2$ , RMSE, NS efficiency, % of misses, FAR, distribution, impact on hydrological applications	POD, FAR, FB, HSS, ME, MAE, Bias, NS efficiency, CDF, scatter plot
Resolution	$0.5^\circ \times 0.5^\circ$ , dekadal	$0.5^\circ \times 0.5^\circ$ , dekadal	$0.5^\circ \times 0.5^\circ$ , daily (occurrence) and dekadal (amount)	Point-to-pixel: daily, dekadal, monthly, annual	$1^\circ \times 1^\circ$ , daily	$0.25^\circ \times 0.25^\circ$ (Sahel + Ethiopia) and point-to-pixel (Sudan); daily and dekadal
Time period	(June-Sept.) 2004-2006	2004-2007	(June-Sept.) 2008	2001-2014	(June-Sept.) 2003-2010	2007-2009
Results	<ul style="list-style-type: none"> <li>- Regionals products best</li> <li>- Real-time products worst (and overestimate)</li> <li>- <b>EPSAT best performance</b>, but RFE2 have the lowest bias and best distribution curve</li> </ul>	<ul style="list-style-type: none"> <li>- <b>RFE2 and TMPA3B42 best performance</b></li> <li>- CMORPH overestimates, RFE2 underestimates</li> <li>- RFE2 highest rainfall frequency, TMPA3B42 lowest</li> </ul>	<ul style="list-style-type: none"> <li>- Rain/no-rain discrimination: <b>RFE2 and CMORPH best</b></li> <li>- Continuous statistics: <b>RFE2 and ARC best</b>, TMPA and PERSIANN worst</li> <li>- Precision: RFE2, ARC and CPC Unified best</li> <li>- all underestimate high rainfall values (TMPA less)</li> </ul>	<ul style="list-style-type: none"> <li>Daily scale: all poor</li> <li>Dekadal and monthly scale:</li> <li>- <b>RFE2 best performance, followed by ARC2 and then CHIRPS</b></li> <li>- TARCAT poor performance (except for FAR)</li> <li>- All underestimate, except PERSIANN which overestimates;</li> <li>Annual scale: all overestimates, except TARCAT</li> </ul>	<ul style="list-style-type: none"> <li>- Regional products underestimate (too many days with low rainfall)</li> <li>- Global products, especially real-time ones, overestimate (high rain rate)</li> <li>- Real-time products good correlation but high bias</li> <li>- <b>EPSAT-SG best correlation</b>, while RFE2 low correlation and bias</li> </ul>	<ul style="list-style-type: none"> <li>- <b>The Sahel:</b></li> <li>- No significant difference at daily scale</li> <li>- At dekadal scale, <b>RFE2 best, followed by TARCAT</b></li> <li>- CMORPH lowest NS efficiency</li> <li>- <b>Ethiopia:</b></li> <li>- At dekadal scale, TMPA3B42 worst performance, followed by RFE2</li> <li>- <b>TARCAT and CMORPH better</b></li> </ul>

Table 2.5: (continued)

Region	Dinku <i>et al.</i> (2007)	Dinku <i>et al.</i> (2008a)	Dinku <i>et al.</i> (2011a)	Asadullah <i>et al.</i> (2008)	Diem <i>et al.</i> (2014)	Cattani <i>et al.</i> (2016)	Toré <i>et al.</i> (2015)
Ethiopia	Ethiopia	Ethiopia, Zimbabwe	Ethiopian highlands, lowlands (parts of Ethiopia, Djibouti and Somalia)	Uganda	Western Uganda	East Africa	Mozambique
<b>Regional rainfall products</b>	RFE2, ARC2, TARCAT	RFE2	ARC, RFE2	RFE2, TARCAT	ARC2, RFE2	RFE2, TARCAT	RFE2, TARCAT
<b>Global rainfall products</b>	GPCP-MS, GPCP-SG, CMAP, TMPA3B43, GPCP-1DD, TMPA3B42, CMORPH 120 gauges	TMPA3B42, TMPA3B42-RT, CMORPH, PER-SIANN, NRLB	TMPA3B42, CMORPH	PERSIANN, TMPA3B42, CMORPH	TMPA3B42	CMORPH, TMPA3B42, SIANN	CHIRPS
<b>'Truth'</b>	120 gauges	~140 stations in Ethiopia, ~60 stations in Zimbabwe	~75 gauges, and FAO reports	39 gauges (divided in 4 regions)	6 gauges	GPCC-FDR	26 gauges
<b>Method</b>	Correlation, ME, RMSE, NS efficiency, bias, scatter plot, CDF	Correlation, ME, MAE, NS efficiency, bias, POD, FAR, CSI, ETS, HK, HSS, CDF	FB, POD, FAR, HSS, correlation, NS efficiency, bias, ME, RMSE	Correlation, bias, NS efficiency, RMSE	FAR, POD, FB, HSS, bias, NS efficiency	Correlation, ME, MAE, RMSE, NS efficiency, bias	Correlation, ME, RMAE, NS efficiency, bias, POD, FAR, ETS, HK, HSS, FB
<b>Resolution</b>	2.5° × 2.5°, monthly; and 1° × 1°, 0.5° × 0.5° and 0.25° × 0.25°, dekadal	0.25° × 0.25° (and 0.5° × 0.5° and 1° × 1° over Ethiopia), daily	gridded (Ethiopia) and point-to-pixel (lowlands); daily (occurrence) and dekadal (amount)	average over each region, monthly average (over 1960-1990)	Point-to-pixel; daily (occurrence), and monthly to annual (amount)	Cluster (with similar rainfall annual cycles), monthly	point-to-pixel; dekadal
<b>Time period</b>	1990-2004 (monthly); (June-Sep), 2000-2004 (dekadal)	(June-Sep); 2003-2004 (Ethiopia); (Jan.-Mar.) 2003 (Zimbabwe)	2003-2004 (Ethiopia); field campaign (lowlands)	1960-1990 (averaged)	2001-2010	2001-2009	2001-2012
<b>Results</b>	- CMORPH and TARCAT best (except for TARCAT's bias) - ARC2 worst, followed by RFE2 - TMPA3B42 better than GPCP-1DD - RFE1 better than RFE2 (RFE1 includes orographic effect, not RFE2) - At low resolution, GPCP, CMAP and TMPA3B43 good (CMAP and TMPA3B43 best)	- Over Ethiopia, CMORPH and TMPA3B42 relationally better - Over Zimbabwe, RFE2 and TMPA3B42 best - TMPA3B42-RT, NRLB and PERSIANN poor over both region - RFE1 better than RFE2 over Ethiopia, while RFE2 slightly better over Zimbabwe - Errors decrease for coarser grid	Over the highlands: - CMORPH best performance, ARC worst rainfall occurrence and amount Over the dry lowland: - All underestimate severely, both occurrence and amount - All poor performance	- CMORPH, TMPA3B42, TARCAT good ability in reproducing temporal seasonal patterns - RFE2 less good but still some skill - PERSIANN worst performance - All better at estimating occurrence than amount - All underestimate in the highland region	- All limited performance - TMPA3B42 best - RFE2 worst performance - Only monthly amount were estimated satisfactorily by some products - All tend to overestimate rainfall days	- TMPA3B42 best performance (but not independent) - PERSIANN worst performance - CMORPH, RFE2 and TARCAT reasonable performance - CMORPH generally better than GSMaP - All less good over complex orography	- CHIRPS best continuous stat. - RFE2 best categorical stat. - RFE2 recommended for dry spell assessments - CHIRPS best during cyclone season - TARCAT best frequency bias

tors derived from IR data. Other products, such as GPCP-1DD<sup>24</sup> or PERSIANN-CDR<sup>25</sup>, are using other rainfall products, namely GPCP-SG<sup>26</sup>. Many satellite-based products, which are listed in Table 2.6, are using gauge data. Gauge data can be used in different ways.

Table 2.6: List of satellite-derived rainfall products using gauge data and how they are used in their algorithms

	Calibration	Bias adjustment	Merged
ARC2			x
CAMS-OPI			x
CHIRPS		x	x
CMAP			x
CMORPHv1.0 CRT		x	
CMORPHv1.0 BLD		x	x
GPCP-SG		x	x
GPM		x	x
GSMaP_gauge		x	
RFE2			x
TARCAT	x		
TMPA		x	x

The bias of a product varies depending on the region of interest, and is different from one product to another. For example, CMORPH tends to overestimate while GSMaP tends to underestimate over the Sahel (Jobard *et al.*, 2011) and PERSIANN overestimates almost everywhere over Africa except over mountainous areas over which it underestimates. Bias correction using gauge data can reduce significantly the bias. It has been shown by Jobard *et al.* (2011) that near-real time products, that do not include bias adjustment, have worse performance than the other global products over the Sahel, they especially have large bias. There are several methods to remove the bias using gauge data, such as scaling by the ratio of the gauge/satellite rainfall estimates (GPCP-SG and TMPA), or matching the probability density function of the satellite estimates with the one from the gauge data (CMORPH-Corrected (CRT)). PERSIANN-CDR is also bias adjusted, using monthly ratio, but based on another satellite-based product.

Some products merged satellite estimates, after bias adjustment or not, with gauge estimates. There are several ways of doing so. Some are using inverse error variance weighting (TMPA, IMERG, GPCP-SG) or other weighted average (CHIRPS), while other products are using directly the gauge-only estimate when reliable, and a blended satellite-gauge estimate elsewhere (ARC2, RFE2, CMAP, CAMS-OPI<sup>27</sup>).

Another way of using gauge data is for calibration as in TARCAT. Indeed, the TARCAT algorithm is calibrated locally to historical gauge data and is then applied to recent

<sup>24</sup>Global Precipitation Climatology Project (GPCP) at 1 day and 1 degree resolution

<sup>25</sup>PERSIANN - Climate Data Record

<sup>26</sup>Global Precipitation Climatology Project (GPCP) - Satellite-Gauge

<sup>27</sup>Climate Anomaly Monitoring System (CAMS) and Outgoing longwave radiation Precipitation Index (OPI)

IR data. **TARCAT** does not use gauge data for bias adjustment or merging, but has been shown to perform well over different parts of Africa despite a dry bias for the high intensity rain-rates. Over Ethiopia, [Dinku et al. \(2007\)](#) found that **TARCAT** performed better than some gauge-adjusted products such as **TMPA3B42**, **RFE2** and **GPCP-IDD** (except with respect to the bias). [Jobard et al. \(2011\)](#) showed that the regional products, including **TARCAT**, performed better than global bias-adjusted ones over the Sahel. A benefit of using historical data, as **TARCAT** does, is that it takes advantage of data from gauges that no longer exist. Similarly, **CMORPH-CRT** uses a two-step approach for the bias adjustment over land. It first removes the climatic bias using historical data and then adjusts to real-time data ([Xie et al., 2017](#)). This approach is particularly beneficial for areas with very sparse gauge coverage.

## 2.4. GAUGE-ONLY PRODUCTS

There exist various gridded gauge-only products (see Table 2.3). Some are updated regularly, from a few days to a few months latency, such as Climate Prediction Center (**CPC**) Unified, PRECipitation REConstruction over Land (**PREC/L**), Global Precipitation Climatology Centre (**GPCC**)-first guess, and **GPCC**-monitoring. Others are updated irregularly, such as **GPCC**-Full Data Reanalysis (**GPCC-FDR**), **GPCC**-Full Data Daily (**GPCC-FDD**), University of Delaware dataset (**UDEL**) and Climatic Research Unit Time-series (**CRU-TS**), for which a new version is available every few years with reprocessed data for the entire period. They are produced at relatively coarse spatial and temporal resolutions compared to satellite-based rainfall products. Their spatial resolution ranges from  $0.5^\circ \times 0.5^\circ$  to  $2.5^\circ \times 2.5^\circ$  and they are available as monthly estimates except for **CPC** Unified, **GPCC**-first guess and **GPCC-FDD** which are available for daily totals.

### 2.4.1. FACTORS INFLUENCING THE PERFORMANCE OF GAUGE-ONLY PRODUCTS

The gauge coverage in Africa, with the exception of a few regions such as South Africa, is sparse. Moreover, the number of recording stations (available for these products) varies over space and time, and has significantly decreased during the last decades. This decrease of available gauge records is shown in [Lorenz and Kunstmann \(2012, Fig. 3 and Fig. 4\)](#) for **GPCC** and **CPC** Unified datasets for the period 1989-2006, in [Cattani et al. \(2016, Fig. 8\)](#) for **GPCC-FDR** over East Africa between 2001-2009, in [Maidment et al. \(2014, Fig. 3d\)](#) for **GPCC-FDR** over Africa for the period 1983-2010 (a clear drop in gauges coverage is visible around 2009) and in [Dinku et al. \(2008b, Fig. 3\)](#) for three **GPCC** products, **PREC/L** and **CRU-TS** over Ethiopia for the period 1981-2000, over which the number of gauges decreases sharply around 1985. The decreasing number of recording stations in Africa is a known issue ([van de Giesen et al., 2014](#)), and is mainly due to a lack of funding for the maintenance and upgrading of the gauge network. **GPCC-FDR** product being a reanalysis, the decrease of records used for the last years is also due to the time delay in obtaining data from national agencies.

The relation between the gauge coverage and the accuracy of gridded products has been observed by [Maidment et al. \(2014\)](#). They compared **TARCAT** with various rainfall products over Africa for the period 1983-2010 and found less agreement between the



three gauge-only products (CRU, GPCC-FDR and PREC/L) during 2000-2010, this period corresponding to a sharp decrease of recording gauges. Similar results were found by Dinku *et al.* (2008b) when comparing PREC/L, CRU-TS, GPCC-FDR and GPCC-clim over Ethiopia for two different periods: 1981-1985 and 1996-2000. Far less gauge records were available for the products during the second period and this decrease had an impact on product accuracy. Indeed, more discrepancies in time series were observed during the second period than during the first one. Moreover, the correlation and Nash-Sutcliffe (NS) efficiency coefficients decreased between the first and the second period, while the mean average error increased for the four products.

Dinku *et al.* (2008b) studied the impact of the number as well as the quality of gauge records on product performance by comparing three GPCC monthly products (GPCC-monitoring, GPCC-FDR and GPCC-clim) over the complex topography of Ethiopia at  $2.5^\circ \times 2.5^\circ$  and  $1.0^\circ \times 1.0^\circ$  resolution. These three products are using the same interpolation method but different number of gauges and different quality requirements. GPCC-monitoring is using reports received through GTS within a month after the observation month while GPCC-FDR is produced irregularly and so can also use non-real-time data and apply higher quality-check so it includes more stations and those stations are of better quality than those in GPCC-monitoring. GPCC-clim uses less stations but of higher quality since it requires the stations to have a time-series that is at least 90% complete. They all had similar performances with GPCC-monitoring having a larger bias, GPCC-clim having higher random error, and GPCC-FDR having a relative better performance. The performances of gridded products vary in time and space depending on the gauges coverage. It is recommended to interpret the gauge-estimate with respect to the gauges density information supplied with it.

The gauge coverage has an impact on the accuracy of the products, but the number of gauge records alone does not determine the performance of the products. When comparing four gauge-only products to the reference at three different spatial resolutions, Dinku *et al.* (2008b) showed that they all have good performance with high correlation and NS efficiency, and very low bias. However, despite using the largest number of stations and high quality-check among the products, CRU-TS had overall the worst statistics, behind GPCC-clim using the least number of stations. So, its limitation comes from its interpolation method. A better gauge coverage does not always mean better accuracy, the interpolation method also has an impact on a product's performance.

To summarize, the accuracy of the estimates do not depend on the gauge coverage alone, but also on the the quality-check and the interpolation method used by a gauge-only product.

#### 2.4.2. GAUGE-ONLY VERSUS SATELLITE-BASED PRODUCTS

The gauge-only products have been evaluated over Ethiopia by Dinku *et al.* (2008b), but not over other parts of Africa. However, gauge-only products have been compared to satellite-based product over different African regions. These studies are summarized in Table 2.7, and their main results with respect to the gauge-only products are described below.

Ali *et al.* (2005) compared the gauge-only GPCC product and three satellite-based ones (CMAP, GPCP and GPI) at monthly scale and  $2.5^\circ$  over the Sahel. They concluded

Table 2.7: Gauge-only products performance over Africa in literature.

	Ali <i>et al.</i> (2005)	Novella and Thiaw (2010)	Okoro <i>et al.</i> (2014)	Maidment <i>et al.</i> (2014)	Dinku <i>et al.</i> (2008a)	Dinku <i>et al.</i> (2011b)
<b>Region</b>	The Sahel	The Sahel	Niger Delta region (Nigeria)	Africa	Ethiopian highlands	Ethiopian highlands
<b>Gauge-only product</b>	GPCC	CPC Unified	CRU	CRU, PREC/L	GPCC-monitoring, GPCC-FDR, GPCC-clim, CRU, PREC/L	GPCC-FDR, CRU
<b>Other rainfall products</b>	GPCP, CMAP, GPI	RFE2, ARC, TMPA3B42-RT, CMORPH, PERSIANN, TARGAT	CMAP	TARGAT, GPCPV2.2, CMAP, ARC2,	none	GPCP, CMAP, RFE2, TMPA3B42, CMORPH
<b>'Truth'</b>	3 gauge networks from AGRHYMET: CILSS (650), CRA (250), and SYNOP (80)	133 gauges (gridded in three different ways)	6 gauges from the Nigerian Meteorological Agency (NIMET)	- (intercomparison)	137 gauges from the NMA of Ethiopia	150 gauges from the NMA of Ethiopia
<b>Method</b>	RMSE, bias, correlation, NS efficiency, scatter plot, histogram, distribution	POD, POFD, HK, OR, correlation, RMSE, bias, precision performance	bias, linear regression, correlation, T-test, RMSE, skill score (BSS), rainfall variability index, moisture flux accumulation	Spatial annual climatology, annual/seasonal mean bias, mean monthly annual cycle, monthly and annual correlation matrix	ME, MAE, NS efficiency, bias, scatter plot	correlation, bias, MAE, NS efficiency, POD, FAR, HSS, scatter plot
<b>Resolution</b>	$2.5^\circ \times 2.5^\circ$ , monthly	$0.5^\circ \times 0.5^\circ$ , daily (currency) and dekadal (amount)	Point-to-pixel, monthly	$2.5^\circ \times 2.5^\circ$ , monthly	$2.5^\circ \times 2.5^\circ$ , $1.0^\circ \times 1.0^\circ$ and $0.5^\circ \times 0.5^\circ$ , monthly	$2.5^\circ \times 2.5^\circ$ , $1.0^\circ \times 1.0^\circ$ and $0.5^\circ \times 0.5^\circ$ monthly, $0.25^\circ \times 0.25^\circ$ , $0.5^\circ \times 0.5^\circ$ and $1.0^\circ \times 1.0^\circ$ , dekadal and daily
<b>Time period</b>	(July-September) 1990-1999	(June-September) 2008	1981-2004	1983-2010	1981-2000	1981-2004 (monthly); (summer) 2003-2004 (daily)
<b>Results</b>	- <b>CMAP best</b> followed by GPCC and GCPC, while GPI worst - GPCC and GPCP perform better in the margins, and CMAP better in core of the rainy season - More discrepancy in the North - All underestimate frequency of low values, and overestimate frequency of medium values	- <b>Rain/no-rain discrimination:</b> RFE2 and CMORPH best - <b>Continuous statistics:</b> RFE2 and ARC best, TMPA and PERSIANN worst, CPC Unified and TARGAT low bias and RMSE - <b>Precision:</b> RFE2, ARC and CPC Unified best - All underestimate high rainfall values (TMPA less) - Overall: RFE2 and ARC best	- CRU better in representing monthly variability - CMAP better in representing interannual variability index for the total and wet season	- TARGAT dry bias - RFE2 dry bias during summer - Less agreement between gauge-only products during 2000-2010 (corresponding in a decrease of recording gauges)	- General good agreement - <b>GPCC-FDR relatively better</b> , followed by PREC/L, CRU and GPCC-clim - All better during wet season, and poor during dry one - GPCC-clim and GPCC-FDR overestimate low and high amount, while CRU overestimate moderate amount - Effect of gauge number and quality on performance	- All good performance - <b>GPCC better than CRU</b> - satellite-based products underestimate - <b>GPCP2.1 better than GPCPV2 and GPCC</b> Daily: - All poor for amount - Good detection skill - Dekad/daily: - <b>CMORPH best</b> , RFE2 worst (severe underestimation)

that **CMAP** had the better performance with, among others, smallest Root Mean Square Error (**RMSE**), and bias and highest coefficient of determination, followed closely by **GPCC** and **GPCP** with **GPI** far behind.

Over Ethiopia, **Dinku et al. (2011b)** evaluated the performance of two gauge-only products (**CRU-TS** and **GPCC-FDR**) and two satellite-based products (**GPCPv2** and **CMAP**), also monthly, at 2.5° resolution. All products gave good results with low bias and mean average error and high correlation and **NS** efficiency. The gauge-only products had no or lower bias but **CRU-TS** had a slightly larger random error. **GPCC-FDR** seemed to perform slightly better than the other ones. However, when **GPCPv2** and **GPCC-FDR** are compared to **GPCPv2.1**, which includes **GPCC-FDR** in his algorithm, the latter outperformed them, except for the bias that remains lower for **GPCC**.

**CPC Unified** was evaluated over the Sahel at higher resolution, which is for dekadal estimates on a 0.5° grid, along six satellite-based estimates by **Novella and Thiaw (2010)**. In terms of rainfall detection, **RFE** and **CMORPH** were outperforming the other products including **CPC Unified**. In term of statistics, **CPC Unified**, **RFE**, **ARC** and **TARCAT** had a low bias and **RMSE**, but **RFE** and **ARC** also had a higher correlation. They concluded that **RFE** and **ARC** had the overall best performances.

Gauge-only products have in general good performance with no or very low bias, but they do not significantly outperform satellite-based products over Africa.

## 2.5. DISCUSSION

### 2.5.1. FACTORS INFLUENCING THE PERFORMANCE

#### TEMPORAL AND SPATIAL SCALE

Performance of rainfall products is influenced by the temporal and spatial resolution at which they are evaluated. Performance improves for decreasing resolution, i.e. for coarser grids. One should pay attention to the temporal and spatial resolution when looking at validation or inter-comparison study of rainfall products.

**Dembélé and Zwart (2016)**<sup>1</sup> compared seven satellite-based rainfall products over Burkina Faso at different temporal resolutions: namely daily, dekadal, monthly and annual scale. They showed that both the continuous and categorical statistics improved when the temporal resolution decreased. At monthly and annual scale, all the products, except **TARCAT**, have very good performance in terms of continuous and categorical statistics. At dekadal scale the products are in good agreement with the gauges (e.g. correlation coefficients equal or larger than 0.80), while at daily scale the performance of the products was very low (with e.g. correlation coefficients smaller than 0.50). Similarly, **Dinku et al. (2011b)**<sup>2</sup> compared several satellite-based and gauge-only products over Ethiopia at different temporal and spatial scales. On a 1.0° × 1.0° grid, **RFE2**, **TMPA3B42** and **CMORPH** had reasonable performances in estimating rainfall amount at dekadal scale, but poor ones at daily despite still good detection skill. They also compared these three products at daily scale on three grids with different resolution, and showed that both continuous and categorical statistics were getting better when the spatial resolution decreased. In **Dinku et al. (2007)**<sup>1</sup>, six satellite-based rainfall products were compared at dekadal scale over Ethiopia using three different grid sizes. A decrease in the product's performance was observed when the spatial resolution was increased. Similar

results were found for the gauge-only products by [Dinku \*et al.\* \(2008b\)](#)<sup>2</sup>. They evaluated five products over Ethiopia at three different spatial resolutions for monthly amounts. Their performance was decreasing with increasing resolution, but still remained good.

### GAUGES

The gauge density varies in space and time, and so influences the performance of the gauge-only and satellite-based products. The reanalyses use ground-stations measurements but no rain-gauge data in their data assimilation process, so they are not directly impacted by gauge density. The exceptions are [MERRA2](#), [CFSR](#) and [CFSv2](#). They use precipitation data (such as [CMAP](#) and [CPC Unified](#)) as part of their land surface forcing. However, [MERRA2](#) uses [CMAP](#) and [GPCPv2.1](#) over Africa ([Bosilovich \*et al.\*, 2015](#), Table 7.1), and [CFSR](#) favored [CMAP](#) over [CPC Unified](#) in the Tropics ([Saha \*et al.\*, 2010](#)). Thus, gauge data have a very limited influence on the reanalyses' precipitation.

The accuracy of gauge-only products depends strongly on the number of gauges available, which is why the gauge density is given along the rainfall estimates for these products. However, as seen in section [2.42.4.1](#), the accuracy does not depend solely on gauge density. The quality of the data and the interpolation method also play an important role.

Many satellite-based products use gauge data (see section [2.32.3.3](#)). Thus, their performances are impacted by the availability of gauge data. For instance, the poor performance of [TMPA3B42](#) over lake Tana has been attributed to the orography and the lack of available gauge data by [Worqlul \*et al.\* \(2014\)](#). Moreover, the gauge data used in satellite-based products are in general a small fraction of the gauge records available (e.g. gauge-only products use a much larger number of gauge records than satellite-based products). An exception is [GPCP-SGv2.1](#) which uses [GPCC](#), a gauge-only product, for bias adjustment and merging. [Dinku \*et al.\* \(2011b\)](#) showed the benefit of adding more gauge data by comparing [GPCP-SGv2.1](#) with its previous version [GPCP-SGv2](#), which incorporated a smaller amount of gauge data, over the Ethiopian highlands. They found that the correlation improved from 0.96 to 0.99, the [NS](#) efficiency from 0.92 to 0.99, and that the random error became lower than the ones of both [GPCP-SGv2](#) and [GPCC](#).

### OROGRAPHY

The orography has an impact on the atmospheric circulation, and so on the precipitation field. It is thus an important regional forcing in numerical weather model. The coarse resolution of reanalysis and GCMs does not allow them to represent accurately complex orography, limiting their performance in simulating orographic rainfall. A possibility to improve the representation of orography and orographic rainfall is to dynamically down-scale the reanalysis using a [RCMs](#) ([Druyan \*et al.\*, 2010](#)).

Complex orography, and more generally warm-cloud processes, is a well-known challenge for satellite-based rainfall products ([Serrat-Capdevila \*et al.\*, 2014](#)). [IR](#)-based estimates have difficulties in capturing warm-cloud precipitation over coastal and orographic regions. This is mainly due to the threshold they use to discriminate between raining and non-raining clouds, which is too cold for such processes ([Dinku \*et al.\*, 2007](#),

<sup>1</sup> see [Table 2.5](#) for more details on the comparison method.

<sup>2</sup> see [Table 2.7](#) for more details on the comparison method.

2008a, 2011a). Products including **PMW** data seem to perform better than the ones mainly based on **IR** (Dinku *et al.*, 2007, 2011a). However, **PMW**-based precipitation estimates also have some limitations with respect to orographic rain. Indeed, **PMW**-algorithms are mainly based on scattering by ice aloft, but orographic rainfall is a warm-cloud process that does not necessarily produce much ice, which can lead to underestimation. Moreover, ice on the mountains can be mistakenly considered as rainfall by such algorithm (Dinku *et al.*, 2007, 2008a, 2011a).

Mountainous areas raise several difficulties for the gauge-only products too. There are few gauges at high elevations, most of the gauges are located at lower altitudes. The difficult access and remoteness of such locations make the installation and maintenance of weather stations complicated. At the same time, the variability of rainfall over mountainous regions is high. For example, Hirpa *et al.* (2010) showed the existence of an elevation-dependent trend, that is the rainfall amounts increase with elevation. Hence, the gauge measurements at the bottom of a mountain is not representative of the rainfall at higher altitudes. Moreover, the high spatial variability is making the interpolation more difficult.

#### RAINFALL REGIME

The characteristics of the seasonal distribution of rainfall at a particular place is called rainfall regime (American Meteorological Society, 2019). Rainfall regimes are influenced by large scale climatic features, such as the Inter Tropical Convergence Zone (**ITCZ**), and also by regional ones such as mountains and lakes. They vary in space and time depending on the climatic region and on the season. The rainfall regimes are influencing the performance of the rainfall products. Hence, their performance can differ over two regions adjacent to each others but with different rainfall regimes.

Some comparison studies took the different rainfall regimes into account. For instance, to compare six satellite-based products over East Africa, Cattani *et al.* (2016) divided this large area in eight smaller areas, each characterized by a specific precipitation seasonality. Areas with higher precipitation intensity showed a bigger standard deviation and mean average errors. The standard deviation also depends on the season since precipitation patterns change over the year. Some areas had an overall better correlation and **NS** efficiency for the different products than others. These differences between the areas show the influence of rainfall regimes on the performance of the products, a product can perform differently over two geographically close areas but having different rainfall regimes. Similarly, Romilly and Gebremichael (2011) compared the bias of three satellite-based products over six river basins in Ethiopia that were divided in four regions based on similar rainfall annual cycles and topography. They showed that the bias of these three products depended on the rainfall regime, i.e. the bias was different from one region to another but could also vary according to the season.

The variation in time of the rainfall products' performance was also shown by Ali *et al.* (2005) who compared three satellite-based products and one gauge-only product over the Sahel. The monthly mean statistics were better in the core of the rainy season for **CMAP** while **GPCP** and **GPCC** had better statistics in its margins. Dinku *et al.* (2008b) evaluated five gauge-only products over Ethiopia, and found that they performed better (i.e. higher correlation and **NS** efficiency) during the wettest season (JJA) and worse dur-

ing the dry season (DJF). They showed that these seasonal differences were more important when the comparison was done at higher spatial resolution. The poor performance during the dry season was attributed to the fact that rainfall during this season is local in both time and space and thus a denser network of gauges would be needed to reproduce the rainfall patterns. On the contrary, reanalyses perform more poorly during the monsoon season due to the convective nature of the rainfall. In general, the satellite-based estimates are expected to perform better in summers and in the tropics while models are expected to be better in winters and high-latitude; because the satellite-estimates tend to reproduce convective rainfall more accurately (Ebert *et al.*, 2007). The reanalyses and global models, in general, have been shown to perform more poorly over the tropics and to fail to reproduce some regional scale features. It is thus not surprising that the reanalyses are outperformed by satellite-based products over Africa and especially during the monsoon season.

Some climates are more difficult than others to represent, which is the case for arid areas by satellite-based products, for example. Jobard *et al.* (2011) compared ten satellite-based products over the Sahel and showed that they all had higher RMSE ratio in the northern part where rainfalls had low intensities. On the contrary, in Cattani *et al.* (2016), the six rainfall products had low RMSE and mean average error over arid areas. However, it has to be taken relatively since the monthly rainfall amount was also very low over these areas. Dinku *et al.* (2010) and Dinku *et al.* (2011a) had specifically studied the limitations of satellite-based precipitation estimates over arid areas. Dinku *et al.* (2011a) evaluated the skills of four rainfall products over an arid region in Ethiopia while Dinku *et al.* (2010) compared seven products over different arid and semi-arid regions. They both concurred on the poor performance of the different satellite products over such regions, especially the drier ones. The products overestimated the frequency of rainfall despite a low Probability Of Detection (POD). The low detection skill and the high overestimation was attributed to several possible reasons. First, the sub-cloud evaporation can play an important role in this overestimation. These regions have a dry atmosphere so the rainfall detected aloft by the satellite might evaporate before reaching the ground. Second, a limitation specific to PMW algorithm is that they can mistakenly identify desert surfaces as raining, because desert and snow cover have spectral characteristic close to rainfall (Wang *et al.*, 2009). Finally, the coarse resolution of the rainfall products can also be an explanation factor for the low POD, especially since they are compared to point-data. Indeed, a pixel might cover both rain and non-rainy (warm) surface, but the pixel represents the averaged values that may not be identified as rain. As mentioned above, gauge-only products can also have difficulties over dry areas, when the rainfall is localized.

### 2.5.2. USE CASES

The “best” rainfall products depends on the intended use cases. Sometimes, requirements on the spatial and/or temporal resolution can limit the possible choices (see Tables 2.1, 2.2 and 2.3 for the resolution of the different products). Depending on the application, some characteristics are more important than others. The important characteristics of seven use cases are discussed below. Recommendation about the rainfall products for these cases are given in Table 2.8.

Table 2.8: Recommendations depending on the use cases (based on literature, see Table 2.5).

Use cases	Recommendations
<b>Drought monitoring</b>	<ul style="list-style-type: none"> <li>- TARCAT, RFE2, ARC2 recommended.</li> <li>- Avoid RFE2 and ARC2 over mountainous areas.</li> <li>- Avoid RT products which have a large wet bias.</li> <li>- CHIRPS developed for drought monitoring, but advised for flood monitoring by <a href="#">Dembélé and Zwart (2016)</a> and <a href="#">Toté et al. (2015)</a>.</li> </ul>
<b>Agriculture / Crop modelling</b>	<ul style="list-style-type: none"> <li>- Not many comparison studies (only <a href="#">Pierre et al. (2011)</a> looks at vegetation modelling).</li> <li>- Depend on the region</li> <li>- RFE2 over the Sahel (both good for occurrence and amount).</li> <li>- CMORPH has good rain-no rain discrimination, but need bias correction (large wet bias).</li> </ul>
<b>Flood monitoring</b>	<ul style="list-style-type: none"> <li>- Avoid TARCAT, RFE2 and ARC2.</li> <li>- CHIRPS: developed for drought, but advised for flood over Burkina Faso and Mozambique by <a href="#">Dembélé and Zwart (2016)</a>. and <a href="#">Toté et al. (2015)</a></li> <li>- CMORPH : good detection skill, and (large) wet bias (except over Zimbabwe).</li> <li>- PERSIANN: high POD and positive bias, but very large bias and do not represent well distribution of high precipitation values (over the Sahel). To be used with caution.</li> <li>- Other possibilities: GPCP-1DD, TMPA3B42, GSMaP (but can have dry bias for some years/locations).</li> </ul>
<b>Hydrological modelling / Reservoir management</b>	<ul style="list-style-type: none"> <li>- Need to account for the bias of rainfall products (especially RT which have large bias).</li> <li>- Possible improvement by calibrating the model. (<a href="#">Gosset et al., 2013</a>; <a href="#">Thiemig et al., 2013</a>)</li> </ul>
<b>Climatology / General</b>	<ul style="list-style-type: none"> <li>- Depend on the regions.</li> <li>- General good agreement at monthly scale<sup>a</sup>.</li> <li>- PERSIANN-CDR, ARC2 (and CHIRPS) developed for climatology.</li> <li>- Gauge-only products: long time period, but accuracy varies in time.</li> <li>- Over the Sahel: regional products (except TARCAT over Burkina Faso), and CMAP at monthly scale (<a href="#">Ali et al., 2005</a>).</li> <li>- CHIRPS: good results, but only two studies (<a href="#">Dembélé and Zwart, 2016</a>; <a href="#">Toté et al., 2015</a>).</li> <li>- CMORPH: the algorithm have been modified during production of version v0.x, prefer v1.0 for climatology<sup>b</sup> (for more consistency in time). Be aware of its relatively large wet bias.</li> <li>- TMPA: in general reasonable performance</li> </ul>
<b>Mountainous areas</b>	<ul style="list-style-type: none"> <li>- CMORPH and TARCAT recommended.</li> <li>- Avoid RFE2, ARC2 and PERSIANN.</li> </ul>
<b>Diurnal cycle</b>	<ul style="list-style-type: none"> <li>- Only few studies at sub-daily scale.</li> <li>- Only studied over Niamey, Ouémé and Dakar. (<a href="#">Pfeifroth et al., 2016</a>; <a href="#">Roca et al., 2010</a>)</li> </ul>

<sup>a</sup>Performance of rainfall product increase for coarser resolution.<sup>b</sup>Version 1.0 has been reprocess with consistent input/algorithm.

- **Drought monitoring:** Droughts have a high economic cost, because of its pos-

sible large spatial and temporal scale. The agriculture in sub-Saharan Africa being mainly rain-fed, the population is vulnerable to such natural disaster. It can also impact the food and water security, for example the drought of the Horn of Africa in 2011 caused famine in several regions, and large population movement (Sheffield *et al.*, 2014). Hence, drought monitoring and early warning system are important in this region. These applications need precipitation data, in general one to ten day accumulation. One should avoid rainfall products that overestimate the occurrence or the amount of rainfall events. The good representation of the low intensity rainfall events is more important than the high ones. In terms of criteria, this translates by:

- Low False Alarm Rate (FAR, no overestimation of occurrence).
  - Low or dry frequency bias (no overestimation of occurrence).
  - Dry bias preferred (no overestimation of amount).
  - Low or negative ME (no overestimation of amount).
  - Distribution representing well the low precipitation values (representation of low rainfall events).
- **Agriculture/Crop modelling:** In sub-Saharan Africa, agriculture is mainly rain-fed, making the population highly vulnerable to rainfall variability. Rainfall information is therefore valuable for farmers, and an important input for crop modelling. Rainfall data are also used to derive rainfall indices for crop insurance. Such insurance helps the smallholder farmer to be more climate-resilient. For these types of applications, the chosen rainfall product should correctly represent the precipitation distribution over time and estimate accurately the amount per event. The good representation of dry spells is also important since they are influencing the vegetation growth. The most important criteria for these types of application are:
    - Low RMSE and MAE (accurate amount at pentadal and dekadal scale).
    - High coefficient of determination  $R^2$  or correlation coefficient
    - Good representation of dry spell occurrence.

This application is probably the most demanding in terms of accuracy and rainfall distribution.

- **Flood monitoring/Extreme events:** Sub-Saharan Africa is also vulnerable to floods. The number of deaths and economic losses due to floods have increased in the last decades (Thiemig *et al.*, 2011). The fast urbanization have increased the population vulnerability to such natural disasters. In this context, flood monitoring and early warning system are needed to reduce the human and economic losses (Thiemig *et al.*, 2011). Good estimation of flood events relies on precipitation data representing well the high intensity rainfalls. For such applications, rainfall products underestimating the occurrence and amount should be avoided. In terms of criteria, this translates by:



- High POD (no underestimation of occurrence).
  - Low or wet frequency bias (no underestimation of occurrence).
  - Wet bias preferred (no underestimation of amount).
  - Low or positive **ME** (no underestimation of amount).
  - Distribution representing well the high precipitation values (representation of intense rainfall events).
- **Hydrological modelling/Reservoir management:** Hydrological modelling is used for many applications linked to water management, such as reservoir management. Decisions made based on the results of such models can have an impact on the population, the economy or the environment ([Thiemig et al., 2013](#)). Precipitation data is one of the main input data, and so it can influence the accuracy of the output. The temporal resolution needed depends on the exact application, and can range from sub-daily to monthly. In general, a good estimation of both the occurrence and the amount of rainfall is needed. Bias correction as a pre-processing step can improve the model results. This is especially true when using a real-time products that have in general large bias. The results are also influenced by the model parameters. These parameters can be specifically calibrated for the chosen rainfall product, in order to improve the result's accuracy.
  - **General / Climatology:** Climatological applications needs long data records in order to study the trends and variations. However, most of the current studies are focused on a small number of years. Studies over longer time period would be interesting. For these types of applications, rainfall products need consistent performance in time. This can be an issue. Gauge-only products have long time coverage, but their performance varies with the gauge density. Similarly, more observations are available for reanalysis in more recent years, improving their performance. The sensors and sometimes the algorithms used for satellite-based products change in time, making them less consistent. The rainfall products should cover a long time period, and be able to represent the yearly and seasonal variability. Thus, the important criteria to look at are:
    - High correlation or coefficient of determination (good representation of the trend, little dispersion).
    - High **NS** efficiency (good fit, low relative residual variance).
    - Low RMSE (good fit, general low misfit).
  - **Mountainous areas:** Complex orography is a well-known difficulty for rainfall products (see section [2.52.5.1](#)). Their accuracy is lower than over flatter areas, and they tend to underestimate. However, some products have been shown to perform relatively better, while some others are more inadequate for mountainous areas.
  - **Diurnal cycle:** Most of the well-known rainfall products are available at a sub-daily scale. However, very few comparison and validation studies considered this scale. Diurnal cycle represents large precipitation variation within a day. They are

specifically studied by Pfeifroth *et al.* (2016) over the two sites of Niamey (Niger) and Ouémé (Benin). The diurnal cycle varies within the rainy season, but also from year to year. It can be characterized by the number of rainy peaks, their timing and their size.

The recommendations given in Table 2.8 focused on the satellite-based products because more literature was available for them. The most used of them are described in more details in the appendix B. The reanalyses and gauge-only products also have some strengths.

The main advantage of the gauge-only products is their long record period that go back to 1901 (while the satellite-based products do not start before 1979). However, the quality of the products varies in time with the gauge network density, which is particularly sparse in some African regions. The product using the highest number of records is GPCP-FDR, and it has to be noted however that this number varies a lot in time (Becker *et al.*, 2013). A drawback of some gauge-only products (GPCP-FDR, CRU-TS and UDEL) is their irregular update, making them unavailable for recent years studies. CRU-TS and UDEL also include other variables, such as the temperature, in a consistent format. Having a consistent dataset for both precipitation and temperature can be an advantage for some applications that need these two measurements.

The reanalysis have a higher temporal resolution than the gauge-only products, but also cover a shorter time period. They include many atmospheric variables. This can be useful for climatological applications that do not focus exclusively on precipitation, for example. They can also be used to understand better the mechanisms producing rainfall.

## 2.6. CONCLUSION

In this paper, we have reviewed the most used rainfall products and their relative performances. The choice of a product will depend on the intended application. However, different use cases have different requirements, that can guide us toward the “best choice”. Users also have to consider some factors influencing the accuracy of the products and so the results of their applications. These factors include the gauge density, the orography and the rainfall regime.

Various methods have been developed to derive rainfall from different types of data. Some of the most recent products build upon older ones. The algorithm of the NASA's newest rainfall product, IMERG, is based on the methods of previously existing products: (i) TMPA for the inter-calibration and merging of the PMW estimates and for the bias-adjustment, (ii) PERSIANN-CCS<sup>28</sup> for the PMW-calibrated IR estimates, and (iii) CMORPH-Kalman Filter for the merging of PMW and IR estimates. Similarly, the recent MSWEP product (first release in 2016 and version 2 in 2017), is not using a new algorithm to derive rainfall estimates from measurements. Instead, it uses already existing gauge-only, (non gauge-adjusted) satellite-based rainfall products, and reanalyses to derive anomalies while a corrected version of CHPClim is used for the the long-term mean precipitation.

<sup>28</sup>PERSIANN-Cloud Classification System

It is important to understand the method behind a rainfall product in order to understand its strengths and its limitations, or, in other words, to know how robust it is and to which extent one can trust it. The diagrams in appendix B are meant to facilitate such understanding across products. When choosing one rainfall product among all the existing ones, one should not only look at validation studies but at the description of the algorithm (Kummerow, 2017). Comparing fairly different products is difficult, the results depend on the reference dataset, on the method and on resolution. Moreover, the conclusion of a study might not hold for another region or rainfall regime. The algorithm's description will give an idea of the robustness of a product and of its limits. Finally, we agree with Kummerow's plea to only build new rainfall products with a clear use case in mind; one that has not yet been catered to by existing products (Kummerow, 2017).

# APPENDIX

## 2.A. SATELLITE-BASED PRODUCTS - DESCRIPTION AND PERFORMANCE

### 2.A.1. CLIMATE ANOMALY MONITORING SYSTEM - OUTGOING LONGWAVE RADIATION PRECIPITATION INDEX (CAMS-OPI)

#### DESCRIPTION

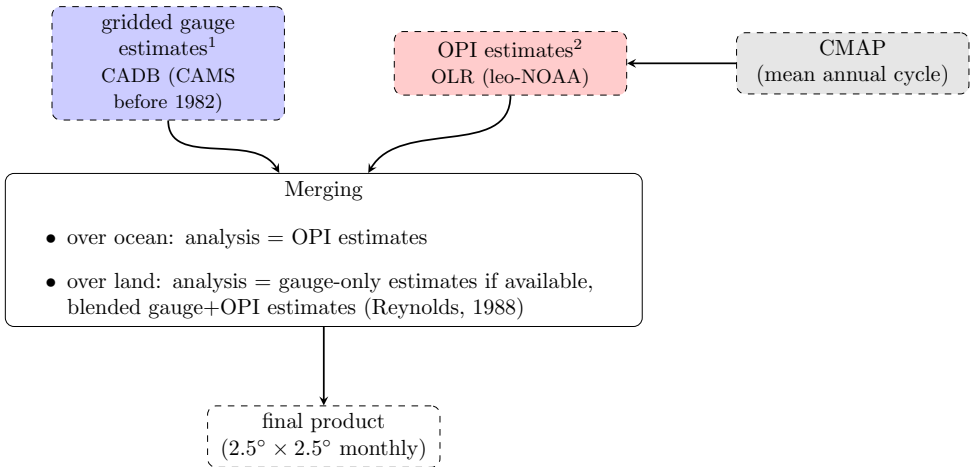
The CAMS-OPI product provides monthly mean and anomaly precipitation on a  $2.5^\circ \times 2.5^\circ$  grid resolution from 1979 up to present. This product has two types of inputs: 1) monthly rain-gauge totals from the Climate Anomaly Data Base (CADB) (initially rain gauges from CAMS were used), and 2) satellite-based estimates derived from Outgoing Longwave Radiation (OLR) observations from NOAA polar-orbiting satellites. These two inputs are merged, such that over the oceans the final estimates are the same as the satellite-based estimates and that over the lands the final estimates take the values of the gauges-based estimates where available, everywhere else the gauge and the satellite estimates are blended. Figure 2.A.1 represents a flowchart of CAMS-OPI's algorithm. A more detailed description of the CAMS-OPI product and a comparison with GPCP and CMAP is given in Janowiak and Xie (1999).

CAMS-OPI has the advantage of being a near real-time product, so it is useful for real-time precipitation monitoring. However for other purposes, it is advised to use other monthly global precipitation products such as GPCP or CMAP. They are not real time products, but they include more observations and use a better quality control for the rain-gauges data.

### 2.A.2. GLOBAL PRECIPITATION CLIMATOLOGY PROJECT (GPCP) - SATELLITE AND GAUGE (SG)

#### DESCRIPTION

GPCP-SG gives global monthly precipitation estimates, and associated error estimates, on a  $2.5^\circ \times 2.5^\circ$  lat/lon grid from 1979 to a delayed present. Precipitation estimates from different sources of observations are merged to create the GPCP-SG final estimates. GPCP-SG is based on: 1) PMW information from SSMI and SSMIS, 2) IR data from geostationary and polar-orbiting satellites, 3) rain-gauges data from GPCC, 4) sounding data from the Television and Infrared Observation Satellite Program (TIROS) Operational Vertical Sounder (TOVS) and the Atmospheric Infrared Sounder (AIRS), and 5) OLR Precipitation Index (OPI) from NOAA. Some of these input data are not available for the entire period: there are no geo-IR estimates before December 1987 and no PMW estimates from SSMI before December 1985. The algorithm is different before and after these dates, in order to adapt to the data availability. This product is thus not consistent in



## Notes

<sup>1</sup>Gridding method: modified spherical version of Shepard (1968)

<sup>2</sup>OPI algorithm: Xie and Arkin (1998)

Figure 2.A.1: CAMS-OPI algorithm.

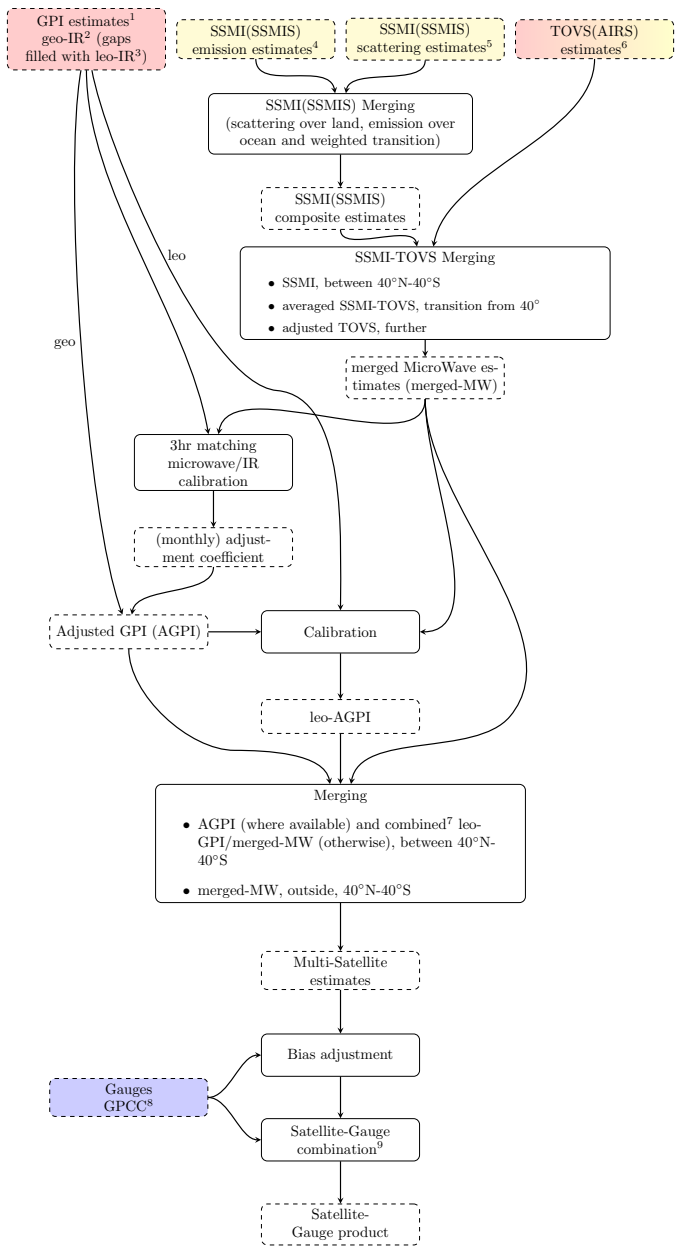
time. The algorithm is shown in Fig. 2.A.2 for the period 1987-present, in Fig. 2.A.3 for 1986-1987, and in Fig. 2.A.4 for 1979-1985.

The merging method as well as more details about the dataset are given in Adler *et al.* (2003) for version 2, Huffman *et al.* (2009) for version 2.1, and Huffman and Bolvin (2013) for version 2.2. A newer version (2.3) recently became available and its differences with the previous version 2.2 are described in Adler *et al.* (2018). The intermediate estimates and their associate errors are also available; there is a total of twenty-seven datasets associated to this product (e.g, long term monthly means from 1981 to 2010).

### 2.A.3. CPC MERGED ANALYSIS OF PRECIPITATION (CMAP)

#### DESCRIPTION

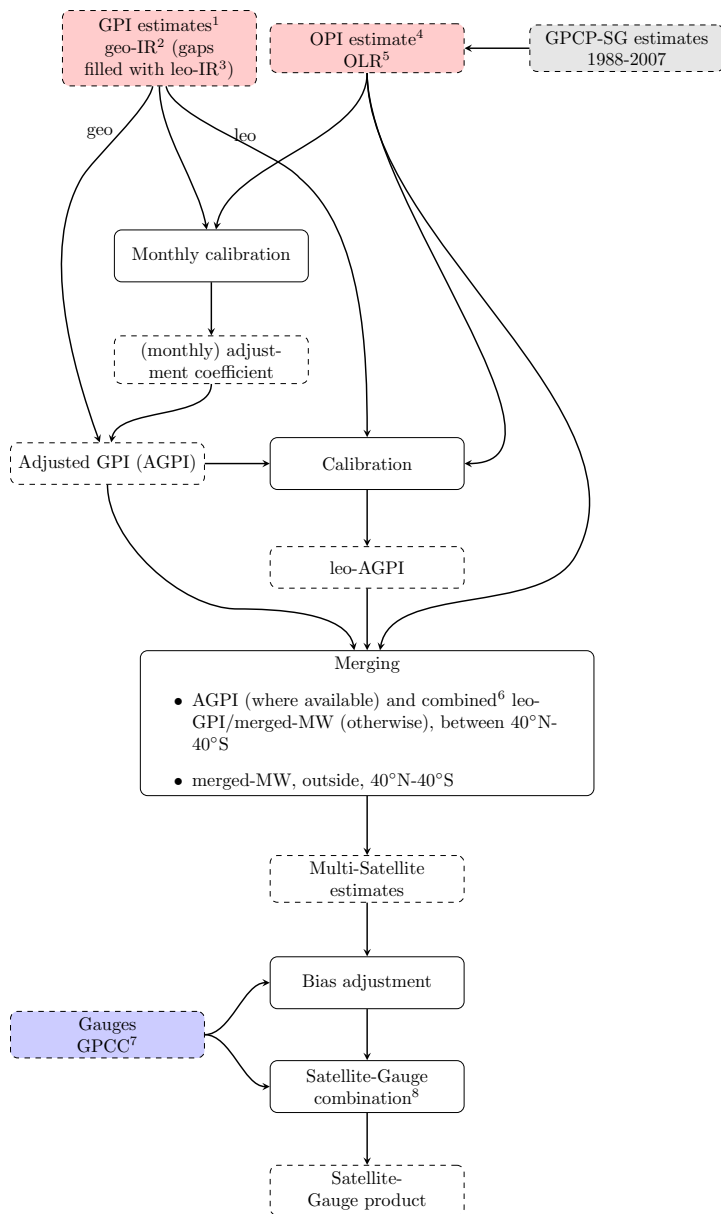
The CMAP product gives pentadal (five days) and monthly global precipitation estimates from 1979 to near present on a  $2.5^\circ \times 2.5^\circ$  lat/lon grid. The estimates are obtained by merging observations from rain-gauges with five different satellite-derived precipitation estimates. The "enhanced" version of CMAP uses the precipitation estimate from NCEP/NCAR reanalysis (R1) as an additional input data. Its resolution and coverage (both spatial and temporal) are otherwise the same as for the original CMAP dataset. The satellite and reanalysis estimates are compared to the gauge analysis and weighted accordingly. In this way, the reanalysis is filling the gaps in the satellite coverage. The amount and the type of data used for the estimation vary in space and time which can be an inconvenient since the quality of the estimates depends on them. A flowchart describing CMAP's algorithm is given in Fig. 2.A.5. The CMAP product is described in Xie



Notes

<sup>1</sup>GPI algorithm: Arkin and Meisner (1987)  
<sup>2</sup>GOES, GMS, MTSat, Meteosat  
<sup>3</sup>NOAA series of polar orbiting satellites  
<sup>4</sup>Produced the GPCP Polar Satellite Precipitation Data Centre using Wilheit et al. (1991)  
<sup>5</sup>Produced the GPCP Polar Satellite Precipitation Data Centre using the Grody Scattering Index (Grody, 1991; Weng and Grody, 1994)  
<sup>6</sup>TOVS algorithm: Susskind et al. (1997)  
<sup>7</sup>weighted combination, the weights being the inversed estimated error variances of the respective estimates  
<sup>8</sup>GPCC-FDR7 (v7) for the period 1979-2013, and GPCC-monitoring (v5) Product after  
<sup>9</sup>weighted average, the weight being the inverse estimated error variance

Figure 2.A.2: GPCP-SG algorithm for the period 1987-present.



## Notes

<sup>1</sup>GPI algorithm: Arkin and Meisner (1987)

<sup>2</sup>GOES, GMS, MTSat, Meteosat

<sup>3</sup>NOAA series of polar orbiting satellites

<sup>4</sup>Xie and Arkin (1998)

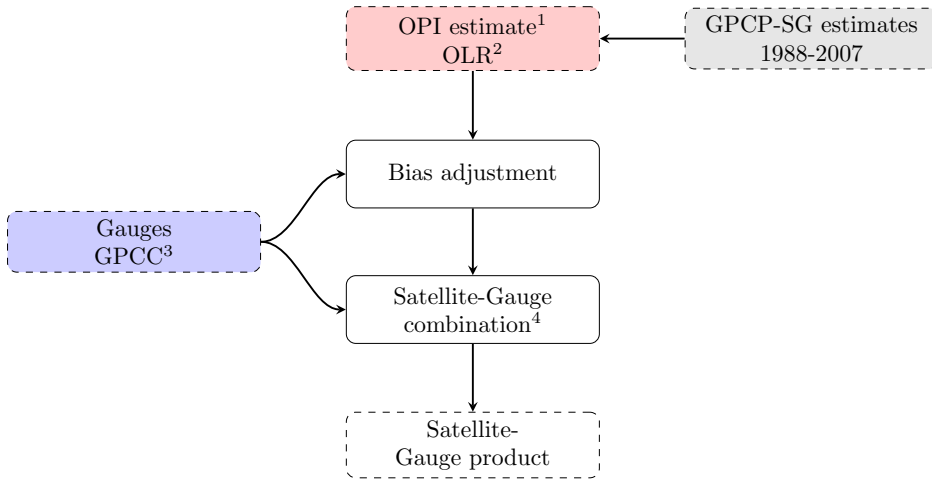
<sup>5</sup>form AVHRR aboard the polar orbiting NOAA series of satellites

<sup>6</sup>weighted combination, the weights being the inversed estimated error variances of the respective estimates

<sup>7</sup>GPCC-FDR7 (v7) for the period 1979-2013, and GPCC-monitoring (v5) Product after

<sup>8</sup>weighted average, the weight being the inverse estimated error variance

Figure 2.A.3: GPCP-SG algorithm for the period 1986-1987.



## Notes

<sup>1</sup>Xie and Arkin (1998)

<sup>2</sup>form AVHRR aboard the polar orbiting NOAA series of satellites

<sup>3</sup>GPCC-FDR7 (v7) for the period 1979-2013, and GPCC-monitoring (v5) Product after

<sup>4</sup>weighted average, the weight being the inverse estimated error variance

Figure 2.A.4: GPCP-SG algorithm for the period 1979-1985.

and Arkin (1997) and Xie and Arkin (1996).

### PERFORMANCE

CMAP's performance seems consistent across different regions. It showed similar good results (i.e. low bias and RMSE and, high NS efficiency and correlation coefficient) in estimating rainfall amount at monthly time scale over Ethiopia (Dinku *et al.*, 2007, 2011b) and over the Sahel (Ali *et al.*, 2005). Its bias remained low despite its tendency to underestimate high rainfall values (the same was observed for the other monthly products compared in these studies). Over the Sahel, Ali *et al.* (2005) noticed an overestimation of low rainfall which lead to an underestimation of the low rainfall frequency and an overestimation of the medium events frequency. According to Okoro *et al.* (2014), CMAP represented well the interannual and spatial variability over the Niger Delta. This result was confirmed over the sahelian region by Ali *et al.* (2005), who also showed that CMAP had better performance in the core of the rainy season than at its edges.

## 2.A.4. GLOBAL PRECIPITATION CLIMATOLOGY PROJECT (GPCP)-1DD

### DESCRIPTION

GPCP produces a global daily product on a  $1.0^\circ \times 1.0^\circ$  lat/lon grid (GPCP-1DD) that covers the period from October 1996 to a delayed present. The GPCP-1DD product is consistent with GPCP-SG in the way that it approximately sums to the monthly estimates of GPCP-SG. GPCP-1DD is mainly based on IR data, it also used PMW data, sounding



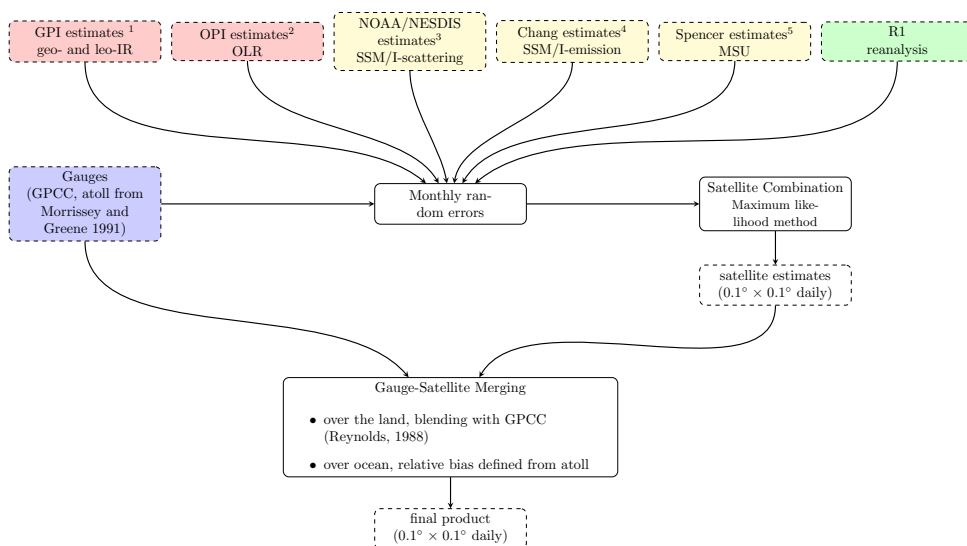
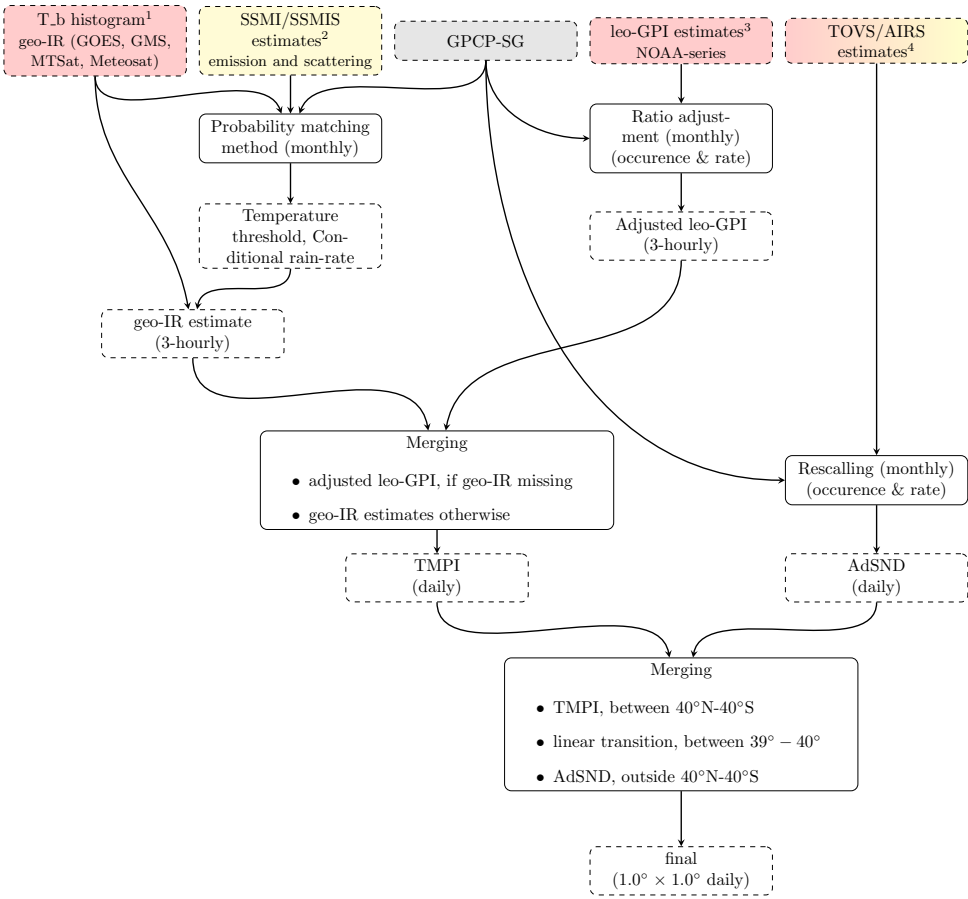


Figure 2.A.5: CMAP algorithm.

data from TOVS and AIRS and [GPCP-SG](#). The 3-hourly infrared brightness temperatures from geo-satellite are compared to a threshold defined from SSMI-based precipitation frequency, and then the "cold" pixels are given a precipitation rate (the conditional rain rate are set locally by month from the [GPCP-SG](#) monthly product). Leo-satellite GPI estimates are adjusted to [GPCP-SG](#) and used to fill the gap when and where the above mentioned geo-IR estimates are missing. The resulting estimates (TMPI) are used between 40°N-40°S. Outside these latitudes, daily TOVS and AIRS precipitation estimates are used. They are rescaled such that TOVS/AIRS-based estimates are matching the ones from TMPI at the boundaries, and that they sum locally to the monthly value of [GPCP-SG](#). The flowchart in Fig. 2.A.6 represents the algorithm of [GPCP-1DD](#). The method and the data used to derive [GPCP-1DD](#) product are described in [Huffman et al. \(2001\)](#) and [Adler et al. \(2017\)](#).

## PERFORMANCE

Over the Sahel, [GPCP-1DD](#) performed relatively well, despite a small overestimation almost everywhere. It performed better than [TMPA3B42](#) over Burkina Faso and the West coast, but worse than regional products like [EPSAT-SG](#), [RFE2](#) or [TARCAT](#). It tended to underestimate weaker rainfall events and overestimate large one ([Jobard et al., 2011](#)). [Gosset et al. \(2013\)](#) evaluated [GPCP-1DD](#) alongside seven other rainfall products over the two sites of Niamey (Niger) and Ouémé (Benin). They showed that [GPCP-1DD](#) had a very low bias over both sites (especially in Benin), but different behaviors. Its per-



Notes

<sup>1</sup>Data processing by Geostationary Satellite Precipitation Data Centre (GSPDC)

<sup>2</sup>GPROF algorithm: Kummerow et al. (1996)

<sup>3</sup>GPI algorithm: Arkin and Meisner (1987)

<sup>4</sup>TOVS algorithm: Susskind et al. (1997)

Figure 2.A.6: GPCP-1DD algorithm.

formance was better over Benin where it represented well the intensity distribution despite a relatively high FAR. Over Niger, its behavior was closer to its behavior over the Sahel, with an underestimation of low rainfall values and an overestimation of high rainfall values. Its tendency to underestimate rainfall frequency and overestimate rainfall amounts (similar to TMPA3B43v6) could be due to the adjustment of daily estimates to the monthly GPCP-SG product. This adjustment method only modifies the precipitation amounts: rainfall amounts are increased during the rainy days to compensate for the underestimation of rainy days occurrence (Gosset et al., 2013). Over West Africa, the performance of GPCP-1DD seemed to be different over the coastal regions (like Benin)

and the ones more north (the Sahel, Niger).

In East Africa, GPCP-1DD has been evaluated over Ethiopia by [Dinku \*et al.\* \(2007\)](#) and over Uganda by [Maidment \*et al.\* \(2013\)](#). Over Ethiopia, GPCP-1DD had a limited performance and was outperformed by TMPA3B42 and CMORPH. It overestimated rainfall at all ranges. However, it performed better over Uganda with a low bias and good correlation to the gauges data. GPCP-1DD has been known to miss warm orographic rain (for instance over India in [Joshi \*et al.\* \(2012\)](#)), this could explain the difference of performance since Ethiopia has a complex topography compared to Uganda. The underestimation of orographic precipitation could be due to the fact that GPCP-1DD is mainly based on IR data (PMW and gauge data are not used directly).

### 2.A.5. CPC MORPHING TECHNIQUE (CMORPH)

#### DESCRIPTION

CMORPH is a high resolution global precipitation product. It takes advantage of the higher temporal resolution of the IR data and the higher accuracy of the PMW precipitation estimates. Low-earth-orbit satellite PMW observations are used to estimate the precipitation fields, which are then propagated by motion vectors derived from geostationary satellite IR data. Half-hourly global precipitation estimates are computed on a  $0.07277^\circ$  ( $\approx 8\text{ km}$ ) lat/lon grid, and are also available as 3-hourly or as daily estimates on a  $0.25^\circ$  lat/lon grid about 18 hours after real-time. The (half-hourly) 8km estimates are obtained by interpolation since the satellite-derived estimates have a coarser resolution (around 12 or 15 km).

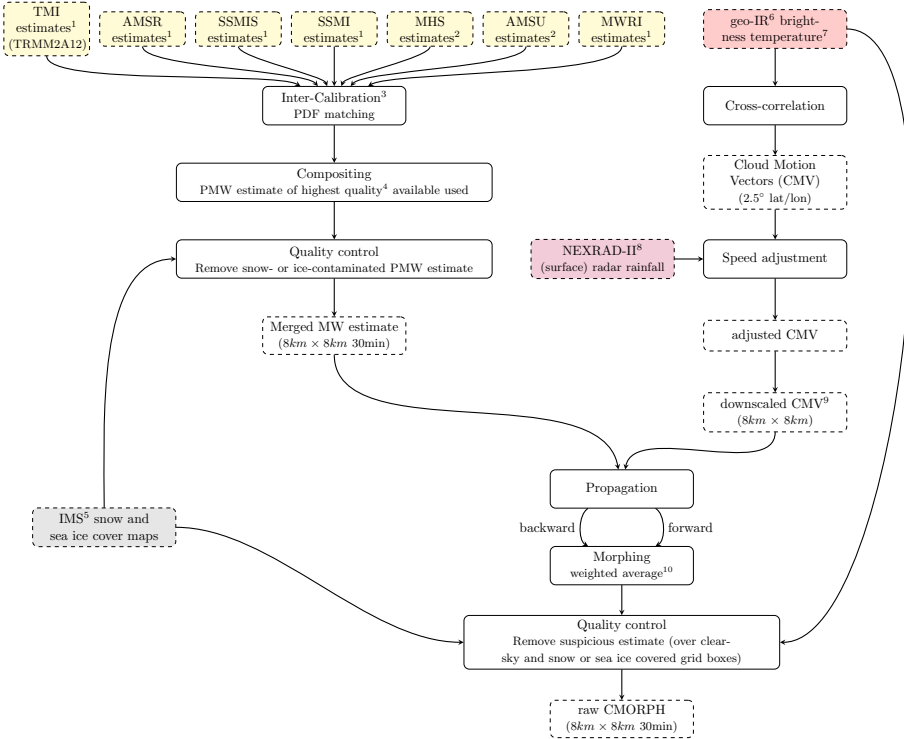
CMORPH exists in two versions. The original one, CMORPHv0.x, covers the period from December 2002 to present. However, the algorithm and the version of the inputs have evolved in time. That is why the CMORPH product has been reprocessed and extended to January 1998, using a fixed algorithm and the same versions for the input data. The reprocessed CMORPH is called CMORPHv1.0. CMORPHv1.0 includes a satellite-only product (CMORPH-RAW, similar to CMORPHv0.x), a bias-corrected (CMORPH-CRT) and a gauge-satellite blended (CMORPH-BLD) products. A flowchart representing the algorithm of CMORPH-RAW and CMORPH-CRT are shown in Figures 2.A.7 and 2.A.8. For more information about the CMORPH products, see [Joyce \*et al.\* \(2004\)](#) for version v0.x and [Xie \*et al.\* \(2017\)](#) for version 1.0. Among the articles cited below only [Cattani \*et al.\* \(2016\)](#) and [Pfeifroth \*et al.\* \(2016\)](#) used CMORPHv1.0 (CRT and RAW respectively).

#### PERFORMANCE

CMORPH had poor performance over the Sahel despite a good discrimination of the rain and no-rain events ([Pierre \*et al.\*, 2011](#); [Novella and Thiaw, 2010](#)). It strongly overestimated rainfall amounts, especially the high rainfall values ([Jobard \*et al.\*, 2011](#); [Pierre \*et al.\*, 2011](#); [Dinku \*et al.\*, 2015](#)). Over the two sites of Niamey (Niger) and Ouémé (Benin), CMORPH also overestimated, but showed a good correlation with the gauges data ([Gosset \*et al.\*, 2013](#)) and represented well the diurnal cycle ([Pfeifroth \*et al.\*, 2016](#)). Thus, CMORPH seemed to have different performances over different parts of West Africa, but overestimated rainfall amount on the whole region.

On the other hand, CMORPH performed very well over Ethiopia ([Dinku \*et al.\*, 2007](#); [Romilly and Gebremichael, 2011](#)). It tended to underestimate rainfall amount, but had

a good detection of rainfall occurrence (Dinku *et al.*, 2015, 2008a, 2011b; Bitew and Gebremichael, 2010). The performance of CMORPH over East Africa varies depending on the regions (Cattani *et al.*, 2016). It has been shown to have good performance over Ethiopia and Zimbabwe by Dinku *et al.* (2008a) and over Uganda by Asadullah *et al.* (2008). CMORPH tended to underestimate orographic rain (Thiemig *et al.*, 2012; Dinku *et al.*, 2011a; Cattani *et al.*, 2016; Haile *et al.*, 2013); however, its performance remained good over mountainous areas, especially compared to other products.

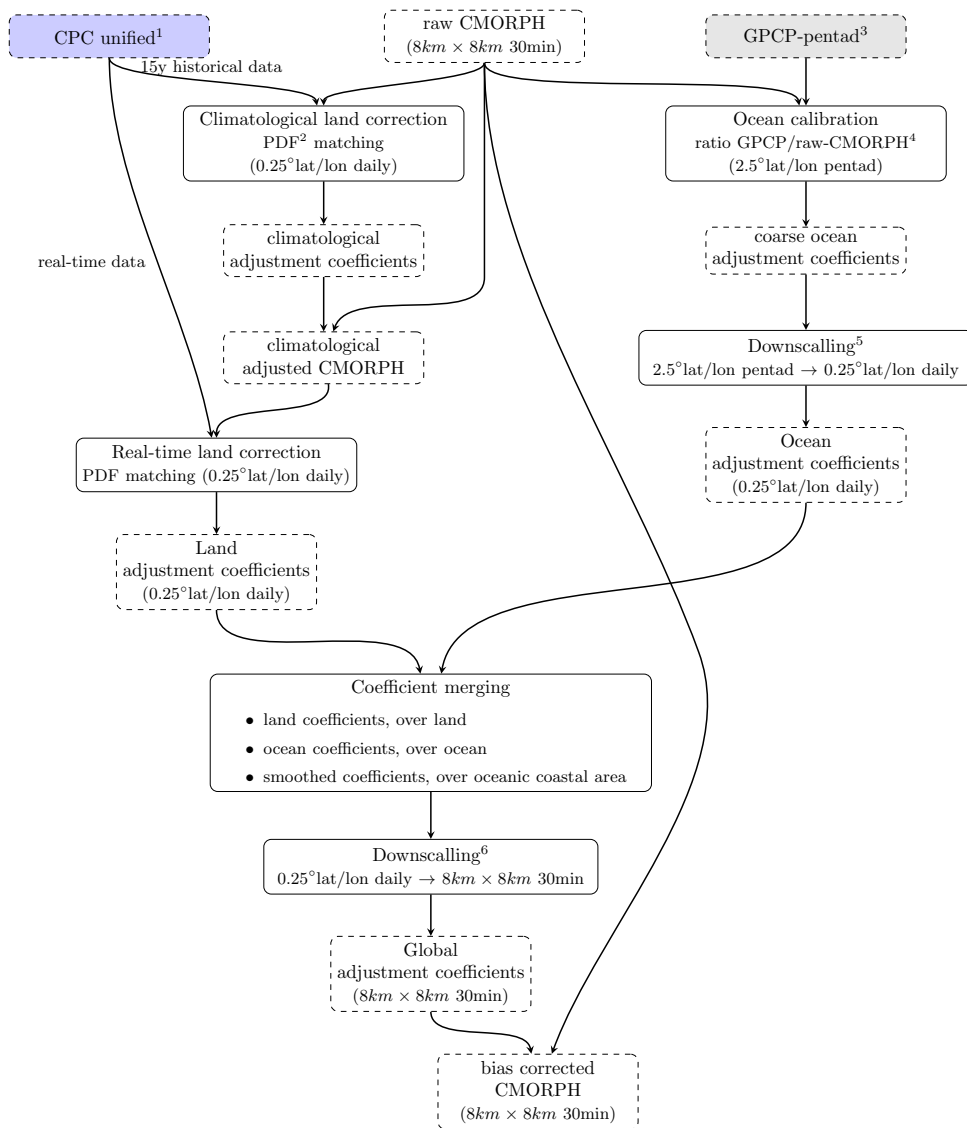


Notes

- <sup>1</sup>generated using the Goddard Profiling Algorithm (GPROF v2004, Kummerow *et al.* (2001))
- <sup>2</sup>generated using Microwave Surface and Precipitation Product System (MSPPS): Ferraro *et al.* (2005)
- <sup>3</sup>calibrated to TMI estimate, after April (when TMI stopped) PDF table from historical data are used
- <sup>4</sup>the ranking being: TMI, AMSR, MWRI, SSMIS, SSMI, MHS and AMSU
- <sup>5</sup>NOAA/NESDIS Interactive Multi-sensor Snow and Ice mapping System (daily 4km). IMS maps are based on satellite and in-situ measurement ([nsidc.org/data/docs/noaa/g02156\\_ims\\_snow\\_ice\\_analysis/](https://nsidc.org/data/docs/noaa/g02156_ims_snow_ice_analysis/))
- <sup>6</sup>from GOES, GMS, MTSat and Meteosat
- <sup>7</sup>from the CPC (NCEP/NEWS/NOAA) Merged 4km Global IR Dataset (Janowiak *et al.*, 2001)
- <sup>8</sup>U.S. NextGeneration Weather Radar - stage II (surface precipitation radar)
- <sup>9</sup>using bilinear interpolation
- <sup>10</sup>the weight being inversely proportional to the temporal length of the (backward or forward) propagation

Figure 2.A.7: CMORPH-RAW algorithm.

2.A.6. TROPICAL RAINFALL MEASURING MISSION (TRMM) MULTI-SATELLITE PRECIPITATION ANALYSIS (TMPA)



## Notes

<sup>1</sup>Xie et al. (2007)

<sup>2</sup>probability density function

<sup>3</sup>Xie et al. (2003)

<sup>4</sup>averaged over a time and space window

<sup>5</sup>assuming no change within a 2.5° pentad cell

<sup>6</sup>assuming no change within a 0.25° daily cell then smoothing across cells

Figure 2.A.8: CMORPH-CRT algorithm.

## DESCRIPTION

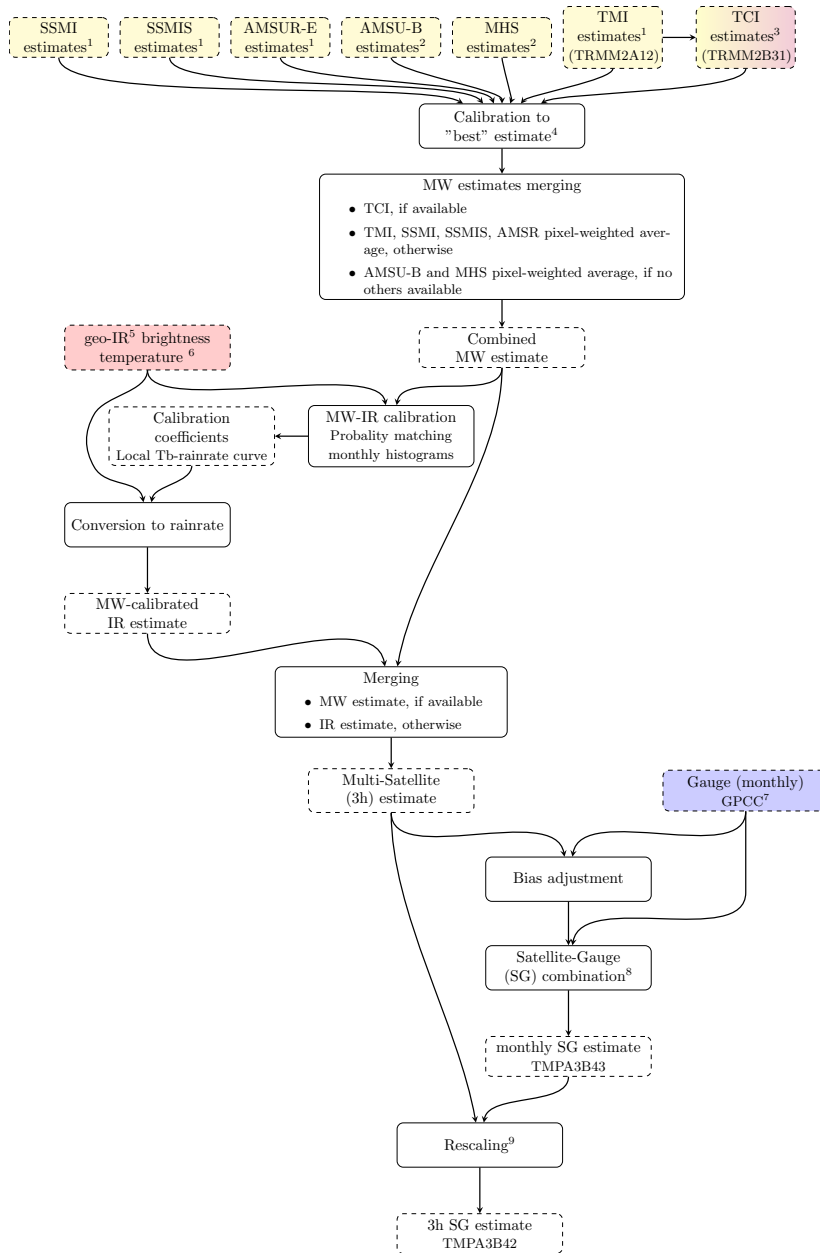
**TRMM** is a joint mission between the National Aeronautics and Space Administration (NASA) and the Japan Aerospace Exploration Agency (JAXA) to study rainfall for weather and climate research. The **TRMM** satellite, launched in November 1997, is equipped with different types of instruments: Precipitation Radar (**PR**), **TRMM** Microwave Imager (**TMI**), Visible and Infrared Scanner (**VIRS**), Clouds and Earth Radiant Energy System (**CERES**) and Lightning Imaging Sensor (**LSI**). Several products are derived from the **TRMM** data including quasi-global (50°N - 50S°) precipitation estimates: the **TRMM** Multi-satellite Precipitation Analysis (**TMPA**) products. They cover the period from 1998 to near-present on a 0.25° × 0.25° lat/lon grid at 3-hourly (**TMPA3B42**), daily (**TMPA3B42** derived) and monthly (**TMPA3B43**) temporal resolution.

The inputs used to derive these products are: 1) **PMW** data from different low earth orbit (LEO) satellites (including **TMI** on **TRMM**), 2) **IR** data from the international constellation of geosynchronous earth orbit (GEO) satellites, 3) **TRMM** Combined Instrument (**TCI**, **TRMM2B31**) based on **TMI** and **TRMM PR** (for calibration), and 4) **GPCC** monthly rainfall estimates. The algorithm for **TMPA3B42** (and **TMPA3B43**) is shown in Fig. 2.A.9. More details about the input datasets and the algorithm can be found in Huffman *et al.* (2007) for version 6 and in Huffman and Bolvin (2018) for version 7. A real time version of **TMPA3B42** (**TMPA3B42-RT**) is also available, it is based on calibration by the **TMI** precipitation product instead of **TCI** and does not incorporate gauge data.

## PERFORMANCE

Overall, **TMPA3B42** product performed well over different parts of Africa (Sahel, Benin, Niger, Ethiopia, Uganda, Zimbabwe). Over the Sahel, the version 6 underestimated the number of rainy days and the high rainfall values (Jobard *et al.*, 2011; Pierre *et al.*, 2011). Its performance was lower over the West coast and Burkina Faso (Jobard *et al.*, 2011). This lower performance over Burkina Faso has also been noticed for version 7 by Dembélé and Zwart (2016). These two studies showed that both versions of **TMPA** underestimated high rainfall value, while Dinku *et al.* (2015) found that version 7 overestimated high rainfall rates over the Sahel. Over Benin and Niger, the version 6 underestimated the number of rainy days as over the Sahel but overestimated the high rain rates (Gosset *et al.*, 2013; Roca *et al.*, 2010). Pfeifroth *et al.* (2016) showed that **TMPA** version 7 was able to reproduce the diurnal cycle and its variability, for two sites in Benin and Niger. However, if the size of the peaks were very close to the gauge data, they were delayed up to two hours. The two versions were quickly compared in Gosset *et al.* (2013), and version 7 showed a general improvement (depending on the statistics).

Over Ethiopia, **TMPA** had more difficulties and was often outperformed by **CMORPH** (Dinku *et al.*, 2007, 2015, 2008a, 2011b), particularly over the lake Tana. This can be due to the fact that no gauges were available near this lake for the bias adjustment (Worqlul *et al.*, 2014; Haile *et al.*, 2013). However, both versions showed satisfactory results over other regions of East Africa such as Uganda (Asadullah *et al.*, 2008; Diem *et al.*, 2014), lake Victoria (Haile *et al.*, 2013) or Zimbabwe (Dinku *et al.*, 2008a). Cattani *et al.* (2016) compared **TMPA** with other rainfall products over the entire East Africa. **TMPA** had overall the best performance over the entire region (but it was not independent from the reference data in this study). The performance of **TMPA** was lower over complex orography where it tended to underestimate rainfall amount (Thiemig *et al.*, 2012; Dinku *et al.*,



## Notes

<sup>1</sup>computed using a sensor-specific version of the Goddard Profiling Algorithm (GPROF, Kummerow et al., 2001)

<sup>2</sup>NESDIS/MSPPS algorithm: Zhao and Weng (2002); Weng et al. (2003)

<sup>3</sup>combined PR-TMI retrieval algorithm, based on Haddad et al. (1997)

<sup>4</sup>First, SSMI, SSMIS, AMSUR, AMSU-B and MHS estimates are first climatologically matched to TMI estimate. Then, they are, as well as TMI estimate, calibrated to TCI using probability matching of precipitation rate histograms

<sup>5</sup>from GOES, GMS, MTSat and MeteoSat

<sup>6</sup>from the Merged 4km IR Tb dataset starting from February 2000, and from the GridSat-B1 IR Tb dataset before this date

<sup>7</sup>GPCC-FDR for the period 1979-2010, and GPCC-monitoring Product after

<sup>8</sup>using inverse error variance weighting

<sup>9</sup>the 3h Multi-Satellite estimates are scaled to sum the monthly SG estimates

Figure 2.A.9: TMPA algorithm.

2011a; Diem *et al.*, 2014). This could explain why it performed less well over Ethiopia which has a complex orography.

### INTEGRATED MULTI-SATELLITE RETRIEVALS FOR GPM (IMERG)

The TRMM satellite stopped collecting data in 2015. The TMPA products will continue until 2018, with some modification in the algorithm due to the data being no longer available. The Global Precipitation Measurement (GPM) mission is build upon and will replace the TRMM mission. The GPM Core Observatory satellite was launched in February 2017 and the new product, the Integrated Multi-satellitE Retrievals for GPM (IMERG), which is based on the GPM satellite constellation will supersede TMPA (starting in 2019).

The IMERG product gives half-hourly quasi-global (60°N - 60S°S) precipitation estimates on a  $0.1^\circ \times 0.1^\circ$  lat/lon grid. It covers the period from March 2014 to the present with a latency of respectively 4 hours, 12 hours and 2.5 months after the end of the month for the Early, Late and Final runs. The inputs are similar to the ones use for TMPA: 1) PMW data from different low earth orbit (LEO) satellites (including TMI and GMI on TRMM and GPM), 2) IR data from the international constellation of geosynchronous earth orbit (GEO) satellites, 3) GPM Combined Instrument (GCI, 2B-CMB) based on GMI and GPM Dual Precipitation Radar (DPR) (for calibration), and 4) GPCC monthly product. In addition, IMERG uses the monthly GPCP-SG product to calibrate the PMW-based rainfall estimates. IMERG's algorithm (shown in Fig. 2.A.10) differs from TMPA algorithm. It uses a similar inter-calibration and merging method for the PMW estimates, and the same bias-adjustment and satellite-gauge combination as TMPA. But, the MW-calibrated IR estimates are derived by the PERSIANN-CCS algorithm, and they are combined to the merge-MW estimates using CMORPH-Kalman Filter (CMORPH-KF) method. More details about the input datasets and a description of the algorithm can be found in Huffman *et al.* (2018).

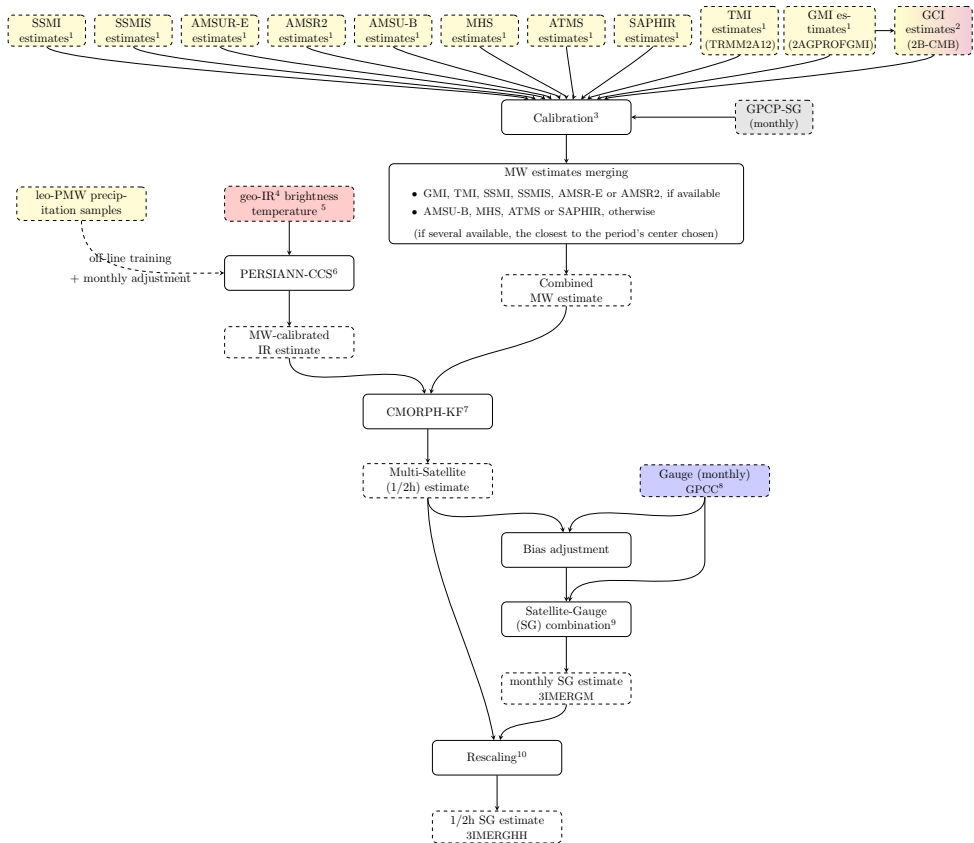
IMERG being a recent product, only few studies have evaluated its performance over Africa. It has been compared to its predecessor TMPA by Dezfuli *et al.* (2017a) over two regions having different rainy season characteristics, one in West Africa and one in East Africa. They showed that IMERG was closer to the gauge data than TMPA, especially for the extreme events. In a follow-up article, Dezfuli *et al.* (2017b) compared IMERG and TMPA with three rain-gauges at three locations having different rainfall characteristics. They showed that the performance of both products depended on the season, the region and the evaluation statistics. Both TMPA and IMERG performed better in East Africa and South West Africa than in South Sahel. This can be expected since the latter has a more arid climate and arid areas are known to be challenging for satellite-based rainfall products. The diurnal cycle was better represented by IMERG, probably because of its higher resolution. However, TMPA represented better the annual cycle for two out of the three rain-gauges.

## 2.A.7. PRECIPITATION ESTIMATION FROM REMOTE SENSING INFORMATION USING ARTIFICIAL NEURAL NETWORK (PERSIANN)

### DESCRIPTION

The PERSIANN product was developed in 1997 at the University of Arizona, Tucson. Quasi-global (60°N-60°S) up to hourly precipitation estimates at  $0.25^\circ$  lat/lon resolution





### Notes

<sup>1</sup>computed using the Goddard Profiling Algorithm 2017 (GPROF2017)

<sup>2</sup>combined DPR-GMI retrieval algorithm

<sup>3</sup>1) Intercalibration to the "best" estimate (currently GCI) using probability matching, and 2) Climatological calibration to GPCP-SG using a simple ratio from GOES, GMS, MTSat and MeteoSat

<sup>4</sup>from the CPC Merged 4km IR Tb dataset (Janowiak et al., 2001) starting from February 2000, and from the GridSat-B1 IR Tb dataset before this date

<sup>5</sup>see Hong et al. (2004)

<sup>6</sup>see Joyce and Xie (2011)

<sup>8</sup>GPCC-FDR for the period 1908-2013, and GPCC-monitoring Product after

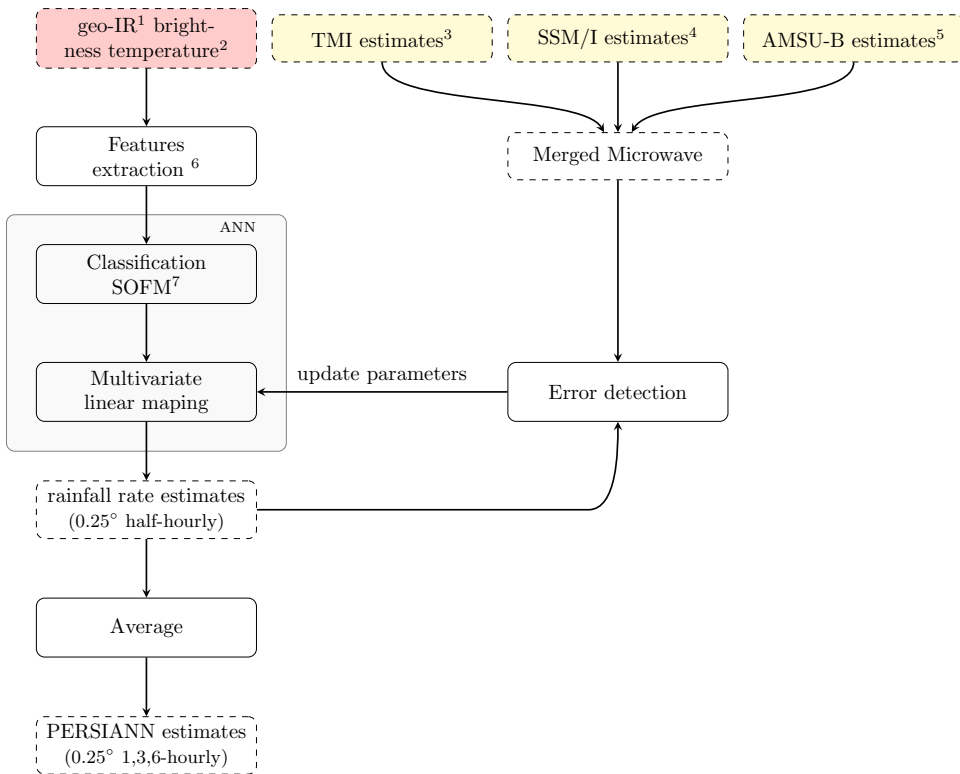
<sup>9</sup>using inverse error variance weighting

<sup>10</sup>the 30min Multi-Satellite estimates are scaled to sum the the monthly SG estimates

Figure 2.A.10: IMERG algorithm.

are available from 2000 to present with two days latency.

PERSIANN is based on an artificial neural network which is applied to IR data from geostationary satellites (CPC/NCEP Merged 4km IR Tb dataset) to obtain intermediate precipitation product at 4km resolution every 30 minutes. The intermediate product is then aggregated to form the final precipitation product. The neural network can be trained with different types of data, such as satellite measurements, gauges, ground-based radar data and ground-surface topographic information. For the operational product, the neural network is trained and updated with PMW data only. The algorithm for the operational product is shown in Fig. 2.A.11.



## Notes

<sup>1</sup>from GOES, GMS, MTSat and Meteosat

<sup>2</sup>from the CPC/NCEP Merged 4km IR Tb dataset (Janowiak et al., 2001)

<sup>3</sup>generated using the Goddard Profiling Algorithm Kummerow et al. (2001)

<sup>4</sup>generated using the algorithm described in Ferraro and Marks (1995)

<sup>5</sup>generated using the algorithm described in Weng et al. (2003)

<sup>6</sup>from 5 × 5 moving window

<sup>7</sup>Self-Organizing Feature Map (SOFM) algorithm, a neural network-based classification scheme

Figure 2.A.11: PERSIANN algorithm.

**PERSIANN - Cloud Classification System (PERSIANN-CCS)**, another PERSIANN product with higher spatial and temporal resolution, was developed at the Center for Hydrometeorology and Remote Sensing (CHRS) at the University of California, Irvine. The method is similar to that of PERSIANN, the main difference being the introduction of a Cloud Classification System (CCS). In PERSIANN, the fitting of infrared cloud images to rain rate is done pixel-to-pixel while PERSIANN-CCS uses cloud-patch regions. The cloud-patch features are categorized and the fitting of infrared images to rain rate is unique for each cloud-patch group. The parameters defining the fitting are calibrated through a neural network (Hong et al., 2004). Contrary to PERSIANN, the neural network is not updated but was initially trained with PMW data. The resulting quasi-global

(60°N-60°S) rain estimates are given on a 0.04° lat/lon grid every hour, and are covering the period from January 2003 to present.

2

**PERSIANN-Climate Data Record (PERSIANN-CDR)** product has been developed for climate and variability studies. It covers a longer period, from 1983 to a delayed present(2015), and is available as daily estimates at 0.25° resolution. **PERSIANN-CDR** is based on the same algorithm as **PERSIANN**. The two main differences are that 1) the neural network in **PERSIANN-CDR** is not updated, and 2) **PERSIANN-CDR** uses a different IR-dataset, namely GridSat-B1. Moreover, **PERSIANN-CDR** is bias-adjusted with the monthly **GPCP.v2.2** product. More detailed descriptions of this product can be found in [Ashouri \*et al.\* \(2015\)](#) and [Hsu \*et al.\* \(2014\)](#).

The evolution of PERSIANN products from 2000 to 2009 is described in [Hsu and Sorooshian \(2008\)](#).

### PERFORMANCE

**PERSIANN** tended to overestimate rainfall, especially high rainfall values, except over mountainous areas where it tended to underestimate.

Over the Sahel, **PERSIANN** performed well in detecting rainfall occurrence (i.e. high POD), but also tended to estimate rain when there was no rain event (i.e. high FAR) ([Jobard \*et al.\* \(2011\)](#), and [Dembélé and Zwart \(2016\)](#) over Burkina Faso). It had a strong wet bias and showed overall poor performance over the region ([Jobard \*et al.\*, 2011](#); [Novella and Thiaw, 2010](#); [Dembélé and Zwart, 2016](#)). This high bias was also observed in Niger and to a lesser extent in Benin, however **PERSIANN** had a better correlation over Niger than Benin ([Gosset \*et al.\*, 2013](#)). **PERSIANN** was able to reproduce the diurnal cycle with reasonably timing (e.g. the peak in Ouémé, Benin, was delayed by around 2h) according to [Pfeifroth \*et al.\* \(2016\)](#).

[Dinku \*et al.\* \(2008a\)](#) found that **PERSIANN** had a large overestimation, and generally poor performance over Ethiopia. However, [Hirpa \*et al.\* \(2010\)](#) and [Romilly and Gebremichael \(2011\)](#) studied the performance of **PERSIANN** at the scale of river basins (located in Ethiopia) and found that **PERSIANN** substantially underestimated rainfall at high elevation while it performed reasonably well at low elevation. **PERSIANN**, unlike **TMPA3B42RT** and **CMORPH**, did not show an elevation-dependent trend, which led to this severe underestimation at high elevation ([Hirpa \*et al.\*, 2010](#)). These results were consistent with other studies over other mountainous area such as the Tibetan plateau ([Gao and Liu, 2013](#)) or Chile ([Zambrano-Bigiarini \*et al.\*, 2017](#)). This trend was also present over Uganda where **PERSIANN** overestimated at low elevation and underestimated at high one according to [Asadullah \*et al.\* \(2008\)](#). The poor performance of **PERSIANN** and its underestimation at high elevation were also confirmed over East Africa by [Cattani \*et al.\* \(2016\)](#) and over four African river basin by [Thiemig \*et al.\* \(2012\)](#). This underestimation at high elevation could be explained by the fact that **PERSIANN** is based on IR data and that orographic precipitation is a warm-cloud process. It has been suggested by [Hirpa \*et al.\* \(2010\)](#) and [Thiemig \*et al.\* \(2012\)](#) that the underestimation could come from the poor detection of light rain or underestimation of total precipitation at high elevation linked to the thermal IR threshold used to discriminate between raining and non-raining clouds.

PERSIANN-CCS showed a similar trend in underestimating light and moderate rainfall at high elevation and overestimating rainfall, especially heavy events, at low latitude (Bitew and Gebremichael, 2010; Hong *et al.*, 2007).

### 2.A.8. RAINFALL ESTIMATE VERSION 2 (RFE2)

#### DESCRIPTION

RFE2 is the second version of the Rainfall Estimate (RFE) product. It was implemented in 2001 based on the method of Xie and Arkin (1996), and replaced the previous version (RFE 1.0, Herman *et al.*, 1997) operational from 1995 to 2000. RFE2 produces daily rainfall estimates on a  $0.1^\circ \times 0.1^\circ$  lat/lon grid for Africa ( $20^\circ\text{W}$ - $55^\circ\text{E}$  and  $40^\circ\text{S}$ - $40^\circ\text{N}$ ) from January 2001 to present. RFE2 computes rainfall estimates based on four operational sources of data: 1) daily GTS rain gauge data, 2) the Geostationary Operational Environmental Satellite (GOES) precipitation index (GPI) calculated from cloud-top IR temperatures on a half-hourly basis, 3) Special Sensor Microwave Imager (SSM/I)-based rainfall estimates, and 4) Advanced Microwave Sounding Unit (AMSU)-based rainfall estimates. The last two inputs are new in RFE2). The thermal IR (input 2) and the passive microwaves (inputs 3 and 4) are compared to the gauge data (input 1), then linearly combined through the maximum likelihood method and finally merged with gauge data (input 1). This process is illustrated in Fig. 2.A.12, representing RFE2 algorithm. More information is given in NOAA, CPC (2001) technical report.

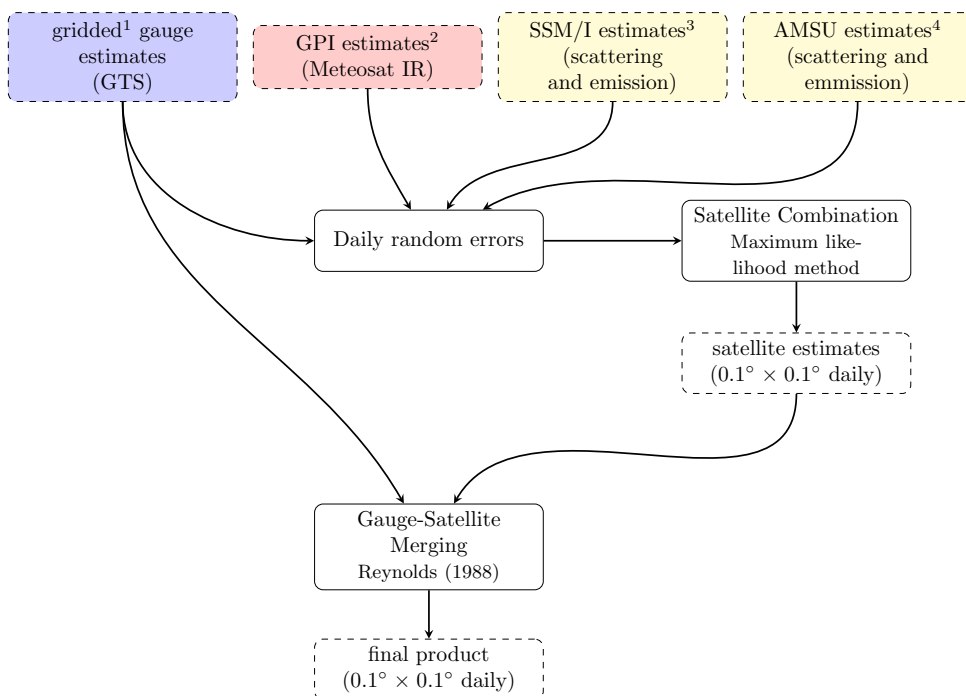
#### PERFORMANCE

The performance of RFE2 varied from region to region, but it overall tended to underestimate (i.e. dry bias).

Over the Sahel, RFE2 had good skill at separating rain and no-rain events and showed good performance at estimating dekadal rainfall amount, despite its tendency to underestimate (Jobard *et al.*, 2011; Pierre *et al.*, 2011; Novella and Thiaw, 2010; Dembélé and Zwart, 2016). Gosset *et al.* (2013) showed that RFE2 also underestimated rainfall amount over Benin and Niger by overestimating occurrence of low rainfall events and underestimating the high ones. Thiemig *et al.* (2012) found that, despite a small underestimation, RFE2 performed well over the Volta basin in Ghana. Thus, RFE2 appeared to perform well over West Africa but presented a dry bias.

Over Ethiopia, RFE2 has been reported as having poor performance, at both daily and dekadal time scale, with severe underestimation (Dinku *et al.*, 2007, 2015, 2008a, 2011b). However, RFE2 still performed reasonably well at detecting rainfall occurrence (Dinku *et al.*, 2008a, 2011b). Its performance over Uganda seemed also limited (including a dry bias), especially during boreal summer rainfall, even if it showed some skill in reproducing spatial patterns (Maidment *et al.*, 2013; Asadullah *et al.*, 2008; Diem *et al.*, 2014). Over East Africa, RFE2 was outperformed by CMORPH and TMPA3B42, but outperformed GSMaP and PERSIANN (Cattani *et al.*, 2016). RFE2 showed good performance with a good detection of rainfall occurrence over Zimbabwe (Dinku *et al.*, 2008a), and very poor one over the desert locust recession region, especially over the Sahara (as the other products studied over this region by Dinku *et al.* (2010)).

A problem of RFE2 product is its underestimation of orographic precipitation (which explains its poor performance over Ethiopian highland) noticed by Cattani *et al.* (2016),



## Notes

<sup>1</sup>Gridding method of Shepard (1968)

<sup>2</sup>GPI algorithm: Arkin and Meisner (1987)

<sup>3</sup>NOAA algorithm: Ferraro and Marks (1995), Ferraro et al. (1996)

<sup>4</sup>NOAA algorithm: Zhao et al. (2000)

Figure 2.A.12: RFE2 algorithm.

Thiemig *et al.* (2012), Dinku *et al.* (2011a), Dinku *et al.* (2011b) and Diem *et al.* (2014). This version of RFE (2.0), unlike the first version (RFE 1.0), does not include orographic effects. The algorithm uses a fixed temperature threshold, and thus has difficulty to capture warm-cloud precipitation, due to orographic effect for instance.

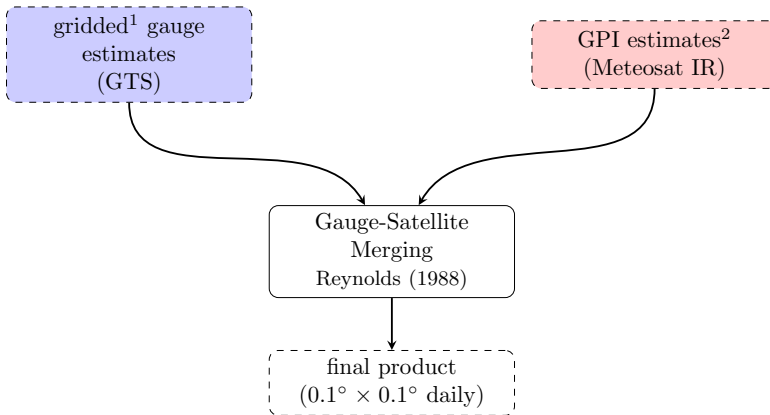
## 2.A.9. AFRICA RAINFALL CLIMATOLOGY VERSION 2 (ARC2)

### DESCRIPTION

RFE2 temporal coverage is too short for climate studies. Thus, another rainfall product based on the same algorithm was developed for climatology in 2004: the Africa Rainfall Climatology (ARC) product. ARC uses only two of the four inputs of RFE2: the gauges and the IR data because of their availability and consistency over time. However, large bias are present in ARC (due to inconsistencies in the original reprocessing) and a longer temporal coverage were needed for climatology. In 2012, the version 2 of ARC (ARC2) was developed, and the production of ARC stopped. The main difference with ARC is that the

time period extended back to 1983, and the re-calibration of the IR data between 1983 and 2005.

The inputs used in [ARC2](#) are the quality-controlled [GTS](#) gauge observations and the 3-hourly geostationary IR data (instead of half-hourly for [RFE2](#)). The algorithm is the same as for [RFE2](#). [ARC2](#) estimates rainfall daily (from 0600 GMT through 0600 GMT) on the same grid than [RFE2](#), i.e.  $0.1^\circ \times 0.1^\circ$  lat/lon grid from  $20^\circ\text{W}$  to  $55^\circ\text{E}$  and from  $40^\circ\text{S}$  to  $40^\circ\text{N}$ . It covers the time period from 1983 to present and is updated on a daily basis. [ARC2](#) shows an improvement compared to [ARC](#) and is consistent with [RFE2](#), [GPCP](#) and [CMAP](#) ([Novella and Thiaw, 2013](#)). The [ARC2](#) product is described in [Novella and Thiaw \(2013\)](#), and a flowchart representing its algorithm is given in [Fig. 2.A.13](#).



## Notes

<sup>1</sup>Gridding method of Shepard (1968)

<sup>2</sup>GPI algorithm: Arkin and Meisner (1987)

Figure 2.A.13: ARC2 algorithm.

## PERFORMANCE

[ARC2](#) has been created to fix some of the problems in the first version of [ARC](#), such as the large dry bias from 1998 to 2000 (that does not appear anymore in [ARC2](#)). [ARC2](#) was an improvement compared to [ARC](#) but still has some systematic errors such as a dry bias during northern hemisphere summer as noticed in [Novella and Thiaw \(2013\)](#) and [Maidment et al. \(2014\)](#).

According to [Novella and Thiaw \(2013\)](#), [ARC2](#) had an overall good performance over Africa, but with some variations depending on the regions. They found that [ARC2](#) outperformed [TMPA3B42](#) and [CMORPH](#) at daily scale over the Sahel, but performed poorly over Ethiopia and the Gulf of Guinea. Over Burkina Faso (which is part of the Sahel), [ARC2](#) was found to have only weak correlation with gauge data at daily scale, but to perform well at dekadal time scale, by [Dembélé and Zwart \(2016\)](#). [Diem et al. \(2014\)](#) showed that [ARC2](#) overestimated the number of rainy day for six stations in West Uganda.

It could estimate well seasonal totals in the northern part, but had difficulties over the more mountainous South.

ARC presented the same region dependency: good performance over the Sahel (Novella and Thiaw, 2010), and poor one over Ethiopia (Dinku *et al.*, 2007). It was also noticed that ARC2 was performing worse over mountainous terrain such as the Ethiopian highland (Novella and Thiaw, 2013) or South-West Uganda (Diem *et al.*, 2014). This poor result can be explained by the low amount of available gauge records (GTS data) in the Ethiopian highland and the Gulf of Guinea and the inability of IR-based estimates to capture warm-cloud precipitation over coastal and orographic regions (Maidment *et al.*, 2014; Dinku *et al.*, 2007; Novella and Thiaw, 2013; Dinku *et al.*, 2011a).

ARC2 and RFE2 use similar algorithm, the main difference is that ARC2 uses less input data. Thus, some similarities in their performances are visible, such as the regions over which they perform well or poorly, or their difficulties over mountainous areas, for example.

## 2.A.10. GLOBAL SATELLITE MAPPING OF PRECIPITATION (GSMaP)

### DESCRIPTION

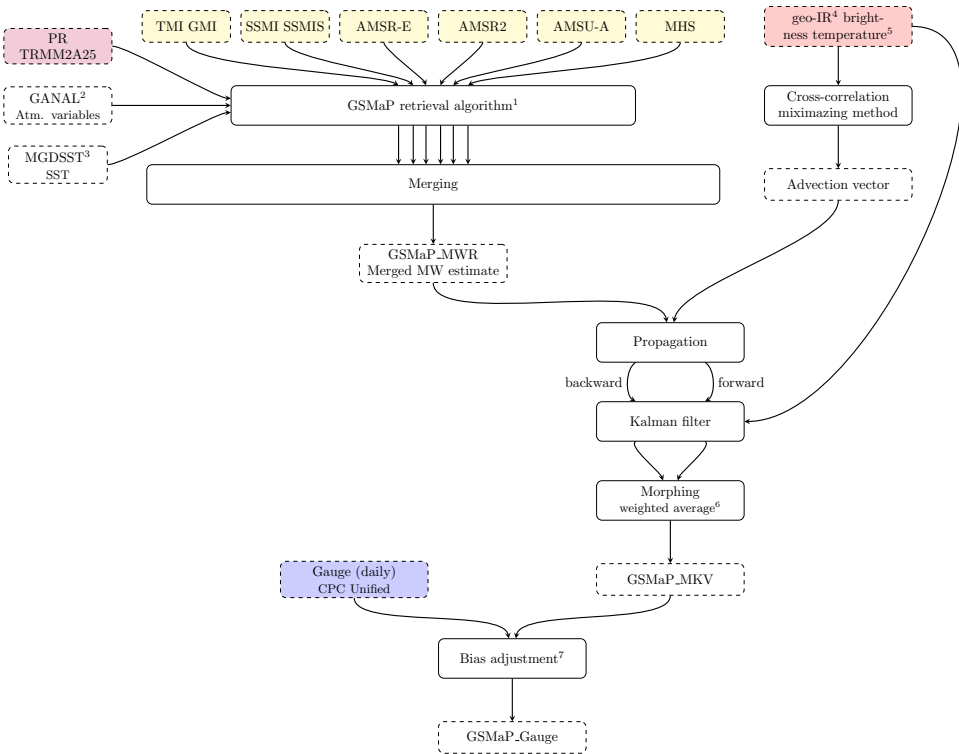
The GSMaP project produces several hourly quasi-global (60°S-60°N) precipitation products with different latencies going to zero hour for the real time product to three days for the standard version. All these precipitation estimates are given hourly on a  $0.1^\circ \times 0.1^\circ$  lat/lon grid. The near-real-time version has a latency of 4 hours and goes from 2008 to present while the standard version (with or without gauge-calibration) goes from 2000 to present. These products are based on PMW-data from TMI, AMSR(-E) and SSM/I, and on IR-data from several geostationary satellites provided by CPC (GOES-8/10, METEOSAT-7/5 and GMS).

The method developed by the GSMaP project has three main steps: 1) retrieval of the rainfall measurements (from microwave imagers and microwave sounders); 2) combination of microwave and infrared data (*GSMaP-MKV*); and, if wanted, 3) the gauge calibration (*GSMaP-Gauge*). The merging method is similar to the one of CMORPH described in Joyce *et al.* (2004): the PMW estimates are propagated using IR-based advection vectors. Then, the estimates are refined to obtain the final estimate (*GSMaP-MKV*) using the correlation between geo-IR measurements (cloud top height) and surface rainfall rate via a Kalman filter. A detailed description of the method can be found in Ushio *et al.* (2009) and Aonashi *et al.* (2009).

A gauge-calibrated version (*GSMaP-Gauge*) of GSMaP exists. It is based on *GSMaP-MKV*, and has the same temporal and spatial resolution. The *GSMaP-MKV* estimates are adjusted, over land, with the global gauge analysis from CPC Unified. The gauge-adjustment method is described in Mega *et al.* (2014). The algorithm used for both *GSMaP-Gauge* and *GSMaP-MKV* is shown in Fig. 2.A.14.

### PERFORMANCE

Over the Sahel, GSMaP has a dry bias, it especially underestimates high precipitation values (Jobard *et al.*, 2011; Roca *et al.*, 2010). Both Roca *et al.* (2010) and Gosset *et al.* (2013) evaluated this product over Niamey (Niger) and Ouémé (Benin). According to Roca *et al.* (2010), GSMaP underestimated high rainfall values, while Gosset *et al.* (2013) noticed an



Notes

<sup>1</sup>Kubota et al. (2006); Aonashi et al. (2009)  
<sup>2</sup>Japan Meteorological Agency (JMA) Global Analysis (GANAL) and Forecast data set  
<sup>3</sup>JMA Merged satellite and in situ data Global Daily Sea Surface Temperatures  
<sup>4</sup>from GOES, GMS, MTSat and Meteosat  
<sup>5</sup>from the CPC Merged 4km Global IR Dataset (Janowiak et al., 2001)  
<sup>6</sup>based on the root-mean-square uncertainty in the estimate after the forward/backward propagation  
<sup>7</sup>Maximization of the probability density function multiplied by a term such that GSMaP estimates sum up to the daily CPC Unified estimate

Figure 2.A.14: GSMaP algorithm.

overestimation of the high rates and an underestimation of the lower ones. This could be due to the fact that they considered different time scales, and that the second study took a longer period into account while the first only considered the rainy season 2006. Moreover, Thiemiig et al. (2012) also noticed the same behavior over the Volta basin, i.e. underestimation of low rain rates and extreme overestimation of high ones. Over the South of West Africa, TMPA seemed to perform better than GSMaP according to these three studies. Gosset et al. (2013) found that, in general, regional products perform better than global ones for this region.

Cattani et al. (2016) evaluated six rainfall products, including GSMaP, over East Africa. They showed that GSMaP was able to reproduce the annual rainfall patterns of the different climates. They found that CMORPHv1 was performing slightly better than GSMaP, while they both use a similar morphing approach. This result can be partially explained by the bias correction used in CMORPH and not in GSMaP. GSMaP was also underesti-



mating orographic precipitation, more than **CMORPH** and **RFE2**.

As the other rainfall products tested over the desert locust recession regions by **Dinku et al. (2010)**, **GSMaP** had poor performance over these regions.

## 2

### 2.A.11. CLIMATE HAZARDS GROUP INFRARED PRECIPITATION (CHIRP) WITH STATION DATA (CHIRPS)

#### DESCRIPTION

**CHIRPS** (version 2, since 2015) gives daily, pentadal and monthly quasi-global (50°S–50°N) precipitation estimates from 1981 to near-present. The estimates are available on a high resolution  $0.05^\circ \times 0.05^\circ$  lat/lon grid, or on a coarser  $0.25^\circ \times 0.25^\circ$  lat/lon grid. It was created by the U.S. Geological Survey (USGS) Earth Resources Observation and Science (EROS) Center and collaborators at the University of California, Santa Barbara Climate Hazards Group. It was developed for drought early warning and environmental monitoring to support FEWS-NET.

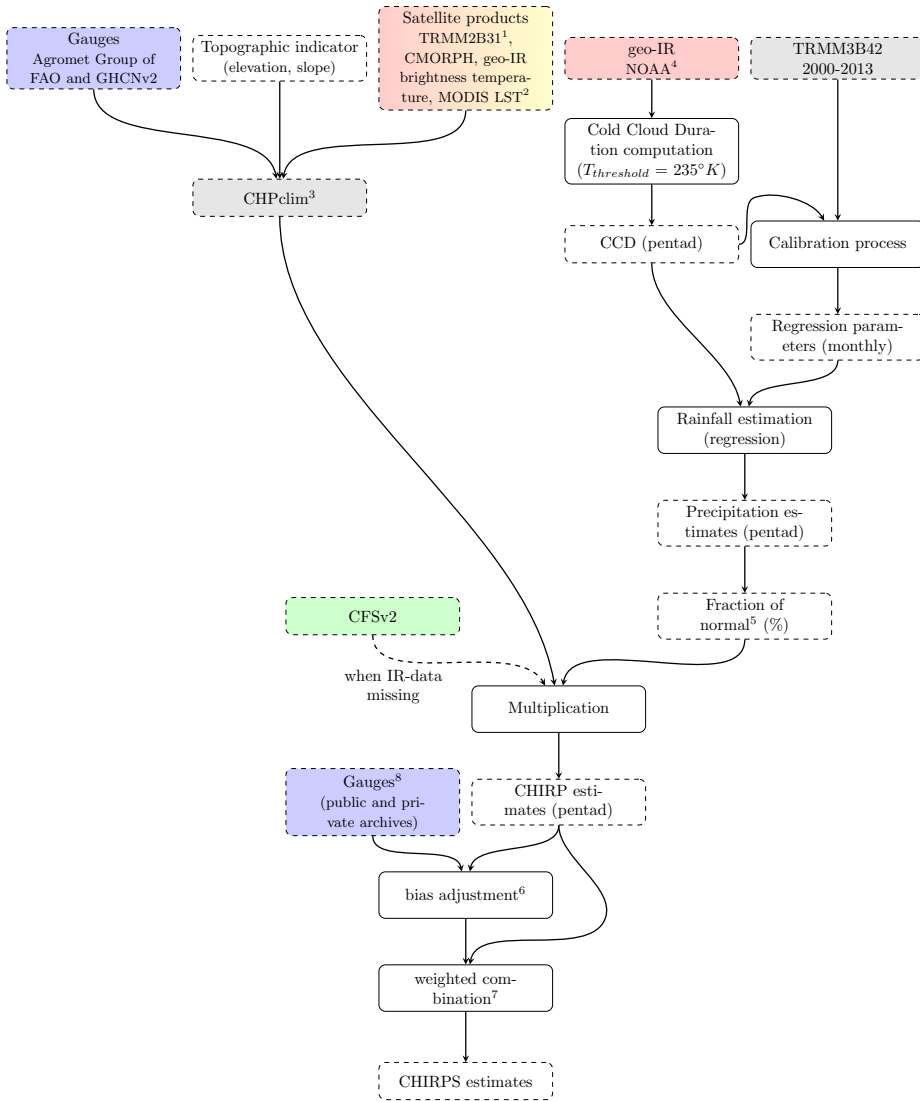
Different types of inputs are used in CHIRPS: 1) global  $0.05^\circ \times 0.05^\circ$  precipitation climatologies from the Climate Hazards group Precipitation climatology, referred as **CHP-clim**; 2) satellite-based precipitation estimates from the **TMPA3B42** product; 3) thermal infrared observations from geostationary satellites; 4) gauge observations from public dataset (GHCN monthly, GHCN daily, Global Summary of the Day (GSOD), **GTS** and Southern African Science Service Centre for Climate Change and Adaptive Land Management (SASSCAL)) and several private archives (from national meteorological agencies, for example); and 5) the atmospheric model rainfall fields from the NOAA Climate Forecast System, version 2 (**CFSv2**) which is used to fill the gap in satellite coverage. Cold Cloud Duration derived from the **IR** data (3) are calibrated against the **TMPA3B42** product (2) to obtain precipitation estimates. These estimates are converted to fraction of normal precipitation, and multiplied to the precipitation climatology from **CHP-clim** (1). The model **CFSv2** (5) is used when and where **IR** data are missing. The new estimates are then bias-adjusted to gauges data (4).

The description of the method can be found in **Funk et al. (2014, 2015a)**. The latter also validated and compared **CHIRPS** with other gridded products, namely **GPCC**, **TMPA3B42 v7** real-time, **CFSv2**, ECMWF reanalysis, and **CPC Unified**). The method is also described by a flowchart in Fig. 2.A.15.

### 2.A.12. TROPICAL APPLICATIONS OF METEOROLOGY USING SATELLITE DATA AND GROUND BASED OBSERVATIONS (TAMSAT) AFRICAN RAINFALL CLIMATOLOGY AND TIMESERIES (TARCAT)

#### DESCRIPTION

The **TAMSAT** Research group, based at the Meteorology Department of the University of Reading (UK) started in the mid-1980s. They produce different rainfall products updated in near-real time as part of the **TARCAT** dataset. **TARCAT** was developed for drought monitoring. Rainfall estimates, climatologies and anomalies are available at pentadal, dekadal, monthly and seasonal time resolution on a  $0.0375^\circ \times 0.0375^\circ$  lat/lon grid ( $\approx 4\text{km}$ ) for Africa. In January 2014, a daily rainfall estimate product was released for the same time period. The particularity of **TARCAT** is that it is only based on **IR** data. It does



Notes

- <sup>1</sup>MicroWave precipitation estimates
- <sup>2</sup>Land Surface Temperature
- <sup>3</sup>CHPclim is described in Funk et al. (2015)
- <sup>4</sup>GriSat-B1 archive (1981-2008) and CPC TIR dataset (2000-present)
- <sup>5</sup>each grid cell's value is divided by the grid cell's 1981-2013 mean precipitation estimate
- <sup>6</sup>the bias is computed from the five closest stations with a modified inverse distance weighting algorithm
- <sup>7</sup>the weights are based on the expected correlation with the nearest station and the expected correlation between the 'truth' and the CHIRP estimates
- <sup>8</sup>GHCN monthly, GHCN daily, Global Summary of the Day(GSOD), GTS, Southern African Science Service Center for Climate Change and Adaptive Land Management(SASSCAL) and different national meteorological agencies

Figure 2.A.15: CHIRPS algorithm.

not use any bias adjustment from gauge data, but this is compensated by regional and monthly calibration parameters (derived from historical IR and gauges data).

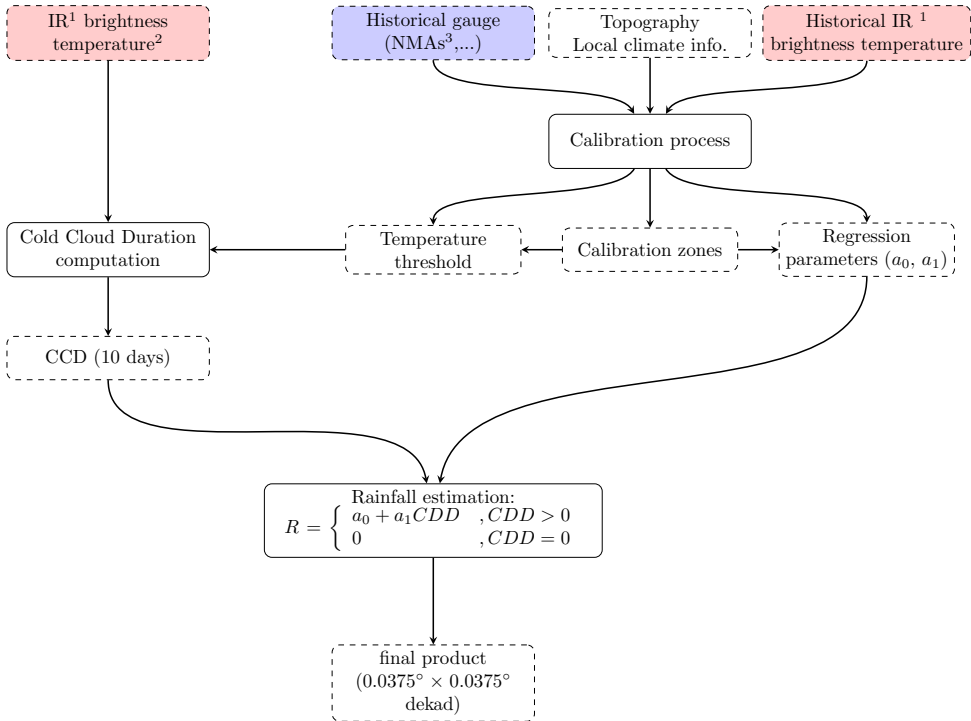
The TARGAT product is based on Meteosat thermal infrared imagery provided by EU-METSAT, and on historical gauges observations (from African National Meteorological and Hydrological Centers, for the majority of them). Cold Cloud Duration (CCD) is derived from the IR data, and are then used to estimate dekadal precipitation through linear regression. The temperature threshold used to compute the CCD and the regression parameters are calibrated locally (Africa is divided into several smaller regions) using historical IR and gauges data. The gauges data covers the period from 1983 to 2010 and are only used for calibration. Thus, TARGAT product is not influenced by current changes in gauges coverage. The daily rainfall are derived from the dekadal estimates and daily CCD. The TARGAT algorithm is described in Tarnavsky *et al.* (2014) and Maidment *et al.* (2014). A flowchart representing this algorithm is shown in Fig. 2.A.16.

A version 3 of TARGAT was release in January 2017 and has been described in Maidment *et al.* (2017) and TAMSAT Group (2016). The algorithm is similar but the calibration differs from version 2. Indeed, the calibration is not done on rectangular areas anymore but on 1.0° grid boxes where the gauge density is sufficient, and then interpolated. The temperature threshold is derived at daily scale and the calibration parameters at pentadal scale, instead of dekadal scale in version 2. In version 3, a bias adjustment based on CHPclim is applied on the calibration parameters. The version 3 being recent, no studies evaluating it against other rainfall products have been found. Thus, below, we are only looking at the performance of the previous version.

#### PERFORMANCE

TARGAT showed good performance over Sahel (Jobard *et al.*, 2011; Novella and Thiaw, 2010; Dinku *et al.*, 2015), Ethiopia (Dinku *et al.*, 2007, 2015), Uganda (Maidment *et al.*, 2013; Asadullah *et al.*, 2008), and East Africa (Cattani *et al.*, 2016). TARGAT tended to underestimate precipitation amount. This dry bias was large over Ethiopia, and relatively low over Sahel. Dembélé and Zwart (2016) found contradictory result over Burkina Faso (part of the Sahel). In their study, TARGAT showed low performance. The main problem of TARGAT, mentioned in most of the studies above, was that it missed high rainfall value.

Dinku *et al.* (2007) showed that RFE2 also underestimated over Ethiopia. They attributed the underestimation of these two products to the information content of IR data in general, and to the warm orographic process in their case. However, this dry bias was recognized later by Maidment *et al.* (2014) when evaluating the performance of TARGAT over Africa, and was attributed to the calibration approach optimized for drought monitoring. Low intensities rainfall events are more important than the high intensity ones for drought monitoring.



**Notes**

<sup>1</sup>from Meteosat  
<sup>2</sup>produced by EUMETSAT  
<sup>3</sup>National Meteorological Agencies

Figure 2.A.16: TARCAT algorithm.



# ACRONYMS

**AMMA** African Monsoon Multi-disciplinary Analyses.

**AMMA-MIP** AMMA - Model Intercomparison Project.

**ARC2** Africa Rainfall Climatology version 2.

**BLD** Blended.

**CAMS-OPI** Climate Anomaly Monitoring System - Outgoing longwave radiation Precipitation Index.

**CDF** Cumulative Density Function.

**CFSR** Climate Forecast System Reanalysis.

**CFSv2** Climate Forecast System version 2.

**CHIRPS** Climate Hazards Group InfraRed Precipitation with Station data.

**CHPclim** Climate Hazards Group's Precipitation Climatology.

**CMAp** **CPC** Merged Analysis of Precipitation.

**CMORPH** **CPC** Morphing technique.

**CORDEX** Coordinated Regional climate Downscaling Experiment.

**CPC** Climate Prediction Center.

**CRT** Corrected.

**CRU-TS** Climatic Research Unit - Time Series.

**CSI** Critical Success Index.

**ENSEMBLES** Ensembles-based Predictions of Climate Changes and Their Impacts.

**EPSAT** Estimation of Precipitation by SATellites.

**ERA** European Centre for Medium-Range Weather Forecasts(ECMWF) ReAnalysis.

**ETS** Equitable Threat Score.

**FAR** False Alarm Ratio.

**FB** Frequency Bias.

**GCM** Global Circulation Model.

**GPCC** Global Precipitation Climatology Centre.

**GPCC-clim** GPCC Climatology.

**GPCC-FDD** [GPCC](#) - Full Data Daily.

**GPCC-FDR** [GPCC](#) - Full Data Reanalysis.

**GPCP** Global Precipitation Climatology project.

**GPCP-SG** GPCP - Satellite and Gauge.

**GPM** Global Precipitation Measurement.

**GSMaP** Global Satellite Mapping of Precipitation.

**GTS** Global Telecommunication System.

**HK** Hanssen and Kuiper discriminant.

**HSS** Heidke Skill Score.

**IMERG** Integrated Multi-satellite Retrievals for [GPM](#).

**IPWG** International Precipitation Working Group.

**IR** InfraRed.

**ITCZ** Inter Tropical Convergence Zone.

**JRA** Japanese Meteorological Agency (JMA) ReAnalysis.

**MAE** Mean Average Error.

**ME** Mean Error.

**MERRA** Modern-[ERA](#) Retrospective Analysis for Research and Applications.

**MSWEP** Multi-Source Weighted-Ensemble Precipitation.

**NS** Nash–Sutcliffe.

**OR** Odds Ratio.

**PERSIANN** Precipitation Estimation from Remote Sensing Information using Artificial Neural Network.

**PERSIANN-CCS** PERSIANN-Cloud Classification System.

**PERSIANN-CDR** PERSIANN-Climate Data Record.

**PMW** Passive Micro-Wave.

**POD** Probability of Detection.

**POFD** Probability of False Detection.

**PR** Precipitation Radar.

**PREC/L** PRECipitation REConstruction over Land.

**R1** NCEP/NCAR Reanalysis.

**R2** NCEP/DOE Reanalysis.

**RCM** Regional Circulation Model.

**RFE2** Rainfall Estimate version 2.

**RMSE** Root Mean Square Error.

**S-RIP** SARC Reanalysis Intercomparison Project.

**SM2RAIN** Soil Moisture to Rainfall.

**SPARC** Stratosphere-troposphere Processes And theIR Role in Climate.

**TAMSAT** Tropical Applications of Meteorology using SATellite data and ground based observations.

**TARCAT** [TAMSAT](#) African Rainfall Climatology And Timeseries.

**TMPA** [TRMM](#) Multi-satellite Precipitation Analysis.

**TRMM** Tropical Rainfall Measuring Mission.

**UDEL** University of Delaware dataset.

**WAM** West African Monsoon.

**WAMME** West African Monsoon Modeling and Evaluation project.



## REFERENCES

- Food and A. Organization, eds., *The State of Food and Agriculture 2016: Climate Change, Agriculture and Food Security* (FAO, 2016) p. 173.
- W. Xu, R. F. Adler, and N.-Y. Wang, *Improving geostationary satellite rainfall estimates using lightning observations: Underlying lightning–rainfall–cloud relationships*, *J. Appl. Meteor. Climatol.* **52**, 213 (2013).
- W. Xu, R. F. Adler, and N.-Y. Wang, *Combining satellite infrared and lightning information to estimate warm-season convective and stratiform rainfall*, *J. Appl. Meteor. Climatol.* **53**, 180 (2014).
- L. Brocca, T. Moramarco, F. Melone, and W. Wagner, *A new method for rainfall estimation through soil moisture observations*, *Geophys. Res. Lett.* **40**, 853 (2013).
- L. Brocca, L. Ciabatta, C. Massari, T. Moramarco, S. Hahn, S. Hasenauer, R. Kidd, W. Dorigo, W. Wagner, and V. Levizzani, *Soil as a natural rain gauge: Estimating global rainfall from satellite soil moisture data*, *J. Geophys. Res. Atmos.* **119**, 5128 (2014).
- E. Kalnay, M. Kanamitsu, R. Kistler, W. Collins, D. Deaven, L. Gandin, M. Iredell, S. Saha, G. White, J. Woollen, Y. Zhu, A. Leetmaa, R. Reynolds, M. Chelliah, W. Ebisuzaki, W. Higgins, J. Janowiak, K. C. Mo, C. Ropelewski, J. Wang, R. Jenne, and D. Joseph, *The NCEP/NCAR 40-year reanalysis project*, *Bull. Amer. Meteor. Soc.* **77**, 437 (1996).
- M. Kanamitsu, W. Ebisuzaki, J. Woollen, S.-K. Yang, J. J. Hnilo, M. Fiorino, and G. L. Potter, *NCEP–DOE AMIP-II Reanalysis (R-2)*, *Bull. Amer. Meteor. Soc.* **83**, 1631 (2002).
- K. Onogi, J. Tsutsui, H. Koide, M. Sakamoto, S. Kobayashi, H. Hatsushika, T. Matsumoto, N. Yamazaki, H. Kamahori, K. Takahashi, S. Kadokura, K. Wada, K. Kato, R. Oyama, T. Ose, N. Mannoji, and R. Taira, *The JRA-25 reanalysis*, *J. Meteor. Soc. Japan. Ser. II* **85**, 369 (2007).
- D. P. Dee, S. M. Uppala, A. J. Simmons, P. Berrisford, P. Poli, S. Kobayashi, U. Andrae, M. A. Balmaseda, G. Balsamo, P. Bauer, P. Bechtold, A. C. M. Beljaars, L. van de Berg, J. Bidlot, N. Bormann, C. Delsol, R. Dragani, M. Fuentes, A. J. Geer, L. Haimberger, S. B. Healy, H. Hersbach, E. V. Hólm, L. Isaksen, P. Kállberg, M. Köhler, M. Matricardi, A. P. McNally, B. M. Monge-Sanz, J.-J. Morcrette, B.-K. Park, C. Peubey, P. de Rosnay, C. Tavolato, J.-N. Thépaut, and F. Vitart, *The ERA-Interim reanalysis: configuration and performance of the data assimilation system*, *Quart. J. Roy. Meteor. Soc.* **137**, 553 (2011).
- M. M. Rienecker, M. J. Suarez, R. Gelaro, R. Todling, J. Bacmeister, E. Liu, M. G. Bosilovich, S. D. Schubert, L. Takacs, G.-K. Kim, S. Bloom, J. Chen, D. Collins, A. Conaty, A. da Silva, W. Gu, J. Joiner, R. D. Koster, R. Lucchesi, A. Molod, T. Owens, S. Pawson, P. Pegion, C. R. Redder, R. Reichle, F. R. Robertson, A. G. Ruddick, M. Sienkiewicz, and J. Woollen, *MERRA: NASA's Modern-Era Retrospective Analysis for Research and Applications*, *J. Climate* **24**, 3624 (2011).

- R. Gelaro, W. McCarty, M. J. Suárez, R. Todling, A. Molod, L. Takacs, C. A. Randles, A. Darmenov, M. G. Bosilovich, R. Reichle, K. Wargan, L. Coy, R. Cullather, C. Draper, S. Akella, V. Buchard, A. Conaty, A. M. da Silva, W. Gu, G.-K. Kim, R. Koster, R. Lucchesi, D. Merkova, J. E. Nielsen, G. Partyka, S. Pawson, W. Putman, M. Rienecker, S. D. Schubert, M. Sienkiewicz, and B. Zhao, *The Modern-Era Retrospective Analysis for Research and Applications, version 2 (MERRA-2)*, *J. Climate* **30**, 5419 (2017).
- S. Kobayashi, Y. Ota, Y. Harada, A. Ebita, M. Moriya, H. Onoda, K. Onogi, H. Kamahori, C. Kobayashi, H. Endo, K. Miyaoka, and K. Takahashi, *The JRA-55 reanalysis: General specifications and basic characteristics*, *J. Meteor. Soc. Japan. Ser. II* **93**, 5 (2015).
- S. Saha, S. Moorthi, H.-L. Pan, X. Wu, J. Wang, S. Nadiga, P. Tripp, R. Kistler, J. Woollen, D. Behringer, H. Liu, D. Stokes, R. Grumbine, G. Gayno, J. Wang, Y.-T. Hou, H.-Y. Chuang, H.-M. H. Juang, J. Sela, M. Iredell, R. Treadon, D. Kleist, P. Van Delst, D. Keyser, J. Derber, M. Ek, J. Meng, H. Wei, R. Yang, S. Lord, H. Van Den Dool, A. Kumar, W. Wang, C. Long, M. Chelliah, Y. Xue, B. Huang, J.-K. Schemm, W. Ebisuzaki, R. Lin, P. Xie, M. Chen, S. Zhou, W. Higgins, C.-Z. Zou, Q. Liu, Y. Chen, Y. Han, L. Cucurull, R. W. Reynolds, G. Rutledge, and M. Goldberg, *The NCEP Climate Forecast System Reanalysis*, *Bull. Amer. Meteor. Soc.* **91**, 1015 (2010).
- H. Hersbach, P. de Rosnay, B. Bell, D. Schepers, A. Simmons, C. Soci, S. Abdalla, M. Alonso-Balmaseda, G. Balsamo, P. Bechtold, P. Berrisford, J.-R. Bidlot, E. de Boisséon, M. Bonavita, P. Browne, R. Buizza, P. Dahlgren, D. Dee, R. Dragani, M. Diamantakis, J. Flemming, R. Forbes, A. J. Geer, T. Haiden, E. Hólm, L. Haimberger, R. Hogan, A. Horányi, M. Janiskova, P. Laloyaux, P. Lopez, J. Muñoz-Sabater, C. Peubey, R. Radu, D. Richardson, J.-N. Thépaut, F. Vitart, X. Yang, E. Zsótér, and H. Zuo, *Operational global reanalysis: progress, future directions and synergies with nwp*, (2018), [10.21957/tkic6g3wm](https://doi.org/10.21957/tkic6g3wm).
- S. Saha, S. Moorthi, X. Wu, J. Wang, S. Nadiga, P. Tripp, D. Behringer, Y.-T. Hou, H.-y. Chuang, M. Iredell, M. Ek, J. Meng, R. Yang, M. P. Mendez, H. van den Dool, Q. Zhang, W. Wang, M. Chen, and E. Becker, *The NCEP Climate Forecast System version 2*, *J. Climate* **27**, 2185 (2014).
- R. I. Maidment, D. Grimes, R. P. Allan, E. Tarnavsky, M. Stringer, T. Hewison, R. Roebeling, and E. Black, *The 30 year TAMSAT African Rainfall Climatology And Time series (TARCAT) data set*, *J. Geophys. Res. Atmos* **119**, 10,619 (2014).
- Q. Sun, C. Miao, Q. Duan, H. Ashouri, S. Sorooshian, and K.-L. Hsu, *A review of global precipitation data sets: Data sources, estimation, and intercomparisons*, *Rev. Geophys.* **56**, 79 (2018).
- H. E. Beck, N. Vergopolan, M. Pan, V. Levizzani, A. I. J. M. van Dijk, G. P. Weedon, L. Brocca, F. Pappenberger, G. J. Huffman, and E. F. Wood, *Global-scale evaluation of 22 precipitation datasets using gauge observations and hydrological modeling*, *Hydrol. Earth Syst. Sci.* **21**, 6201 (2017a).

- T. Dinku, P. Ceccato, E. Grover-Kopec, M. Lemma, S. J. Connor, and C. F. Ropelewski, *Validation of satellite rainfall products over East Africa's complex topography*, *Int. J. Remote Sens.* **28**, 1503 (2007).
- V. Maggioni, P. C. Meyers, and M. D. Robinson, *A review of merged high-resolution satellite precipitation product accuracy during the Tropical Rainfall Measuring Mission (TRMM) era*, *J. Hydrometeor.* **17**, 1101 (2016).
- J. E. Janowiak and P. Xie, *CAMS-OPI: A global satellite-rain gauge merged product for real-time precipitation monitoring applications*, *J. Climate* **12**, 3335 (1999).
- G. J. Huffman and D. T. Bolvin, *GPCP Version 2.2 SG Combined Precipitation Data Set Documentation*, NASA Tech. Doc. (NASA GSFC Mesoscale Atmospheric Processes Laboratory, 2013) [Available online at [ftp://meso.gsfc.nasa.gov/pub/gpcp-v2.2/doc/V2.2\\_doc.pdf](ftp://meso.gsfc.nasa.gov/pub/gpcp-v2.2/doc/V2.2_doc.pdf)].
- R. Adler, M. Sapiiano, G. Huffman, J.-J. Wang, G. Gu, D. Bolvin, L. Chiu, U. Schneider, A. Becker, E. Nelkin, and et al., *The Global Precipitation Climatology Project (GPCP) monthly analysis (new version 2.3) and a review of 2017 global precipitation*, *Atmosphere* **9**, 138 (2018).
- P. Xie and P. Arkin, *Analyses of global monthly precipitation using gauge observations, satellite estimates, and numerical model predictions*, *J. Climate* **9**, 840 (1996).
- P. Xie and P. A. Arkin, *Global precipitation: A 17-year monthly analysis based on gauge observations, satellite estimates, and numerical model outputs*, *Bull. Amer. Meteor. Soc.* **78**, 2539 (1997).
- P. Xie, J. E. Janowiak, P. A. Arkin, R. Adler, A. Gruber, R. Ferraro, G. J. Huffman, and S. Curtis, *GPCP pentad precipitation analyses: An experimental dataset based on gauge observations and satellite estimates*, *J. Climate* **16**, 2197 (2003).
- G. J. Huffman, R. F. Adler, M. M. Morrissey, D. T. Bolvin, S. Curtis, R. Joyce, B. McGavock, and J. Susskind, *Global precipitation at one-degree daily resolution from multisatellite observations*, *J. Hydrometeor.* **2**, 36 (2001).
- R. Adler, M. Sapiiano, and J.-J. Wang, *Global Precipitation Climatology Project (GPCP) Daily Analysis*, Climate Algorithm Theoretical Basis Document CDRP-ATBD-0913 (NOAA Climate Data Record, 2017).
- L. Brocca, P. Filippucci, S. Hahn, L. Ciabatta, C. Massari, S. Camici, L. Schüller, B. Bojkov, and W. Wagner, *Sm2rain-ascats (2007–2018): global daily satellite rainfall from ascats soil moisture*, *Earth System Science Data Discussions* **2019**, 1 (2019).
- G. J. Huffman, D. T. Bolvin, E. J. Nelkin, D. B. Wolff, R. F. Adler, G. Gu, Y. Hong, K. P. Bowman, and E. F. Stocker, *The TRMM Multisatellite Precipitation Analysis (TMPA): Quasi-global, multiyear, combined-sensor precipitation estimates at fine scales*, *J. Hydrometeor.* **8**, 38 (2007).

- G. J. Huffman and D. T. Bolvin, *TRMM and Other Data Precipitation Data Set Documentation*, NASA Tech. Doc. (NASA GSFC Mesoscale Atmospheric Processes Laboratory, 2018) [Available online at [https://pmm.nasa.gov/sites/default/files/document\\_files/3B42\\_3B43\\_doc\\_V7\\_180426.pdf](https://pmm.nasa.gov/sites/default/files/document_files/3B42_3B43_doc_V7_180426.pdf)].
- K. Hsu, H. Ashouri, D. Braithwaite, and S. Sorooshian, *PERSIANN-CDR*, Climate Algorithm Theoretical Basis Document CDRP-ATBD-0286 (NOAA Climate Data Record, 2014) [Available online at [https://www.ncdc.noaa.gov/sites/default/files/cdr-documentation/CDRP\\_ATBD\\_01B-16\\_05122014.pdf](https://www.ncdc.noaa.gov/sites/default/files/cdr-documentation/CDRP_ATBD_01B-16_05122014.pdf)].
- H. Ashouri, K.-L. Hsu, S. Sorooshian, D. K. Braithwaite, K. R. Knapp, L. D. Cecil, B. R. Nelson, and O. P. Prat, *PERSIANN-CDR: Daily precipitation climate data record from multisatellite observations for hydrological and climate studies*, *Bull. Amer. Meteor. Soc.* **96**, 69 (2015).
- R. J. Joyce, J. E. Janowiak, P. A. Arkin, and P. Xie, *CMORPH: A method that produces global precipitation estimates from passive microwave and infrared data at high spatial and temporal resolution*, *J. Hydrometeor.* **5**, 487 (2004).
- P. Xie, R. Joyce, S. Wu, S.-H. Yoo, Y. Yarosh, F. Sun, and R. Lin, *Reprocessed, bias-corrected CMORPH global high-resolution precipitation estimates from 1998*, *J. Hydrometeor.* **18**, 1617 (2017).
- S. Sorooshian, K.-L. Hsu, X. Gao, H. V. Gupta, B. Imam, and D. Braithwaite, *Evaluation of PERSIANN system satellite-based estimates of tropical rainfall*, *Bull. Amer. Meteor. Soc.* **81**, 2035 (2000).
- K.-L. Hsu and S. Sorooshian, *Satellite-based precipitation measurement using PERSIANN system*, in *Hydrological Modelling and the Water Cycle: Coupling the Atmospheric and Hydrological Models*, edited by S. Sorooshian, K.-L. Hsu, E. Coppola, B. Tomassetti, M. Verdecchia, and G. Visconti (Springer Berlin Heidelberg, 2008) pp. 27–48.
- N. S. Novella and W. M. Thiaw, *African rainfall climatology version 2 for famine early warning systems*, *J. Appl. Meteor. Climatol.* **52**, 588 (2013).
- NOAA, CPC, *The NOAA Climate Prediction Center African Rainfall Estimation Algorithm Version 2.0*, NOAA CPC Tech. Note (NOAA CPC, 2001) [Available online at [http://www.cpc.noaa.gov/products/fews/RFE2.0\\_tech.pdf](http://www.cpc.noaa.gov/products/fews/RFE2.0_tech.pdf)].
- H. E. Beck, A. I. J. M. van Dijk, V. Levizzani, J. Schellekens, D. G. Miralles, B. Martens, and A. de Roo, *MSWEP: 3-hourly 0.25° global gridded precipitation (1979–2015) by merging gauge, satellite, and reanalysis data*, *Hydrol. Earth Syst. Sci.* **21**, 589 (2017b).
- H. E. Beck, E. F. Wood, M. Pan, C. K. Fisher, D. G. Miralles, A. I. J. M. van Dijk, T. R. McVicar, and R. F. Adler, *MSWEP v2 global 3-hourly 0.1° precipitation: Methodology and quantitative assessment*, "*Bull. Amer. Meteor. Soc.*" **100**, 473 (2019).
- T. Ushio, K. Sasashige, T. Kubota, S. Shige, K. Okamoto, K. Aonashi, T. Inoue, N. Takahashi, T. Iguchi, M. Kachi, R. Oki, T. Morimoto, and Z.-I. Kawasaki, *A Kalman filter*

- approach to the global satellite mapping of precipitation (GSMaP) from combined passive microwave and infrared radiometric data*, *J. Meteor. Soc. Japan. Ser. II* **87A**, 137 (2009).
- K. Aonashi, J. Awaka, M. Hirose, T. Kozu, T. Kubota, G. Liu, S. Shige, S. Kida, S. Seto, N. Takahashi, and Y. N. Takayabu, *GSMaP passive microwave precipitation retrieval algorithm : Algorithm description and validation*, *J. Meteor. Soc. Japan. Ser. II* **87A**, 119 (2009).
- T. Mega, T. Ushio, T. Kubota, M. Kachi, K. Aonashi, and S. Shige, *Gauge adjusted global satellite mapping of precipitation (GSMaP Gauge)*, in *Extended Abstract, XXXIth URSI Gen. Assembly and Sci. Symp.* (IEEE, Beijing, China, 2014) pp. 1–4.
- G. J. Huffman, D. T. Bolvin, D. Braithwaite, K. Hsu, R. Joyce, C. Kidd, E. J. Nelkin, S. Sorooshian, J. Tan, and P. Xie, *NASA Global Precipitation Measurement (GPM) Integrated Multi-satellitE Retrievals for GPM (IMERG)*, Algorithm Theoretical Basis Document Version 5.2 (NASA GSFC, Greenbelt, MD 20771, USA, 2018) [Available online at [https://pmm.nasa.gov/sites/default/files/document\\_files/IMERG\\_ATBD\\_V5.2\\_0.pdf](https://pmm.nasa.gov/sites/default/files/document_files/IMERG_ATBD_V5.2_0.pdf)].
- C. C. Funk, P. J. Peterson, M. F. Landsfeld, D. H. Pedreros, J. P. Verdin, J. D. Rowland, B. E. Romero, G. J. Husak, J. C. Michaelsen, and A. P. Verdin, *A Quasi-Global Precipitation Time Series for Drought Monitoring*, U.S. Geological Survey Data Series, Vol. 832 (USGS EROS, 2014) p. 4, [doi:10.3133/ds832].
- C. Funk, P. Peterson, M. Landsfeld, D. Pedreros, J. Verdin, S. Shukla, G. Husak, J. Rowland, L. Harrison, A. Hoell, and J. Michaelsen, *The climate hazards infrared precipitation with stations—a new environmental record for monitoring extremes*, *Sci. Data* **2** (2015a).
- Y. Hong, K.-L. Hsu, S. Sorooshian, and X. Gao, *Precipitation Estimation from Remotely Sensed Imagery using an Artificial Neural Network Cloud Classification System*, *J. Appl. Meteor.* **43**, 1834 (2004).
- E. Tarnavsky, D. Grimes, R. Maidment, E. Black, R. P. Allan, M. Stringer, R. Chadwick, and F. Kayitakire, *Extension of the TAMSAT satellite-based rainfall monitoring over Africa and from 1983 to present*, *J. Appl. Meteor. Climatol.* **53**, 2805 (2014).
- R. I. Maidment, D. Grimes, E. Black, E. Tarnavsky, M. Young, H. Greatrex, R. P. Allan, T. Stein, E. Nkonde, S. Senkunda, E. Misael, and U. Alcántara, *Data descriptor: A new, long-term daily satellite-based rainfall dataset for operational monitoring in Africa*, *Sci. Data* **4** (2017), 10.1038/sdata.2017.63.
- G. Nikulin, S. Asharaf, M. E. Magariño, S. Calmanti, R. M. Cardoso, J. Bhend, J. Fernández, M. D. Frías, K. Fröhlich, B. Früh, S. H. García, R. Manzananas, J. M. Gutiérrez, U. Hansson, M. Kolax, M. A. Liniger, P. M. Soares, C. Spirig, R. Tome, and K. Wyser, *Dynamical and statistical downscaling of a global seasonal hindcast in eastern africa*, *Climate Services* **9**, 72 (2018).

- S. H. Gebrechorkos, S. Hülsmann, and C. Bernhofer, *Statistically downscaled climate dataset for East Africa*, "Sci. Data" **6**, 31 (2019).
- Y. Xue, F. De Sales, W. K.-M. Lau, A. Boone, J. Feng, P. Dirmeyer, Z. Guo, K.-M. Kim, A. Kitoh, V. Kumar, I. Pocard-Leclercq, N. Mahowald, W. Moufouma-Okia, P. Pegion, D. P. Rowell, J. Schemm, S. D. Schubert, A. Sealy, W. M. Thiaw, A. Vintzileos, S. F. Williams, and M.-L. C. Wu, *Intercomparison and analyses of the climatology of the West African Monsoon in the West African Monsoon Modeling and Evaluation project (WAMME) first model intercomparison experiment*, *Climate Dyn.* **35**, 3 (2010).
- F. Hourdin, I. Musat, F. Guichard, P. M. Ruti, F. Favot, M.-A. Filiberti, M. Pham, J.-Y. Grandpeix, J. Polcher, P. Marquet, A. Boone, J.-P. Lafore, J.-L. Redelsperger, A. Dell'Aquila, T. L. Doval, A. K. Traore, and H. Gallée, *AMMA-Model Intercomparison Project*, *Bull. Amer. Meteor. Soc.* **91**, 95 (2010).
- J. Crétat, E. K. Vizy, and K. H. Cook, *How well are daily intense rainfall events captured by current climate models over Africa?* *Climate Dyn.* **42**, 2691 (2014).
- T. Haiden, M. J. Rodwell, D. S. Richardson, A. Okagaki, T. Robinson, and T. Hewson, *Intercomparison of global model precipitation forecast skill in 2010/11 using the SEEPS score*, *Mon. Wea. Rev.* **140**, 2720 (2012).
- E. E. Ebert, J. E. Janowiak, and C. Kidd, *Comparison of near-real-time precipitation estimates from satellite observations and numerical models*, *Bull. Amer. Meteor. Soc.* **88**, 47 (2007).
- U. Schneider, A. Becker, P. Finger, A. Meyer-Christoffer, M. Ziese, and B. Rudolf, *GPCC's new land surface precipitation climatology based on quality-controlled in situ data and its role in quantifying the global water cycle*, *Theor. Appl. Climatol.* **115**, 15 (2014).
- I. Harris, P. Jones, T. Osborn, and D. Lister, *Updated high-resolution grids of monthly climatic observations – the CRU TS3.10 Dataset*, *Int. J. Climatol.* **34**, 623 (2014).
- K. Matsuura and C. J. Willmott, *Terrestrial Precipitation: 1900-2014 Gridded Monthly Time Series (version 4.01)*, Archive Doc. (University of Delaware, Newark, DE, 2015) [Available online at [http://climate.geog.udel.edu/~climate/html\\_pages/Global2014/README\\_GlobalTsP2014.html](http://climate.geog.udel.edu/~climate/html_pages/Global2014/README_GlobalTsP2014.html).].
- M. Chen, P. Xie, J. E. Janowiak, and P. A. Arkin, *Global Land Precipitation: A 50-yr Monthly Analysis Based on Gauge Observations*, *J. Hydrometeor.* **3**, 249 (2002).
- P. Xie, M. Chen, S. Yang, A. Yatagai, T. Hayasaka, Y. Fukushima, and C. Liu, *A gauge-based analysis of daily precipitation over East Asia*, *J. Hydrometeor.* **8**, 607 (2007).
- M. Chen, W. Shi, P. Xie, V. B. S. Silva, V. E. Kousky, R. W. Higgins, and J. E. Janowiak, *Assessing objective techniques for gauge-based analyses of global daily precipitation*, *J. Geophys. Res. Atmos.* **113** (2008), 10.1029/2007JD009132.

- M. Fujiwara, J. S. Wright, G. L. Manney, L. J. Gray, J. Anstey, T. Birner, S. Davis, E. P. Gerber, V. L. Harvey, M. I. Hegglin, C. R. Homeyer, J. A. Knox, K. Krüger, A. Lambert, C. S. Long, P. Martineau, A. Molod, B. M. Monge-Sanz, M. L. Santee, S. Tegtmeier, S. Chabrilat, D. G. H. Tan, D. R. Jackson, S. Polavarapu, G. P. Compo, R. Dragani, W. Ebisuzaki, Y. Harada, C. Kobayashi, W. McCarty, K. Onogi, S. Pawson, A. Simmons, K. Wargan, J. S. Whitaker, and C.-Z. Zou, *Introduction to the SPARC Reanalysis Intercomparison Project (S-RIP) and overview of the reanalysis systems*, *Atmos. Chem. Phys.* **17**, 1417 (2017).
- M. G. Bosilovich, J. Chen, F. R. Robertson, and R. F. Adler, *Evaluation of global precipitation in reanalyses*, *J. Appl. Meteor. Climatol.* **47**, 2279 (2008).
- R. I. Maidment, D. I. F. Grimes, R. P. Allan, H. Greatrex, O. Rojas, and O. Leo, *Evaluation of satellite-based and model re-analysis rainfall estimates for Uganda*, *Meteor. Appl.* **20**, 308 (2013).
- C. Funk and J. Verdin, *Comparing satellite rainfall estimates and reanalysis precipitation fields with station data for Western Kenya*, in *Extended Abstract, JRC-FAO International Workshop on Crop Monitoring for Food Security in Africa* (JRC-FAO, Nairobi, Kenya, 2003).
- A. J. Koutsouris, D. Chen, and S. W. Lyon, *Comparing global precipitation data sets in eastern Africa: a case study of Kilombero Valley, Tanzania*, *Int. J. Climatol.* **36**, 2000 (2016).
- V. Thiemig, R. Rojas, M. Zambrano-Bigiarini, V. Levizzani, and A. De Roo, *Validation of satellite-based precipitation products over sparsely gauged African river basins*, *J. Hydrometeorol.* **13**, 1760 (2012).
- A. W. Worqlul, B. Maathuis, A. A. Adem, S. S. Demissie, S. Langan, and T. S. Steenhuis, *Comparison of rainfall estimations by TRMM 3B42, MPEG and CFSR with ground-observed data for the Lake Tana basin in Ethiopia*, *Hydrol. Earth Syst. Sci.* **18**, 4871 (2014).
- K. Hennermann, *ERA5 data documentation*, <https://confluence.ecmwf.int/display/CKB/ERA5+data+documentation> (2019).
- M. Bosilovich, S. Akella, L. Coy, R. Cullather, C. Draper, R. Gelaro, K. Robin, L. Qing, M. Andrea, N. Peter, W. Krzysztof, C. Winston, R. Rolf, T. Lawrence, V. Yury, B. Steve, C. Allison, F. Stacey, L. Gordon, P. Gary, P. Steven, R. Oreste, S. Siegfried D., and S. Max, *MERRA-2: Initial Evaluation of the Climate*, Technical Report Series on Global Modeling and Data Assimilation, Vol. 43 (2015).
- J.-E. Kim and M. J. Alexander, *Tropical precipitation variability and convectively coupled equatorial waves on submonthly time scales in reanalyses and TRMM*, *J. Climate* **26**, 3013 (2013).
- E. Nkiaka, N. R. Nawaz, and J. C. Lovett, *Evaluating global reanalysis precipitation datasets with rain gauge measurements in the sudano-sahel region: case study of the Logone catchment, Lake Chad Basin*, *Meteor. Appl.* **24**, 9 (2017).

- L. M. Druyan, J. Feng, K. H. Cook, Y. Xue, M. Fulakeza, S. M. Hagos, A. Konaré, W. Moufouma-Okia, D. P. Rowell, E. K. Vizy, and S. S. Ibrah, *The WAMME regional model intercomparison study*, *Climate Dyn.* **35**, 175 (2010).
- M. B. Sylla, I. Diallo, and J. S. Pal, *West African monsoon in state-of-the-science regional climate models*, in *Climate Variability-Regional and Thematic Patterns*, edited by A. Tarhule (InTechOpen, 2013) pp. 3–36.
- H. Paeth, N. M. Hall, M. A. Gaertner, M. D. Alonso, S. Moumouni, J. Polcher, P. M. Ruti, A. H. Fink, M. Gosset, T. Lebel, A. T. Gaye, D. P. Rowell, W. Moufouma-Okia, D. Jacob, B. Rockel, F. Giorgi, and M. Rummukainen, *Progress in regional downscaling of West African precipitation*, *Atmos. Sci. Lett.* **12**, 75 (2011).
- G. Nikulin, C. Jones, F. Giorgi, G. Asrar, M. Büchner, R. Cerezo-Mota, O. B. Christensen, M. Déqué, J. Fernandez, A. Hänsler, E. van Meijgaard, P. Samuelsson, M. B. Sylla, and L. Sushama, *Precipitation climatology in an ensemble of CORDEX-Africa regional climate simulations*, *J. Climate* **25**, 6057 (2012).
- L. M. Druyan and M. Fulakeza, *Downscaling reanalysis over continental Africa with a regional model: NCEP versus ERA Interim forcing*, *Climate Res.* **56**, 181 (2013).
- C. Kidd and V. Levizzani, *Status of satellite precipitation retrievals*, *Hydrol. Earth Syst. Sci.* **15**, 1109 (2011).
- C. Kidd and G. Huffman, *Global precipitation measurement*, *Meteor. Appl.* **18**, 334 (2011).
- C. Funk, A. Verdin, J. Michaelsen, P. Peterson, D. Pedreros, and G. Husak, *A global satellite-assisted precipitation climatology*, *Earth Syst. Sci. Data* **7**, 275 (2015b).
- I. Jobard, F. Chopin, J. C. Berges, and R. Roca, *An intercomparison of 10-day satellite precipitation products during West African monsoon*, *Int. J. Remote Sens.* **32**, 2353 (2011).
- C. Pierre, G. Bergametti, B. Marticorena, E. Mougin, T. Lebel, and A. Ali, *Pluriannual comparisons of satellite-based rainfall products over the Sahelian belt for seasonal vegetation modeling*, *J. Geophys. Res. Atmos* **116** (2011), 10.1029/2011JD016115.
- N. Novella and W. Thiaw, *Validation of satellite-derived rainfall products over the Sahel*, (2010), [Available online at <https://pdfs.semanticscholar.org/c826/2ff005dc7d2c79e1c60e205076ba1a8f8821.pdf>.].
- M. Dembélé and S. J. Zwart, *Evaluation and comparison of satellite-based rainfall products in Burkina Faso, West Africa*, *Int. J. Remote Sens.* **37**, 3995 (2016).
- M. Gosset, J. Viarre, G. Quantin, and M. Alcoba, *Evaluation of several rainfall products used for hydrological applications over West Africa using two high-resolution gauge networks*, *Quart. J. Roy. Meteor. Soc.* **139**, 923 (2013).
- T. Dinku, S. Alessandrini, M. Evangelisti, and O. Rojas, *A description and evaluation of FAO satellite rainfall estimation algorithm*, *Atmos. Res.* **163**, 48 (2015).



- T. Dinku, S. Chidzambwa, P. Ceccato, S. J. Connor, and C. F. Ropelewski, *Validation of high-resolution satellite rainfall products over complex terrain*, *Int. J. Remote Sens.* **29**, 4097 (2008a).
- T. Dinku, P. Ceccato, and S. J. Connor, *Challenges of satellite rainfall estimation over mountainous and arid parts of East Africa*, *Int. J. Remote Sens.* **32**, 5965 (2011a).
- A. Asadullah, N. Mcintyre, and M. Kigobe, *Evaluation of five satellite products for estimation of rainfall over Uganda / Evaluation de cinq produits satellitaires pour l'estimation des précipitations en Ouganda*, *Hydrolog. Sci. J.* **53**, 1137 (2008).
- J. E. Diem, J. Hartter, S. J. Ryan, and M. W. Palace, *Validation of satellite rainfall products for Western Uganda*, *J. Hydrometeor.* **15**, 2030 (2014).
- E. Cattani, A. Merino, and V. Levizzani, *Evaluation of monthly satellite-derived precipitation products over East Africa*, *J. Hydrometeor.* **17**, 2555 (2016).
- C. Toté, D. Patricio, H. Boogaard, R. Van der Wijngaart, E. Tarnavsky, and C. Funk, *Evaluation of satellite rainfall estimates for drought and flood monitoring in mozambique*, *"Remote Sens."* **7**, 1758 (2015).
- C. Lorenz and H. Kunstmann, *The hydrological cycle in three state-of-the-art reanalyses: Intercomparison and performance analysis*, *J. Hydrometeor.* **13**, 1397 (2012).
- T. Dinku, S. J. Connor, P. Ceccato, and C. F. Ropelewski, *Comparison of global gridded precipitation products over a mountainous region of Africa*, *Int. J. Climatol.* **28**, 1627 (2008b).
- N. van de Giesen, R. Hut, and J. Selker, *The Trans-African Hydro-Meteorological Observatory (TAHMO)*, *WIREs Water* **1**, 341 (2014).
- A. Ali, A. Amani, A. Diedhiou, and T. Lebel, *Rainfall estimation in the Sahel. Part II: Evaluation of rain gauge networks in the CILSS countries and objective intercomparison of rainfall products*, *J. Appl. Meteor.* **44**, 1707 (2005).
- U. K. Okoro, W. Chen, C. Chineke, and O. Nwofor, *Comparative analysis of gridded datasets and gauge measurements of rainfall in the Niger Delta region*, *Res. J. Environ. Sci.* **8**, 373 (2014).
- T. Dinku, S. Connor, and P. Ceccato, *Evaluation of satellite rainfall estimates and gridded gauge products over the Upper Blue Nile region*, in *Nile River Basin: Hydrology, Climate and Water Use*, edited by A. M. Melesse (Springer Netherlands, 2011) pp. 109–127.
- A. Serrat-Capdevila, J. B. Valdes, and E. Z. Stakhiv, *Water management applications for satellite precipitation products: Synthesis and recommendations*, *J. Am. Water Resour. Assoc.* **50**, 509 (2014).
- F. A. Hirpa, M. Gebremichael, and T. Hopson, *Evaluation of high-resolution satellite precipitation products over very complex terrain in Ethiopia*, *J. Appl. Meteor. Climatol.* **49**, 1044 (2010).

- American Meteorological Society, *Precipitation regime. Glossary of Meteorology*, (cited 2019), available online at [http://glossary.ametsoc.org/wiki/Precipitation\\_regime](http://glossary.ametsoc.org/wiki/Precipitation_regime).
- T. G. Romilly and M. Gebremichael, *Evaluation of satellite rainfall estimates over Ethiopian river basins*, *Hydrol. Earth Syst. Sci.* **15**, 1505 (2011).
- T. Dinku, P. Ceccato, K. Cressman, and S. J. Connor, *Evaluating detection skills of satellite rainfall estimates over Desert Locust recession regions*, *J. Appl. Meteor. Climatol.* **49**, 1322 (2010).
- N.-Y. Wang, C. Liu, R. Ferraro, D. Wolff, E. Zipser, and C. Kummerow, *TRMM 2A12 land precipitation product - Status and future plans*, *J. Meteor. Soc. Japan. Ser. II* **87A**, 237 (2009).
- V. Thiemig, R. Rojas, M. Zambrano-Bigiarini, and A. D. Roo, *Hydrological evaluation of satellite-based rainfall estimates over the Volta and Baro-Akobo Basin*, *J. Hydrol.* **499**, 324 (2013).
- U. Pfeifroth, J. Trentmann, A. H. Fink, and B. Ahrens, *Evaluating satellite-based diurnal cycles of precipitation in the African Tropics*, *J. Appl. Meteor. Climatol.* **55**, 23 (2016).
- R. Roca, P. Chambon, I. Jobard, P.-E. Kirstetter, M. Gosset, and J. C. Bergès, *Comparing satellite and surface rainfall products over West Africa at meteorologically relevant scales during the AMMA campaign using error estimates*, *J. Appl. Meteor. Climatol.* **49**, 715 (2010).
- J. Sheffield, E. F. Wood, N. Chaney, K. Guan, S. Sadri, X. Yuan, L. Olang, A. Amani, A. Ali, S. Demuth, and L. Ogallo, *A drought monitoring and forecasting system for sub-Saharan African water resources and food security*, "*Bull. Amer. Meteor. Soc.*" **95**, 861 (2014).
- V. Thiemig, A. de Roo, and H. Gadain, *Current status on flood forecasting and early warning in Africa*, "*Int. J. River Basin Manag.*" **9**, 63 (2011).
- A. Becker, P. Finger, A. Meyer-Christoffer, B. Rudolf, K. Schamm, U. Schneider, and M. Ziese, *A description of the global land-surface precipitation data products of the Global Precipitation Climatology Centre with sample applications including centennial (trend) analysis from 1901-present*, *Earth System Science Data* **5**, 71 (2013).
- C. Kummerow, *Global precipitation – the successes and shortcomings at different space and time resolutions*, in *Boussinesq Lecture 2017: Precipitation* (Boussinesq Center for Hydrology, Delft, Netherlands, 2017).
- R. F. Adler, G. J. Huffman, A. Chang, R. Ferraro, P.-P. Xie, J. Janowiak, B. Rudolf, U. Schneider, S. Curtis, D. Bolvin, A. Gruber, J. Susskind, P. Arkin, and E. Nelkin, *The version-2 Global Precipitation Climatology Project (GPCP) monthly precipitation analysis (1979–present)*, *J. Hydrometeor.* **4**, 1147 (2003).
- G. J. Huffman, R. F. Adler, D. T. Bolvin, and G. Gu, *Improving the global precipitation record: GPCP version 2.1*, *Geophys. Res. Lett.* **36**, L17808 (2009).

- M. K. Joshi, A. Rai, and A. C. Pandey, *Validation of TMPA and GPCP 1DD against the ground truth rain-gauge data for Indian region*, *Int. J. Climatol.* **33**, 2633 (2012).
- M. M. Bitew and M. Gebremichael, *Evaluation through independent measurements: Complex terrain and humid tropical region in Ethiopia*, in *Satellite Rainfall Applications for Surface Hydrology*, edited by M. Gebremichael and F. Hossain (Springer Netherlands, 2010) pp. 205–214.
- A. T. Haile, E. Habib, M. Elsaadani, and T. Rientjes, *Inter-comparison of satellite rainfall products for representing rainfall diurnal cycle over the Nile basin*, *Int. J. Appl. Earth Obs. Geoinf.* **21**, 230 (2013).
- A. K. Dezfuli, C. M. Ichoku, G. J. Huffman, K. I. Mohr, J. S. Selker, N. van de Giesen, R. Hochreutener, and F. O. Annor, *Validation of IMERG precipitation in Africa*, *J. Hydrometeor.* **18**, 2817 (2017a).
- A. K. Dezfuli, C. M. Ichoku, K. I. Mohr, and G. J. Huffman, *Precipitation characteristics in West and East Africa from satellite and in situ observations*, *J. Hydrometeor.* **18**, 1799 (2017b).
- Y. C. Gao and M. F. Liu, *Evaluation of high-resolution satellite precipitation products using rain gauge observations over the Tibetan Plateau*, *Hydrol. Earth Syst. Sci.* **17**, 837 (2013).
- M. Zambrano-Bigiarini, A. Nauditt, C. Birkel, K. Verbist, and L. Ribbe, *Temporal and spatial evaluation of satellite-based rainfall estimates across the complex topographical and climatic gradients of Chile*, *Hydrol. Earth Syst. Sci.* **21**, 1295 (2017).
- Y. Hong, D. Gochis, J.-t. Cheng, K.-l. Hsu, and S. Sorooshian, *Evaluation of PERSIANN-CCS rainfall measurement using the NAME event rain gauge network*, *J. Hydrometeor.* **8**, 469 (2007).
- A. Herman, V. B. Kumar, P. A. Arkin, and J. V. Kousky, *Objectively determined 10-day African rainfall estimates created for famine early warning systems*, *Int. J. Remote Sens.* **18**, 2147 (1997).
- TAMSAT Group, *TAMSAT version 3 calibration methodology*, Draft TAMSAT Tech.l Rep. (University of Reading, Reading, UK, 2016) [Available online at [http://www.met.reading.ac.uk/~emily/TAMSAT\\_technical\\_report.pdf](http://www.met.reading.ac.uk/~emily/TAMSAT_technical_report.pdf)].

# 3

## CORRECTING POSITION ERROR IN PRECIPITATION ESTIMATES USING IMAGE WARPING

*Clouds do not always mean rain,  
but smoke is a sure sign of fire.*

African proverb

*In this chapter, we investigate the use of a warping method to correct position error in rainfall estimates. Warping is a field deformation method that transforms an image (or in this case a rainfall field) by modifying the coordinates. Satellite-based estimates usually use gauge data for bias correction, that is to correct the rainfall intensity. Here, our goal is to gauge-adjust a satellite-based estimate with respect to the position of the rain event instead of its intensity.*

---

This chapter is based on:

**C. Le Coz**, A. Heemink, M. Verlaan, M.-C. ten Veldhuis, and N. van de Giesen, *Correcting Position Error in Precipitation Data Using Image Morphing*, [Remote Sensing](#) **11**, 2557 (2019).

### 3.1. INTRODUCTION

Rain-gauges are the most direct way to measure precipitation. However, the gauge networks in Africa are not dense enough to derive high resolution precipitation estimates. Indeed, the rain-gauge distribution is sparse in many African regions and their number has been decreasing in the recent decades [Lorenz and Kunstmann \(2012\)](#). During the same period, many efforts have been made to derive precipitation estimates from satellite data. Satellites do not measure precipitation directly but have the advantage of covering large areas. This is especially interesting for Africa where gauge networks are sparse and there are also almost no radar observations available.

There is an increasing number of satellite-based rainfall products, providing rainfall estimates at different spatial and temporal resolutions ([Le Coz and van de Giesen, 2020](#)). Most rainfall products use additional sources of data, such as gauge estimates, for bias correction. Bias correction methods focus on correcting the intensity. However, the intensity is not the only possible error in precipitation. Rainfall events are coherent moving systems and, in the case of convective rainstorms, they are also very localized. This can lead to errors in the estimation of the position and shape of the rain events beside the errors in their intensity. For some applications, such as hydrological modeling [Morin et al. \(2006\)](#); [Cristiano et al. \(2017\)](#), flash flood warnings [Arnaud et al. \(2002\)](#) or data assimilation in a numerical weather model [Xiao et al. \(2000\)](#); [Lopez \(2011\)](#), detecting the correct location of the rain events can be as important as their intensity.

The position errors in weather forecast models, including precipitation, have been taken into account in the field of forecast verification. Several spatial verification approaches have been developed ([Gilleland et al., 2009](#); [Ahijevych et al., 2009](#)). They can be divided into four categories: neighborhood, scale-decomposition (e.g., [Briggs and Levine \(1997\)](#); [Casati et al. \(2004\)](#); [Casati \(2010\)](#)), object- (or feature-)based (e.g., [Ebert and McBride \(2000\)](#); [Davis et al. \(2006\)](#); [Marzban and Sandgathe \(2006\)](#)) and field deformation. In this chapter, we focus on a method belonging to the latter category. We now give an overview of field deformation method used for weather-related variables. Field deformation methods are based on a spatial mapping or displacement that makes a field (e.g., forecast) more similar to a target field or observation. The deformation is determined by minimizing a cost function. The Feature Calibration and Alignment technique (FCA [Hoffman et al. \(1995\)](#); [Hoffman and Grassotti \(1996\)](#); [Grassotti et al. \(1999\)](#)) is one of these methods. FCA has also been used for correcting position errors in cloud or water vapor related fields in the framework of data assimilation. For instance, [Hoffman and Grassotti \(1996\)](#) and [Nehrkorn et al. \(2015\)](#) corrected position error in a numerical weather model background fields using integrated water vapor measurements from satellite. In [Aonashi and Eito \(2011\)](#), the FCA is used as a preprocessing step of an ensemble-based variational assimilation scheme for (satellite) brightness temperature. [Nehrkorn et al. \(2014\)](#) tested this method with several types of observations: integrated water vapor, lower level pressure, brightness temperature and simulated radar reflection. Other feature alignment techniques have been developed and used in data assimilation schemes, such as [Brewster \(2003\)](#) (for simulated radar observation), [Lawson and Hansen \(2005\)](#) and [Ravela et al. \(2007\)](#) (for some idealized cases). The FCA technique has been applied directly to rainfall data in [Grassotti et al. \(1999\)](#). They corrected rainfall estimates derived from SSM/I data with ground-based radar estimates. They illustrated the perfor-

mance of their approach for different types of rainfall events, such as Hurricane Andrew, a squall line in Oklahoma and coastal rainfall in Australia.

Some field deformation methods for spatial verification originate from image processing, such as the optical flow techniques developed in [Keil and Craig \(2007, 2009\)](#) or in [Marzban and Sandgathe \(2010\)](#) and evaluated in [Marzban \*et al.\* \(2009\)](#) and [Han and Szunyogh \(2016\)](#). Image warping has also been used in data assimilation frameworks. [Alexander \*et al.\* \(1998\)](#) assimilated integrated water vapor from satellite to improve a numerical weather model forecast. However, this method requires the manual selection of pairs of points to perform the image warping. [Beezley and Mandel \(2008\)](#) combined image morphing with an ensemble Kalman filter (EnKF) for a wild fire model. They use an automatic registration technique that only requires two fields to derive the displacement field, without any manual specification needed. Using the same morphing and registration method, a morphing fast Fourier transform (FFT) EnKF for radar precipitation is described in [Mandel \*et al.\* \(2010\)](#). However, this morphing FFT EnKF has not been implemented or applied to rainfall data.

This chapter investigates the use of a warping approach for the position correction of rainfall estimates, using the approach proposed by [Beezley and Mandel \(2008\)](#) and [Mandel \*et al.\* \(2010\)](#) (warping being a part of morphing). While the goal of [Mandel \*et al.\* \(2010\)](#) was to derive a method to assimilate radar precipitation into a numerical weather model, we aim to correct the position error of satellite-based precipitation estimates using gauge measurements. We apply the warping approach to real precipitation data, namely the (non-gauge adjusted) IMERG<sup>1</sup>-Late estimates and the new TAHMO<sup>2</sup> gauge network (described in [Huffman \*et al.\* \(2018\)](#) and [van de Giesen \*et al.\* \(2014\)](#) respectively). We extend the registration method so that several time steps can be processed at once, allowing time steps to influence each other (or not).

The warping and automatic registration methods, including the case of irregularly spaced observations and the time expansion, are described in Section 3.2. The warping approach is applied to two cases. The first case uses synthetic rainfall events represented by ellipses (Section 3.3). The second case is a real rainfall event occurring in southern Ghana during the monsoon season (Section 3.4). The results of both cases are evaluated with respect to the intensity, position and timing of the events. In addition, the synthetic case is used to investigate the impact of several parameters of the registration method on the results. The results of the two cases are compared and discussed in Section 3.5, before the conclusion in Section 3.6. Possible future work and improvement are discussed in Section 3.7.

## 3.2. METHODOLOGY

In this section, we define the image registration and warping methods, before focusing on the implementation of an automatic registration. We use the framework described by [Mandel \*et al.\* \(2010\)](#).

---

<sup>1</sup>Integrated Multi-satellitE Retrievals for GPM.

<sup>2</sup>Trans-African Hydro-Meteorological Observatory.

### 3.2.1. DEFINITIONS

Let  $u$  and  $v$  be two signals (or images) defined on a domain  $D \subset \mathbb{R}^2$ , and  $T : (x, y) \in \mathbb{R}^2 \mapsto (T_x(x, y), T_y(x, y)) \in \mathbb{R}^2$  be a mapping function. The goal of **image registration** is to determine a spatial mapping  $T$  such that,  $\forall (x, y) \in D$ ,

$$\begin{aligned} v(x, y) &\approx u[(I + T)(x, y)] \\ &\approx u[x + T_x(x, y), y + T_y(x, y)] \end{aligned} \quad (3.1)$$

where  $I$  is the identity function. In the remainder of this chapter, we adopt a more compact expression  $u \circ (I + T)$  for the application of a mapping  $T$  to a signal  $u$ , where  $\circ$  is the composition operator.

There can be several mappings  $T$  that meet the requirement  $v \approx u \circ (I + T)$ . Especially in areas without rainfall, the mapping  $T$  is not unique. We define three criteria to characterize one optimal mapping :

$$T \approx 0 \quad (3.2)$$

$$\nabla T \approx 0 \quad (3.3)$$

$$\nabla \cdot T \approx 0 \quad (3.4)$$

That is, the optimal mapping has to be as small, smooth, and divergent-free (i.e. it is not shrinking or expanding the field) as possible.

Several approaches have been used to define the optimality of the mapping. For the FCA method applied on precipitation, [Grassotti et al. \(1999\)](#) use smoothness and barrier conditions. Contrary to our condition on the magnitude (Equation (3.2)), their barrier does not impact small scale displacements. Using the FCA for data assimilation, [Nehrkorn et al. \(2015, 2014\)](#) added two more constraints, one on the magnitude and one on the divergent. [Ravela et al. \(2007\)](#) did not use any magnitude or barrier approach, and only had constraints on the gradient and the divergence. Our constraints on the magnitude and on the smoothness are the same as the ones used in [Beezley and Mandel \(2008\)](#). Constraints on the divergence were used in several similar field distortion methods ([Nehrkorn et al. \(2015, 2014\)](#); [Ravela et al. \(2007\)](#)). Thus, we also added a third constraint on the divergence in order to observe its impact. The sensitivity of the results to these three coefficients is presented in Section 3.3.3.

**Image warping** is the distortion of an image based on a spatial transformation of the domain. Warping can be used to transform an image into another one by using the spatial mapping  $T$  obtained from the registration method. The mapping  $T$  is gradually applied to the original image  $u$  as follows:

$$u_{\text{warp}(\lambda)} = u \circ (I + \lambda T) \quad 0 \leq \lambda \leq 1 \quad (3.5)$$

Warping is a spatial transformation: it only acts on the coordinates, it does not modify the intensity of the image  $u$ .

### 3.2.2. AUTOMATIC REGISTRATION

The spatial mapping  $T$  used for the image warping is determined by the image registration. Several registration methods are available. However, many of them require to

define manually a set of corresponding points from the images  $u$  and  $v$ . We are interested in an automatic registration procedure that only needs the images  $u$  and  $v$  as inputs without any extra specifications. This requires the images to be similar enough for the automatic registration procedure to work.

We use the method described by [Mandel \*et al.\* \(2010\)](#) based on the minimization of a cost function  $J$  with respect to the mapping  $T$ . The cost function can be divided in two terms (Equation (3.6)). The first one ( $J_o$ ) represents the mapping error between the displaced original signal  $u \circ (I + T)$  and the target signal  $v$ . The second one ( $J_b$ ) is a background term that consists of the three criteria for 'optimal' mapping given in Equations (3.2), (3.3) and (3.4). These three criteria are used as weak constraints.

$$\begin{aligned} J(T) &= J_o(T) + J_b(T) & (3.6) \\ J_o(T) &= \|v - u \circ (I + T)\| \\ J_b(T) &= C_1 \|T\| + C_2 \|\nabla T\| + C_3 \|\nabla \cdot T\| \end{aligned}$$

where  $C_1$ ,  $C_2$  and  $C_3$  are three coefficients determined empirically, and  $\|\cdot\|$  is the  $L^2$ -norm.

The minimization problem is solved iteratively, for  $T$  defined on increasingly fine grids. The iterative approach has two advantages. It helps reduce the computational cost and avoids the local minima problem (see below).

In our application, the domain  $D$  is rectangular. It can be represented by different uniform grids. The regular  $n_x \times n_y = n$  grid on which  $u$ ,  $v$  and  $u_{\text{morph}(\lambda)}$  are given is called the *pixel grid*  $D_n$ . The mapping function  $T$  is defined on a set of coarser grids  $D_i$  ( $i = 1, \dots, I$ ), called *morphing grids*. It is then represented by two gridded arrays (one for  $T_x$  and one for  $T_y$ ). The grids  $D_i$  are uniform  $(2^i + 1) \times (2^i + 1) = m_i$  grids (for  $i = 1, \dots, I$ ) covering the domain  $D$ . For  $i = 1, \dots, I$ , the mapping  $T$  discretized on  $D_i$  is noted  $T_i$ .

The signals  $u$  and  $v$ , and so the observation term  $J_o$  of the cost function, are discretized on the pixel grid  $D_n$ . The background term  $J_b$  is discretized on the morphing grid  $D_i$ . We use the second order central scheme except at the boundaries where the first order backward or forward schemes are used. We use bilinear interpolation to estimate the value of  $u$  and  $v$  on the distorted grid (e.g.  $u \circ (I + T)$ ), and to interpolate  $T$  on the different morphing grids  $D_i$ .

The finest morphing grid  $D_I$  does not need to be the same as the pixel grid  $D_n$ . On the contrary, it is computationally advantageous when the morphing grid  $D_I$  has a much coarser resolution. When the number of nodes  $m_i$  of the morphing grids is much smaller than the number of nodes  $n$  of the pixel grid, solving the minimization problem on the set of morphing grids  $D_i$  is less computationally expensive than to solve it for  $T$  defined on the high resolution pixel grid  $D_n$ .

**Algorithm** The algorithm iterates over the morphing grids  $D_i$  ( $i = 1, \dots, I$ ), starting on the coarsest 3-by3 grid  $D_1$ , until it reaches the finest morphing grid  $D_I$ . For each iteration, the three main steps are similar as in [Beezley and Mandel \(2008\)](#) and are illustrated in Figure 3.2.1.



1. **Smoothing** of the images  $u$  and  $v$ : the images are smoothed by convolution with a 2D-Gaussian

$$G_{2D}(x, y) = \frac{1}{2\pi\sigma^2} \exp\left(-\frac{x^2 + y^2}{2\sigma^2}\right),$$

where  $\sigma = 0.05 / (2^{2i} + 1)$ . The finer the grid  $D_i$  is, the narrower the Gaussian is. Thus, for small  $i$ , the fine features are ignored and the focus is given to the large-scale ones. When  $i$  increases, more and more fine features are taken into account. This way,  $T_i$  for small  $i$  will make the larger features match. Then, for increasing  $i$ , more and more detailed images are matched.

The cost function  $J$  is often non-convex with respect to  $T$ , and so can have several local minima. The smoothing combined with the hierarchy of grids reduce the local minima problem. They ensure that the large-scale features are fitting first, hence avoiding local minima.

After the smoothing, the two fields are normalized such that their maximum is the same. The images obtained after smoothing and normalization are noted as  $\tilde{u}_i$  and  $\tilde{v}_i$ .

2. **Initialization**: solving the minimization problem on grid  $D_i$  requires a first guess  $T_i^{\text{fg}}$ . For  $i = 1$ ,  $T_1^{\text{fg}}$  is set to zeros, i.e. no deformation. For  $i = 2, \dots, I$ , the mapping  $T_{i-1}^*$  obtained by solving the minimization problem on grid  $D_{i-1}$  is interpolated into the grid  $D_i$ , and used as the first guess  $T_i^{\text{fg}}$ .
3. **Optimization**: The actual minimization problem to be solved is based on the smoothed fields, i.e.  $J_o(T) = \|\tilde{v}_i - \tilde{u}_i \circ (I + T)\|$ . Contrary to [Beezley and Mandel \(2008\)](#), we solved the minimization problem for all the nodes at the same time.

There is a number of inequality constraints on this minimization problem, due to our requirements of invertibility. An iterative barrier approach is used to transform this constrained minimization problem into an unconstrained one ([Jon \(2004\)](#); [Noc \(2006\)](#)). In the barrier approach, the minimization is applied to a penalized cost function  $J_p(T) = J(T) + \beta \sum_h C_h(T)$ , where  $C_h$  are the constraint functions, and  $\beta$  the barrier coefficient (over which we iterate when the constraints are not respected). The constraints and the minimization method are described with more details in appendix [3.A](#).

The python scripts for the automatic registration and the warping are available at [https://github.com/clecoz/spatial-warping\\_thesis](https://github.com/clecoz/spatial-warping_thesis). The scripts permit to reproduce the results and some of the plots for the two case studies presented in this chapter.

**Pre-processing** The precipitation data undergoes a pre-processing before being used as input for the automatic registration:

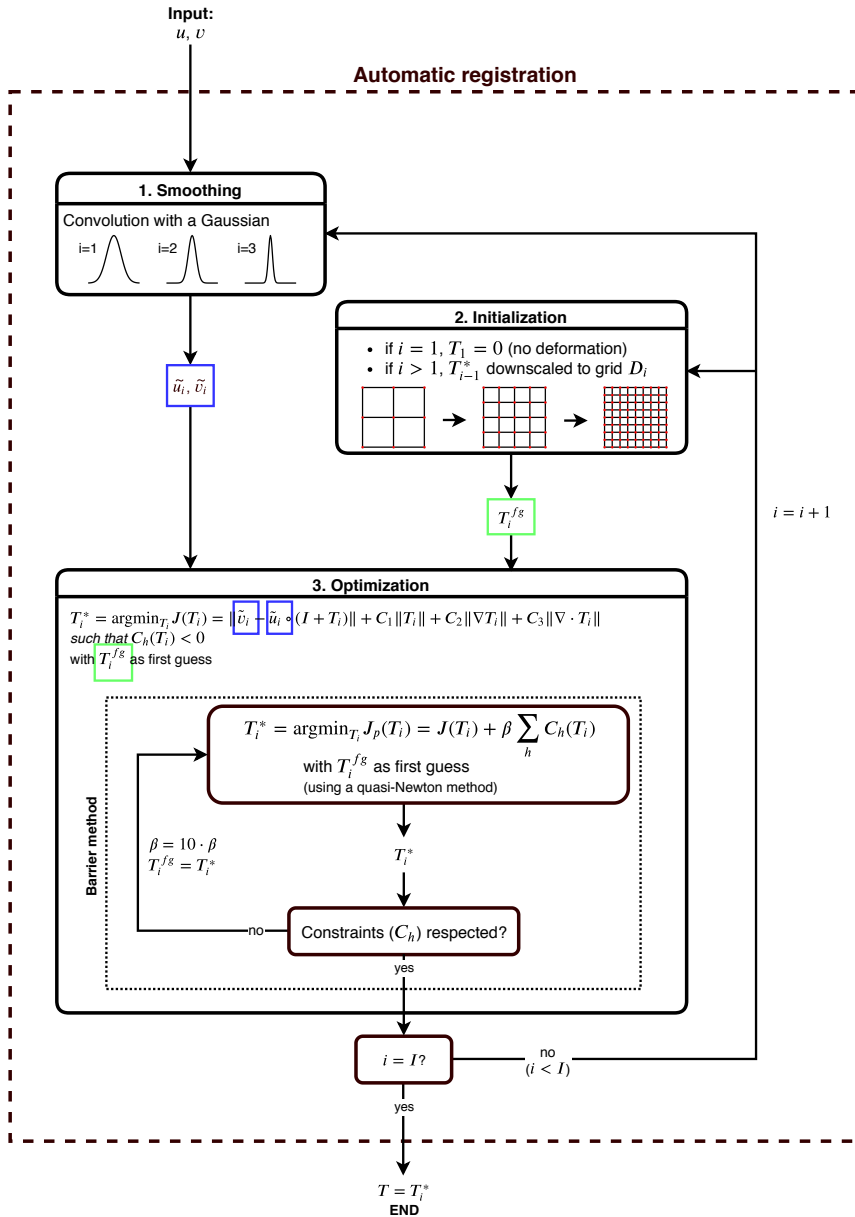


Figure 3.2.1: Algorithm for the automatic registration.

1. The light precipitation is removed from the fields (i.e. precipitation under 1mm/h). This first step is particularly useful for the southern Ghana case which uses real noisy dataset. Low precipitation is more difficult to measure or estimate, and so

subject to more uncertainties. It only has a limited impact on the synthetic case.

2. A padding area (with zero precipitation) is added around the domain. The padding area helps to avoid problems near the boundary on the domain. The constraints on the minimization problem (i.e. no nodes can leave the domain) can lead to unphysical distortion in the mapping when the rainfall event is located near the boundary. The extended domain corresponds to a  $n_x \times n_y$  pixel grid, with  $n_x = n_y = 65$ .

The warped field is obtained by applying the mapping to the original precipitation data. The pre-processed data are only used for the automatic registration.

**Dealing with irregularly spaced observations** The automatic registration algorithm described above assumes that both signals  $u$  and  $v$  are on the same regular grid. However, in practice, one might deal with irregularly spaced observations, such as rain-gauge data.

In such a case, the observations are interpolated on the same regular grid, using kriging (details about the kriging are given in Section 3.3.1). In the remainder of the article, we will refer to the gauge interpolation as “kriging”, while “interpolation” will refer to the bi-linear interpolation used in the automatic registration and warping. The cost function  $J$  from Equation (3.6) is modified to take the unequal coverage of the domain into account. A mask function  $M$  is added in the first term of  $J$ :

$$J(T) = \|M \cdot (v - u \circ (I + T))\| + C_1 \|T\| + C_2 \|\nabla T\| + C_3 \|\nabla \cdot T\| \quad (3.7)$$

where  $\cdot$  is the element-wise matrix multiplication. The mask function is defined such that it is equal to 1 in a given perimeter around the observations, and zero everywhere else. So, the difference  $v - u \circ (I + T)$  for the grid points far from any observation does not weigh in the cost function  $J$ .

### 3.2.3. EXTENSION TO SPACE-TIME DATA

In practice, we have two rain fields  $u_k$  and  $v_k$  for each time  $k$  ( $k = 1, \dots, K$ ). One approach is to apply the registration to each time step separately, but it is also possible to process several time steps at the same time. We investigate three different approaches to take into account (or not) the temporal dimension.

#### APPROACH 1 (A1): DIFFERENT SPATIAL MAPPINGS FOR EACH TIME INDEPENDENTLY

This is a fully 2D spatial approach that does not account for the temporal dimension. A different mapping  $T^k$  is determined for each time  $k$  independently. That is, in the automatic registration, the minimization problem  $\min_{T_k} J^k(T_k)$  is solved for each time  $k$  independently, with

$$J^k(T_k) = \|\tilde{v}_k - \tilde{u}_k \circ (I + T_k)\| + C_1 \|T_k\| + C_2 \|\nabla T_k\| + C_3 \|\nabla \cdot T_k\| \quad (3.8)$$

#### APPROACH 2 (A2): ONE SPATIAL MAPPING FOR ALL TIMES

In this approach, the mapping  $T$  is assumed to be the same at all times. The observation term  $J_o$  in the cost function compares the rain fields at all time  $k$  at once, while the

background term  $J_b$  is unchanged. The minimization problem only has to be solved once, since only one mapping  $T$  has to be found.

The cost function can be written as

$$J(T) = \frac{1}{K_0} \|V - U_T\| + C_1 \|T\| + C_2 \|\nabla T\| + C_3 \|\nabla \cdot T\| \quad (3.9)$$

where  $V$  and  $U_T$  are  $(n \times K)$  vectors containing the signals of the  $K$  time steps

$$V = \begin{bmatrix} \tilde{v}_1 \\ \tilde{v}_2 \\ \dots \\ \tilde{v}_K \end{bmatrix} \quad U_T = \begin{bmatrix} \tilde{u}_1 \circ (I + T) \\ \tilde{u}_2 \circ (I + T) \\ \dots \\ \tilde{u}_K \circ (I + T) \end{bmatrix} \quad (3.10)$$

and  $K_0$  is the number of time steps at which the original signal has detected precipitation (i.e.  $u_k > 0.1\text{mm/h}$  on at least one grid point of  $D$ ). Time steps at which the rain fields are zeros are not adding information about the spatial distortion. Dividing by the total number of time steps,  $K$ , would make the results of the registration depend on how large the selected time window around the rain event is (i.e. on how many time steps with no precipitation, the vectors  $U$  and  $V$  contains). A large time window would artificially reduce the observation term.

This approach is the less computationally expensive one. The number of variables to be optimized is the same as for one minimization problem for approach A1, but the minimization problem only has to be solved once, while approach A1 needs to solve  $K$  problems.

### APPROACH 3 (A3): DIFFERENT SPATIAL MAPPINGS CORRELATED IN TIME

This third approach is a mix of the first two. Each time step can have a different transform  $T_k$ , but the transforms  $T_k$  are connected through time. Unlike approach A1, the transforms  $T_k$  are not independent, but have more degrees of freedom than in approach A2. All the transforms are found at once by solving one minimization problem. They are linked through a correlation matrix. This is done by adding an extra background term. The cost function is modified as follow

$$J\left(\begin{bmatrix} T_1 \\ T_2 \\ \dots \\ T_K \end{bmatrix}\right) = \left\| \begin{bmatrix} \tilde{v}_1 - \tilde{u}_1 \circ (I + T_1) \\ \tilde{v}_2 - \tilde{u}_2 \circ (I + T_2) \\ \dots \\ \tilde{v}_K - \tilde{u}_K \circ (I + T_K) \end{bmatrix} \right\| + C_1 \left\| \begin{bmatrix} T_1 \\ T_2 \\ \dots \\ T_K \end{bmatrix} \right\| + C_2 \left\| \begin{bmatrix} \nabla T_1 \\ \nabla T_2 \\ \dots \\ \nabla T_K \end{bmatrix} \right\| + C_3 \left\| \begin{bmatrix} \nabla \cdot T_1 \\ \nabla \cdot T_2 \\ \dots \\ \nabla \cdot T_K \end{bmatrix} \right\| \\ + c_t \left\| \begin{bmatrix} T_1 - T_2 \\ T_2 - T_3 \\ \vdots \\ T_{k-1} - T_k \end{bmatrix} \right\| \quad (3.11)$$

The additional term in the cost function links the mapping through time. The coefficient  $c_t$  determines how strong the connection is between time steps.

The minimization problem is solved for all  $T_k$  at the same time, bringing to  $K \times i$  the number of variables to be optimized at step  $i$  (with  $i = 1, \dots, D$ ). Thus, this approach is the most computationally expensive one of the three approaches described here.

## SUMMARY

For more clarity, the different steps of the method, from the interpolation of the gauges to the warping, are summarized in Figure 3.2.2.

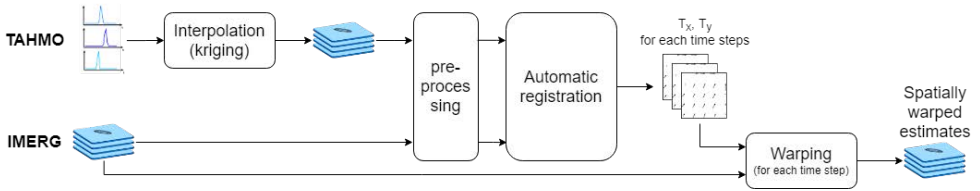


Figure 3.2.2: Flowchart of the spatial warping method.

## 3.3. SYNTHETIC CASES

### 3.3.1. STUDY CASES

A synthetic case is used to investigate the convergence and accuracy of the automatic registration approaches. The synthetic precipitation fields are generated on a regular grid. Both input fields  $u$  and  $v$  have one rainfall event, represented by a 3D ellipse with a maximum of 50mm/h (see Figure 3.3.1). The two fields differ by the position and orientation of the ellipse. The two ellipses have a different center both in space (by  $\sim 50$ km) and time (by 2 hours). The propagation direction and speed of the events are also different. In the field  $u$  the event is moving at  $\sim 40$ km/h, while in the field  $v$  the event is faster with a speed of  $\sim 47$ km/h.

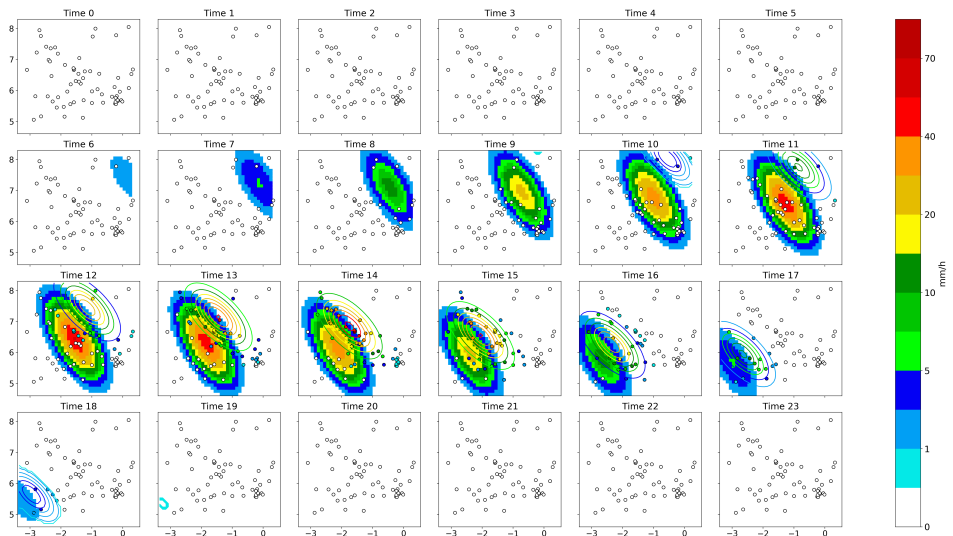


Figure 3.3.1: Precipitation fields  $u$  (background) and  $v$  (contour lines) for the synthetic case. The fictive stations are represented by circles.

In real cases, we would not know the true target field  $\nu$ , but only measurements of it. In order to test the space warping method in a more realistic setting, we extracted time series from the target field to simulate gauge observations. We use the same gauge network configuration as for the Southern Ghana case (see Section 3.4.1). They are represented by circles in Figure 3.3.1. The automatic registration algorithm only takes data defined on a regular grid as inputs. The fictive gauge measurements are kriged on the same grid as the field  $u$  using ordinary kriging with a square root transform Soenario and Sluiter (2010). We use an exponential variogram with a sill of  $1.0 \text{ (mm}^2/\text{h}^2)$ , a range of  $1.5^\circ$  and a nugget of  $0.01 \text{ (mm}^2/\text{h}^2)$ , i.e. the same kriging as used in the Southern Ghana case. For the synthetic case, the obtained kriged fields are shown in Figure 3.3.2

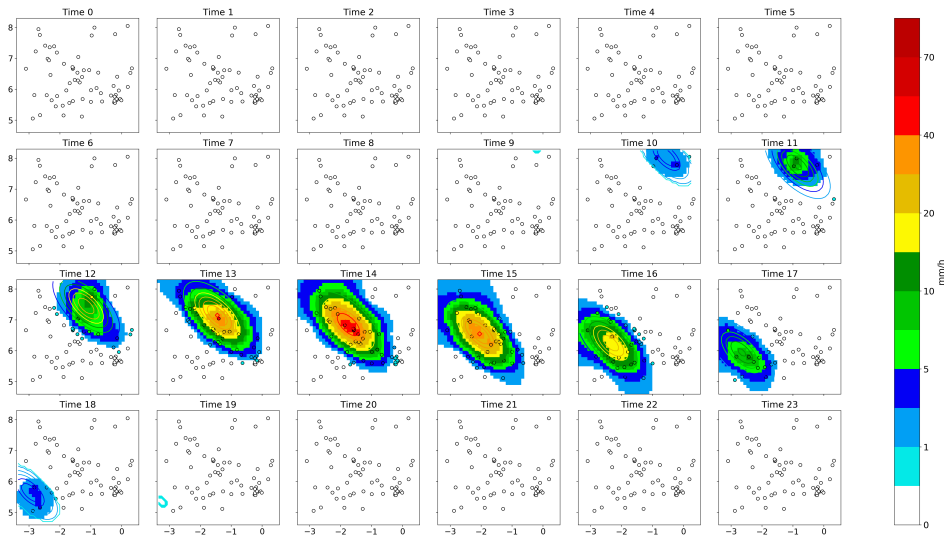


Figure 3.3.2: Interpolated field (background) and the original field  $\nu$  for the synthetic case. The fictive stations are represented by circles.

### 3.3.2. RESULTS

In this section we will show the results obtained with the three approaches (described in 3.2.3) for two different experiments. In the first one 'Full', we use the field  $\nu$  as input for the automatic registration. In the second one 'Interpolated', we use the interpolated field from the fictive gauge network. The interpolation is adding some uncertainties in the method. Comparing the two experiments will help to evaluate the impact of the interpolation.

All results shown here are obtained for  $C_1 = 0.1$ ,  $C_2 = C_3 = 1$  and  $c_t = 0.3$ , and for  $I = 4$  except when stated otherwise. The coefficients  $C_1$ ,  $C_2$ ,  $C_3$  and  $c_t$  are set empirically in this section. The sensitivity of the results to these coefficients will be discussed in Section 3.3.3. The number of steps,  $I$ , can also be adjusted. With  $I = 4$ , the number of nodes on the morphing grid is much lower than on the pixel grid ( $m_I = 17 \times 17 < n = n_x \times n_y = 65 \times 65$ ), which is computationally advantageous. The impact of  $I$  on the results

will also be examined in Section 3.3.3.

### MAPPING COMPARISON

The automatic registration provides a mapping  $T$  based on the given inputs. The mappings obtained with the three different approaches are shown in Figures 3.3.3, 3.3.4 and 3.3.5 for approaches A1, A2 and A3 respectively. For the sake of clarity, we only show the mappings at some selected time steps for approaches A1 and A3. At the other time steps, the distortions were much smaller or zero, due to the absence of precipitation in the target field  $v$ . The output of the automatic registration depends on the inputs. So, for each approach, the mapping obtained with the ‘true’ field  $v$  and the one obtained with the interpolated field as input are shown in black and red respectively.

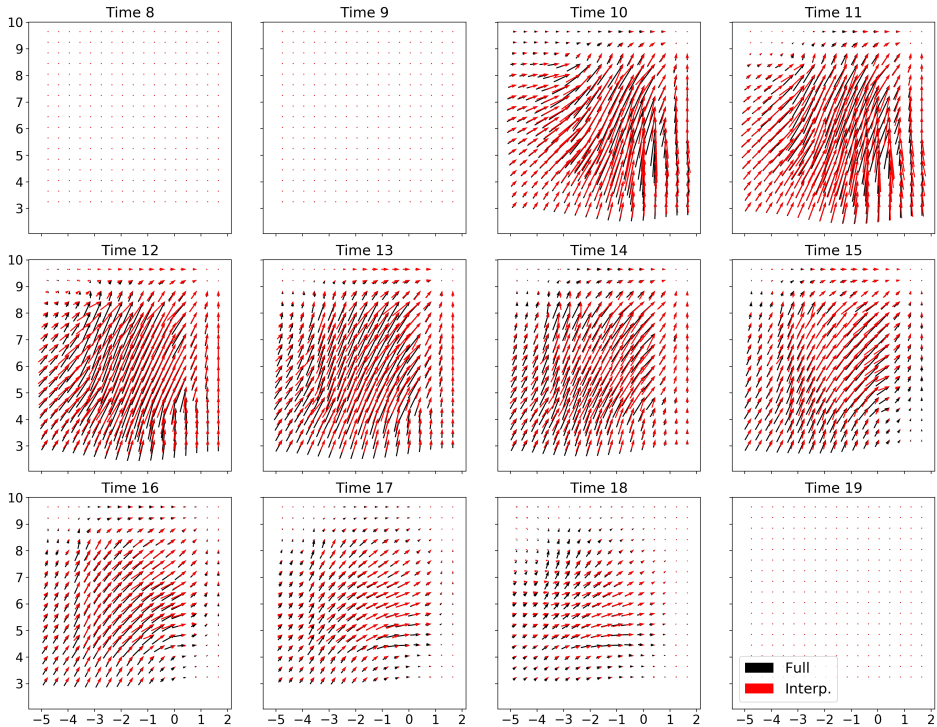


Figure 3.3.3: Mappings  $T$  obtained with approach A1 for selected time steps for the two experiments (in black for “Full” and in red for “Interpolated”).

In all cases, one can notice that the largest distortions occur in the center of the domain where the rain event is located. The relatively smaller distortion near the boundary is due to the padding area and the first regulation term of the cost function which ensures that the mapping is as “small” as possible. The second term ensures that the mapping is as “smooth” as possible, avoiding abrupt distortions. It is responsible for the smooth transformation between the larger distortions in the center and the areas with no or little distortions. The effect of the third term is more difficult to observe. The goal of this term

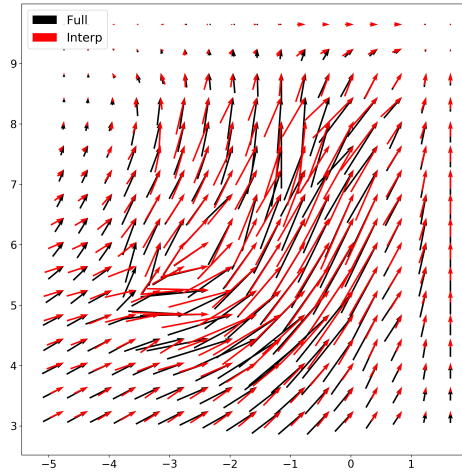


Figure 3.3.4: Mappings  $T$  obtained with approach A2 for the two experiments (in black for “Full” and in red for “Interpolated”).

is to avoid the grid cell to shrink or expand.

There are differences between the mappings depending on which target field was used as input, i.e. the “true” field or the interpolated one. For example, the distortion tends to be more horizontal on the left side of the domain when using the interpolated field. In the interpolated field, the intensity and the shape of the rainfall events can differ from the true field  $v$  depending on position of the rain and the configuration of the network (see Figure 3.3.2). These differences influence the output of the automatic registration.

Mappings obtained by different approaches have appreciable differences. In approach A1, there are no distortion for the time steps 8, 9 and 19 (and the other time steps not shown in Figure 3.3.3). At these time steps, there is no precipitation in the target field, so the observation term  $J_o$  of the cost function is null, leaving only the background term  $J_b$ . In approach A2, the same mapping is applied for all time steps, including the ones without recorded rainfall. This mapping is less spatially uniform than the ones obtained with approaches A1 and A3 (Figure 3.3.4). It seems that the smoothness and the divergent-free regulation terms have less weight in this case. This is due to the fact that this mapping has to make rainfall fields from all the time steps coincide. One can see from the input data in Figure 3.3.1, that the position mismatch between the fields  $u$  and  $v$  is more important at the beginning of the event than at the end. This is also reflected in the mappings obtained with approaches A1 and A3. The mapping obtained with approach A3 is very similar to the one from approach A1 from time steps 10 to 18. In contrast to approach A1, there are some distortions occurring at time steps 8, 9 and 10 in approach A3 (Figure 3.3.5). This is due to the time correlation added to the cost function, which ensures a smooth transition between the time steps.



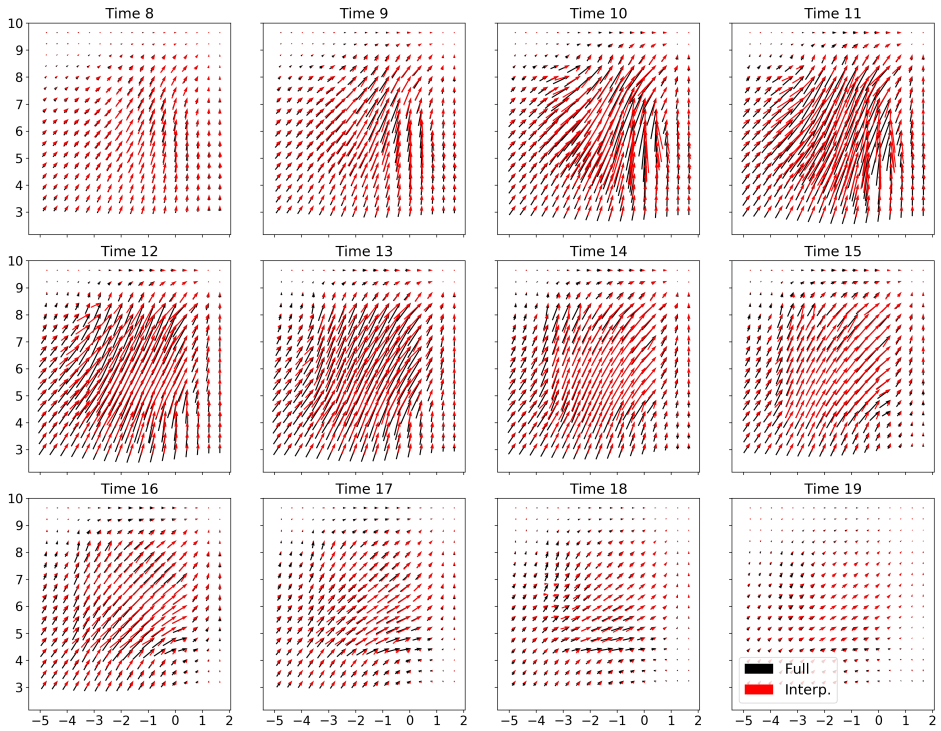


Figure 3.3.5: Mappings  $T$  obtained with approach A3 for selected time steps for the two experiments (in black for “Full” and in red for “Interpolated”).

### VALIDATION

The mappings obtained with the three approaches were applied to the field  $u$ . The warped fields can be seen in Appendix 3.B. The warping does not modify the intensity of the rainfall event, only its spatial position. Thus, the over- or under-estimation at a particular time is not corrected. However, the position of the event is corresponding more closely to the “truth” after warping than before. This can also be seen in Figure 3.3.6a, which shows the trajectory of the rainfall peak according to the “truth” ( $v$ ), the original field ( $u$ ) and the warped fields (the position of the peak is defined as the pixel with the maximum rainfall). For the approach A2, the events in the warped fields and in the “true” field are less aligned than for the other approaches because of the same mapping being used for all time steps (Figures 3.B.3 and 3.B.4). The position of the peak match perfectly at time 14, at which the maximum rainfall occurs according to the “truth”  $v$ . At the beginning of the event, the mapping does not move the rainfall peak enough, while it moves it too far at the end of the event. For approaches A1 and A3, the position of the peaks are fitting at all time steps when both the fields  $u$  and  $v$  have rainfall. The main differences occurs at the beginning of the event (time steps 6 to 9). There is very little or no rainfall in the “true” field before time step 10. Thus, the mapping obtained with approach A1 is null at these time steps because they are treated independently from each other. This

creates an unnatural discontinuity between time steps 9 and 10. This discontinuity does not occur with approach A2, and is reduced by approach A3 due to the time correlation. In the “Full” experiment, the position of the peaks are matching exactly for approaches A1 and A3 between time 12 and time 17. The position of the peak is not matching as well when using the interpolated field as input, but it is still greatly improved. The peak is not located exactly at the same location in the interpolated field and in the “truth” due to the interpolation.

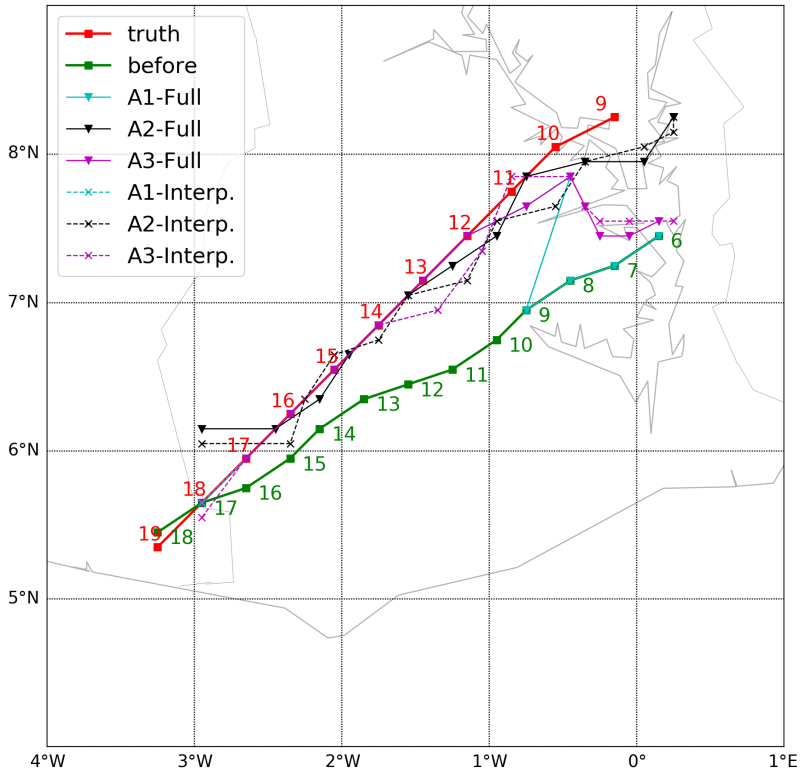
Table 3.3.1: Average position error (in km) before and after spatial warping. The average is done over all time steps at which the peak (in the target field  $v$ ) is above a certain threshold of rainfall.

Threshold	Sample number	Before			Full			Interpolated		
			A1	A2	A3	A1	A2	A3		
>1mm/h	n=10	98.54	19.94	27.43	11.07	23.54	27.57	15.78		
>10mm/h	n=7	90.76	2.24	21.06	2.24	7.37	20.96	7.37		
>20mm/h	n=5	89.54	0.00	16.18	0.00	8.10	17.39	8.10		
>40mm/h	n=3	87.78	0.00	10.45	0.00	8.28	12.63	8.28		

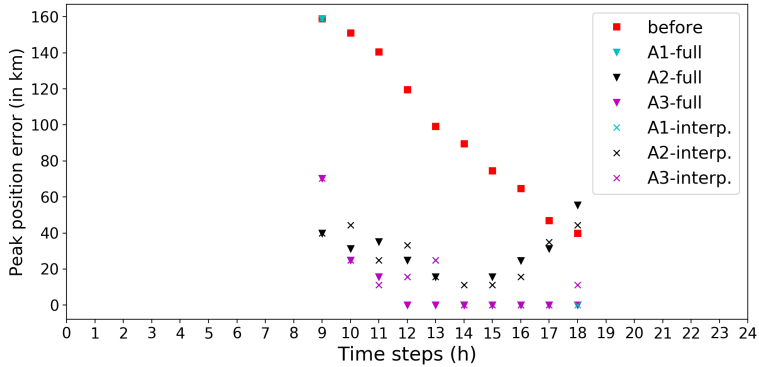
The spatial correction is evaluated more quantitatively in Table 3.3.1. We compute the average position error over several time steps with peak above a certain threshold. Approach A3 has the smallest position error, followed closely by approach A1. Their results are identical for the thresholds of 10 mm/h or higher. In general, the error is smaller for the “Full” experiment than the “Interpolated” one. However, the decrease of the error remains very important, from 98.54km before correction to 27.57km for approach A2 and 15.78km for approach A3 for example (when considering all times with more than 1mm/h rainfall). The warping seems more efficient at time steps with higher rainfall rate. The error decreases when the threshold increases. For the “full” experiment, the error is divided by 8 (A3) or 3 (A2) over all times with some rainfall, but by more than 10 (for A1 and A3) when only considering times with more than 10mm/h precipitation (by 5 for A2). The peaks above 20mm/h are even fitting perfectly for approaches A1 and A3 with the “truth” as input. The errors are down to 8.28km when using the interpolated fields, which is approximately the length of one grid cell.

Figure 3.3.6b shows the position error for each time step. The position error decreases for all the approaches and experiences, except at time 18 for approach A2. As observed above, the best results are obtained when using the “true” field as input with approach A1 and A3. The reduction of the error is smaller with approach A2, but still very important. Using the interpolated field as input increases the error slightly. The main difference between approach A1 and A3 occurs at time 9. Because of the very low rainfall, approach A1 does not correct the position at this time, while the time correlation helps approach A3. This is the only time when approach A2 has the best result.

The warping does not modify the intensity of the rainfall, but impacts it indirectly by removing the double-penalty part of the error. The statistics of the warped fields from the three approaches (A1, A2 and A3) and the two experiments (“Full” and “Interpolated”) are shown in Table 3.3.2. For all approaches and experiences, the RMSE and MAE are reduced compared to before the spatial correction. The MAE is divided by at least two. The decrease in the RMSE is smaller, from 5.62mm/h to 2.68-3.38mm/h. The correla-



(a) Path of the peak before and after spatial warping. The numbers indicated the time steps represented by the points.



(b) Distance between the “true” peak and the estimated one before and after spatial warping as a function of time.

Figure 3.3.6: Position error of the peak before and after warping for time steps with more than 0.1mm/h rainfall (in both  $u$  and  $v$ ). The peak is defined as the pixel with the maximal rainfall at a given time step.

Table 3.3.2: Statistics before and after spatial warping compared to the “truth”  $v$ . The results are shown for the two experiments (“Full” and “Interpolated”) and the three approaches (A1, A2 and A3). The statistics are computed over all the domain and all time steps.

	Before	Full			Interpolated		
		A1	A2	A3	A1	A2	A3
RMSE (mm/h)	5.62	2.80	3.38	2.71	2.72	3.24	2.65
MAE (mm/h)	1.65	0.70	0.79	0.65	0.68	0.77	0.64
Correlation	0.12	0.78	0.69	0.79	0.78	0.72	0.79

tion is greatly improved by the warping, it goes from 0.12 before correction to 0.79 with approach A3. Approaches A1 and A3 have similar results with A3 slightly better, while approach A2 has a slightly more limited impact. The result was expected. Approach A2 applies the same mapping at all times, while, by construction, the spatial error is different at every time step in this synthetic case. The statistics are similar for the “Full” and “Interpolated” experiments. They are even slightly better for the latter.

### TIMING ERROR

The synthetic case has been built with both a position and a timing error between the two fields  $u$  and  $v$ . The spatial warping corrects the spatial position of the rainfall event at different times. Here, we will look at the impact of this correction on the timing error.

The timing error between the fields  $u$  and  $v$  is shown in Figure 3.3.7. The field  $u$  is in time ahead of the “truth”. This time difference increases from West to East up to 4h. The timing error strongly decreases after the spatial warping (see Figure 3.3.8) for all approaches and experiments. The results are very similar for the “Full” and “Interpolated” experiments. However, some differences are noticeable between approaches. Approach A3 yields the best results in terms of timing. Approach A1 has similar results except in the South-East corner of the domain. This is related to the fact that approach A1 is not impacting time 9 (and earlier). The pixels in this area have two peaks (see Figures 3.B.1 and 3.B.2). The first one occurs at time 9, since the field  $u$  is not modified at that time. The second one at time 12 or 13 is smaller, and corresponds to the peak in the “truth”  $v$ . It has to be noted that the stronger timing differences occur at pixels with little precipitation. Approach A2 also largely corrected the timing, especially in the center of the domain. Because of the same mapping being used for all time steps, the warped estimate still is 1h in advance in the North-East corner, while it is now 1h late in the South-West corner. It is interesting to note that there are little differences between the “Full” and the “Interpolated” experiments. The main difference is observed for approach A3 near the eastern boundary, in an area without gauges and relatively low precipitation.

Table 3.3.3 provides average absolute timing errors before and after spatial warping. They are given for different rainfall thresholds. The average timing error is reduced by the spatial warping for all the approaches, with approach A3 showing the largest improvement followed closely by approach A1. The results of the “Full” and “Interpolated” experiments are very similar. The “Interpolated” experiment has a slightly lower average error for the low thresholds, while the “Full” experiment performs slightly better for the higher ones. As for the average position error (Table 3.3.1), the average timing error

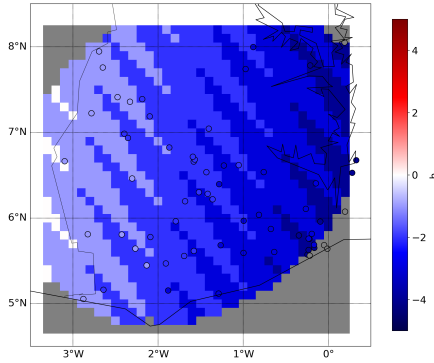


Figure 3.3.7: Timing error before spatial warping at each pixel of the domain. In red, the peak in  $u$  is late (compared to the one in the “truth”  $v$ ). In blue, the peak in  $u$  is in advance. In grey, one of the time series does not have a peak (rainfall  $< 0.1\text{mm/h}$ ). It has to be noted that the timing error can only be given at the hourly resolution due to the definition of the time steps.

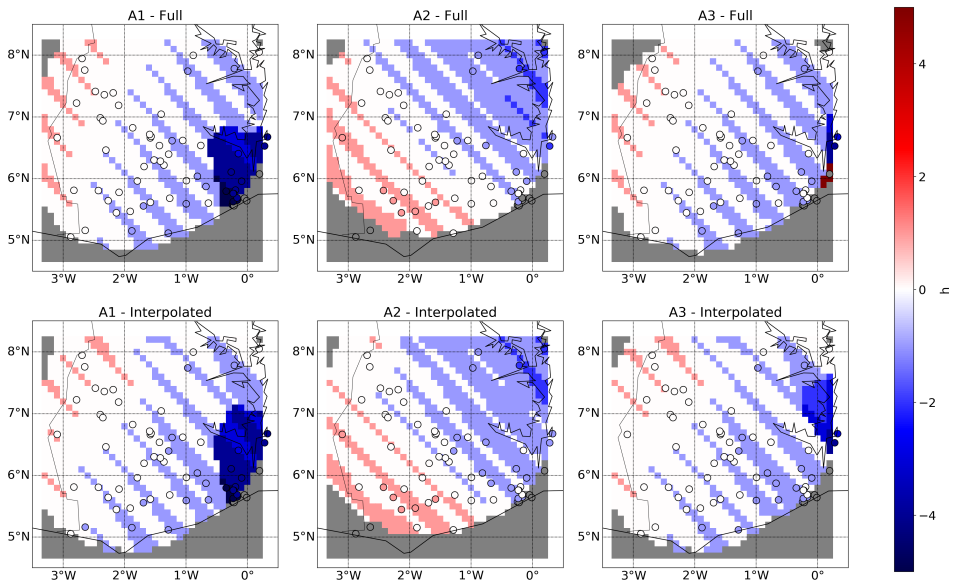


Figure 3.3.8: Timing error after spatial warping at each pixel of the domain. In red, the peak in  $u$  is late (compared to the one in the target field  $v$ ). In blue, the peak in  $u$  is in advance. In grey, one of the time series does not have a peak (rainfall  $< 0.1\text{mm/h}$ ). It has to be noted that the timing error can only be given at the hourly resolution due to the definition of the time steps. The results are shown for the two experiments: (top) “Full” and (bottom) “Interpolated”, and the three approaches: (left) A1, (middle) A2 and (right) A3.

decreases when the threshold increases. The difference between the approaches is also

smaller for the higher precipitation thresholds.

Table 3.3.3: Average absolute timing error before and after spatial warping. The average is done over all pixels recording at least one time step with more rainfall than a certain threshold according to  $v$  (and with non-zero rainfall according to  $u$ ).

Threshold	Sample number	Before	Full			Interpolated		
			A1	A2	A3	A1	A2	A3
>1mm/h	n=1128	2.21	0.91	1.90	0.71	0.70	1.73	0.50
>10mm/h	n=435	2.15	0.29	0.38	0.24	0.26	0.40	0.23
>20mm/h	n=218	2.17	0.23	0.30	0.22	0.23	0.34	0.22
>40mm/h	n=18	2.06	0.06	0.11	0.06	0.11	0.17	0.11

### 3.3.3. SENSITIVITY

#### STEP 1

In this section, we investigate the impact of the number of steps  $I$  on the mapping performance. We apply the mappings obtained with different numbers of steps  $I$  to the original field  $u$ . These warped fields are then compared to the “truth”  $v$  with respect to rainfall position and intensity.

Table 3.3.4 presents the average position error of the peak for different numbers of steps  $I$ . As for Table 3.3.1, the position error is defined as the distance between the peaks in the warped field and the “truth” at each time step. The results for the cases  $I = 1, 2$  and 3 are similar to the ones observed above for the case  $I = 4$  (see Table 3.3.1). That is, approach A1 and A3 give similar results, especially for the highest threshold (10mm/h), with A3 having slightly smaller errors. The errors are smaller for the higher threshold. The position error is already divided almost by two with  $I = 1$  for the threshold >1mm/h and by 2.6 or 3 for threshold >10mm/h (depending on the approach). The error decreases further when the numbers of steps  $I$  increases, but with smaller and smaller improvement. For example, the position error decreases by at least 10km between  $I = 1$  and  $I = 2$ , but by at most 4km between  $I = 2$  and  $I = 3$ , when considering all time steps with precipitation (threshold >1mm/h). For approach A1, increasing the number of steps above 2 does not improve the position of the peak further. The same can be observed with approach A3 for the times with higher precipitation (threshold >10mm/h). For  $I \geq 2$ , the position error remains 2.61km.

We also look at the impact of the numbers of steps  $I$  on several statistics (see Table 3.3.5). Despite the coarse resolution of the mapping at  $I = 1$ , applying it to the field  $u$  divides the RMSE and the MAE by 1.5 and 2.2 for all approaches. Similarly, the correlation coefficient goes from 0.12 before the warping to 0.69 or 0.70 after. Using additional steps, improves further the three statistics for approaches A1 and A3. While the position error continues to decrease when  $I$  increases, the RMSE and MAE start to increase again for approach A2 when  $I > 2$ . Similarly, the correlation decreases slightly.

Table 3.3.4: Average position error (in km) before and after spatial warping for different numbers of steps  $I$ . The average position error is done over all times at which the peak is above a certain threshold.

Threshold		Before	After (“Full”)		
			A1	A2	A3
>1mm/h	$I = 4$	98.54	19.94	27.43	11.07
	$I = 3$		19.94	31.46	11.59
	$I = 2$		19.94	34.00	18.12
	$I = 1$		42.22	50.57	40.99
>10mm/h	$I = 4$	98.04	2.61	19.34	2.61
	$I = 3$		2.61	21.88	2.61
	$I = 2$		2.61	23.10	2.61
	$I = 1$		32.57	36.45	30.42

Table 3.3.5: Statistics before and after spatial warping for different numbers of steps  $I$ . The statistics are computed over the full domain and all time steps. The results are shown for the three approaches for the “Full” experiment.

		Before	Full		
			A1	A2	A3
RMSE	$I = 4$	5.62	2.80	3.38	2.71
	$I = 3$		2.91	3.60	2.88
	$I = 2$		2.96	3.34	2.92
	$I = 1$		3.05	3.07	3.06
MAE	$I = 4$	1.65	0.70	0.79	0.65
	$I = 3$		0.74	0.89	0.71
	$I = 2$		0.76	0.83	0.73
	$I = 1$		0.76	0.74	0.75
Correlation	$I = 4$	0.12	0.78	0.69	0.79
	$I = 3$		0.76	0.64	0.76
	$I = 2$		0.75	0.68	0.76
	$I = 1$		0.70	0.69	0.69

### REGULATION COEFFICIENTS

The automatic registration is based on the minimization of the cost function  $J$ , which is composed of an observation term and a background term. The background term  $J_b$  consists of criteria defining the ‘optimal’ mapping  $T$ . The three approaches have the same three criteria concerning the magnitude (Equation (3.2)), the smoothness (Equation (3.3)) and the divergence (Equation (3.4)) of the mapping  $T$ . Approach A3 has a fourth criterion, introducing a time correlation. These four criteria can be tuned with the regulation coefficients  $C_1$ ,  $C_2$ ,  $C_3$ , and  $c_t$  respectively. In this section, we look at the influence of the first three common coefficients on the automatic registration. The impact of the fourth criterion is specific to approach A3 and will be investigated separately.

In the result section above, we empirically set the coefficients to  $C_1 = 0.1$  and  $C_2 = C_3 = 1$ . Here, we consider four more cases, summarized in Table 3.3.6. We first look at the impact of the individual coefficients, setting the two others to zero. Then we examine

the influence of their intensity by multiplying them by five. The only difference between the results shown here and the ones in Section 3.3.2 are the regulation coefficients.

Table 3.3.6: Summary of the four cases used in the sensitivity study of the regulation coefficients.

	Original	Only $C_1$	Only $C_2$	Only $C_3$	All coeff. x5
$C_1$	0.1	0.1	0	0	0.5
$C_2$	1	0	1	0	5
$C_3$	1	0	0	1	5
$c_t$ (only for A3)	0.3	0.3	0.3	0.3	1.5

The regulation coefficients are part of the automatic registration, and so impact directly the mapping  $T$ . The mappings obtained for the four sensitivity cases are compared to the original one in Figures 3.3.9, 3.3.10 and 3.3.11 (for approaches A1, A2 and A3 respectively). The mappings from the sensitivity cases are very similar to the original one in the rainy areas. The main differences occur further away from the rainy events, especially in the padding area near the boundary. The case with only the magnitude constraint ( $C_1 = 0.1$ ) shows no distortion in the padding area. The distortion in the padding area is similar to the one near the rain event when only the smoothness constraint is used ( $C_2 = 1$ ). This is especially true in the lower and left boundary. Because of the direction of the mapping and the constraints at the boundary (i.e. no nodes can leave the domain), the mapping is going to zero in the upper-right corner. The divergence-free constraint ( $C_3 = 1$ ) leads to rotation-like patterns. These rotations appear in order to conserve the volume of the grid cells. This third coefficient alone seems to have a weaker impact on the mapping. Large distortions occur in the padding area in the “only  $C_3$ ” case, especially with approach A1 (e.g. at time 10). Multiplying the coefficients by five has a limited impact on the mapping. It stays similar to the original one in the rainy area, and the distortion is slightly smaller and smoother in the non-rainy area.

Table 3.3.7: Average position error (in km) after spatial warping for different regulation coefficients  $C_1$ ,  $C_2$  and  $C_3$ . The position error is averaged over all time steps recording at least one pixel with more rainfall than a certain threshold.

	Original	Only $C_1$	Only $C_2$	Only $C_3$	All coeff. x5
<b>Threshold</b>					
>1mm/h	19.94	17.05	19.94	7.53	19.94
A1 >10mm/h	2.61	2.61	2.61	2.61	2.61
>20mm/h	0.00	0.00	0.00	0.00	0.00
<b>Threshold</b>					
>1mm/h	27.43	27.97	27.97	27.97	28.73
A2 >10mm/h	19.34	19.34	19.34	19.34	19.34
>20mm/h	14.04	14.04	14.04	14.04	14.04
<b>Threshold</b>					
>1mm/h	11.07	8.63	7.56	7.84	11.07
A3 >10mm/h	2.61	2.61	2.61	2.61	2.61
>20mm/h	0.00	0.00	0.00	0.00	0.00



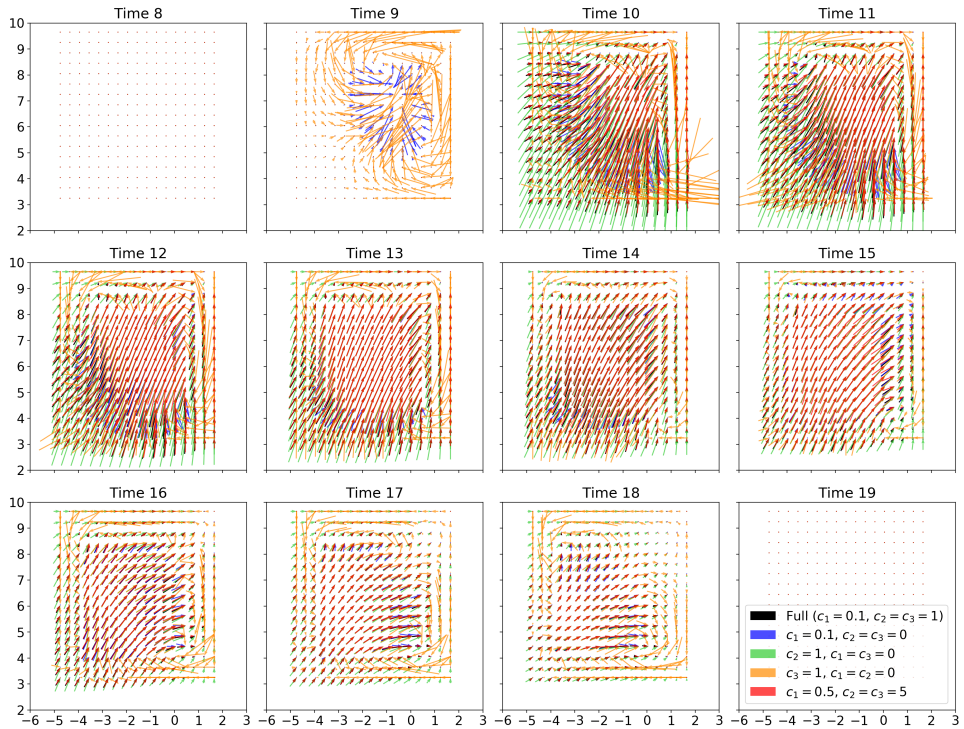


Figure 3.3.9: Mappings  $T$  obtained with approach A1 for the four sensitivity cases compared to the original one. For clarity sake, the mappings are shown for selected time steps.

The impact of the coefficients on the warped fields is examined through the average position error (Table 3.3.7) and continuous statistics (Table 3.3.8). The average position errors of the four new cases are equal to the one of the original case for the higher thresholds (10 and 20 mm/h). This holds for the three approaches. Some differences in the position error can be seen for the low threshold (1mm/h). For approach A2, the difference is less than a kilometer. The differences are larger for approaches A1 and A3. The position error is smaller when only one of the coefficients is non-zero, and increases slightly or is similar when all the coefficients are multiplied by 5. The impact of the coefficient on the statistics of the warped fields is limited. The RMSE, the MAE and the correlation coefficient are staying similar to the ones of the original case.

The impact of the coefficients on the warped fields is examined through the average position error (Table 3.3.7) and continuous statistics (Table 3.3.8). The average position errors of the four new cases are equal to the one of the original case for the higher thresholds (10 and 20 mm/h). This holds for the three approaches. Some differences in the position error can be seen for the low threshold (1mm/h). For approach A2, the difference is less than a kilometer. The differences are larger for approaches A1 and A3. The position error is smaller when only one of the coefficients is non-zero, and increases slightly or is similar when all the coefficients are multiplied by 5. The impact of the co-

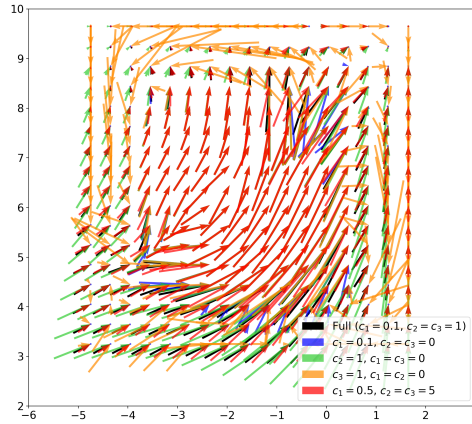


Figure 3.3.10: Mappings  $T$  obtained with approach A2 for the four sensitivity cases compared to the original one.

Table 3.3.8: Statistics after spatial warping for different regulation coefficients  $C_1$ ,  $C_2$  and  $C_3$ . The statistics are computed over all the domain and all time steps.

		Original	Only $C_1$	Only $C_2$	Only $C_3$	All coeff. x5
A1	RMSE	2.796	2.659	2.796	2.680	2.800
	MAE	0.698	0.640	0.698	0.641	0.700
	Correlation	0.775	0.792	0.775	0.790	0.775
A2	RMSE	3.376	3.386	3.381	3.380	3.359
	MAE	0.791	0.793	0.792	0.792	0.788
	Correlation	0.692	0.691	0.692	0.692	0.694
A3	RMSE	2.712	2.686	2.670	2.650	2.726
	MAE	0.652	0.628	0.614	0.598	0.655
	Correlation	0.786	0.790	0.792	0.795	0.785

efficient on the statistics of the warped fields is limited. The RMSE, the MAE and the correlation coefficient are staying similar to the ones of the original case.

To summarize, the three regulation terms mainly affect the mapping in the areas with no or little rainfall. This is reflected in the small influence they have on the statistics of the warped fields. Similarly, only the position of the lower rainfall peaks are impacted by the coefficient (Table 3.3.7). The regulation terms act as weak constraints and prevent unnatural distortion (such as sharp changes or stretches).

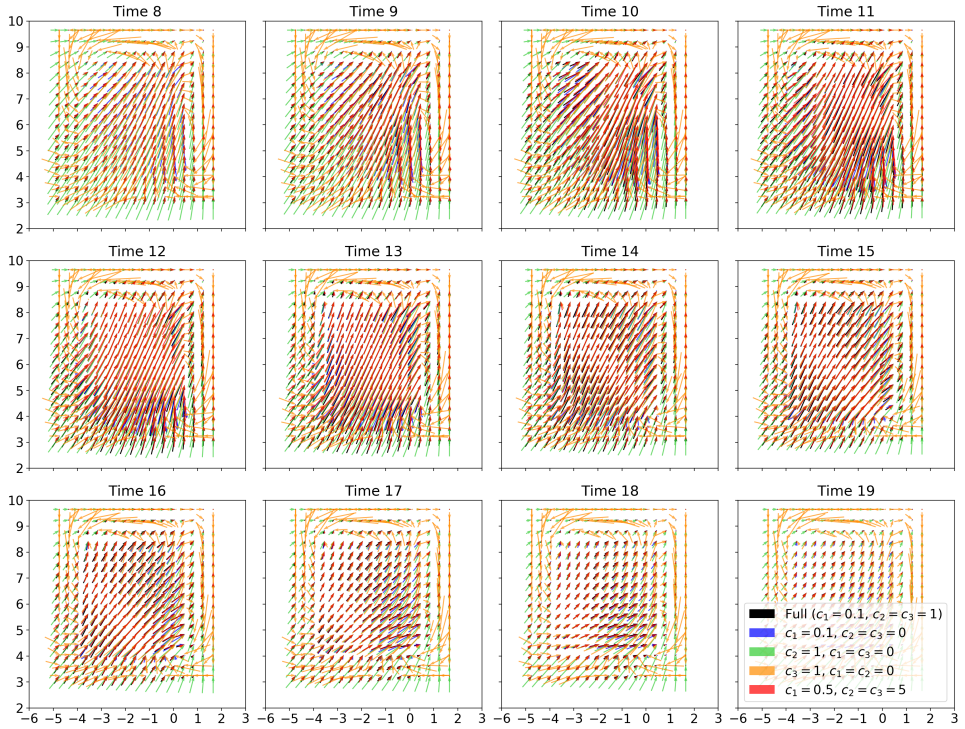


Figure 3.3.11: Mappings  $T$  obtained with approach A3 for the four sensitivity cases compared to the original one. For clarity sake, the mappings are shown for selected time steps.

### TEMPORAL REGULATION TERM FOR APPROACH A3

In approach A3, the cost function has an extra regulation term representing time consistency (see Eq. (3.11)). This term can be tuned with the regulation coefficient  $c_t$ . The coefficient defines how strongly the mappings are linked through time. In this section, we investigate the influence of the coefficient  $c_t$  on the mappings and on the warped fields. The coefficients of the three other regulation terms ( $C_1$ ,  $C_2$  and  $C_3$ ) have already been examined above.

We consider two more cases,  $c_t = 0.1$  and  $c_t = 0.5$ , and compare them with the previous results obtained with  $c_t = 0.3$ . Figure 3.3.12 shows the mappings corresponding to these three cases. The mappings are similar for time steps with recorded rainfall (time steps 10 to 18), and even identical in the rainy areas. The main differences occur at the time steps without rainfall. The coefficient  $c_t$  influences how strongly the time steps are influencing each other. The rainy event stops at time 18 (according to  $\nu$ ), however, the mappings of the following time steps show some distortion due to the temporal regulation term. One can observe distortion at time 19 for  $c_t = 0.1$ , up to time 20 for  $c_t = 0.3$  and several time-steps further for  $c_t = 0.5$ .

The impact of the coefficient  $c_t$  on the warped fields is examined through the average position error (Table 3.3.9) and continuous statistics (Table 3.3.10). The impact of  $c_t$  on

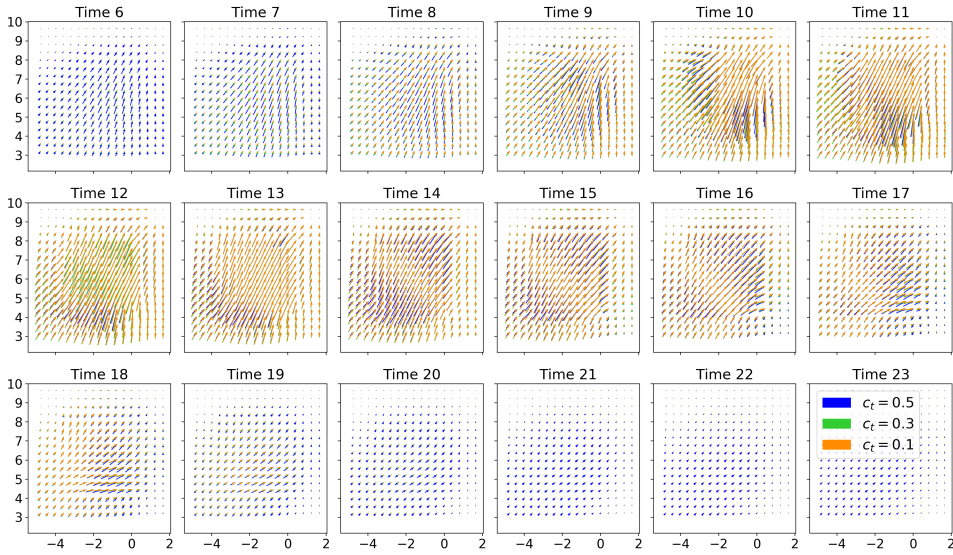


Figure 3.3.12: Mappings  $T$  obtained with approach A3 for three different temporal regulation coefficients  $c_t$ . For clarity sake, the mappings are shown for selected time step.

the average position error is limited. For the higher thresholds (10mm/h and 20mm/h), the errors are identical in the three cases. For the lowest threshold (1mm/h), the position errors are different for the three cases, but the differences are less than three kilometres. Similarly, the continuous statistics show little differences for the different values of  $c_t$ . The RMSE and MAE vary by less than 0.02mm/h, and the correlations are identical.

Table 3.3.9: Average position error (in km) after spatial warping for three different regulation coefficients  $c_t$ . The position errors are computed over all time steps recording at least one pixel with more rainfall than a certain threshold.

Threshold	Before		After		
		$c_t = 0.1$	$c_t = 0.3$	$c_t = 0.5$	
>1mm/h	98.54	12.14	11.07	9.71	
>10mm/h	98.04	2.61	2.61	2.61	
>20mm/h	95.74	0.00	0.00	0.00	

As the three other regulation terms, the temporal one mainly affects areas with no or little rainfall. The mappings obtained with different values of  $c_t$  have noticeable differences (Figure 3.3.12), but the corresponding warped fields show similar errors in term of RMSE and correlation (Table 3.3.10). Similarly, the average position errors only differ when considering the lowest threshold (Table 3.3.9).

Table 3.3.10: Statistics after spatial warping for three different temporal regulation coefficients  $c_t$ . The statistics are computed over all the domain and all time steps.

	Before	After		
		$c_t = 0.1$	$c_t = 0.3$	$c_t = 0.5$
RMSE	5.62	2.72	2.71	2.70
MAE	1.65	0.66	0.65	0.64
Correlation	0.12	0.79	0.79	0.79

### 3.4. SOUTHERN GHANA CASE

#### 3.4.1. STUDY CASE

The Southern Ghana case is used to test the automatic registration and the spatial warping on real precipitation data. We will use gauge data to spatially adjust satellite-based estimates. The gauge measurements are assumed to be more accurate than the satellite-based estimates. On the other hand, such estimates have a higher spatial variability that cannot be reproduced by the gauge because of their density. Our goal is to apply the spatial warping to the satellite-based estimates to correct the position error (with respect to the gauges), while keeping their higher spatial variability. In this study case, we use the gauge measurements from the Trans-African Hydro-Meteorological Observatory (TAHMO) network, and the satellite-based estimates from IMERG-Late.

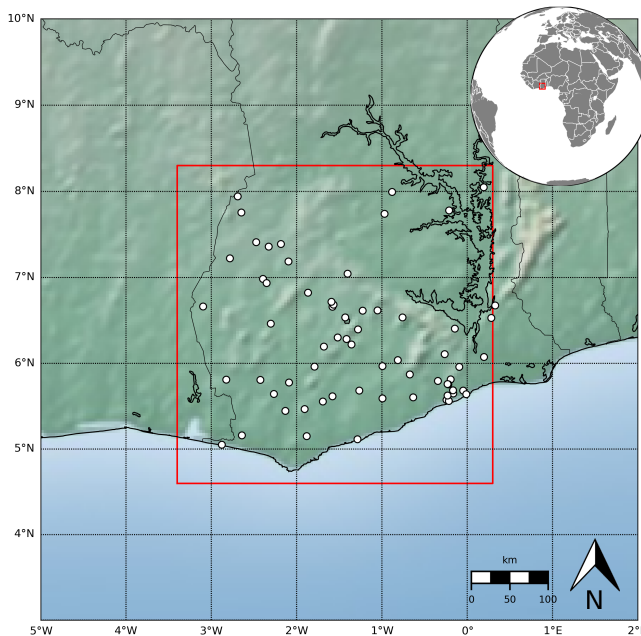


Figure 3.4.1: Study domain (red rectangle) and the TAHMO stations available within the domain (white dots).

The study area is a square domain over southern Ghana encompassing the Ghanaian cocoa region. This corresponds to a  $37 \times 37$  grid points area for IMERG-Late. This domain has been chosen because of the particular high density of the TAHMO network in this area (Figure 3.4.1).

Southern Ghana has two rainy seasons. The main one extends from March to mid-July and the second one occurs during September and October. We selected a 25 hours window containing a rainfall event, and used hourly accumulated precipitation data. The window goes from 06:00 on 22 April to 06:00 on 23 April 2018 (included). Data from 65 TAHMO stations are available within the study area for this time window (we only consider stations with a complete record for these 25 hours).

#### PRECIPITATION DATASETS

IMERG (Integrated Multi-satellitE Retrievals for GPM) is a high resolution global precipitation product produced by NASA as part of the Global Precipitation Measurement (GPM) mission [Huffman \*et al.\* \(2018\)](#); [Dezfuli \*et al.\* \(2017a,b\)](#). IMERG merges several satellite estimates from infrared, passive-microwave and satellite-radar. Three versions are available at half-hourly and  $0.1^\circ$  lat/lon resolution: the Early, Late and Final runs. The Final run is gauge-adjusted at monthly scale with the GPCC (Global Precipitation Climatology Centre) gauge product. This product is not available for the Early and Late runs, which have respectively 5 h and 15 h latency. Instead, they are climatologically adjusted to the Final run. So, they indirectly incorporate past gauge data through this climatological adjustment, but are independent of recent rainfall measurements.

The Trans-African Hydro-Meteorological Observatory (TAHMO [van de Giesen \*et al.\* \(2014\)](#)) initiative aims to develop a dense network of 20,000 hydro-meteorological stations in sub-Saharan Africa (equivalent to one station each 30 km). These cost-efficient stations measure the standard meteorological variables, including precipitation, at a high temporal resolution (5 min). The current TAHMO network contains over 600 stations, mainly in West and East Africa. The gauge measurements are interpolated using the same kriging as in the synthetic case. That is ordinary kriging with a square root transform and an exponential variogram (with a sill of  $1.0 \text{ (mm}^2/\text{h}^2)$ , a range of  $1.5^\circ$  and a nugget of  $0.01 \text{ (mm}^2/\text{h}^2)$ ).

IMERG-Late estimates and TAHMO measurements for the selected time window can be seen in Figure 3.4.2. Both show one main rainfall event, with a peak of 53.45mm rainfall at 18:00 according to TAHMO. In IMERG-Late, the peak has a lower intensity but has a longer timespan. The accumulated rainfall is estimated around 19mm for both 18:00 and 19:00. There is also a spatial shift between the peaks. For example, at 18:00, IMERG's peak is about 55km North-East of TAHMO's.

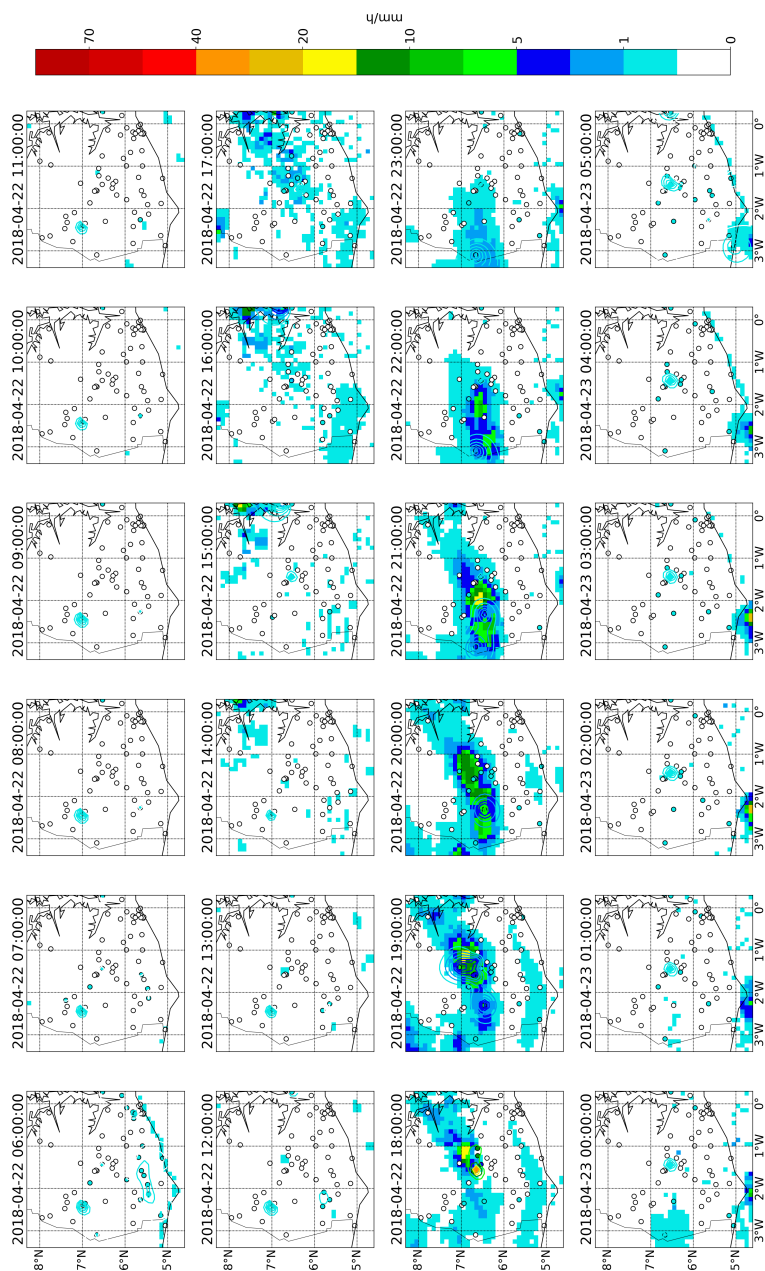


Figure 3.4.2: Input data for the southern Ghana case. IMERG-Late (background), TAHMO (circle) and corresponding gridded field (contour line) 1 hour accumulated rainfall from 06:00 the 22 April to 06:00 the 23 April 2018.

### 3.4.2. RESULTS

For the southern Ghana case, we do not know the “truth” as we did for the synthetic case. Thus, we will use a leave-one-out-validation (LOOV) to evaluate the accuracy of the method. That is, we remove one of the 65 TAHMO stations from the input data. We interpolate the 64 other stations to obtain the input field  $v$ . This is done for each of the 65 stations. The automatic registration is run 65 times, once for each of these 65 new interpolated fields used as input (after pre-processing). We obtain 65 mappings. From each of the 65 corresponding warped fields, we extract the timeseries at the location of the removed station. These timeseries can then be compared to the gauge measurement for validation since it was not used as input.

For comparison, we run a second experiment using all the stations in the interpolation to obtain  $v$ . We call this second experiment “All”. The results of the “All” experiment are not independent from the validation data. However, it will provide an insight on the impact of the gauge network configuration on the efficiency of the method, and on what is the “best” possible results with the current network.

As for the synthetic case, all the results shown here are obtained for  $C_1 = 0.1$ ,  $C_2 = C_3 = 1$  and  $c_t = 0.3$ , and for  $I = 4$  except stated otherwise.

#### SENSITIVITY OF THE SPATIAL TRANSFORM

From the LOOV experiment, we obtained 65 mappings  $T$  based on 65 different interpolated fields used as input. The output of the automatic registration depends on the inputs. Thus, with 65 different interpolated fields  $v$ , the LOOV experiment give us an insight into the sensitivity of the automatic registration to the input data.

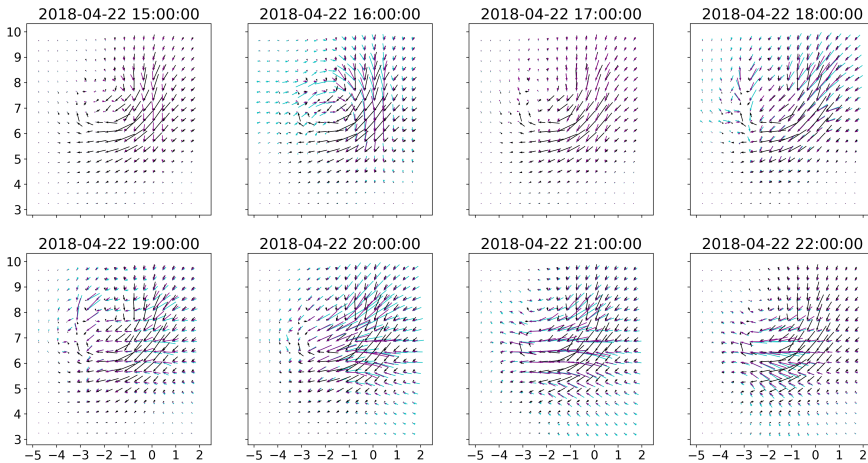


Figure 3.4.3: Average mappings obtained from the LOOV with approaches A1 (blue), A2 (black) and A3 (purple). The mappings have been averaged over the 65 realizations of the LOOV. For the sake of clarity, we only show the mapping at some selected time steps. At the other time steps, the distortion was much smaller or null, due to the absence of precipitation in the target field  $v$ .

For each of the three approaches, we look at the average mapping (over the 65 realizations) and the corresponding standard deviation. The average mappings obtained



with the three different approaches are shown in Figure 3.4.3. The mappings obtained with the “All” experiment (i.e. using all the stations as input) are very similar to the average mappings from the “LOOV” experiment, and so are not shown here. For all three approaches, the largest distortions occur in the rainy areas (see Figure 3.4.2). The distortions become smaller further away from the rainy peaks, due to the first regulation term of the cost function which ensures a mapping as “small” as possible. The second regulation term ensures that the mapping is as “smooth” as possible, and responsible for the smooth transition between these areas. The third regulation term penalizes grid cell shrinkage or expansion. Its impact is more difficult to observe.

The (average) mapping obtained with approaches A1 and A3 are similar, except at 15:00 and 17:00 on April 22. At these two times, the gauges did not record any precipitation. Thus, by construction, approach A1 does not distort the grid at these times. On the contrary, the mapping obtained with approach A3 is not zero at these times, due to the time correlation included in the cost function. It ensures a smooth transition of the mapping from one time to the next. Beside these two time steps, the main differences between the mappings from A1 and A3 occur at 18:00 near -3 degree East and 6 degree North. At that time, the mapping from A3 is closer to the one from A2 than from A1, which suggests that these differences are due to the spatial correlation term dominating the observation term in this area at that time. While approaches A1 and A3 produce similar mappings, the one obtained with approach A2 is significantly different at all time steps (Figure 3.4.3). The mapping from approach A2 is the same for every time, which also means that it is not optimal at all times. As for the synthetic case (see Section 3.3.2), different time steps need different mappings.

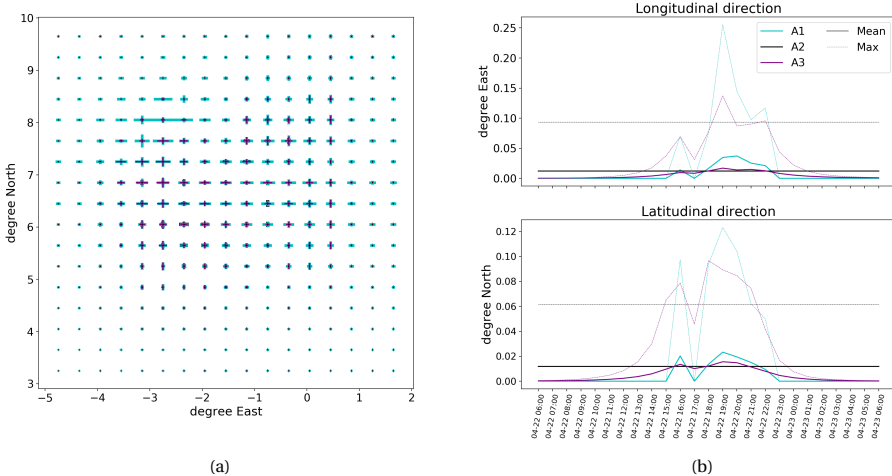


Figure 3.4.4: Standard deviation of the mappings in the LOOV experiment for the three approaches A1, A2 and A3. (a) Maximum standard deviation at each grid point. (b) Mean and maximum standard deviation at each time step.

The standard deviation of the “LOOV” experiment is shown in Figure 3.4.4. On the

left, one can see the average standard deviation (over space), as well as the maximum, for each time step. The standard deviation of the mapping from approach A2 is constant in time, since the mapping is the same for all time steps. The standard deviations from approaches A1 and A3 vary in time. The standard deviation is zero at all time steps without recorded rainfall (gauge) for approach A1, and at time steps far away from the rainy times for approach A3. This is due to the fact that, by construction, the mappings are zero at these time steps for these approaches. One can see that for all the other time steps, where the gauges recorded some precipitation, both the mean and the maximum standard deviation is higher for approach A1 than for approach A3. The standard deviation from approach A2 is, in general, equal or lower than both approaches A1 and A3 at these time steps. For the three approaches, the standard deviation is larger in the longitudinal direction than in the latitudinal one. For example, the average standard deviation goes up to 0.018 degree in the latitudinal direction, and up to 0.025 degree in the longitudinal direction for approach A3. Its maximum standard deviation goes up to 0.10 degree in the latitudinal direction, and up to 0.18 degree in the longitudinal direction. This can also be seen when looking at the maximum (in time) standard deviation at each grid cell (Figure 3.4.4a). At most grid cells, the maximum standard deviation is larger in the longitudinal direction than in the latitudinal one, especially for approach A1. The approach A2, with its time constant mapping, has the smaller maximum standard deviation, but the larger average one over time. The average standard deviation over time is not shown because of its small scale. In general, approach A1 has a larger maximum standard deviation than A3 and A2. However, the average standard deviation of approaches A1 and A3 are very similar.

#### VALIDATION

In contrast to the synthetic case, we do not know the “truth” here. It is thus more difficult to evaluate quantitatively the improvement of the position error, especially with the “LOOV” experiment from which we obtained 65 mappings and 65 time series (one for each station). We will use the “All” experiment to estimate the position accuracy (the average mapping from the “LOOV” experiment is very similar to the one from the “All” experiment). The warped fields for the three approaches can be seen in Appendix 3.C. After spatial warping, the position of the event corresponds better to the gauge data. This can also be seen more quantitatively in Figure 3.4.5, which shows the position error of the peak for each time step (with more than 1mm/h). The position error is the distance between the rainfall peaks in the interpolated field  $v$  and in the warped field  $u_{\text{warp}}$ , the peak being defined as the pixel with the maximum rainfall intensity. The position error is lower after the spatial warping than before, except at 15:00 with approach A1 and at 19:00 with approach A2. As seen previously, there is no distortion at time 15:00 and 17:00 with approach A1, so the error is the same before and after warping. Approaches A1 and A3 have similar position error at most time steps, except at 15:00, 16:00 and 20:00. In general, the position error is higher for approach A2. The lowest position error is achieved at 18:00 for the three approaches. This time step has the highest recorded rainfall according to the gauges.

Table 3.4.1 gives the position error averaged over time for different rainfall thresholds. For all the thresholds, the average position error is smaller after the warping for the three approaches. When considering all time steps with at least 0.1mm/h, the decrease

of the error is very small. The low rainfall has more spatial variability than the higher ones, the peaks are less obvious. Moreover, the low rainfall is not taken into account in the automatic registration, since it is removed during the preprocessing step. The time steps with the higher rainfall seem to benefit more from the warping. For example, with approach A3, the average position error is divided by 3 for a threshold of 1mm/h, and by 4.6 for a threshold of 5mm/h. The average position error is always higher with approach A2, and approach A3 has the lowest error. At the time step at which the peak of the event occurs, the three methods have the same position error of 11.04km, which corresponds to the length of one grid cell.

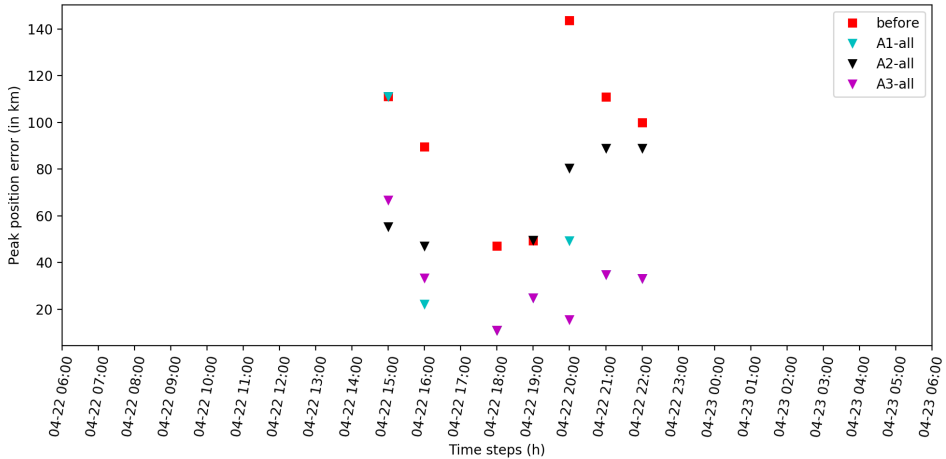


Figure 3.4.5: Distance between the “true” peak (gauge) and the estimated ones before and after spatial warping, for the “All” experiment, at each time step with more than 1mm/h recorded rainfall (in  $v$ ).

Table 3.4.1: Average position error (km) before and after spatial warping for the “All” experiment. The average is done over all time steps at which the peak (in  $v$ ) is above a certain threshold.

Threshold (peak)	Sample number	Before	A1	A2	A3
>0.1mm/h	n=15	173.79	149.45	146.26	145.81
>1mm/h	n=7	93.15	40.98	60.25	31.39
>5mm/h	n=3	93.45	27.58	46.17	20.03
>10mm/h	n=1	47.01	11.04	11.04	11.04

The results of the “All” experiment are not independent from the validation data. The TAHMO stations are used both as input to the automatic registration (after interpolation) and for the validation. However, this experiment provides an insight on the “best” possible results. We use the “LOOV” experiment to have a more independent validation. The statistics for both experiments are shown in Table 3.4.2. For the “LOOV” experiment, all three approaches are improving the RMSE, the MAE and the correlation coefficient. The RMSE goes from 1.89mm/h before warping to 1.50mm/h with approach A3. The MAE also decreases, from 0.20mm/h to 0.14mm/h with approaches A1 and A3. The decrease

is less significant with approach A2. The correlation coefficient before warping is low (0.18), and is significantly increased by the warping (to 0.55 with A2 and 0.63 with A1). Approaches A1 and A3 have very similar statistics, with A1 slightly better. The statistics of approach A2 show less improvement. For approaches A1 and A3, the statistics are better for the “All” experiment than for the “LOOV” one. The RMSEs are 0.1mm/h smaller, and the correlation are increasing to 0.70 (versus 0.6 for the “LOOV”). The better statistics of the “All” experiment was to be expected since the validation data was not independent of the input data. Surprisingly, the statistics for approach A2 are similar for the two experiments, and even slightly better for the “LOOV” one.

Table 3.4.2: Statistics before and after the spatial warping compared to the station measurements. The results are shown for the two experiments (“LOOV” and “All”) and the three approaches (A1, A2 and A3). The statistics are computed over all stations and all time steps.

	Before	All			LOOV		
		A1	A2	A3	A1	A2	A3
RMSE (mm/h)	1.89	1.39	1.57	1.39	1.48	1.56	1.49
MAE (mm/h)	0.20	0.13	0.19	0.13	0.14	0.18	0.14
Correlation	0.18	0.70	0.53	0.70	0.63	0.55	0.62

#### TIMING ERROR

Figure 3.4.6 shows the timing error between the stations and the satellite estimate. At most station locations, the rainfall peak is late compared to the gauges. Often, position and timing errors are related, and a timing error can be translated as a position error from the point of view of a station. Thus, we examine the impact of spatial warping on the timing error. In Figure 3.4.7, one can see the improvement of the (absolute) timing error after warping. With approaches A1 and A3, the timing error has decreased by one or two hours at most stations. The improvement is more limited when using approach A2, with more stations showing a neutral improvement. The results of the “LOOV” experiment are very similar to the “All” experiment.

Table 3.4.3: Average absolute timing error before and after spatial warping. The average is done over all stations recording at least one time step with more rainfall than a certain threshold.

Threshold	Sample number	Before	All			LOOV		
			A1	A2	A3	A1	A2	A3
>0.1mm/h	n=15	2.07	1.33	2.13	1.40	1.40	2.07	1.40
>1mm/h	n=10	1.10	0.30	1.30	0.40	0.40	1.30	0.40
>5mm/h	n=7	1.00	0.14	1.43	0.29	0.14	1.29	0.14
>10mm/h	n=5	1.20	0.20	1.00	0.40	0.20	1.00	0.20

For easier comparison, Table 3.4.3 gives the absolute timing error averaged over the stations recording more than a certain threshold. As seen in Figure 3.4.7, the average error decreases after spatial warping for approaches A1 and A3. These two approaches have identical average error for the “LOOV” experiment, while approach A1 leads to smaller timing error for the “All” experiment. The average timing error decreases when

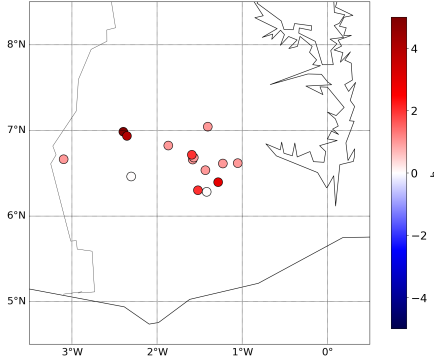


Figure 3.4.6: Timing error before spatial warping at each station (only at stations which recorded >0.1mm/h). In red, the peak in  $u$  is late (compared to the one in the station measurement). In blue, the peak in  $u$  is in advance. It has to be noted that the timing error can only be given at the hourly resolution due to the definition of the time steps.

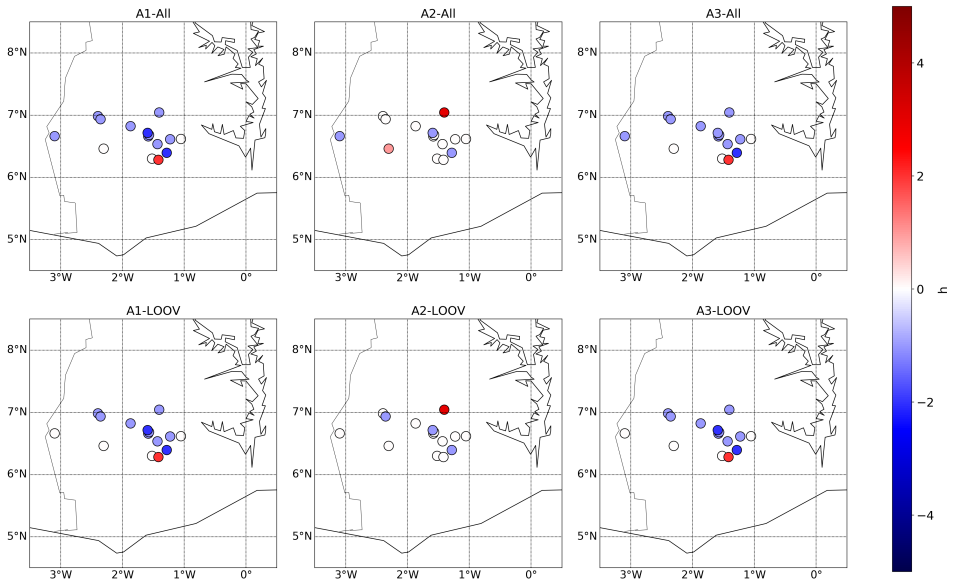


Figure 3.4.7: Improvement in timing error after spatial warping (only at stations which recorded >0.1mm/h). In blue, the absolute timing error decreased after the warping. In red, the timing error increased. The results are shown for the two experiments: (top) “All” and (bottom) “LOOV”, and the three approaches: (left) A1, (middle) A2 and (right) A3.

the threshold increases. It is divided by 3.75 for the threshold of 1mm/h and by 6 when considering only stations with more than 10mm/h rainfall (for the “LOOV” experiment).

The spatial warping with approach A2 does not improve positively the timing error. In contrast, the average error increases after warping, except for the higher threshold of 10mm/h. Since approach A2 applies the same mapping at all time steps, it has less influence on the timing error. It seems to correct better the time steps with higher precipitation, forcing the other ones to move along.

### 3.5. DISCUSSION

The spatial warping has been evaluated in terms of the position and the timing of the rainfall peak, and of the intensity of the event. The position error is explicitly corrected by the spatial warping. It was shown that this error was significantly reduced for both the synthetic and the real data case. The timing error also decreased after the spatial warping. The distinction between a time delay or a spatial shift can be ambiguous. Part of the timing error can be due to a position error, and vice versa. So, by correcting the position, the warping also reduced the timing error. The continuous statistics on the intensity are improved by the spatial warping too. The warping does not modify the rainfall intensity (there is no bias adjustment). However, by removing the double-penalty part of the error, it improves the intensity. This can be seen by the increase of the correlation after warping.

One shortcoming observed in the results is that the spatial warping seems to prioritize correcting the higher rainfall values, sometimes to the detriment of the lower rainfall values. For example, the average position error is smaller for the higher threshold (Tables 3.3.1 and 3.4.1). This can be explained by the method used to derive the mappings. The automatic registration is based on the minimization of a cost function. The higher rainfall values have more weight than the lower ones in the observation term, and so are corrected first. This shortcoming points to a limitation of the metrics used to evaluate the position and timing errors. They are defined with respect to the rainfall peak, so they do not reflect the spatial and temporal variation of the lower rainfall. Thus, they might be biased, since the method favours the higher rainfall values.

The improvement of position, and its positive impact on the continuous statistics were observed for the three approaches. However, there were some differences among them. Approach A2 leads to a more limited improvement. This approach is built on the assumption that the spatial distortion is the same at all time steps. The further the data are from this assumption, the less efficient approach A2 is. On the other side, this assumption makes approach A2 the least computationally expensive. Approaches A1 and A3 have similar results in terms of position, timing and intensity. Most differences between these two approaches occur in low or non rainy areas/time steps. In both approaches, each time step has a different mapping. The mappings are derived independently in approach A1, while they are linked in approach A3. Thus, in approach A1, mappings of two adjacent time steps can be very different. This can cause some non-physical discontinuities, such as the one between times 9 and 10 in the synthetic case (Figure 3.B.1). This discontinuity does not appear with approaches A2 and A3. Approach A1 is more computationally expensive than approach A2 and less than approach A3. On a personal computer, the automatic registration needed less than two minutes with approach A2, 10 minutes for approach A1 and approximately 70 minutes for approach A3 to run for the synthetic case and  $I = 4$ . Since the time steps are independent of each other

in approach A1, it could easily be adapted to run in parallel to reduce the computational time. Approach A3 is the most computationally expensive of the three approaches due to the higher number of variables to be optimized. A solution to reduce the cost of approach A3 would be to reduce the time window. If it is not possible due to the length of the rainfall event, an alternative would be to use a moving time window. We would then run several smaller minimization problems instead of one large one.

The mappings are derived from the automatic registration that can be tuned by several parameters, such as the number of steps  $I$  and the regulation coefficients  $C_1$ ,  $C_2$ ,  $C_3$  and  $c_t$  (for approach A3). These parameters are affecting the mappings. We looked at the impact of the regulation coefficients on the mapping for the synthetic case (Sections 3.3.3 and 3.3.3). The regulation terms represent properties one wants for the mappings. The coefficients permit to give more or less weight to these properties. The regulation terms mainly affect the area (or time steps) with no or low rainfall. Thus, their impact on the RMSE and correlation are limited, but their effects are still valuable. For example, the fourth term in approach A3 prevents non-physical discontinuities in time like the one seen with approach A1 (e.g. between time 9 and 10). Similarly, the “smoothness” properties ( $C_2$ ) avoid non-physical discontinuity in space. Since the low precipitation is removed in the pre-processing step, this property ensures that it is still moved along the higher rainfall values.

The number of steps  $I$  defines the resolution of the mapping  $T$ . A higher number of steps  $I$  means that more details are taken into account (less smoothing), and that mapping itself has more details, because of the higher resolution of the warping grid  $D_I$ . On the other hand, the computational time increases exponentially with  $I$ . The minimization problem is solved for all the grid points at the same time, yet the number of grid points increases exponentially with  $I$ . For example, the first step (i.e.  $i = 1$ ) takes 20 seconds, the second one more than 2 minutes, the third one 17 minutes and the fourth step 47 minutes with approach A3. The impact of  $I$  on the warped fields differs depending on the approach. For approaches A1 and A3, increasing  $I$  improves the errors in terms of position, RMSE and correlation. However, the improvement becomes smaller when  $I$  increases. Thus, it would be possible to decrease the number of steps  $I$  in order to reduce the computational time without losing too much accuracy. For approach A2, increasing  $I$  improves the average position error but worsens the continuous statistics. It seems that this approach prioritizes the high rainfall, such as the peak, to the detriment of the lower rainfall in the other time steps, which would have needed a different spatial correction.

In this chapter, we use spatial warping to correct the position in satellite-based estimates using gauges. The automatic registration method used was similar to the one described in [Beezley and Mandel \(2008\)](#); [Mandel et al. \(2010\)](#). There are four main differences between our method and the morphing described in [Beezley and Mandel \(2008\)](#) and [Mandel et al. \(2010\)](#). First, we modified the cost function by adding a third regulation term based on divergence. Second, they solved the minimization problem for one grid point at a time, while we solve it for all the grid points together (i.e., we have one multi-variable minimization problem instead of several 1D ones). Thirdly, we use irregularly spaced (i.e. non-gridded) gauge measurements as observations instead of (gridded) radar data. Finally, we extended the method to take into account several time steps

at the same time (e.g. approaches A2 and A3).

In order to use non-gridded data (i.e. gauges), we added a pre-processing step before the automatic registration. In this step, the gauge measurements are kriged onto the same grid as the satellite estimate. The kriging introduces some interpolation errors, especially in the areas far from the gauges. In the synthetic case, we compare two experiments: the first one uses the “truth”  $\nu$  as input (i.e. no kriging), while in the second one the target field  $\nu$  is obtained by kriging. The mappings from the two experiments exhibit similar patterns but there are also differences. The kriging experiment has higher average position errors and slightly better RMSE and MAE than the one using the “truth”. Depending on the position of the event, the rainfall event is more or less well captured by the gauges and so represented by the kriged field. Due to the interpolation method (kriging), the peak of the event is necessarily near a gauge in the kriged field. This explains the larger position error in the second experiment. In the southern Ghana case, the LOOV experiment allows us to look at the sensitivity of the mapping to the gauge network configuration. The standard deviation of the mappings is very low, however, some members do show a large deviation from the mean. Some stations have a bigger impact than others on the accuracy of the kriging and, thereby, on the automatic registration. In these two study cases, the rainfall event is relatively well captured by the gauges. In practice that would not always be the case, depending on the position of the event and on the network configuration.

The main limitation of the automatic registration, and, thereby, of the spatial warping, is the need for the input fields  $u$  and  $\nu$  to be similar enough. We did not derive criteria to determine beforehand if the fields are similar enough. However, there are some minimum conditions, such as having the same number of events and the proximity of the events. The smoothing in the automatic registration can be increased or decreased to allow the events to move further or not. In this chapter, we explored the potential of spatial warping for position correction of precipitation data. The next step will be to apply this method to other cases, involving different rainfall regimes. More study cases, including extreme ones, are needed to determine the boundaries within which the automatic registration succeeds, and to determine “feasibility” thresholds.

### 3.6. CONCLUSION

We have investigated the use of a warping approach for the gauge-adjustment of satellite-based rainfall estimates with respect to position error. The warping method, adapted from [Beezley and Mandel \(2008\)](#), has been applied to two cases. Synthetic rainfall events, represented by ellipses, have been used to test the warping method and its sensitivity to several parameters. The second case, a convective rainfall event in southern Ghana, showed the potential of the method when applied to real, noisy precipitation data. We applied the position correction such that the gauge data were down-scaled while keeping the high spatial variability of the satellite-based product. The rain events estimated by IMERG-Late were spatially shifted to match the gauge data.

The automatic registration was extended to take (3D) space-time data as input, that is, 2D rainfall fields at several times. We tried three different approaches with different assumptions regarding the behaviour along the time dimension. The first one assumes that all the time steps are independent. In contrast, the second one assumes that all



time steps have the same mapping. The third approach allows each time step to have a different mapping but assumes that they are linked through time. All three approaches improve the position and intensity errors. However, they have different performances in terms of accuracy and computational cost. All three approaches only modified the spatial coordinates. The first approach completely ignores the temporal dimension, while the second and third ones are taking it into account by adding some constraints (i.e. all time steps have the same mapping, or that their mappings are linked). The two latter approaches are an alternative to a fully space-time warping, or at least a first step. Such 3D warping would warp the rainfall field both in space and time, and so would fully consider the relationship between the spatial and temporal dimensions. However, it would also be more computationally expensive due to the larger number of variables to optimize during the automatic registration.

### 3.7. FUTURE WORK

This chapter explores the use of an image warping method to correct location errors in precipitation estimates. The next step will be to extend the study to other case studies, including different rainfall regimes. It should also be pushed to more extreme cases to determine the method's limitations more precisely. More cases would permit to derive feasibility criteria to quantify beforehand if the input are too dissimilar for the automatic registration to work. It would also allow us to have a better idea of the sensitivity with respect to the regulation coefficients, and so to better tune the automatic registration. A more robust way of selecting the regulation coefficients could be developed, for example by defining adaptive coefficients, as opposed to the empirical choices made here.

Another step would be to combine spatial adjustment and bias adjustment. In this chapter, we only looked at the warping part of the morphing method described in [Mandel et al. \(2010\)](#) and [Beezley and Mandel \(2008\)](#), that is the spatial correction. Morphing is based on warping, which modifies the spatial coordinate, and cross-dissolving, which modifies the amplitude or intensity. Thus, morphing impacts both the position and the intensity. The morphing formula is similar to the warping one, but an extra term is added to correct the intensity:

$$u_{morph} = (u + r) \circ (I + T) = u_{warp} + r \circ (I + T)$$

where  $r = v \circ (I + T)^{-1} - u$  is the residual. However, the morphing cannot be applied directly in the case of point measurements (such as gauge observations). We do not know the true rainfall at all grid points, so the kriged field is assumed to be the "truth"  $v$ . The morphing would "correct" the intensity everywhere to make it correspond to the kriged field, including in areas far from the stations. We would need to take into account the kriging error into the morphing. A possibility would be to add a coefficient depending on the kriging variance ( $\sigma_{kriging}$ ) in front of the residual:

$$u_{morph} = (u + \alpha \cdot r) \circ (I + T)$$

with the coefficient  $\alpha$  being a function of the kriging variance  $\sigma_{kriging}$ . Another possibility is to apply an existing bias adjustment method after the warping as a second step, for example the additive or multiplicative adjustment or the PDF matching method.

In this chapter, we assumed that the gauge measurements correspond to the true rainfall values at these points. However, gauges also have uncertainties. Similarly, we do not take into account the kriging error in the automatic registration. That is, the kriged field is assumed to be the “truth”. These two errors could be taken into account in the automatic registration by adding an observational error covariance  $R$  in the observation term of the cost function  $J_o = (v - u \circ (I + T))^T R^{-1} (v - u \circ (I + T))$ .



# APPENDIX

## 3.A. OPTIMIZATION STEP OF THE AUTOMATIC REGISTRATION ALGORITHM

The automatic registration is based on the minimization of the cost function  $J$  given in Equation (3.6). This is done in the third step of the algorithm (Figure 3.2.1). In this appendix, we give more information about this important step of the algorithm, with a focus on the constraints (Section 3.A.1) and on the minimization method (Section 3.A.2).

### 3.A.1. CONSTRAINTS

This minimization problem includes a certain number of constraints. These constraints come from two requirements. First, we require that the nodes stay within the domain  $D$  (i.e.,  $(I + T)(x_k, y_j) \in D \ \forall (x_k, y_j) \in D_i$ ). That is, the nodes on the boundary of the domain are allowed to move inside the domain but no nodes are allowed to leave it. These constraints can be seen as inequality constraints or as bounds. Second, the mapping  $I + T$  has to be invertible. Each node  $(x_k, y_j)$  of the grid  $D_i$  is constrained to the domain between the points  $(x_{k+1}, y_j)$ ,  $(x_k, y_{j-1})$ ,  $(x_{k-1}, y_j)$  and  $(x_k, y_{j+1})$ , in order to insure that the inverse mapping  $(I + T)^{-1}$  exists (see [Beezley and Mandel \(2008\)](#)). This second requirement translates as inequality constraints.

Since nodes on the boundary are allowed to move inside the domain, some computations will need the value of an image outside the domain  $D$  (e.g.,  $u \circ (I + T)^{-1}$  on  $D$  or the smoothing of  $u$  and  $v$ ). To allow these computations, all the images are extended on  $\mathbb{R}^2$  by assuming that there is no precipitation outside the domain, that is,  $\forall (x, y) \notin D, \ u(x, y) = v(x, y) = 0$ .

### 3.A.2. MINIMIZATION METHOD

In [Beezley and Mandel \(2008\)](#), the minimization problem was solved by optimizing  $T_i$  one node after each other (for all nodes of the grid  $D_i$ ). For each node, the coordinates  $x$  and  $y$  were updated alternatively using a 1-D constrained non-linear optimization function. We use a different approach and optimize all the nodes at the same time. The solution does not depend on the order in which the nodes are optimized. However, the number of variables to optimize ( $2 \cdot (2^i + 1)^2$  for grid  $D_i$ ) increases exponentially with  $i$ . Constrained optimization algorithms become computationally expensive for such large numbers of independent variables. Thus, for computation efficiency, we used an iterative barrier approach ([Jon \(2004\)](#); [Noc \(2006\)](#)).

In the barrier approach, the inequality constraints are added to the cost function  $J$  as penalization terms:

$$J_p(T_i) = J(T_i) + \beta \sum_h C_h(T_i) \quad (3.12)$$

where  $C_h$  are constraint functions and  $\beta$  is the barrier coefficient. The constraints that cannot be written as bounds are converted into constraint functions  $C_h$ , such that  $C_h(T_i) > 0$  if the constraint is violated and  $C_h(T_i) = 0$  if it is respected.

This new minimization problem does not have inequality constraints, only bounds from our first requirement. Here, we minimized the penalized cost function  $J_p$  using the limited-memory quasi-Newton method for bound-constrained problems (L-BFGS-B) method (with the Python function `scipy.optimize.minimize`).

As mentioned above, the barrier approach is iterative. First, the cost function  $J_p$  is minimized using the L-BFGS-B method with  $\beta = 1$ . If all the constraints are respected, the procedure stops. Otherwise, the iterations continue with  $\beta = 10 \cdot \beta$ . The iterations continue until all the constraints are respected or until one of the stopping criteria is reached. We set two stopping criteria: 1) the decrease of the cost function  $P$  is smaller than  $< 10^{-5}$  and 2) the root mean square difference of the grids  $D_i$  before and after is smaller  $< 10^{-5}$ .

### 3.B. EXTRA RESULTS FROM THE SYNTHETIC CASE

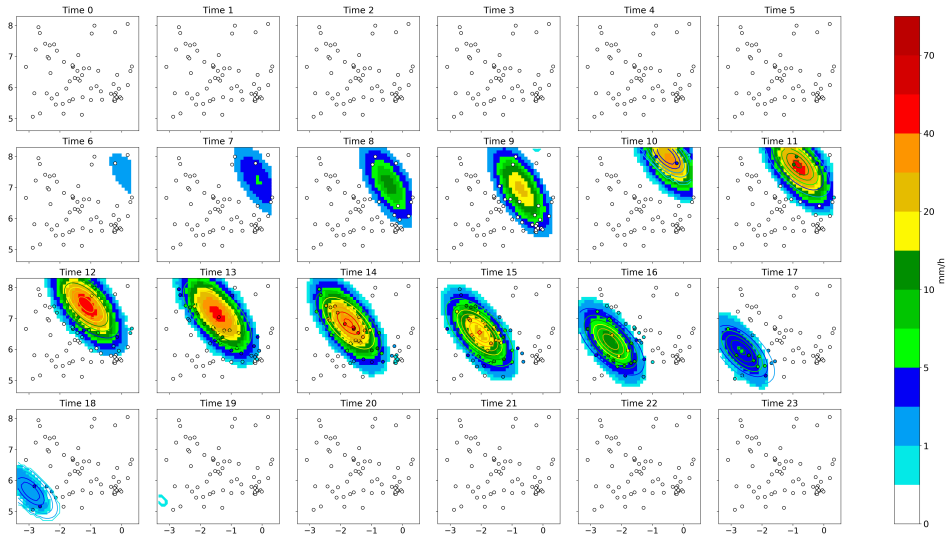


Figure 3.B.1: Warped precipitation field  $u_{\text{warp}}$  obtained with the approach A1 and the “Full” experiment (background), and the “true” precipitation field  $v$  (contour lines) for the synthetic case. The fictive stations are represented by circles.

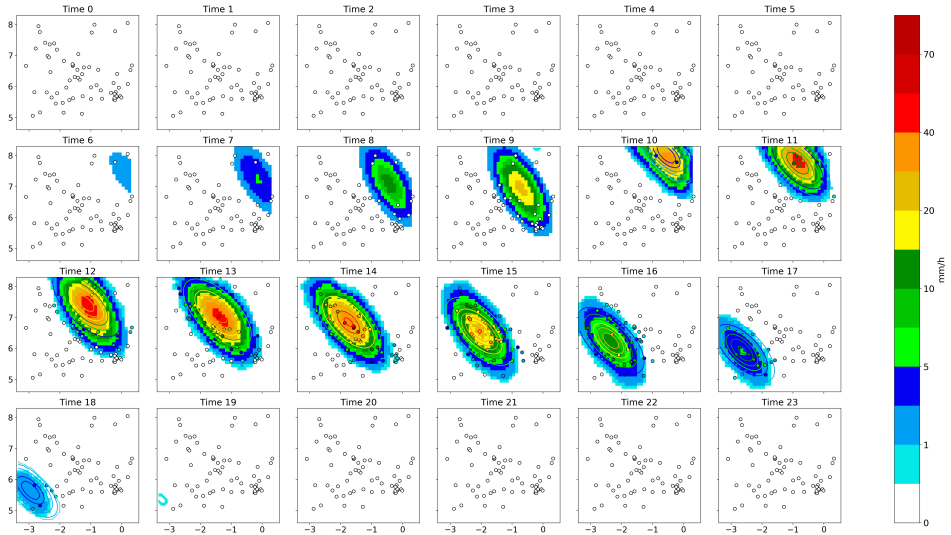


Figure 3.B.2: Warped precipitation field  $u_{\text{warp}}$  obtained with the approach A1 and the “Interpolated” experiment (background), and the “true” precipitation field  $v$  (contour lines) for the synthetic case. The fictive stations are represented by circles.

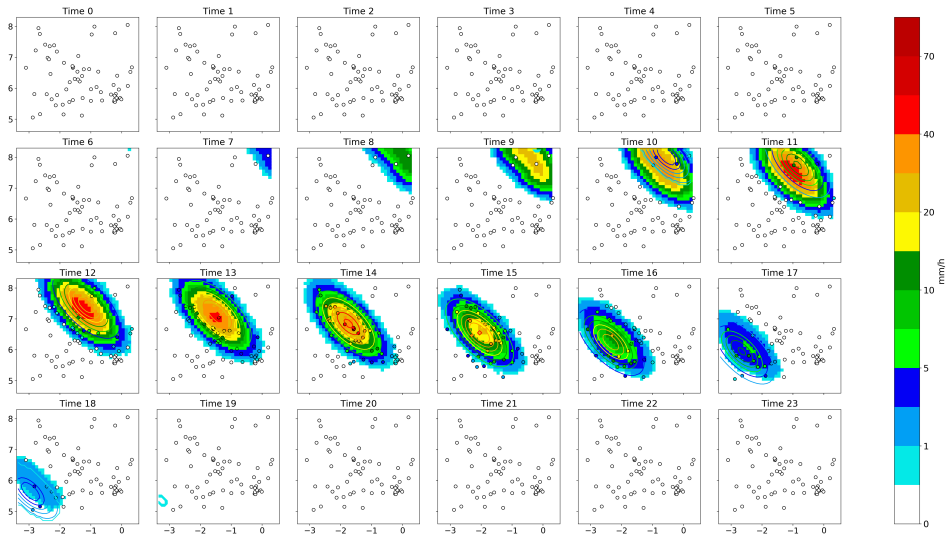


Figure 3.B.3: Warped precipitation field  $u_{\text{warp}}$  obtained with the approach A2 and the “Full” experiment (background), and the “true” precipitation field  $v$  (contour lines) for the synthetic case. The fictive stations are represented by circles.

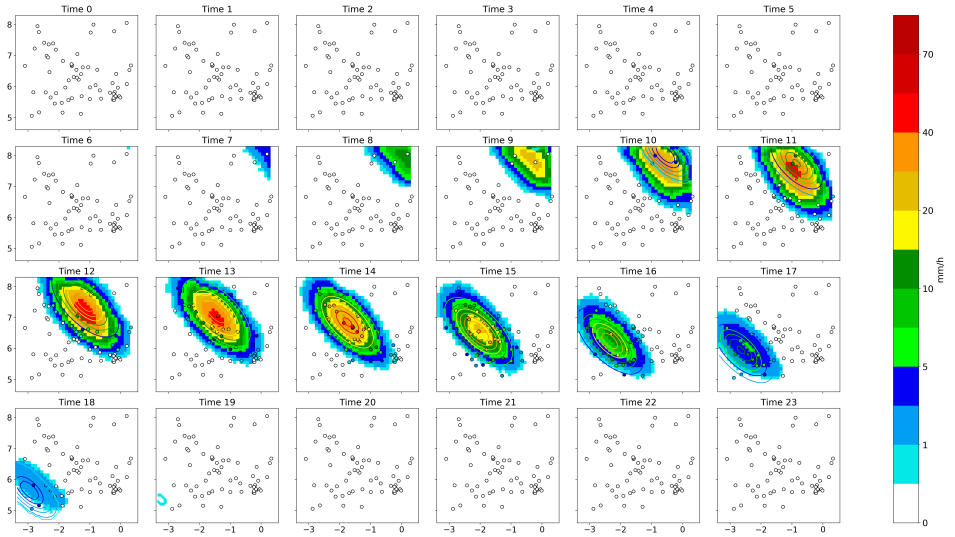


Figure 3.B.4: Warped precipitation field  $u_{\text{warp}}$  obtained with the approach A2 and the “Interpolated” experiment (background), and the “true” precipitation field  $v$  (contour lines) for the synthetic case. The fictive stations are represented by circles.

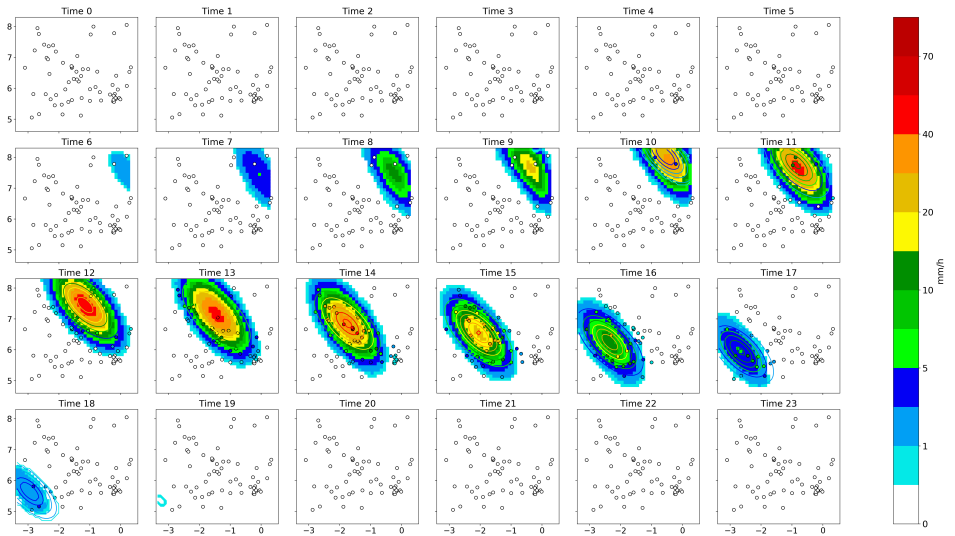


Figure 3.B.5: Warped precipitation field  $u_{\text{warp}}$  obtained with the approach A3 and the “Full” experiment (background), and the “true” precipitation field  $v$  (contour lines) for the synthetic case. The fictive stations are represented by circles.

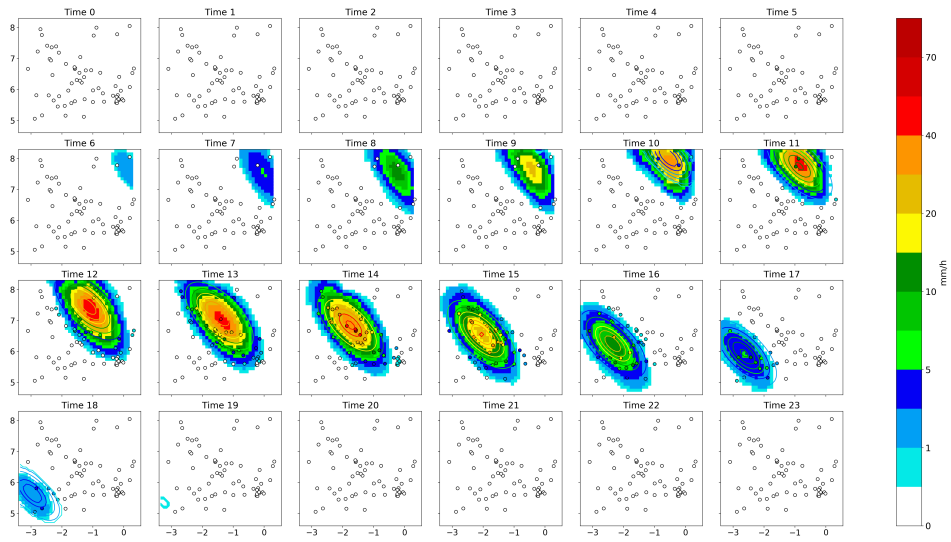


Figure 3.B.6: Warped precipitation field  $u_{\text{warp}}$  obtained with the approach A3 and the “Interpolated” experiment (background), and the “true” precipitation field  $\nu$  (contour lines) for the synthetic case. The fictive stations are represented by circles.



### 3.C. EXTRA RESULTS FROM THE SOUTHERN GHANA CASE

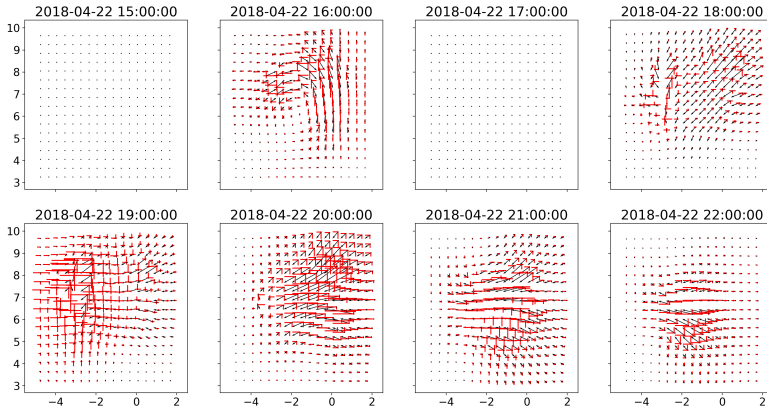


Figure 3.C.1: Mappings obtained from the LOOV with approach A1. The mean mapping is represented by the black arrows. The maximum deviation from the average in both the latitude and the longitude directions are shown in red. For the sake of clarity, we only show the mapping at some selected time steps. At the other time steps, the distortion was much smaller or null, due to the absence of precipitation in the target field  $\nu$ .

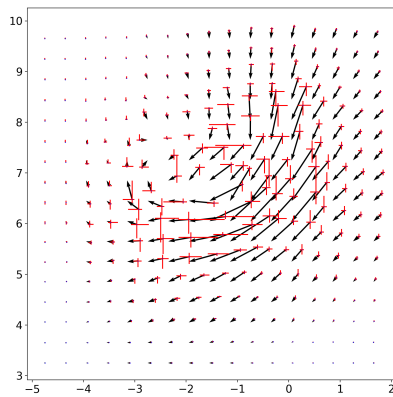


Figure 3.C.2: Mappings obtained from the LOOV with approach A2. The mean mapping is represented by the black arrows. The maximum deviation from the average in both the latitude and the longitude directions are shown in red.

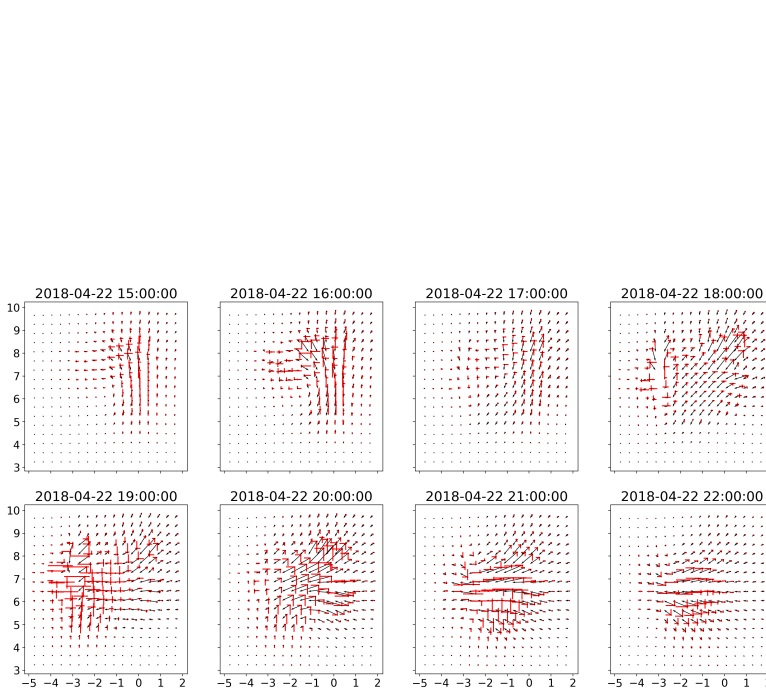


Figure 3.C.3: Mappings obtained from the LOOV with approach A3. The mean mapping is represented by the black arrows. The maximum deviation from the average in both the latitude and the longitude directions are shown in red. For the sake of clarity, we only show the mapping at some selected time steps. At the other time steps, the distortion was much smaller or null, due to the absence of precipitation in the target field  $\nu$ .

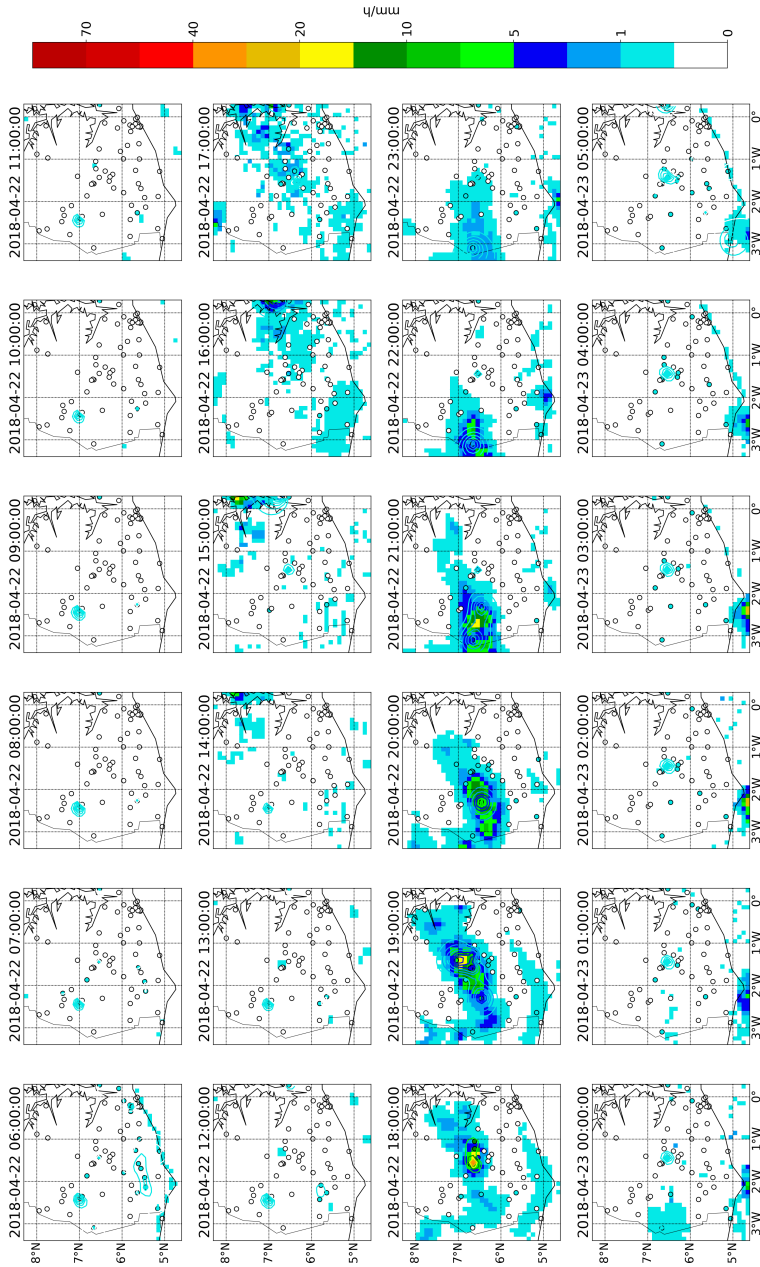


Figure 3.C.4: Warped precipitation field  $u_{warp}$  obtained with the approach A1 and the “All” experiment (background) for the Southern Ghana case. The station measurements are represented by circles, and the corresponding interpolated field  $v$  by contour lines.

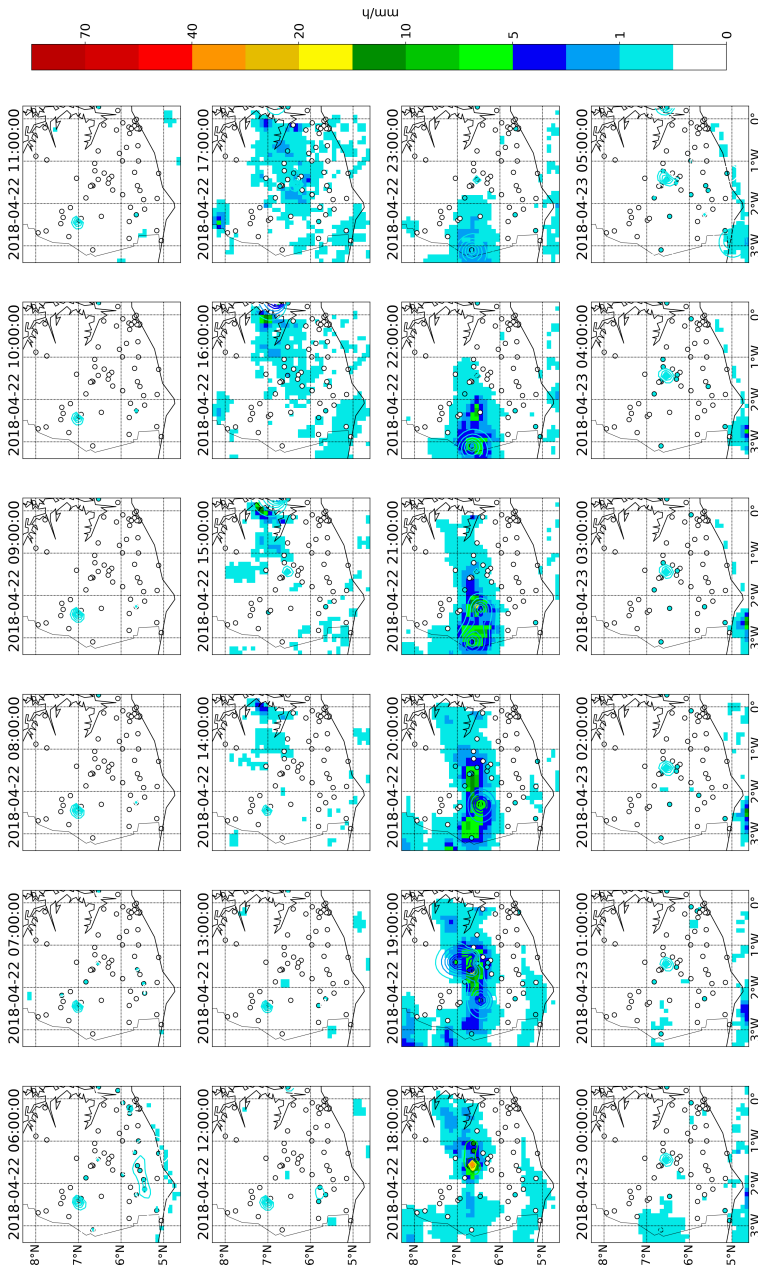


Figure 3.C.5: Warped precipitation field  $u_{warp}$  obtained with the approach A2 and the “All” experiment (background) for the Southern Ghana case. The station measurements are represented by circles, and the corresponding interpolated field  $v$  by contour lines.

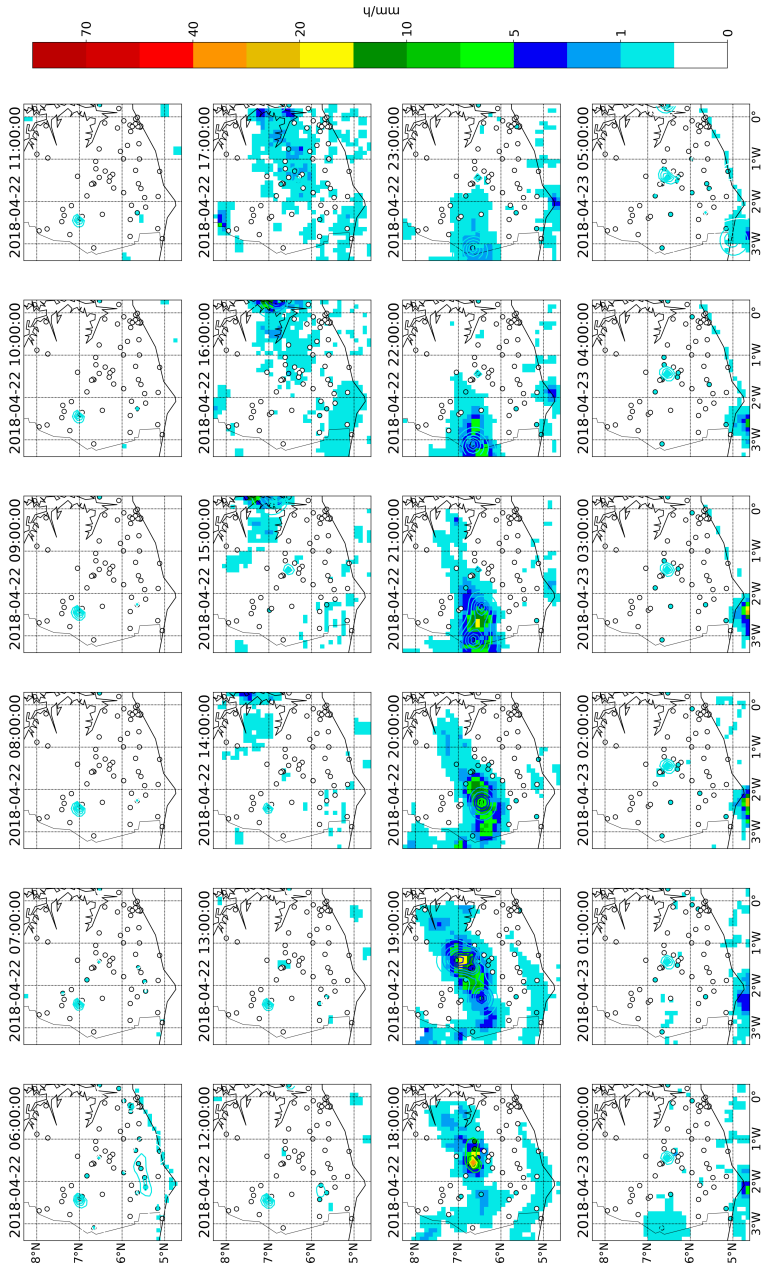


Figure 3.C.6: Warped precipitation field  $u_{warp}$  obtained with the approach A3 and the “All” experiment (background) for the Southern Ghana case. The station measurements are represented by circles, and the corresponding interpolated field  $v$  by contour lines.

## REFERENCES

- C. Lorenz and H. Kunstmann, *The hydrological cycle in three state-of-the-art reanalyses: Intercomparison and performance analysis*, *Journal of Hydrometeorology* **13**, 1397 (2012).
- C. Le Coz and N. van de Giesen, *Comparison of rainfall products over sub-Saharan Africa*, *Journal of Hydrometeorology* **21**, 553 (2020).
- E. Morin, D. C. Goodrich, R. A. Maddox, X. Gao, H. V. Gupta, and S. Sorooshian, *Spatial patterns in thunderstorm rainfall events and their coupling with watershed hydrological response*, *Advances in Water Resources* **29**, 843 (2006).
- E. Cristiano, M.-C. ten Veldhuis, and N. van de Giesen, *Spatial and temporal variability of rainfall and their effects on hydrological response in urban areas – a review*, *Hydrology and Earth System Sciences* **21**, 3859 (2017).
- P. Arnaud, C. Bouvier, L. Cisneros, and R. Dominguez, *Influence of rainfall spatial variability on flood prediction*, *Journal of Hydrology* **260**, 216 (2002).
- Q. Xiao, X. Zou, and Y.-H. Kuo, *Incorporating the ssm/i-derived precipitable water and rainfall rate into a numerical model: A case study for the erica iop-4 cyclone*, *Monthly Weather Review* **128**, 87 (2000).
- P. Lopez, *Direct 4D-Var assimilation of NCEP Stage IV radar and gauge precipitation data at ECMWF*, *Monthly Weather Review* **139**, 2098 (2011).
- E. Gilleland, D. Ahijevych, B. G. Brown, B. Casati, and E. E. Ebert, *Intercomparison of spatial forecast verification methods*, *Weather and Forecasting* **24**, 1416 (2009).
- D. Ahijevych, E. Gilleland, B. G. Brown, and E. E. Ebert, *Application of spatial verification methods to idealized and NWP-gridded precipitation forecasts*, *Weather and Forecasting* **24**, 1485 (2009).
- W. M. Briggs and R. A. Levine, *Wavelets and field forecast verification*, *Monthly Weather Review* **125**, 1329 (1997).
- B. Casati, G. Ross, and D. B. Stephenson, *A new intensity-scale approach for the verification of spatial precipitation forecasts*, *Meteorological Applications* **11**, 141 (2004).
- B. Casati, *New developments of the intensity-scale technique within the spatial verification methods intercomparison project*, *Weather and Forecasting* **25**, 113 (2010).
- E. Ebert and J. McBride, *Verification of precipitation in weather systems: determination of systematic errors*, *Journal of Hydrology* **239**, 179 (2000).
- C. Davis, B. Brown, and R. Bullock, *Object-based verification of precipitation forecasts. Part I: Methodology and application to mesoscale rain areas*, *Monthly Weather Review* **134**, 1772 (2006).

- C. Marzban and S. Sandgathe, *Cluster analysis for verification of precipitation fields*, [Weather and Forecasting](#) **21**, 824 (2006).
- R. N. Hoffman, Z. Liu, J.-F. Louis, and C. Grassotti, *Distortion representation of forecast errors*, [Monthly Weather Review](#) **123**, 2758 (1995).
- R. N. Hoffman and C. Grassotti, *A technique for assimilating ssm/i observations of marine atmospheric storms: Tests with ecmwf analyses*, [Journal of Applied Meteorology](#) **35**, 1177 (1996).
- C. Grassotti, H. Iskenderian, and R. N. Hoffman, *Calibration and alignment*, [Journal of Applied Meteorology](#) **38**, 677 (1999).
- T. Nehr Korn, B. K. Woods, R. N. Hoffman, and T. Auligné, *Correcting for position errors in variational data assimilation*, [Monthly Weather Review](#) **143**, 1368 (2015).
- K. Aonashi and H. Eito, *Displaced ensemble variational assimilation method to incorporate microwave imager brightness temperatures into a cloud-resolving model*, [Journal of the Meteorological Society of Japan. Ser. II](#) **89**, 175 (2011).
- T. Nehr Korn, B. Woods, T. Auligné, and R. N. Hoffman, *Application of feature calibration and alignment to high-resolution analysis: Examples using observations sensitive to cloud and water vapor*, [Monthly Weather Review](#) **142**, 686 (2014).
- K. A. Brewster, *Phase-correcting data assimilation and application to storm-scale numerical weather prediction. Part I: Method description and simulation testing*, [Monthly Weather Review](#) **131**, 480 (2003).
- W. G. Lawson and J. A. Hansen, *Alignment error models and ensemble-based data assimilation*, [Monthly Weather Review](#) **133**, 1687 (2005).
- S. Ravela, K. Emanuel, and D. McLaughlin, *Data assimilation by field alignment*, [Physica D: Nonlinear Phenomena](#) **230**, 127 (2007), data Assimilation.
- C. Keil and G. C. Craig, *A displacement-based error measure applied in a regional ensemble forecasting system*, [Monthly Weather Review](#) **135**, 3248 (2007).
- C. Keil and G. C. Craig, *A displacement and amplitude score employing an optical flow technique*, [Weather and Forecasting](#) **24**, 1297 (2009).
- C. Marzban and S. Sandgathe, *Optical flow for verification*, [Weather and Forecasting](#) **25**, 1479 (2010).
- C. Marzban, S. Sandgathe, H. Lyons, and N. Lederer, *Three spatial verification techniques: Cluster analysis, variogram, and optical flow*, [Weather and Forecasting](#) **24**, 1457 (2009).
- F. Han and I. Szunyogh, *A morphing-based technique for the verification of precipitation forecasts*, [Monthly Weather Review](#) **144**, 295 (2016).

- G. D. Alexander, J. A. Weinman, and J. L. Schols, *The use of digital warping of microwave integrated water vapor imagery to improve forecasts of marine extratropical cyclones*, *Monthly Weather Review* **126**, 1469 (1998).
- J. D. Beezley and J. Mandel, *Morphing ensemble Kalman filters*, *Tellus A* **60**, 131 (2008).
- J. Mandel, J. D. Beezley, K. Eben, P. Jirus, V. Y. Kondratenko, and J. Resler, *Data assimilation by morphing fast fourier transform ensemble Kalman filter for precipitation forecasts using radar images*, (2010) UCD/CCM Report 289.
- G. J. Huffman, D. T. Bolvin, D. Braithwaite, K. Hsu, R. Joyce, C. Kidd, E. J. Nelkin, S. Sorooshian, J. Tan, and P. Xie, *NASA Global Precipitation Measurement (GPM) Integrated Multi-satellite Retrievals for GPM (IMERG)*, Algorithm Theoretical Basis Document Version 5.2 (NASA GSFC, Greenbelt, MD 20771, USA, 2018) [Available online at [https://pmm.nasa.gov/sites/default/files/document\\_files/IMERG\\_ATBD\\_V5.2\\_0.pdf](https://pmm.nasa.gov/sites/default/files/document_files/IMERG_ATBD_V5.2_0.pdf).].
- N. van de Giesen, R. Hut, and J. Selker, *The Trans-African Hydro-Meteorological Observatory (TAHMO)*, *Wiley Interdisciplinary Reviews: Water* **1**, 341 (2014).
- Penalty-, barrier-, multiplier-, interior point-methods*, in *Optimization Theory* (Springer US, Boston, MA, 2004) pp. 153–172.
- Penalty and augmented lagrangian methods*, in *Numerical Optimization* (Springer New York, New York, NY, 2006) pp. 497–528.
- I. Soenario and R. Sluiter, *Optimization of rainfall Interpolation*, Tech. Rep. (Ministerie van Verkeer en Waterstaat, Koninklijk Nederlands Meteorologisch Instituut, De Bilt: KNMI, 2010) intern rapport.
- A. K. Dezfuli, C. M. Ichoku, G. J. Huffman, K. I. Mohr, J. S. Selker, N. van de Giesen, R. Hochreutener, and F. O. Annor, *Validation of IMERG precipitation in Africa*, *Journal of Hydrometeorology* **18**, 2817 (2017a).
- A. K. Dezfuli, C. M. Ichoku, K. I. Mohr, and G. J. Huffman, *Precipitation characteristics in West and East Africa from satellite and in situ observations*, *Journal of Hydrometeorology* **18**, 1799 (2017b).





# 4

## CORRECTING TIMING ERROR IN PRECIPITATION ESTIMATES USING IMAGE WARPING

*De regen die vandaag valt, valt morgen niet .*

Dutch proverb

*A rainfall event is a coherent moving system, and as such can be described by its intensity, its position and timing. Bias correction methods are generally focusing on the intensity. In the previous chapter, we investigated the possibility to gauge-adjust a rainfall estimate with respect to the position using a warping method. In this chapter, we focus on the possible timing errors. The warping method is adapted to work on time-series instead of rainfall fields. It is then applied to gauge-adjust a satellite-based estimate with respect to the timing of the rain event.*

## 4.1. INTRODUCTION

Timing errors have been studied in the field of hydrological modelling because of the large impact temporal patterns of rainfall can have on the models' outputs (Ball, 1994; Singh, 1997; Máca and Torfs, 2009). However, timing errors have not been studied much in terms of validation or comparison of rainfall estimates. There are some exceptions. For example, Pfeifroth *et al.* (2016) evaluated the capacity of several satellite-based estimates in reproducing the daily cycle at two sites in West Africa. They showed that the rainfall peaks (of the diurnal cycle) can be delayed by up to 2h.

There are several techniques to study timing differences between time series such as cross-correlation and dynamic time warping (DTW). Cross-correlation only allows for fixed time lags between time series. DTW is more flexible. It was developed for speech recognition (Velichko and Zagoruyko, 1970; Sakoe and Chiba, 1978), and is now used in many fields such as data mining, robotics, manufacturing or medicine (see Keogh and Pazzani for references). It also has been applied to precipitation in several studies. McIntosh and Yuan (2005) used DTW (with a combination of six indices) to compare rainfall events and select events that were similar. Lu *et al.* (2020) and Mantas *et al.* (2015) applied DTW in combination with a clustering method to classify time series into rainfall regimes. Mantas *et al.* (2015) used it in the framework of rainfall estimate validation, while the goal of Lu *et al.* (2020) was to derive precipitation estimates from cloud top temperature. Dilmli *et al.* (2020) developed a multi-scale DTW and used it as a dissimilarity measure. They applied it to yearly time series in Paris to study the impact of climate change on rainfall variability (Dilmli *et al.*, 2019).

The goal of this chapter is to investigate the use of time warping to correct temporal error. We apply warping to gauge-adjust a satellite-based estimate with respect to the timing. We use a different warping method than the above mentioned DTW. Instead, we adapt the spatial warping method from the previous chapter to operate with (1D) time series instead of (2D) rainfall fields. Using this method will allow us to compare more fairly the space and time warping. It also enables the possibility to combine them at a later stage in order to take both the position and timing error into account at the same time. Such space-time approach would permit to fully take into account the relationship between time and space. However, it would also be very computationally expensive. Thus, we first consider the time warping independently from the spatial warping as an intermediate step. We examine three alternative approaches with different assumptions on the spatial dimension. These approaches are warping in time only but take into account (or not) the spatial component.

Section 4.2 described the warping and automatic registration for time series. It includes three approaches with different assumption on the spatial relationship of the time series. The time warping is applied to two cases. The first case uses synthetic rainfall events represented by ellipses (Section 4.3). This case is also used to test the sensitivity of the method to several parameters (Section 4.3.3). The second case is a real rainfall event occurring in southern Ghana during the monsoon season (Section 4.4). The results of both cases are evaluated with respect to the intensity, the timing and the position of the event. Section 4.5 compares and discussed the two cases, before the conclusion in Section 4.6. In Section 4.7, we discuss some possible improvements and future works.

## 4.2. METHODOLOGY

### 4.2.1. DEFINITIONS

In the case of temporal warping, the signals  $u$  and  $v$  are representing time series on a domain  $D = [t_{min}, t_{max}] \subset \mathbb{R}$ . The warped signal is obtained by applying a mapping function  $T_t$  on the time coordinates:

$$u_{\text{warp}}(t) = u(t + T_t(t)) \quad (4.1)$$

In the remainder of this chapter, we adopt a more compact expression  $u \circ (I + T)$  for the application of a mapping  $T$  to a signal  $u$ , where  $\circ$  is the composition operator.

The mapping  $T$  is derived by a (1D-)registration method. The goal of the registration is to determine the temporal mapping  $T : t \in \mathbb{R} \mapsto T_t(t) \in \mathbb{R}$  such that,  $\forall (t) \in D$ ,

$$\begin{aligned} v(t) &\approx u \circ (I + T)(t) \\ &\approx u[t + T_t(t)] \end{aligned} \quad (4.2)$$

where  $I$  is the identity function.

There can be several mappings  $T$  that meet the requirement  $v \approx u \circ (I + T)$ . Especially in time periods without rainfall, the mapping  $T$  is not unique. We define two criteria to characterize one optimal mapping :

$$T \approx 0 \quad (4.3)$$

$$\nabla T \approx 0 \quad (4.4)$$

That is, the optimal mapping has to be as small, and as smooth as possible. These two criteria are similar to the first two criteria used for the spatial registration in Chapter 3. For the temporal cases, we do not have a divergent-free constraint as we had in the spatial one.

### 4.2.2. AUTOMATIC REGISTRATION

We are using a similar automatic registration method than the one used for the spatial warping in the previous chapter (see 3.2.2). We adapted it to the 1D data (i.e. time series) and the new constraints. The automatic registration procedure only needs the signals  $u$  and  $v$  as input. It does not require any manual selection of matching points or features. A downside of such method is that the input signals need to be similar enough for it to work.

The registration is based on the minimization of a cost function  $J$  with respect to the mapping  $T$ . The cost function can be divided in two terms. The first one ( $J_o$ ) represents the error between the displaced signal  $u \circ (I + T)$  and the target signal  $v$ . The second one ( $J_b$ ) is a background term that consists of the two criteria for “optimal” mapping given in Equations (4.3) and (4.4).

$$J(T) = J_o(T) + J_b(T) \quad (4.5)$$

$$J_o(T) = \|v - u \circ (I + T)\| \quad (4.6)$$

$$J_b(T) = C_1 \|T\| + C_2 \|\nabla T\| \quad (4.7)$$

where  $C_1$  and  $C_2$  are two coefficients determined empirically, and  $\|\cdot\|$  is the  $L^2$ -norm.

As for the spatial 2D-case, the minimization problem is solved iteratively, for  $T$  defined on increasingly fine grid. In the temporal 1D-case, the domain  $D$  is a segment  $[t_{min}, t_{max}]$ , and is represented by different regular grids. The regular  $n(= n_t)$  grid on which  $u$  and  $v$  are given is called the *pixel grid*  $D_n$ . The mapping  $T$  is defined on a set of coarser grids  $D_i$  ( $i = 1, \dots, I$ ), called *warping grids*. The grids  $D_i$  are uniform  $2^i + 1 = m_i$  grids (for  $i = 1, \dots, I$ ) covering the domain  $D$ . For  $i = 1, \dots, I$ , the mapping  $T$  discretized on  $D_i$  is noted  $T_i$ . Thus, the observation term  $J_o$  of the cost function is discretized on the pixel grid  $D_n$ , while the background term  $J_b$  is discretized on the warping grid  $D_i$ .

**Algorithm** The algorithm iterates over the warping grids  $D_i$  ( $i = 1, \dots, I$ ), from the coarsest 3-point grid  $D_1$ , until the finest one  $D_I$ . For each iteration, the three main steps are the same as for the spatial regulation algorithm (described in Section 3.2.2):

1. **Smoothing** of the images  $u$  and  $v$ : the images are smoothed by convolution with a 1D-Gaussian

$$G_{1D}(t) = \frac{1}{2\pi\sigma^2} \exp\left(-\frac{t^2}{2\sigma^2}\right),$$

where  $\sigma = 0.1/(2^{2i} + 1)$ . The finer the grid  $D_i$  is, the narrower the Gaussian is. Thus, for small  $i$ , the fine features are ignored and the focus is given to the large-scale ones. When  $i$  increases, more ever finer features are taken into account. This way,  $T_i$  for small  $i$  will make the larger features match. Then, for increasing  $i$ , more and more detailed images are matched.

After the smoothing, the two time series are normalized such that their maximum is the same. The time series obtained after smoothing and normalization are noted as  $\tilde{u}_i$  and  $\tilde{v}_i$ .

2. **Initialization**: solving the minimization problem on grid  $D_i$  requires a first guess  $T_i^{fg}$ . For  $i = 1$ ,  $T_1^{fg}$  is set to zeros, i.e. no deformation. For  $i = 2, \dots, I$ , the mapping  $T_{i-1}^*$  obtained by solving the minimization problem on grid  $D_{i-1}$  is interpolated onto the grid  $D_i$ , and used as the first guess  $T_i^{fg}$ .
3. **Optimization**: The actual minimization problem to be solved is based on the smoothed fields, i.e.  $J_o(T) = \|\tilde{v}_i - \tilde{u}_i \circ (I + T)\|$ . As for the spatial algorithm, it is solved for all the nodes at the same time. The minimization problem has some inequalities constraints. First, we want the mapping to be invertible, so we require that  $t_k + T(t_k) \leq t_{k+1} + T(t_{k+1})$ . Second, we require that all nodes stay in the domain  $D$ . We use the Sequential Least Squares Programming algorithm (SLSQP, from `scipy.optimize` package) to solve this constrained minimization problem.

The algorithm is illustrated in Figure 4.2.1. It is very similar to the one for the automatic spatial registration. The main difference is the method used to solve the minimization problem. Here, the number of nodes is much smaller than in the spatial case, so the constrained minimization problem is solved directly. In the spatial case, it was transformed to the unconstrained minimization of a penalized cost function.

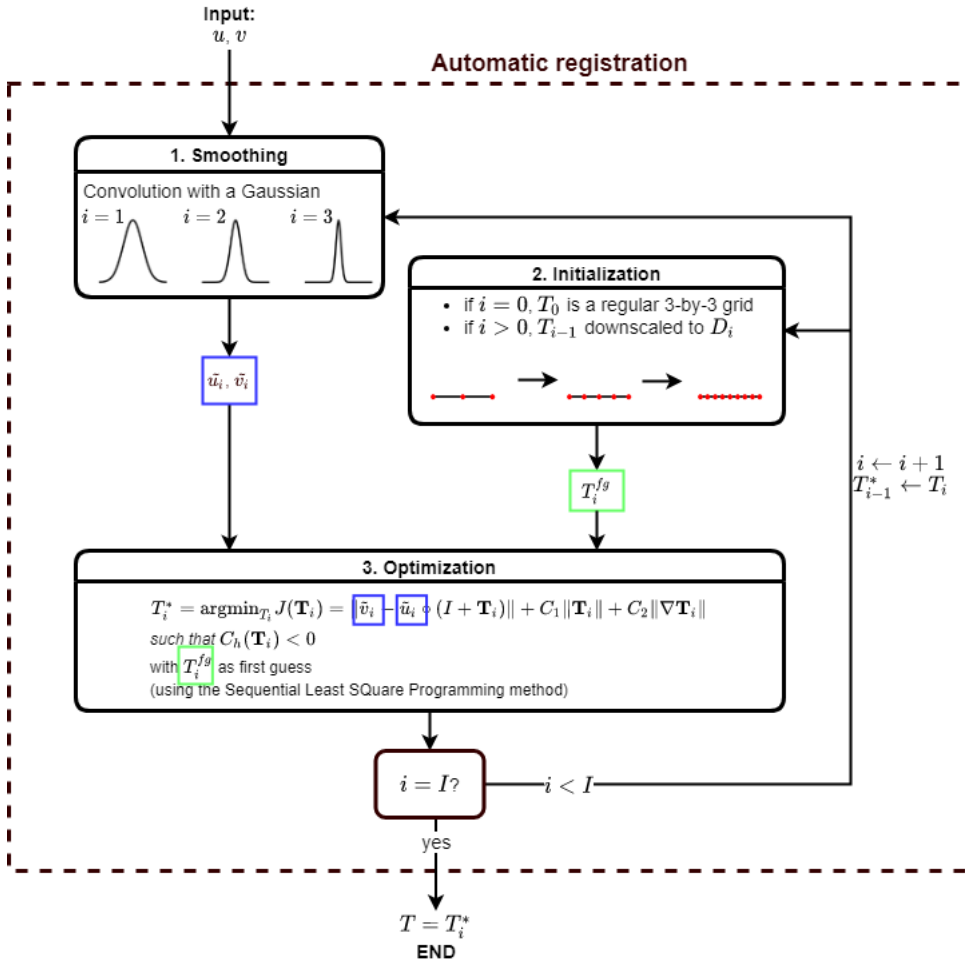


Figure 4.2.1: Algorithm for the automatic registration.

The python scripts for the automatic registration and the warping are available at [https://github.com/clecoz/time-warping\\_thesis](https://github.com/clecoz/time-warping_thesis). The scripts permit to reproduce the results and some of the plots for the two case studies presented in this chapter.

### 4.2.3. EXTENSION TO SPACE-TIME DATA

In practice, we have two time series  $u_j$  and  $v_j$  for each station  $j$  ( $j = 1, \dots, J$ ). We investigate three different approaches to take into account (or not) this spatial dimension.

#### APPROACH 1 (A1): DIFFERENT TIME MAPPINGS FOR EACH STATION INDEPENDENTLY

This approach only considers the temporal dimension, it does not take into account the spatial dimensions. A different mapping  $T^j$  is determined for each station  $j$  independently. That is, in the automatic registration, the minimization problem  $\min_{T_j} J^j(T_j)$  is

solved for each station  $j$  separately, with

$$J^j(T_j) = \|\tilde{v}_j - \tilde{u}_j \circ (I + T_j)\| + C_1 \|T_j\| + C_2 \|\nabla T_j\| \quad (4.8)$$

#### APPROACH 2 (A2): ONE UNIQUE TIME MAPPING FOR ALL STATIONS

In this approach, the mapping  $T$  is the same for all the stations. The observation term  $J_o$  in the cost function compares the time series of all the stations  $j$  at once, while the background term  $J_b$  is unchanged. The minimization problem only has to be solved once to find the unique mapping  $T$ .

The cost function can be written as

$$J(T) = \|V - U_T\| + C_1 \|T\| + C_2 \|\nabla T\| \quad (4.9)$$

where  $V$  and  $U_T$  are  $(n_t \times K)$  vectors containing the signals of the  $K$  stations

$$V = \begin{bmatrix} \tilde{v}_1 \\ \tilde{v}_2 \\ \dots \\ \tilde{v}_K \end{bmatrix} \quad U_T = \begin{bmatrix} \tilde{u}_1 \circ (I + T) \\ \tilde{u}_2 \circ (I + T) \\ \dots \\ \tilde{u}_K \circ (I + T) \end{bmatrix} \quad (4.10)$$

This approach is computationally the least expensive one. The number of variables to be optimized is the same as for one minimization problem for approach A1, but it only has to be solved once (while approach A1 needs to solve  $J$  problems).

#### APPROACH 3 (A3): DIFFERENT TIME MAPPINGS CORRELATED IN SPACE

This approach is a mix of the first two. We assume that each station  $j$  has a different mapping  $T_j$ , and that the mappings  $T_j$  are linked through space. Unlike approach A1, the mappings  $T_j$  are not independent, but have more degrees of freedom than in approach A2. All the mappings are found at once by solving one minimization problem. They are linked through a correlation matrix based on distance (derived from a variogram). This is done by adding an extra background term. The cost function is modified as follows:

$$J \left( \begin{bmatrix} T_1 \\ T_2 \\ \dots \\ T_K \end{bmatrix} \right) = \left\| \begin{bmatrix} \tilde{v}_1 - \tilde{u}_1 \circ (I + T_1) \\ \tilde{v}_2 - \tilde{u}_2 \circ (I + T_2) \\ \dots \\ \tilde{v}_K - \tilde{u}_K \circ (I + T_K) \end{bmatrix} \right\| + C_1 \left\| \begin{bmatrix} T_1 \\ T_2 \\ \dots \\ T_K \end{bmatrix} \right\| + C_2 \left\| \begin{bmatrix} \nabla T_1 \\ \nabla T_2 \\ \dots \\ \nabla T_K \end{bmatrix} \right\| \\ + c_s \sum_{j_1, j_2 \in J, j_1 \neq j_2} c(d_{j_1, j_2}) \|T_{j_1} - T_{j_2}\| \quad (4.11)$$

where  $d_{j_1, j_2}$  is the distance between the stations  $j_1$  and  $j_2$ . The influence function  $c$  determines the strength of the connection between the stations based on their distance. This strength is given on a scale of 0 to 1. The function is based on an exponential variogram with a range of 150km and no nugget. The spatial regulation coefficient  $c_s$  defines the weight of the spatial background term in the cost function.

The minimization problem is solved for all  $T_j$  at the same time, bringing to  $J \times i$  the number of variables to be optimized at step  $i$  (with  $i = 1, \dots, J$ ). Thus, this approach is the most computationally expensive one of the three approaches described here.

#### 4.2.4. WORK-FLOW

In practice, we want to adjust satellite based estimates using gauge measurements. The satellite estimates are given on a 2D-grid, and do not correspond to gauge locations. Thus, the first step is to *extract* the time series at the gauge locations from the series of rainfall fields given on this grid. Once we have the two time series for each station (one  $v$  from the gauge and one  $u$  from the satellite estimates), they are going through a *pre-processing* step which consists in resampling. The time series have a low resolution of 1 hour, they are resampled at a higher resolution of 6 minutes using linear interpolation. This has two advantages. First, by increasing the number of grid points, we are preventing extreme shrinking of the time interval (i.e. of the grid cells). Second, it prevents the warping to decrease the peak intensity artificially by sampling away from it. The resampled time series are used as input for the automatic registration.

The automatic registration provides the temporal mappings at the station locations. Our goal is to warp the full satellite estimates. That is, we want the temporal mapping for each node of the 2D-grid. They are obtained by kriging the mappings. We use the same exponential variogram as the one used for approach A3 (i.e. with a range of 150 km and no nugget). Then, the mappings are used to warp the (resampled) time series of each node. The kriging is not needed for approach A2, since it is assumed that the mapping is the same everywhere. The unique mapping obtained with this approach can directly be applied to all the time series.

The complete workflow of the method, from the time series extraction to warping, is summarized in Figure 4.2.2.

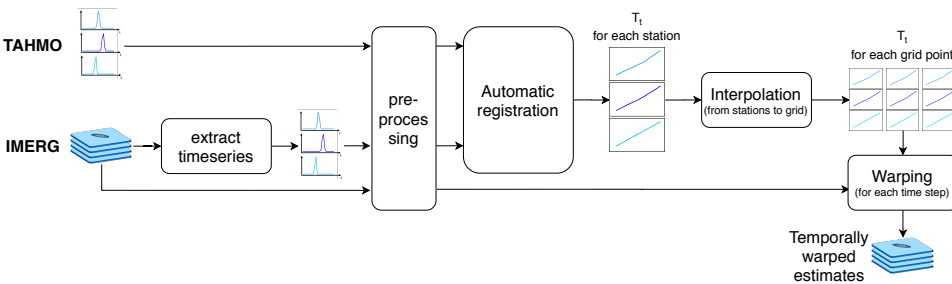


Figure 4.2.2: Flowchart of the temporal warping method.

## 4.3. SYNTHETIC CASE

### 4.3.1. STUDY CASE

The synthetic case was used to investigate the accuracy of the three automatic registration approaches. The synthetic case used in this chapter is the same as the one used for the spatial warping in the previous chapter (in Section 3.3). Here, we repeat the description of this case for the sake of readability and consistency.

The synthetic case was generated by 3D ellipses on a regular grid. The two input fields (the first guess and the target) both have one rainfall event moving toward the South-West, as can be seen in Figure 4.3.1. They have the same maximum of 50mm/h



for the rainfall peak, but different position, timing and path. This is done by giving the ellipses different positions and orientations. The peak of the rainfall events differ by  $\sim 50\text{km}$  and by 2 hours. They also differ by the propagation direction and speed. The event is moving at  $\sim 40\text{km/h}$  in the first guest and at  $\sim 47\text{km/h}$  in the target field.

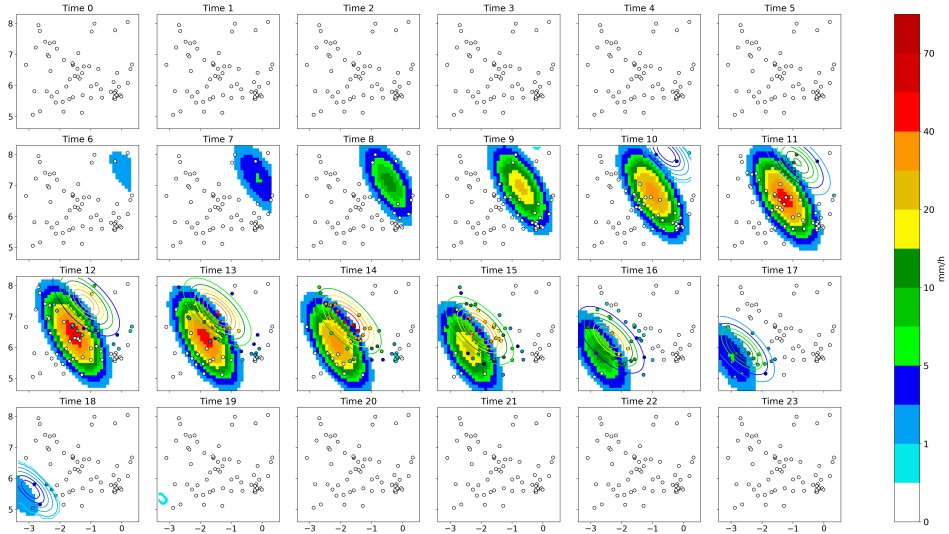


Figure 4.3.1: First guess  $u_{grid}$  (background) and true precipitation field  $v_{grid}$  (contour lines) for the synthetic case. The fictive station measurements  $v$  are represented by circles.

In a real case, the first guess would be a satellite-based estimate and the target field would be observations from radar or gauges, for example. When using gauge measurements, the “true” rainfall is only known at the station’s locations. We simulate this case by extracting time series from the “true” rainfall field. The locations of the fictive stations follow the configuration of the gauge network used in the Southern Ghana case (described in Section 4.4.1), and are represented by circles in Figure 4.3.1. These time series are used as input  $v$  in the automatic registration. We use linear interpolation to derive the rainfall values at the gauge locations. The same method is used to extract the time series  $u$  from the first guess before the pre-processing step (see Figure 4.2.2). We denote  $u_{grid}$  and  $v_{grid}$  the two input fields from which the time series  $u$  and  $v$  are extracted.

### 4.3.2. RESULTS

In this section, we will show the results obtained with the three approaches (described in 4.2.3). All the results are obtained with  $C_1 = 0.1$ ,  $C_2 = 1$  and  $c_s = 1$ , and with  $I = 3$  except when stated otherwise. The coefficients  $C_1$ ,  $C_2$  and  $c_s$  are set empirically in this section. The sensitivity of the results to these coefficients will be discussed in Section 4.3.3. The number of steps  $I$  can also be adjusted, its impact will also be examined in Section 4.3.3.

## MAPPING COMPARISON

The automatic registration provides a mapping  $T$  for each of the stations. Figure 4.3.2 shows the mappings for three of these stations, as well as the corresponding warped fields. The mappings for the other stations can be seen in Appendix 4.B. The mappings for the whole domain are obtained by kriging, and are displayed in Figure 4.3.3.

For all three approaches, the distortion is null at the last time step (Figure 4.3.2). This is due to the constraint that no node can leave the domain. The distortion  $T$  cannot be strictly negative at this time step without violating this constraint. Similarly the distortion cannot be strictly positive at time step 0 (see the southern Ghana case in 4.4.2). The distortion is smaller at the beginning of the time series, before the rainfall occurs. This is due to the first regulation term that ensures that the mapping is as “small” as possible. The distortion is the smallest with approach A1 and the largest with approach A2. This regulation term has the most impact with approach A1, since it is taking only one station at a time. The second regulation term ensures that the mappings are as smooth as possible. The mappings obtained with approaches A1 and A3 are almost identical at time steps with rainfall, which leads to similar warped fields (Figure 4.3.2). Approach A2 can differ significantly from approaches A1 and A3. This is due to its assumption that the mappings are constant in space. It cannot accommodate exactly the specificity of each station, but has to find a compromise.

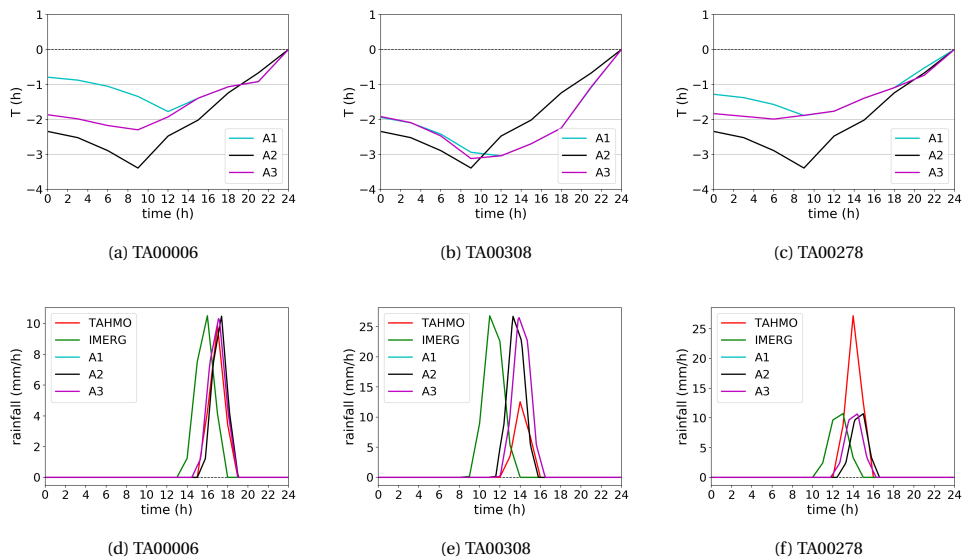


Figure 4.3.2: Mappings  $T$  (top) and corresponding warped signals (bottom) for the three approaches at three stations: (left) TA00006, (center) TA00308, and (right) TA00278.

The mappings provided by the automatic registration are kriged onto the 2D-grid. Figure 4.3.3 allows us to examine their spatial variation. Approach A2 gives a fully homogeneous mapping in space, while approach A1 is the most heterogeneous one. Approach A3 authorized variation in space (each station has its own mapping), while keeping some spatial consistency due to the spatial regulation term. This extra regulation term pre-

vents two stations next to each other to have too different mappings, as it happens with approach A1 (e.g. at time 9 in the lower right corner). This spatial variability has some impacts on the warped fields (shown in Appendix 4.C). The shape of the rainfall event is preserved with approach A2, since the same mapping is applied at all grid points. On the other hand, the shape of the event is modified with approach A1, especially at the beginning (time steps 8 to 11) and at its edge. This is due to the fact that the time series are not moved uniformly. The alteration of the event's shape still occurs with approach A3, but it is more limited.

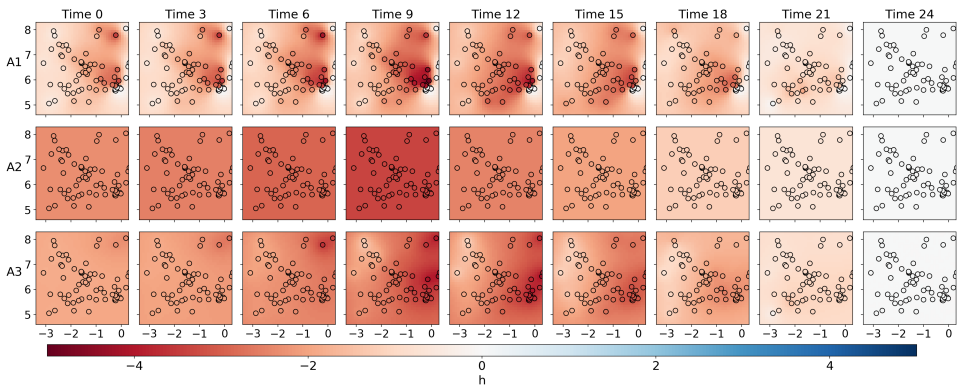


Figure 4.3.3: Mapping  $T$  for each node of the pixel grid (background) and at the station locations (circles) at the 9 times of the warping grid for the three approaches: (top) A1, (center) A2 and (bottom) A3. In red, the mapping is pushing the time series forward in time. In blue, the time series is pushed backward.

## VALIDATION

The goal of the temporal warping is to correct timing error between the first guess ( $u_{grid}$ ) and the true rainfall ( $v_{grid}$ ). The timing error for the synthetic case is shown in Figure 4.3.4. The timing error is defined as the time difference between the peaks in  $u_{grid}$  and  $v_{grid}$ , the peak being defined as the time step with the maximum rainfall. The peak in the field  $u_{grid}$  is early with respect to the truth  $v_{grid}$ . The delay between the two fields increases from none in the West to 4 hours in the East. All three methods improve significantly the timing error (Figure 4.3.5). Approach A3 yields the largest improvement, closely followed by A1. The results for approaches A1 and A3 are very similar, except in the East where the peak still occurs too early with approach A1. The timing at the two most eastern stations is not corrected with approach A1, the mapping is very small at these locations (see Fig. 4.3.3). This could be due to the very low rainfall intensity recorded at these stations (less than 1mm/h), and the regulation terms. When the rainfall intensity is very low, the observation term is small too, and the background term dominates the cost function. The timing correction with approach A2 is still important but more limited. The rainfall is still early in the East, and is now slightly late on the West. By construction, the timing error is not the same over the whole domain (Fig. 4.3.4), while the mapping is with approach A2. Thus, the mapping moves the time series too much in the West and not enough in the East.

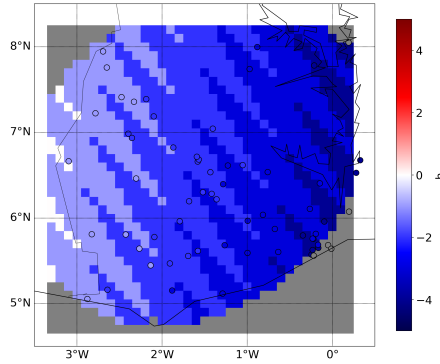


Figure 4.3.4: Time delay before time warping at each pixel of the domain. In red, the peak in  $u_{grid}$  is late (compared to the one in the “truth”  $v_{grid}$ ). In blue, the peak in  $u_{grid}$  is in advance. In grey, one of the time series does not have a peak (rainfall < 0.1mm/h).

4

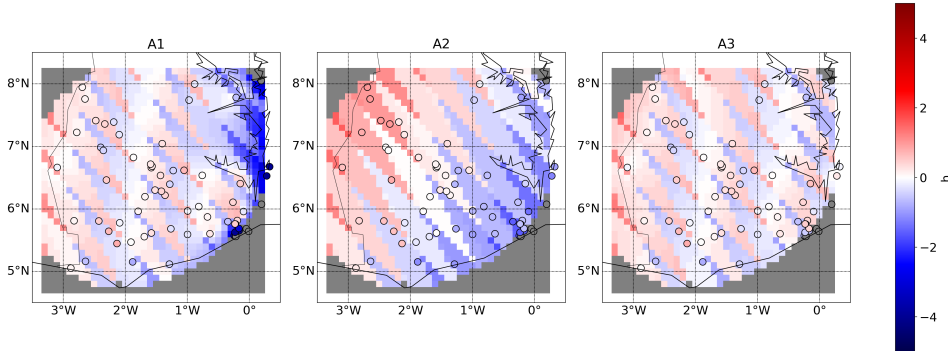


Figure 4.3.5: Time delay after time warping at each pixel of the domain. In red, the peak in  $u$  is late (compared to the one in the target field  $v$ ). In blue, the peak in  $u$  is in advance. In grey, one of the time series does not have a peak (rainfall < 0.1mm/h).

The time correction is evaluated more quantitatively in Table 4.3.1, which provides the average absolute timing error before and after warping. The average error is given for different rainfall thresholds. All three approaches decrease significantly the average error. The decrease is more important for the higher thresholds. When considering all pixels with at least 0.1mm/h rain, the timing error is divided by at least four. The error is divided by 5 or 6 for a threshold of 20mm/h, and by almost 10 for the threshold of 40mm/h. Approaches A1 and A3 gives similar results, except for the lowest threshold (1mm/h) for which the error is smaller for A3. This is linked to the remaining delay in the East observed in Figure 4.3.5. The error is larger for approach A2. However, the difference between the approaches decreases when the threshold increases. The error is the same for all approaches for the higher threshold (40mm/h). The larger errors for approach A2

was to be expected since the same mapping is applied at all pixels, while the timing error varies in space.

Table 4.3.1: Average absolute timing error before and after time warping. The average is done over all pixels recording at least one time step with more rainfall than a certain threshold according to  $v$  (and with non-zero rainfall according to  $u$ ).

Threshold (peak)	Sample number	Before	After		
			A1	A2	A3
>1mm/h	1128	2.21	0.48	0.52	0.35
>10mm/h	565	2.07	0.33	0.42	0.32
>20mm/h	315	2.07	0.33	0.37	0.33
>40mm/h	55	2.05	0.21	0.20	0.21

The warping does not modify the intensity of the rainfall but impacts it indirectly by removing the double-penalty part of the error. Table 4.3.2 gives quantitative measures of the error before and after the warping. For all approaches, both the RMSE and the MAE are reduced by the warping. The MAE is divided by 3, while the RMSE is divided by at least 2.5. The correlation is also greatly improved by the warping, it goes from 0.18 before to 0.86 (A2) or 0.89 (A1 and A3). Approaches A1 and A3 have similar statistics, with A3 being slightly better in terms of RMSE and MAE. Approach A2 has slightly higher RMSE and MAE and a lower correlation. However, the differences between the approaches remain very small.

Table 4.3.2: Statistics before and after temporal warping compared to the “truth”  $v$ , for the three approaches (A1, A2 and A3). The statistics are computed over the whole domain and all time steps.

	Before	After		
		A1	A2	A3
RMSE (mm/h)	5.21	1.86	2.03	1.82
MAE (mm/h)	1.62	0.52	0.54	0.50
Correlation	0.18	0.89	0.86	0.89

#### POSITION ERROR

The synthetic case has been built with both a timing and a position error between the fields  $u_{grid}$  and  $v_{grid}$ . Part of the position error can be interpreted as timing error and vice-versa. Thus, we also examine the impact of the temporal warping on the position error.

Figure 4.3.6 shows the position error at each time step (with non-zero rainfall). The position error is defined as the distance between the rainfall peaks in the first guess and the truth, the peak being the pixel with the maximum rainfall at a given time. All three approaches decrease the position error, with the exception of approach A1 between time 9 and 10. Very few stations are detecting rainfall at these times. The mapping obtained with approach A1 is thus spatially heterogeneous at these time distorting unnaturally the fields (see Fig. 4.C.1). After time 11, approach A1 and A3 have similar position error which is slightly lower than the one of A2 between times 11 and 13, and larger after

time 15. At the beginning of the rainfall event (times 9 and 10) very few stations are detecting rainfall in  $v$ , and at its end (times 17 and 18) very few stations has rainfall in  $u$ . The assumptions of approaches A2 and A3 are enforcing spatial consistency, which prevents unnatural distortions as observed with approach A1.

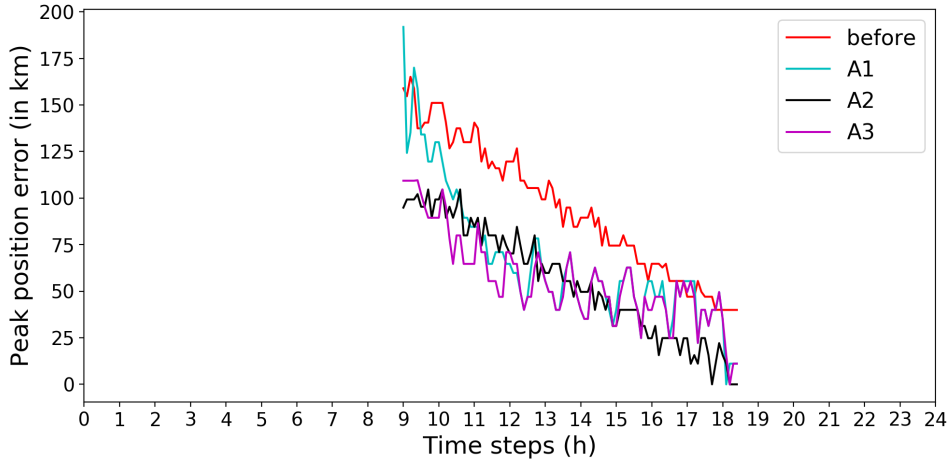


Figure 4.3.6: Distance between the “true” peak ( $v$ ) and the estimated ones before and after time warping at each time step with more than 0.1mm/h recorded rainfall.

Table 4.3.3 gives the average position error for different thresholds. All approaches improve the position error by at least 30km. Approaches A2 and A3 have similar errors for all thresholds, while approach A1 has slightly higher errors. The error differences between the approaches is more important for the lowest threshold (1mm/h), and then decrease when the threshold increases. All three approaches have similar position errors for the highest threshold (40mm/h). As for the timing error, but in a lesser way, the position error decreases when the threshold increases. The position error goes from 62.9km for threshold 1mm/h to 46.9km for threshold 40mm/h with approach A1.

Table 4.3.3: Average position error (in km) before and after time warping. The average is done over all time steps at which the rainfall peak (in the target field  $v$ ) is above a certain threshold.

Threshold	Sample number	After			
		Before	A1	A2	A3
>1mm/h	109	95.26	62.91	53.23	54.49
>10mm/h	65	89.65	55.56	51.72	51.62
>20mm/h	47	89.53	52.96	51.56	50.36
>40mm/h	11	89.57	46.86	49.52	46.08

### 4.3.3. SENSITIVITY

In this section, we examine the sensitivity of the automatic registration to several parameters, such as the number of steps  $I$  and the regulation coefficients  $C_1$  and  $C_2$ . For ap-

proach A3, we also investigated two other parameters that are specific to this approach: the regulation coefficient  $c_s$  and the variogram's range. After the automatic registration, the time mappings at the station locations are kriged into the regular 2D-grid. The impact of this step on the warped field is also evaluated below by modifying the range of the variogram used for the kriging.

#### NUMBER OF STEPS $I$

In this section, we investigate the impact of the number of steps  $I$  on the mapping performance. The mappings obtained with the different  $I$  are kriged in order to warp the estimate over the entire domain. The warped fields were then compared to the gridded "truth" ( $v_{grid}$ ) with respect to the rainfall timing and intensity.

Table 4.3.5 gives the average timing error of the rainfall peak for different numbers of steps  $I$ . Observations made for  $I = 3$  (see Table 4.3.1) are holding for  $I = 1$  and  $I = 2$ . That is, approaches A1 and A3 have similar timing error, except for the lowest threshold. Approach A2 has larger errors than A1 and A3, for all thresholds but the highest one. As observed previously, the timing error decreases when the threshold increases. The timing error is already greatly reduced with  $I = 1$ . Increasing  $I$  does not necessarily improve the timing error. For approach A2, the timing error is slightly lower with  $I = 1$ , except for the highest threshold. For approach A3, the smallest timing error is reached with  $I = 3$  for the lowest and highest threshold, while the error is the same for all  $I$  for the two other thresholds. In general, the error differences with respect to the number of steps are very small and not really significant. The largest impact of  $I$  is observed for the lowest threshold, for which the error differences are still under 0.1h (i.e. 6min which is the temporal resolution of the resampled time series).

Table 4.3.4: Average timing error (in h) after temporal warping for different numbers of steps  $I$ . The timing error is averaged over all pixels with more rainfall than a certain threshold.

Threshold		Before	A1	A2	A3
>1mm/h	I=3	2.21	0.48	0.52	0.35
	I=2	2.21	0.51	0.60	0.37
	I=1	2.21	0.47	0.59	0.40
>10mm/h	I=3	2.07	0.33	0.42	0.32
	I=2	2.07	0.34	0.45	0.33
	I=1	2.07	0.31	0.43	0.32
>20mm/h	I=3	2.07	0.33	0.37	0.33
	I=2	2.07	0.34	0.37	0.33
	I=1	2.07	0.31	0.37	0.33
>40mm/h	I=3	2.05	0.21	0.20	0.21
	I=2	2.05	0.21	0.17	0.22
	I=1	2.05	0.24	0.19	0.25

Table 4.3.5 shows the impact of the numbers of steps  $I$  on several statistics. As for the timing error, there are more differences between the approaches than with respect to  $I$ . The RMSE and the MAE are the largest with  $I = 2$ , and the lowest with  $I = 1$  for approaches A1 and A3. The smallest RMSE and MAE are reached with  $I = 2$  for approach

A2. The correlation is not sensitive to  $I$ , and remains the same for all  $I$  for the three approaches. The resolution of the mapping seems to have little impact on the warped fields.

Table 4.3.5: Statistics before and after time warping for different numbers of steps  $I$ . The statistics are computed over all the domain and all time steps.

Threshold		Before	A1	A2	A3
RMSE (mm/h)	I=3	5.21	1.86	2.03	1.82
	I=2	5.21	1.94	2.18	1.90
	I=1	5.21	1.78	2.06	1.80
MAE (mm/h)	I=3	1.62	0.52	0.54	0.50
	I=2	1.62	0.56	0.61	0.54
	I=1	1.62	0.49	0.57	0.48
Correlation	I=3	0.18	0.89	0.86	0.89
	I=2	0.18	0.89	0.85	0.89
	I=1	0.18	0.89	0.86	0.89

### REGULATION COEFFICIENTS

The automatic registration is based on the minimization of the cost function  $J$ , which is composed of an observation term and a background term. The background term  $J_b$  consists of criteria defining the ‘optimal’ mapping  $T$ . The three approaches have the same two criteria concerning the magnitude (Equation (4.3)) and the smoothness (Equation (4.4)) of  $T$ . Approach A3 has a third criterion introducing spatial consistency. These three criteria can be tuned with the regulation coefficients  $C_1$ ,  $C_2$  and  $c_s$ , respectively. In this section, we look at the influence of the two common coefficients ( $C_1$  and  $C_2$ ) on the automatic registration. The impact of the third criterion is specific to approach A3 and will be investigate separately.

In the result section above, we empirically set the coefficients to  $C_1 = 0.1$  and  $C_2 = 1$ . Here, we consider three more cases, summarized in Table 4.3.6. We first look at the impact of the individual coefficients, setting the other one to zero. Then, we examine the influence of their intensity by multiplying them by five. The only difference between the results shown here and the ones in Section 4.3.2 are the regulation coefficients.

Table 4.3.6: Summary of the four cases used in the sensitivity study of the regulation coefficients.

	Original	Only $C_1$	Only $C_2$	All coeff. x5
$C_1$	0.1	0.1	0	0.5
$C_2$	1	0	1	5
$c_s$ (only for A3)	1	1	1	5

The mappings obtained for the three sensitivity cases are compared to the original one in Figures 4.3.7, 4.3.8 and 4.3.9 for approaches A1, A2 and A3 respectively. For approaches A1 and A2, each station has a different mapping. For brevity, we are only showing the mappings for two stations. The station TA00282 has very low rainfall values (3mm/h according to IMERG and less than 1mm/h recorded by TAHMO), while the



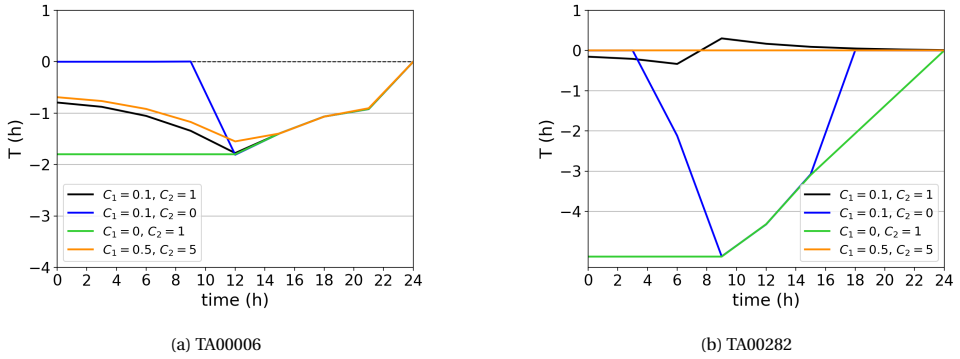


Figure 4.3.7: Mappings  $T$  obtained with approach A1 for the four sensitivity cases compared to the original one at two stations.

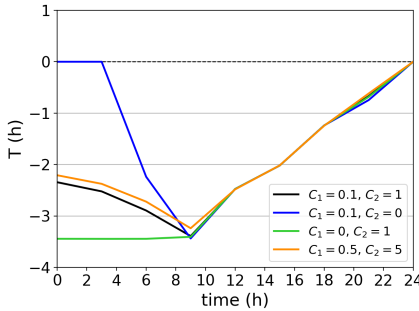


Figure 4.3.8: Mappings  $T$  obtained with approach A2 for the four sensitivity cases compared to the original.

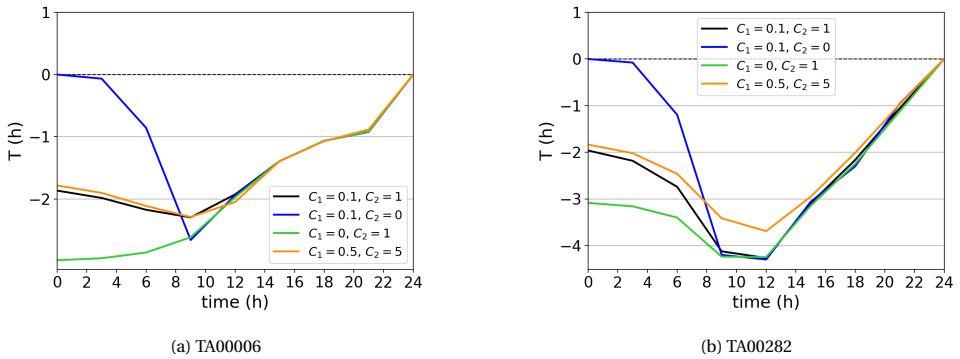


Figure 4.3.9: Mappings  $T$  obtained with approach A3 for the four sensitivity cases compared to the original one at two stations.

station TA00006 records a rainfall peak at 10mm/h. The second one is representative of most of the stations (in this specific case), the first one is used to illustrate the case of

stations with little rainfall. The mappings from the sensitivity cases are very similar to the original one at the rainy times. Noticeable differences during the rainy events occur only at stations with low rainfall such as station TA00282 (Figures 4.3.7b and 4.3.9b). For these stations, the background term starts dominating the cost function when all regulation coefficients are multiplied by five. For approach A3, the distortion is smaller and the time series is not moved as far as it should be. For approach A1, the distortion is already very small in the original case. Increasing the coefficients makes the distortion even smaller. The distortion is more important when only one of the coefficients is non-null. In these cases where  $C_1 = 0$  or  $C_2 = 0$ , the background term is smaller, and so the observation term has relatively more weight in the cost function. For stations recording higher rainfall values, the mappings are similar during the rainy times (Figures 4.3.7a, 4.3.8 and 4.3.9a). The main differences occur before the rainfall event. Multiplying all the coefficients by five has a very limited impact on the mappings. In the sensitivity case with only the magnitude constraint, the distortion is going to zero away from rainfall times. On the contrary, the distortion is larger at the beginning of the time series in the case with only the smoothness constraint than in the original one. Without the magnitude constraint to compensate, the distortion before the rainfall event is similar to the one during the event in order to make the mapping as “smooth” as possible. This is not observed after the event because of the constraint on the boundary that no nodes can leave the time window. That is, this constraint ensures that the mapping cannot be strictly negative at the end of the time period or strictly positive at the beginning.

Table 4.3.7: Average timing error (in h) after time warping for different regulation coefficients  $C_1$  and  $C_2$ . The timing error is averaged over all pixels with more rainfall than a certain threshold.

		Original	Only $C_1$	Only $C_2$	All coeff. x5
A1	<b>Threshold</b>				
	>1mm/h	0.53	0.44	0.44	0.56
	>10mm/h	0.37	0.36	0.36	0.37
	>20mm/h	0.34	0.34	0.34	0.34
	>40mm/h	0.19	0.19	0.19	0.20
A2	<b>Threshold</b>				
	>1mm/h	0.52	0.52	0.52	0.52
	>10mm/h	0.42	0.42	0.42	0.43
	>20mm/h	0.37	0.37	0.37	0.37
	>40mm/h	0.20	0.20	0.20	0.20
A3	<b>Threshold</b>				
	>1mm/h	0.41	0.40	0.41	0.41
	>10mm/h	0.36	0.36	0.36	0.36
	>20mm/h	0.34	0.35	0.35	0.34
	>40mm/h	0.21	0.21	0.21	0.20

We also examine the impact of the regulation coefficients on the warped fields through the average timing error (Table 4.3.7) and the continuous statistics (Table 4.3.8). The timing errors are similar in the four cases for all thresholds. An exception is observed for the lowest threshold with approach A1. The timing error is lower when only one of

Table 4.3.8: Statistics after time warping for different regulation coefficients  $C_1$  and  $C_2$ . The statistics are computed over all the domain and all time steps.

		Original	Only $C_1$	Only $C_2$	All coeff. x5
A1	RMSE	1.94	1.89	1.88	1.96
	MAE	0.56	0.53	0.53	0.56
	Correlation	0.88	0.89	0.89	0.88
A2	RMSE	2.03	2.03	2.03	2.04
	MAE	0.54	0.54	0.54	0.54
	Correlation	0.86	0.86	0.86	0.86
A3	RMSE	1.88	1.88	1.88	1.88
	MAE	0.52	0.52	0.52	0.53
	Correlation	0.89	0.89	0.89	0.89

the regulation coefficient is non-zero, and is slightly larger when all the coefficients are multiplied by five. The impact of the coefficients on the continuous statistics is also limited. The RMSE, MAE and correlation remain the same in the four cases for approaches A2 and A3. Small variations can be observed for approach A1. The three statistics are slightly better for the cases with only one regulation term.

To summarize, the two regulation terms mainly affect the mapping at the times with no or little rainfall. This is reflected in the small influence they have on the warped fields both in terms of timing error and in terms of continuous statistics. Approach A1 is more sensitive to the coefficients than the two other approaches, especially for the lower rainfall values (see the timing error for the lowest threshold).

#### SPATIAL REGULATION TERM FOR APPROACH A3

Approach A3 assumes that each station has a different mapping and that the mappings are linked through space. This is implemented through an extra regulation term in the cost function (see Eq.(4.11)). This spatial regulation term can be tuned with the coefficient  $c_s$  or with the range of the variogram. The coefficient  $c_s$  determines weight of the spatial regulation term in the cost function with respect to the others. The range determine the distance at which stations can influence each other. The strength of the influence decays with the distance (according to a decay function  $c$ , see 4.2.3).

**Spatial regulation coefficient  $c_s$ :** In the results above, the coefficient has been set empirically to  $c_s = 1$ . We now consider three more cases  $c_s = 0.1$ ,  $c_s = 10$  and  $c_s = 100$ .

We first investigate the influence of the coefficient  $c_s$  on the mappings. Figure 4.3.10 shows the mapping corresponding to these four cases at four stations. The first two stations (TA00004 and TA00047) are located near other stations, while the two others (TA00266 and TA00015) are more isolated and located toward the edge of the domain. The positions of all the stations mentioned in this chapter including these four are indicated in Figure 4.A.1. Except for the highest coefficient  $c_s = 100$ , the mappings are almost identical during the rain. Most differences are observed before. The mapping obtained for  $c_s = 0.1$  is the one closest to the mapping from approach A1. The difference between approaches A1 and A3 increases when the coefficient increases. The exception is station

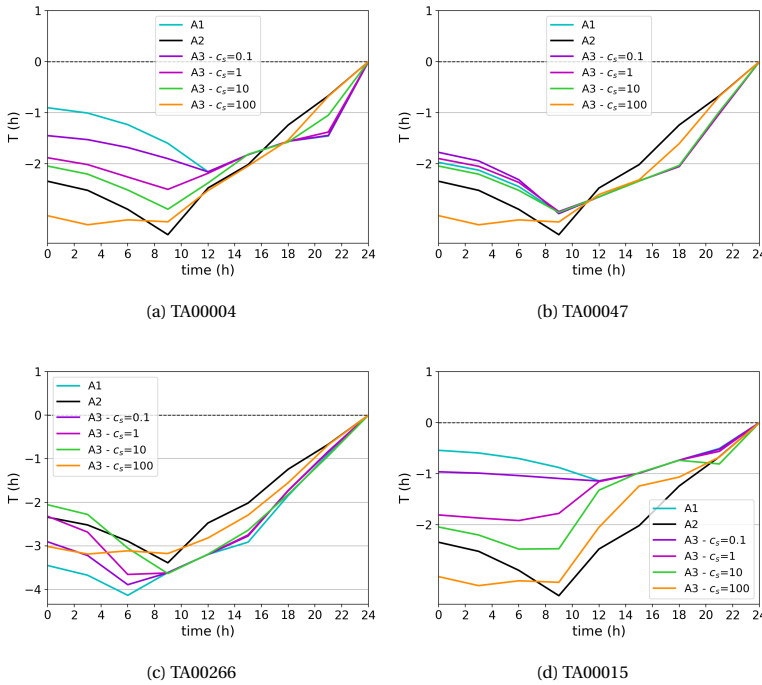


Figure 4.3.10: Mappings  $T$  obtained with Approach A3 for four different spatial regulation coefficients  $c_s$  at four stations. For comparison the mappings obtained with approaches A1 and A2 are displayed too.

TA00047. At this station, the mappings obtained with the three lowest coefficients are close to each other. That can be explained by the high amount of rainfall recorded at this station (with a maximum of  $\sim 30\text{mm/h}$ ), making the observation term dominating the cost function. The mappings obtained with  $c_s = 100$  are different than the ones obtained with the other coefficients and the one of approach A1. They are similar at the four stations during the non-rainy time, but differ during the event (more strongly at station TA00015). These mappings are also different from the one of approach A2. The mappings are not converging to this “unique” mapping because of the limited radius of influence controlled by the range. Still, because of the large range (150km), most stations are linked even if only by a small coefficient.

Table 4.3.9: Average timing error (in h) after time warping for three different spatial regulation coefficients  $c_s$ . The timing errors are computed over all pixels with rainfall above a certain threshold at least one time step.

threshold	before	$c_s=0.1$	$c_s=1$	$c_s=10$	$c_s=100$
$>1\text{mm/h}$	2.21	0.35	0.35	0.35	0.44
$>10\text{mm/h}$	2.07	0.32	0.32	0.32	0.35
$>20\text{mm/h}$	2.07	0.33	0.33	0.33	0.34
$>40\text{mm/h}$	2.05	0.21	0.21	0.21	0.21

Table 4.3.10: Statistics before and after time warping for four different spatial regulation coefficients  $c_s$ . The statistics are computed over the full the domain and all time steps

	before	$c_s=0.1$	$c_s=1$	$c_s=10$	$c_s=100$
RMSE	5.21	1.82	1.82	1.83	1.88
MAE	1.62	0.50	0.50	0.50	0.51
Correlation	0.18	0.89	0.89	0.89	0.89

The impact of the coefficient  $c_s$  on the warped field is limited. We saw above that the mappings are almost identical during the rain, except for  $c_s = 100$ . The impact of the spatial regulation coefficient  $c_s$  on the warped fields is examined through the average timing error (Table 4.3.9) and continuous statistics (Table 4.3.10). The impact of  $c_s$  on the peak timing is limited. The results are similar for the three lower values of  $c_s$  for all thresholds. Some differences can be observed for the highest coefficient  $c_s = 100$ , mostly for the lower thresholds. For  $c_s = 100$ , the average timing error is 0.09h larger for the lowest threshold of 1mm/h, and 0.03h larger for the 10mm/h threshold. The average timing errors are the same for all  $c_s$  for the highest threshold (40mm/h). Thus, for any threshold, the timing error varies by less than 0.1h, which is the temporal resolution after resampling, even for the lowest threshold. Similarly, the continuous statistics show little sensitivity to  $c_s$ . The correlations are the same for all  $c_s$ . The MAE only varies by 0.01mm/h for  $c_s = 100$ . The RMSE is equal to 1.82mm/h for both  $c_s = 0.1$  and  $c_s = 1$ , and increases by 0.01mm/h and 0.06mm/h for  $c_s = 10$  and  $c_s = 100$  respectively.

As for the two other regulation terms, the spatial one mainly affects times with no or little rainfall. A very high value of  $c_s$  is needed in order to influence period with rain (e.g.  $c_s = 100$ ). Thus, the impact on the warped signal is limited. Only the lower precipitation values are impacted, and only for the higher coefficients  $c_s$ .

**Range** All the previous results have been obtained with a range of 150km. We now consider three other possible ranges: 10km, 50km and 300km. The four corresponding influence functions are shown in Figure 4.3.11.

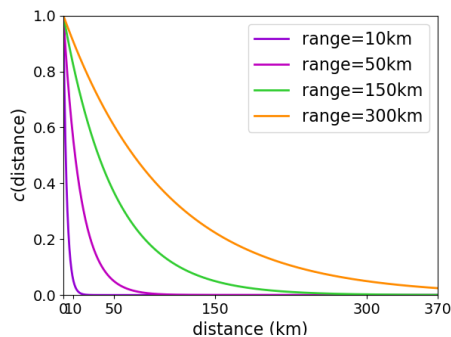


Figure 4.3.11: Influence function  $c$  for four different ranges: 10km, 50km, 150km and 300km.

Figure 4.3.12 shows the mapping obtained with these four range at four stations (the same as in Fig. 4.3.10). The mappings are similar during periods with rain. This can be explained by the choice of the coefficient  $c_s$ . We saw above that a very large coefficient is needed in order to impact the rainy times. However, differences are observed before and after the rain event. The mappings obtained with the 10km range are the one closer to the mappings from approach A1, at most stations. The mappings are moving away from the ones of approach A1 when the range increases. When the range increases, the links between the stations are becoming stronger (i.e. the influence coefficient increases), and new links appear with stations that were too far before. This is not observed at station TA00047, at which the four mappings are close to each other and to the one of approach A1. The small impact of the range on the mappings can be explained by the high rainfall values recorded by this station. The observation term is then dominating the cost function, and the background term has a comparatively small influence. At stations TA00266 and TA00015, there is little difference between the 10km and the 50km range. This is due to the isolated location of these stations (see Fig. 4.A.1). For the two lower ranges, no stations are close enough to influence them. On the contrary, station TA00004 is located near several other stations. The mappings obtained with the 10km and 50km are clearly distinguishable.

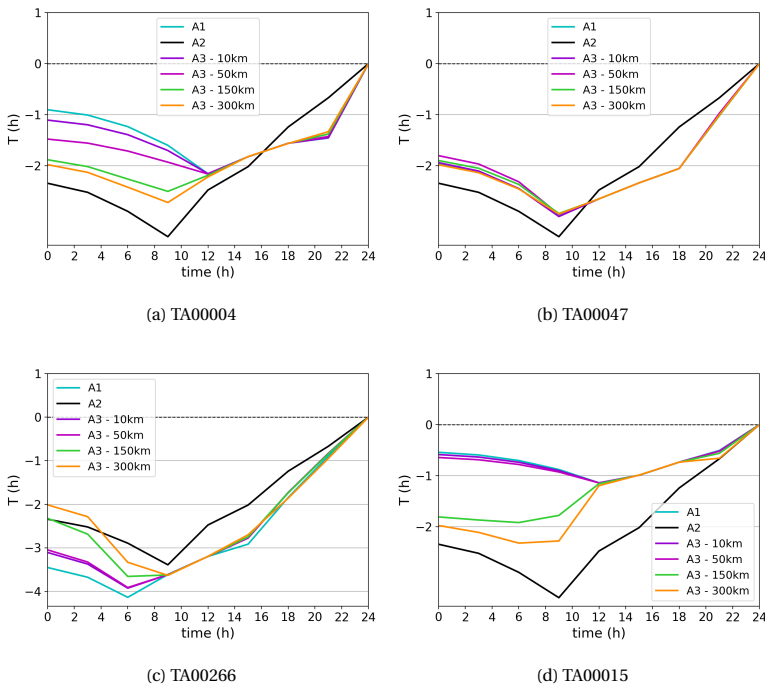


Figure 4.3.12: Mappings  $T$ , at four stations, obtained with Approach 3 for four different range. For comparison the mappings obtained with approaches A1 and A2 are displayed too.

The mappings at the station locations are kriged to obtained the mappings for the 2D-grid. Previously, for consistency, the kriging used the same variogram as the influ-

ence function in approach A3. The variogram depends on the range. In Figure 4.3.13, one can see the kriged mappings of the 2D-grid when a range of 150km is used for the kriging of the four cases. Figure 4.3.14 shows the kriged mappings of the same four cases when the range used in the warping is the same as the range of the influence function. When the range of 150km is used for the kriging, the kriged mappings of the four cases are similar. The kriging tends to smooth the differences. The case with the 10km range is the one showing most variation. The most noticeable one is due to a station near the eastern boundary which has a null mapping only for this case. The kriged mappings for the 150km and 300km ranges are very similar. On the other hand, there are more spatial variations between the four cases when the range is the same both in the spatial regulation term and in the kriging (see Fig. 4.3.14). One can see that the influence of the stations spread further when the range increases. For the 10km range, the influence radius of the stations is very limited; the mappings are the same at most grid nodes. For the 50km range, the individual stations starts to influence their surrounding, even if this influence remains very localized. The kriged mappings seem very similar for the 150km and 300km ranges, probably due to the large dimension of these ranges compared to the length/width of the domain (that is  $3.7^\circ \sim 370\text{km}$ ).

4

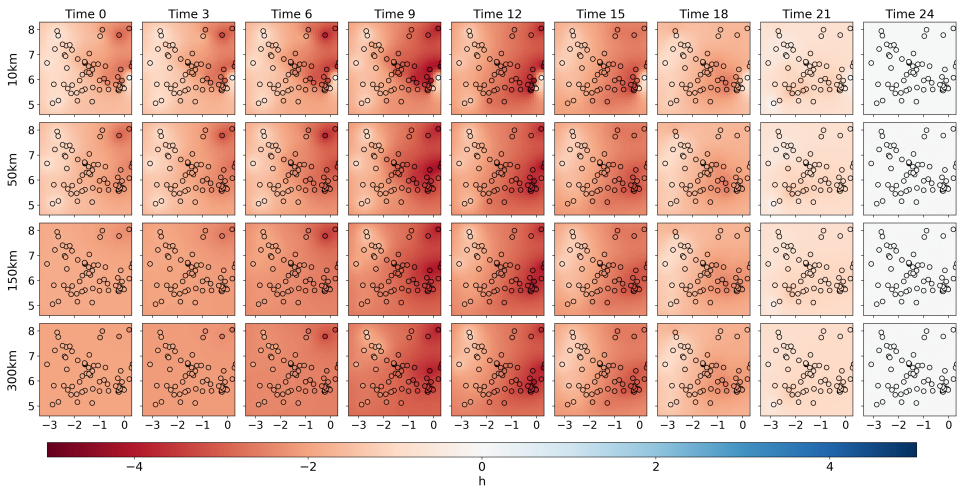


Figure 4.3.13: Mapping  $T$  for each node of the 2D-grid (background) and at the station locations (circles) at the 9 times of the warping grid. The mappings are shown for approach A3 using four different ranges: 10km, 50km, 150km and 300km from (top) to (bottom). In red, the mapping is pushing the time series forward in time. In blue, the time series is pushed backward.

We also examine the impact of the range on the warped fields. When the range of 150km is kept for the kriging of the four cases, the range of the influence function has a very limited impact on the warped fields. The average timing errors and the continuous statistics are the same in the four cases (up to the second decimal), and so are not shown here. The only exception is the correlation which is 0.01 higher for the 10km range. The range has more impact when the same one is used for the influence function and the kriging. This is seen in the average timing errors (Table 4.3.11) and in the continuous

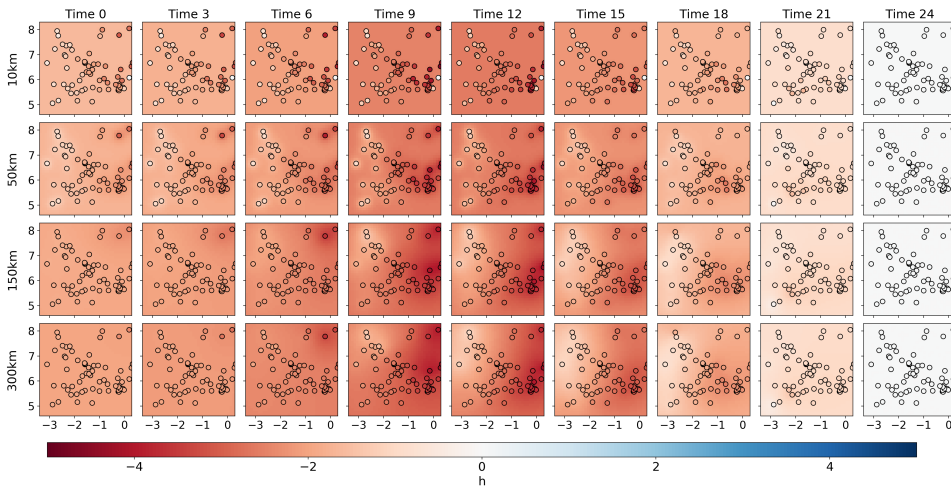


Figure 4.3.14: Mapping  $T$  for each node of the 2D-grid (background) and at the station locations (circles) at the 9 times of the warping grid. The mappings are shown for approach A3 using four different ranges in both the cost function and the kriging: 10km, 50km, 150km and 300km from (top) to (bottom). In red, the mapping is pushing the time series forward in time. In blue, the time series is pushed backward.

statistics (Table 4.3.12). As observed in Figure 4.3.14, the 150km and 300km ranges give similar results: the average timing errors vary by 0.03h or less, and the RMSE and MAE differ by 0.01mm/h (the correlation by 0.01). Both the timing errors and the statistics improve when the range increases. For all thresholds, the 10km range has the largest error, while the 300km range has the lowest ones (except for the 40mm/h threshold). The error variation between the four cases decreases when the threshold increases. For the lowest threshold (1mm/h), there is a 0.30h error difference between the 10km and the 300km cases, and a 0.16h difference between the 50km and the 300km cases. The difference is reduced to 0.11h and 0.02h for the highest threshold (40mm/h) for the 10km and 50km cases respectively. Similarly, the RMSE and the MAE are the largest and the correlation the lowest for the range of 10km, while the ranges of 150km and 300km have the best statistics.

Table 4.3.11: Average timing error (in h) before and after time warping for approach A3 with four different ranges (in both the influence function and the kriging). The timing error is averaged over all pixels with more rainfall than a certain threshold.

Threshold	Before	10km	50km	150km	300km
>1mm/h	2.21	0.62	0.48	0.35	0.32
>10mm/h	2.07	0.50	0.41	0.32	0.30
>20mm/h	2.07	0.45	0.37	0.33	0.32
>40mm/h	2.05	0.33	0.24	0.21	0.22

To summarize, the range impacts the outputs of the automatic registration, that is the mappings at the locations of the stations. It only influences the times with no or little



Table 4.3.12: Statistics before and after time warping for approach A3 with four different ranges (in both the influence function and the kriging). The statistics are computed over all the domain and all time steps.

	Before	10km	50km	150km	300km
RMSE (mm/h)	5.21	2.16	1.97	1.82	1.81
MAE (mm/h)	1.62	0.61	0.56	0.50	0.49
Correlation	0.18	0.85	0.88	0.89	0.90

rainfall, due to the choice of spatial regulation coefficient  $c_s = 1$  (see above). However, the range has a very limited impact on the kriged mappings of the 2D-grid and on the warped fields, if the range used for the kriging is not modified accordingly. The range seems to have a bigger impact on the kriging than in the automatic registration, with respect to the results on the 2D-grid. The sensitivity of the results to the kriging is investigated further below.

#### KRIGING OF THE MAPPINGS

The automatic registration derives the mappings at the positions of the stations used as input. These mappings need to be interpolated onto the 2D-grid in order to warp the time series at all grid points. This interpolation has an impact on the mappings and, thereby, on the warped fields. We use the ordinary kriging method for the interpolation with an exponential variogram. We previously saw that the range of the variogram influences the results. In this section, we are investigating this influence. We consider four ranges: 50km, 100km, 150km and 300km. We used these different ranges for the kriging of the mappings for approaches A1 and A3. Since approach A2 assumes the mappings are constant in space, it does not need kriging. In these four cases, only the range used in the kriging changes, the mappings at the station locations are the same than the one shown in the results section above (4.3.2).

We first examined the impact of the kriging on the mappings. Figures 4.3.15 and 4.3.16 show the mappings on the 2D-grid obtained with the four different ranges for approaches A1 and A3 respectively. For the shortest range of 50km, the stations influence only very local areas. In the rest of the domain, the mappings seem constant in time. The influence radius of the stations increases with the range. The spatial variation of the mappings becomes more smooth with increasing range. Some sharp spatial variations can be observed for all ranges with approach A1, due to the large differences between neighboring stations. Most of these differences are caused by stations recording zero precipitation located next to stations with precipitation. By construction, the mapping is null at station without rainfall (in  $v$ , i.e. according to the gauge) for approach A1.

The impact of the kriging range on the warped fields can be seen in terms of average timing error in Table 4.3.13. We have already observed that, for the 150km kriging range, the average timing errors are similar for approaches A1 and A3 (they vary by 0.01h or less), except for the lowest threshold of 1mm/h (see Table 4.3.1 in Section 4.3.2). This is also the case for the 100km and 300km ranges. For the shortest kriging range (50km), the average timing errors of the two approaches also differ for the highest threshold of 40mm/h (by 0.07h). The timing errors are in general larger for shorter kriging ranges, an exception is error for the 40mm/h threshold with the 50km range. There are also larger

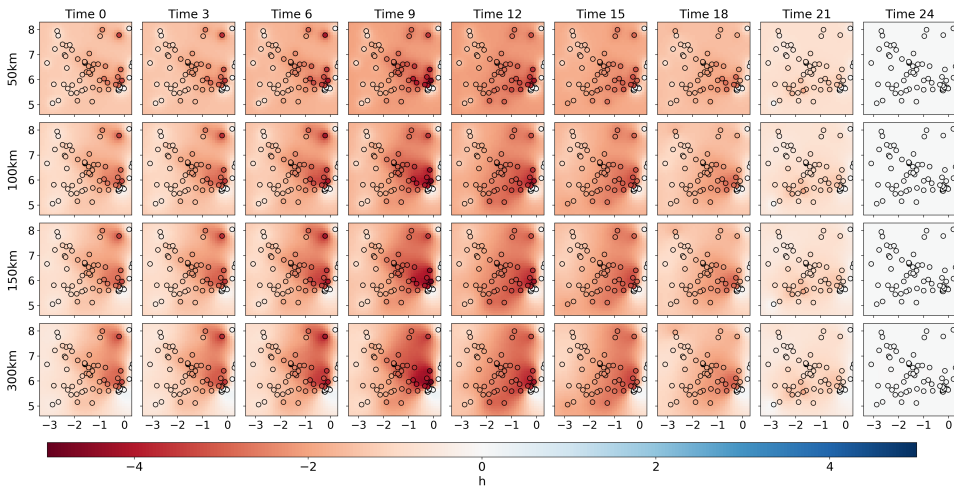


Figure 4.3.15: Mapping  $T$  for each node of the 2D-grid (background) and at the station locations (circles) at the 9 times of the warping grid. The mappings are shown for approach A1 using four different ranges for the kriging: 50km, 100km, 150km and 300km from (top) to (bottom). In red, the mapping is pushing the time series forward in time. In blue, the time series is pushed backward.

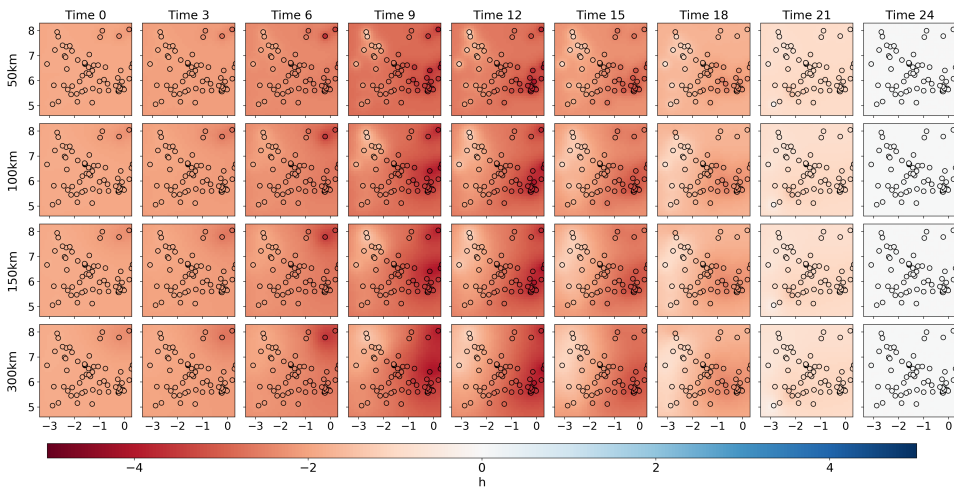


Figure 4.3.16: Mapping  $T$  for each node of the 2D-grid (background) and at the station locations (circles) at the 9 times of the warping grid. The mappings are shown for approach A3 using four different ranges for the kriging: 10km, 50km, 150km and 300km from (top) to (bottom). In red, the mapping is pushing the time series forward in time. In blue, the time series is pushed backward.

variations in the timing errors for the lower thresholds. For the 1mm/h threshold, the average timing error goes from 0.32h with the 30km range to 0.38h and 0.47h with the 100km and 50km ranges respectively for approach A3. That is a 0.04h and 0.15h decrease. For the 20mm/h threshold, the error goes from 0.32h with the 300km to 0.37h with the

Table 4.3.13: Average timing error (in h) after time warping using four different ranges for the kriging. The timing error is averaged over all pixels with more rainfall than a certain threshold.

Threshold	50km		100km		150km		300km	
	A1	A3	A1	A3	A1	A3	A1	A3
>1mm/h	0.57	0.47	0.51	0.38	0.48	0.35	0.45	0.32
>10mm/h	0.40	0.41	0.35	0.35	0.33	0.32	0.31	0.30
>20mm/h	0.35	0.37	0.34	0.34	0.33	0.33	0.32	0.32
>40mm/h	0.18	0.25	0.20	0.21	0.21	0.21	0.22	0.22

50km range. The error decreases by 0.05h, that is three times less than for the 1mm/h threshold. The timing errors varies by 0.02h or less for the 40mm/h threshold, with the exception of the 50km range. The timing errors are similar for the 150km and 300km ranges, more differences are observed among the lower ranges. The error variations due to the range (e.g. 50km compared to 150km or 300km ranges) can be as large as the one due to the approach (e.g. A1 versus A3).

Table 4.3.14: Statistics after time warping using four different ranges for the kriging. The statistics are computed over the full domain and all time steps.

	50km		100km		150km		300km	
	A1	A3	A1	A3	A1	A3	A1	A3
RMSE	2.02	1.97	1.91	1.85	1.86	1.82	1.83	1.81
MAE	0.58	0.55	0.54	0.51	0.52	0.50	0.51	0.49
Correlation	0.87	0.88	0.89	0.89	0.89	0.89	0.89	0.90

We also looked at the continuous statistics of the warped fields in Table 4.3.14. Both the RMSE and MAE increase when the kriging range decreases. The RMSE goes from 1.81mm/h with the 300km range to 1.97mm/h with the 50km range for approach A3. The largest increase occurs between the 50km and the 100km ranges, while there are little differences between the 150km and 300km ranges. The impact of the kriging range on the correlation is more limited. The correlation after warping is equal to 0.89 for the 100km, 150km and 300km ranges. It goes to 0.87 and 0.88 for the 50km range for approaches A1 and A3 respectively. The largest RMSE variation due to the range is 0.19mm/h and 0.16mm/h for approaches A1 and A3 respectively, while the largest variation between the two approaches is 0.06mm/h for the 100km range.

To summarize, the kriging of the mappings has an impact on the warped field for approaches A1 and A3. This impact can be as large as the variation between the approaches. Larger kriging ranges lead to smoother spatial variation of the mappings. Both the average timing errors and the continuous statistics improves when the range increases. However, in this synthetic case, the event is well-defined and smooth, and so might favour a smoother solution (i.e. larger range). Rainfall events from real data will not be as smooth, and larger spatial variations can be expected.

## 4.4. SOUTHERN GHANA CASE

### 4.4.1. STUDY CASE

The Southern Ghana case is used to test the automatic registration and the time warping on real precipitation data. This case is the same as the one used for the spatial warping in the previous chapter (in Section 3.4). Here, we repeat its description for the sake of readability and consistency. For the datasets, we refer to the description given in the previous chapter in Section 3.4.1.

In this study case, the first guess is the satellite-based estimate IMERG-Late and the target is gauge data from the TAHMO network. We assume that the gauge measurements are more accurate, but that the spatial variability of the rainfall is better represented by the IMERG estimate because of his higher resolution and the relative low density of the gauge network in the area. Our goal is to use the gauge data to correct the IMERG-estimate with respect to time while preserving its higher spatial variability.

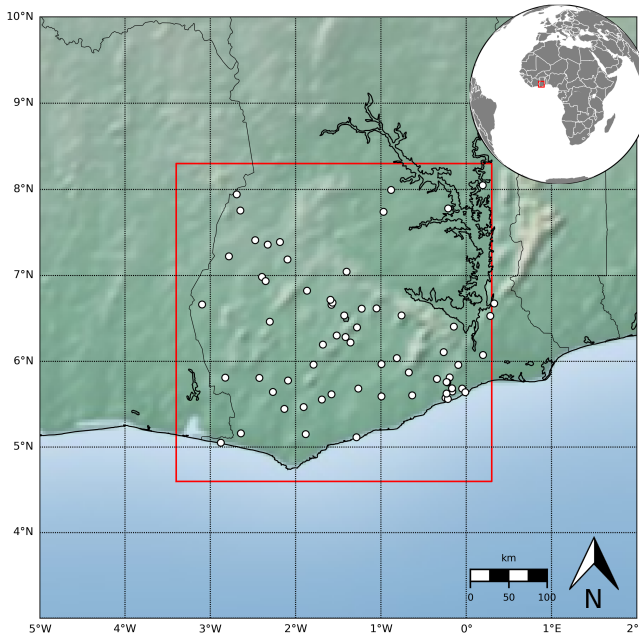


Figure 4.4.1: Study domain (red rectangle) and the TAHMO stations available within the domain (white dots).

The study area is located in southern Ghana and covers the Ghanaian cocoa region. This area has been selected because of the important number of TAHMO stations located in it. The domain corresponds to a square of  $0.37^\circ$  latitude by  $0.37^\circ$  longitude, that is to  $37 \times 37$  grid points for IMERG estimate. We selected a 25 hour time period during the main rainy season of 2018 with a resolution of one hour (of accumulated rainfall). The period extends from 06:00 the 22 April to 06:00 the 23 April 2018 (included), and contains one rainfall event. We use the data from 65 TAHMO stations that were located in the

domain and have a complete record for this time window (Figure 4.4.1).

Figure 4.4.2 shows the one-hour accumulated rainfall according to the IMERG-Late estimates and the TAHMO measurements for the selected domain and time window. In both datasets, we can observe one main rainfall event, but with different characteristics. The rainfall peak is higher in TAHMO measurements (53.45mm/h) than in IMERG-Late (19mm/h). The position and the timing of the peak differ too. The peak occurs at 18:00 according to TAHMO, while it has a larger time span in the IMERG estimates (18:00 and 19:00). In the latter, the peak is located more North-East than in TAHMO. There is a spatial shift of about 55km in the peak's position at 18:00.

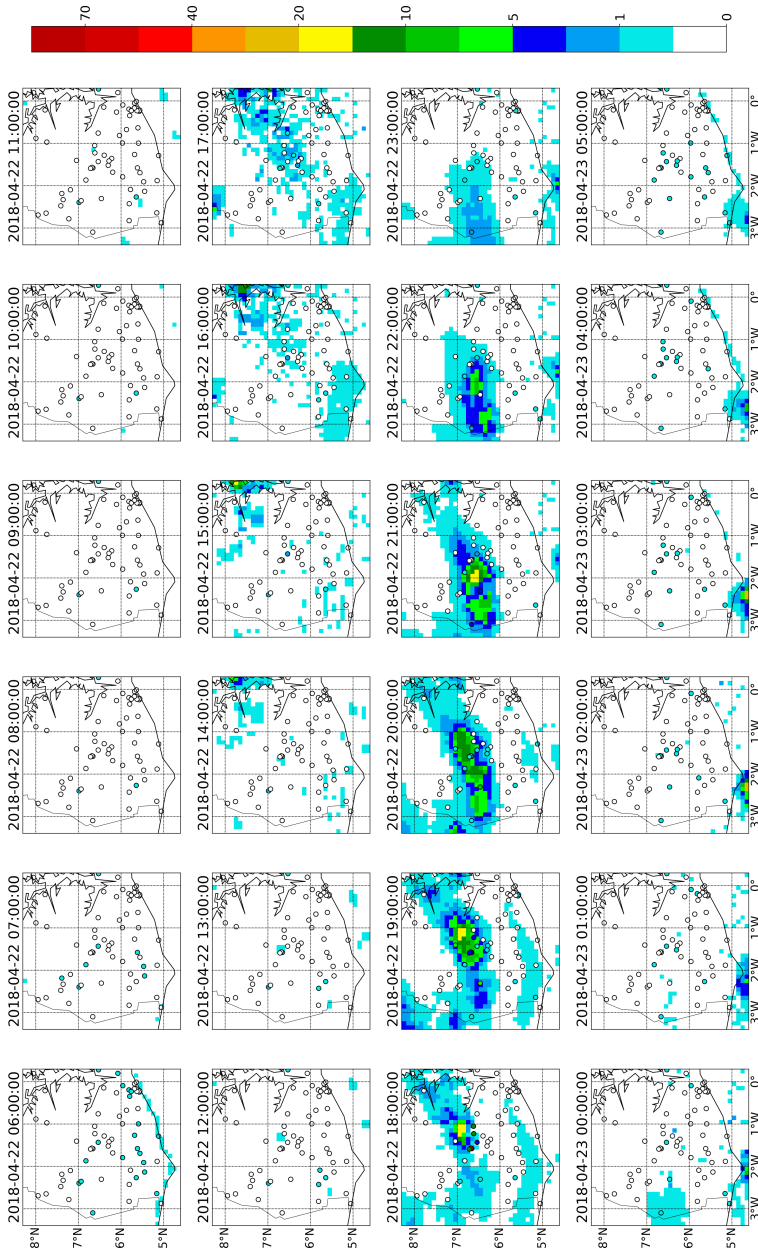


Figure 4.4.2: Input data for the southern Ghana case. IMERG-Late (background) and TAHMO (circle) 1 hour accumulated rainfall from 06:00 the 22 April to 06:00 the 23 April 2018.

#### 4.4.2. RESULTS

For the southern Ghana case, we do not know the “truth” as we did for the synthetic case. Thus, we will use a leave-one-out-validation (LOOV) to evaluate the accuracy of the method. That is, we remove one of the 65 TAHMO stations from the input data to use for validation, and we use the time series of the 64 other stations as input  $v$ . The automatic registration provides the time mapping for these 64 stations. They are kriged to obtain the mapping at the location of the removed station. We can then warp the corresponding IMERG time series, and compare it to the gauge measurement for validation since it was not used as input. We repeat this 65 times, once for each station, and obtain 65 warped time series that we use for validation.

For comparison, we run a second experiment using the time series of all the stations as input  $v$ . We call this second experiment “All”. The results of the “All” experiment are not independent from the validation data. However, it provides an insight on the impact of the gauge network configuration on the efficiency of the method, and on what is the “best” possible results with the current network.

As for the synthetic case, all the results shown here are obtained for  $C_1 = 0.1$ ,  $C_2 = 1$  and  $c_s = 1$ , and for  $I = 3$  except stated otherwise.

#### SENSITIVITY OF THE MAPPING TO THE GAUGE NETWORK

We examine the impact of the individual station on the mapping  $T$  by comparing the “All” and the “LOOV” experiments at the station locations in Figure 4.4.3. The corresponding warped time series can be seen in the appendix in Figure 4.D.1. For all approaches, the distortions are larger in the center of the time series, and become smaller at the beginning and at the end, away from the rainfall event. This is due to the first regulation term ensuring that the mapping is as “small” as possible and to the boundary condition requiring that no node leaves the domain (thus the mapping cannot be strictly positive at time 0). The second regulation term ensures a smooth transition between the time steps. In general, the differences between the two experiments are more important for approach A1, while approach A2 seems the most stable. With approach A2, the mappings from the two experiences are similar at most stations. The most noticeable differences for approach A2 are observed for stations TA00393, TA00276 and TA00143. Stations TA00393 and TA00143 are the stations recording the highest amounts of rainfall with peaks above 40mm/h. Station TA00276 recorded a much lower peak (8mm/h), but is the only station recording a significant amount of rainfall at time 14 (20:00). On the contrary, there are large differences between the two experiments for approach A1. They are particularly important at some stations. For example, at station TA00312, after time 15, the time series is moved backward in the “All” experiment and forward in the “LOOV” experiment. At stations TA00276 and TA00046, the distortions are much lower in the “LOOV” experiment (less than 1h) than in the “All” one (more than 3h). In approach A3, the results of the two experiments are more dissimilar than in approach A2, but less than in approach A1.

In practice, in order to warp the entire domain (and not just the stations), we kriged the mappings from the stations to the 2D grid on which IMERG is defined. These mappings are then applied to the time series of the grid points. The warped fields are shown in the appendix in Figures 4.D.2, 4.D.3 and 4.D.4 for approaches A1, A2 and A3 respectively. For the “LOOV” experiment, we repeated the kriging for the 65 realizations, and

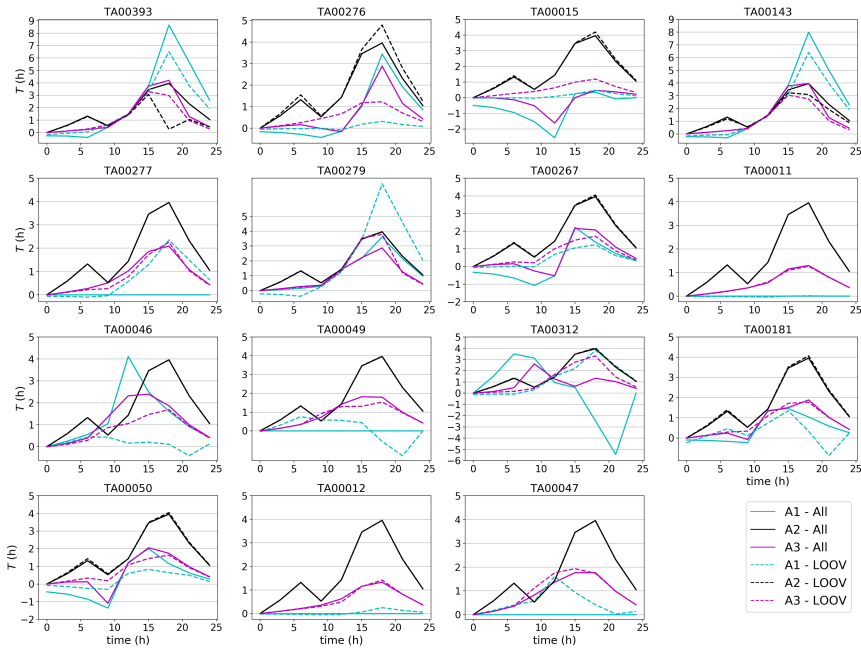


Figure 4.4.3: Mappings at the station locations obtained from the “All” (continuous line) and “LOOV” (dashed line) experiments with the three approaches A1 (blue), A2 (black) and A3 (purple). Only the stations with more than 0.1mm/h rainfall according to both TAHMO and IMERG are shown.

obtain 65 sets of mappings. The average mappings (over the 65 realizations) obtained with the three approaches are shown in Figure 4.4.4. The mappings obtained with the “All” experiment are very similar to these average mappings, and so are not shown here. The areas and times with the most important deviations do not necessarily correspond to the ones with the highest rainfall amount. As for the synthetic case, there is more spatial variation with approach A1 than with A3, while the mappings are spatially homogeneous with approach A2 (by construction). For approaches A1 and A3, the distortions are becoming smaller away from the stations due to the kriging. This decrease is more marked for approach A1 than for A3. For approach A1, the distortions are more localized and less consistent in space. Far away from the stations, the kriged mapping tends to the mean, which is lower for approach A1 than A3. In approach A1, the mapping is null when a station records no rainfall. This is not the case in approach A3 if a station is close enough to stations recording rainfall.

The standard deviation of the “LOOV” experiment (Figure 4.4.5) gives us an insight into the sensitivity of the mappings with respect to the gauge network. The standard deviation varies in both space and time, except for approach A2 which is constant in space by construction. For approaches A1 and A2, the higher standard deviations are localized around specific stations and decrease away from them. The area and times with the highest standard deviations generally correspond to the ones with the largest distortions (Figure 4.4.4). The highest standard deviation is reached at time 00:00 for approaches



A2 and A3, and at time 03:00 for approach A1 (with 0.45h, 0.5h and 0.8h respectively). The standard deviation is thus smaller than the original temporal resolution of the data (1h), but larger than the resolution of the resampled time series (0.1h). The maximum standard deviation is reached by A1, but approach A2 has the largest mean standard deviation due to its spatial uniformity (the average being computed over space and time).

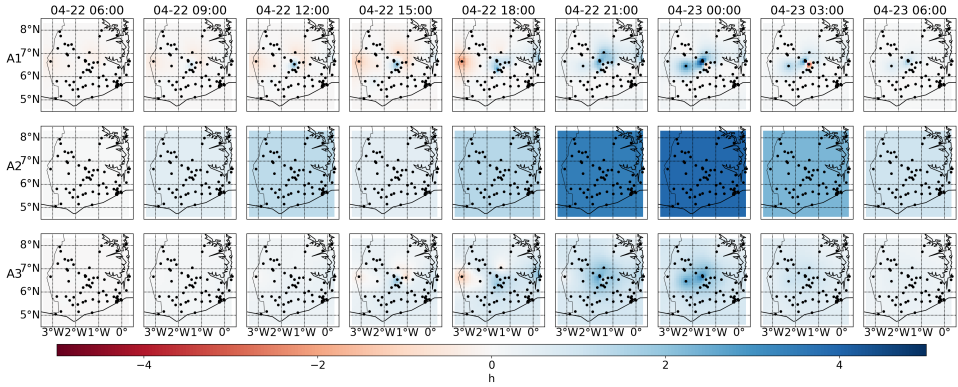


Figure 4.4.4: Mean of the mappings in the LOOV experiment for the three approaches. The positions of the stations are marked by black dots.

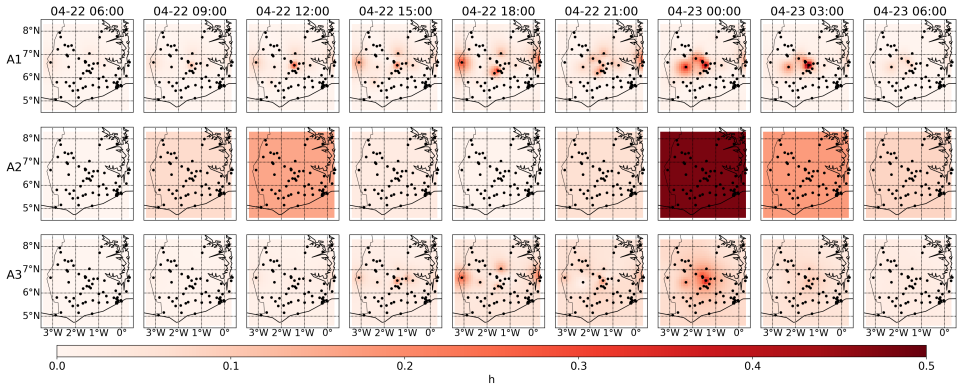


Figure 4.4.5: Standard deviation of the mappings in the LOOV experiment for the three approaches. The positions of the stations are marked by black dots.

### VALIDATION

In contrast to the synthetic case, we do not know the “truth”. It is thus more difficult to evaluate quantitatively the impact of the time warping on the rainfall estimates. For the purpose of the validation, we assume that the gauge measurements have no error and are giving the true rainfall values.

The timing error of the rainfall peak for the southern Ghana case is shown in Figure 4.4.6 (only for the stations with a peak above 0.1mm/h). At most stations, the peak

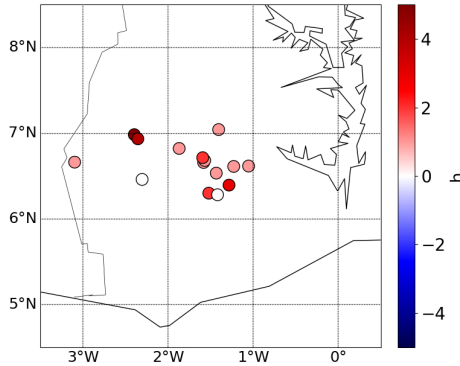


Figure 4.4.6: Time delay before spatial warping at each pixel of the domain. In red, the peak in  $u$  is late (compared to the one in the “truth”  $u$ ). In blue, the peak in  $u$  is in advance.

in IMERG is late compared to the gauges. After warping, some stations are now in advance while others are still late with respect to the gauges. However, the absolute timing error decreased for most stations (Figure 4.4.7). Among the 15 stations with more the 0.1mm/h (in both IMERG and TAHMO time series), only two show deterioration after warping for approaches A1 and A3, and three for approach A2. At station TA00276 (at 6.5° N, 2.3° W), the shape of the TAHMO and IMERG time series are slightly different (see Figure 4.D.1). The peak is near the beginning of the event in IMERG, while it is toward the end in TAHMO. Thus, with approach A1 (“All”) and A3, the span of the event in TAHMO and IMERG are matching better after warping, but the peaks are less aligned. With approach A1 in the “LOOV” experiment, the warped field is very close to the initial guess IMERG because of the small amplitude of the mapping (due to the kriging and the isolation of this station). Approach A2 leads to a stronger degradation at this station. The unique mapping is more adapted to the stations West of TA00276. The second station showing deterioration is TA00047 (at 6.3° N, 1.4° W). This deterioration can be explained by the low rainfall peak (0.1mm/h and 0.4mm/h according to TAHMO and IMERG respectively) compared to the surrounding stations, and the difference of the time series shapes (see Figure 4.D.1). In approaches A2 and A3, the mapping is influenced by the (surrounding) stations which recorded higher rainfall values and, therefore, have more weight in the cost function. In the “LOOV” experiment, the mapping depends of the surrounding stations’ mappings sine it is found by kriging them. Station TA00047 needs a different mapping than its neighbouring stations. Moreover, the shape difference between the time series makes it more difficult to find an adapted mapping. The absence of improvement or deterioration in the “All” experiment with approach A1 is explained by a null mapping (see Figure 4.4.3), probably because of the very low rainfall and the complex shape of the time series. With approach A3, a third station (TA00015) shows a light deterioration of the peak timing. Since this station is isolated from the other ones

(see Figure 4.A.1), the mapping of approach A3 is closer to the mapping of A1 than that of A2.

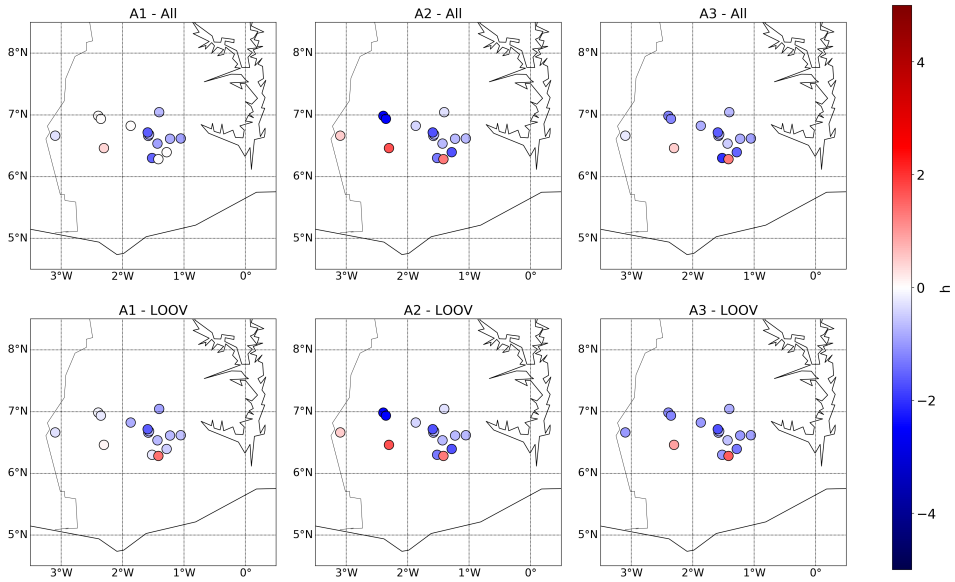


Figure 4.4.7: Improvement of the timing error after time warping (only at stations which more than 0.1mm/h rainfall). In blue, the timing error decreased after time warping. In red, the timing error increased. The results are shown for the two experiments: (top) “All” and (bottom) “LOOV”, and for the three approaches: (left) A1, (center) A2 and (right) A3.

The improvement of the timing error is similar in both experiments for approaches A2 and A3. More differences can be observed between the two experiments for approach A1. This is shown more quantitatively in Table 4.4.1 which gives the average absolute timing error for several thresholds. The average timing error decreases after time warping for the three approaches. The error is the same for the “All” and “LOOV” experiments with approach A2. There are some small differences with approach A3, with the “LOOV” experiment leading to slightly smaller timing error for the higher threshold (0.20h instead of 0.26h). As observed in Figure 4.4.7, approach A1 is the most impacted by the LOOV. For most thresholds, the average timing error is higher for the “LOOV” experiment than the “All” one, which was expected since the “All” experiment is not independent from the validation data. Approaches A1 and A3 have similar timing errors in the “All” experiment, while A3 is slightly better for the “LOOV” one. When considering all stations recording rainfall peaks above 0.1mm/h, the average timing error is largest with approach A1. For the other threshold, the error is larger with approach A2, except for the highest threshold in the “LOOV”. The error differences between the approaches decrease when the threshold increases. In general, the average timing error decreases for increasing threshold.

Table 4.4.2 provides statistics of the warped fields from the three approaches. The

RMSE, the MAE and the correlation are very similar for both experiments and for the three approaches. The RMSE decreased by 0.33mm/h after time warping, and the MAE by 0.06mm/h. The correlation goes from 0.28 before warping to 0.69-0.71 depending on the experiment/approach. Approach A2 leads to similar statistics as approaches A1 and A3, while it has larger timing errors (Table 4.4.1). The time series with larger rainfall values have more impact on the RMSE and the MAE than the ones with low rainfall, and we saw that approach A2 had similar average timing error for the highest threshold. For the correlation, all time series with rainfall contributes.

Table 4.4.1: Average absolute timing error before and after spatial warping. The average is done over all stations recording at least one time step with more rainfall than a certain threshold according to the gauges  $v$  (and with non-zero rainfall according to  $u$ ).

Threshold	Sample number	All							LOOV		
		Before	A1	A2	A3	A1	A2	A3	A1	A2	A3
>0.1mm/h	15	2.07	1.55	1.37	1.33	1.63	1.37	1.37	1.37	1.37	1.37
>1mm/h	10	1.10	0.33	0.64	0.34	0.47	0.64	0.64	0.35	0.35	0.35
>5mm/h	7	1.00	0.29	0.56	0.30	0.27	0.56	0.30	0.30	0.30	0.30
>10mm/h	5	1.20	0.26	0.30	0.26	0.34	0.30	0.30	0.20	0.20	0.20

Table 4.4.2: Statistics before and after temporal warping compared to the station measurement. The statistics are computed over all stations and all time steps. They are shown for the two experiments (“All” and “LOOV”) and the tree approaches (A1, A2 and A3).

	Before	All			LOOV		
		A1	A2	A3	A1	A2	A3
RMSE	1.56	1.22	1.23	1.22	1.22	1.23	1.21
MAE	0.19	0.12	0.13	0.12	0.13	0.13	0.12
Correlation	0.28	0.69	0.70	0.70	0.69	0.70	0.71

#### POSITION ERROR

In contrast to the synthetic case, we do not know the “truth” at all grid points, only at the station locations (we assume that the gauge measurements were the “true” rainfall rates at these locations). It is thus more difficult to compute the position error. The gauge measurements are kriged onto the grid, and this kriged field will be used as reference for the position error. Thus, the position error has to be considered with caution, since the kriging is adding uncertainty. From the “LOOV” experiment, we obtained 65 set of mappings, one for each realization, which makes the computation of the peak position ambiguous. Moreover, the average mapping from the “LOOV” experiment is very similar to the one from the “All” experiment. Thus, we will only estimate the position error for the “All” experiment.

Figure 4.4.8 shows the position errors before and after warping at each time step (with more than 1mm/h rainfall). At most time steps, the time warping has a limited, and sometimes negative, impact on the position error. Between 16:00 and 17:00, the position error increased after warping, especially with approach A3. At 17:00, the gauges

detected light and scattered precipitation (Figure 4.4.2). Our definition of the peak is not adapted to such rainfall pattern with several (low) peaks. For approaches A2 and A3, the position error is larger after warping toward the end of the event, starting at 20:00 for A2 and 22:00 for A3. The large position error at the end of the event is due to a second event in the southern part of the domain that is detected by IMERG but not by TAHMO (see warped fields in Figures 4.D.3 and 4.D.4). In the warped fields, this second event is identified as the peak, while the kriged field still identifies the central event as the peak. In approaches A2 and A3, the second event is moved forward in time due to the spatial consistency, while the same event is only marginally impacted by the warping in approach A1. Between 18:00 and 21:00, the position error decreases after warping for approach A1 and A3. At these time steps, the event is well defined (i.e. the peak is easily identifiable), and gauges record significant amount of rainfall. The results for approach A2 are more mixed between 18:00 and 20:00.

4

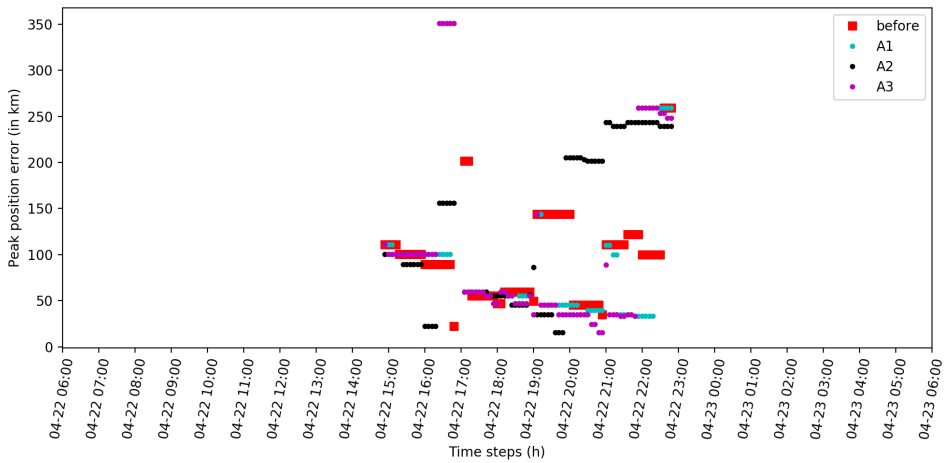


Figure 4.4.8: Distance between the “true” peak (gauge) and the estimated ones before and after time warping, for the “All” experiment, at each time step with more than 1mm/h recorded rainfall (in  $v_{grid}$  (for the “All” experiment)).

The spatial correction is evaluated more quantitatively in Table 4.4.3, which gives the position errors averaged over time for different thresholds. As seen in Figure 4.4.8, the time warping has a small and mixed impact on the position error. The largest decrease in the position error (-22km) is observed with approach A1 for the 5mm/h threshold. For approaches A2 and A3, the position error increases for the two lowest thresholds, but decreases for the two highest ones. The bad performance of approaches A2 and A3 for the lowest threshold can be explained by their large position error at the end of the event due to the second event present in IMERG.

Table 4.4.3: Average position error (in km) before and after time warping for the “All” experiment. The average is taken over all time steps at which the rainfall peak (in  $\nu$ ) is above a certain threshold.

Threshold	Sample number	Before	A1	A2	A3
>0.1mm/h	116	140.74	133.47	165.85	145.91
>1mm/h	83	104.53	94.34	132.99	110.95
>5mm/h	48	88.80	66.67	81.48	72.70
>10mm/h	18	66.07	58.33	52.18	56.71

## 4.5. DISCUSSION

The time warping has been evaluated in terms of the timing and the position of the rainfall peak, and of the intensity of the event. The correction of the timing error is the goal of the time warping, and is explicitly corrected. The timing error was significantly decreased in both cases. It was reduced by at least a factor of two for the synthetic case, and even more for the time series with large precipitation values. The improvement is more limited, especially for the time series with little precipitation and for approach A2. However, the average timing error is still considerably reduced for the higher rainfall thresholds. The continuous statistics are showing a clear improvement after the time warping in both the synthetic and real case data. The time warping does not modify directly the rainfall intensity, but helps by removing the double-penalty part of the error. We also looked at the position error since it can partially be interpreted as a timing error, and vice versa. In the synthetic case, the position error decreases after warping but remains significant. The remaining average position error is around 50km, which is by definition the position error of the event’s center (see description of the synthetic case in 4.3.1). The time warping has removed the part of the position error due to the timing difference. The position error is more difficult to estimate for the southern Ghana case, especially at times with lower precipitation rates. At these times, the peak is not well defined (there are several local maxima), causing an artificial increase of the position error. The rainfall event is better defined for the times with higher rainfall rates. A decrease of the average position errors is observed for the higher rainfall thresholds. This decrease stays however limited, the maximum decrease being about 20km for A1 (that is around two grid cells).

The time warping seems to benefit the large rainfall values. We observed, in both cases, that the average timing error decreases more for the higher thresholds than the lower ones. This is not due directly to the warping but to the registration method. The automatic registration method is based on the minimization of a cost function. The higher rainfall values have more weight than the low ones in the cost function, and so are corrected in priority during the minimization. The correction of the high rainfall values can be at the detriment of the lower ones, especially for approach A2 and its “unique” mapping. This can be seen in spatial variation of the timing error (Figure 4.3.5). The peak is in advance in the East and late in the West so that it is on time in the center, where the higher rainfall values are recorded. This characteristic can be seen as a drawback, especially for applications for which lower rainfall amounts are important. It also raises a limitation about our validation method, since the timing and position errors are defined with respect to the peak (i.e. the maximum rainfall). They are not taking into account

the spatial or temporal variation of the surrounding stations or time. Thus, they can be biased and have to be considered with caution.

For all three approaches, we observed an improvement of the timing and of the continuous statistics. However, there were some differences in their performance. In general, approach A2 leads to a more limited improvement in terms of timing and statistics. Approach A2 assumes that the time mapping is the same everywhere. It can thus not accommodate all stations/grid points if they have different timing errors. In that case, it corrects the time series with the higher rainfall values in priority. The spatial rigidity of approach A2 is limiting its impact on the timing error, but not necessarily on the position error. In the synthetic case, approach A2 yields the lowest average position error for all thresholds except for the highest one. The shape of the event is not modified because of its spatial homogeneity assumption. This prevents unnatural distortion of the event, and mostly benefits low rainfall rates (despite limiting the improvement of their timing). Approaches A1 and A3 have similar results in terms of timing for the synthetic case and the “All” experiment of the southern Ghana case. They mainly differ for the zero or low rainfall values (see the average timing error for the lowest threshold). In both approaches, each station has a different time mapping. The mappings are completely independent in approach A1, while they are linked through space in approach A3. This link is written as regulation term in the cost function, and mostly affects low rainfall values (because of the relative weight of this term compared to the observation term). Because of the independence of the mappings in approach A1, two stations next to each other can have different mappings. That can lead to unnatural distortion of the shape of the event, such as in Figure 4.C.1. Large differences between the mappings of neighbouring stations are in general due to the fact that one is recording rainfall and not the other (in the second case the mapping is null by construction). The impact of the approaches on the position error is more difficult to compare, especially for the southern Ghana case for which the rainfall “peak” is not always well defined. The influence of the choice of the approach on the continuous statistics stays limited. Approaches A1 and A3 have slightly better statistics for the synthetic case, but there are no significant difference between the approaches for the southern Ghana case.

The three approaches also differ with respect to their computational cost. The assumption of a “unique” mapping for all stations makes approach A2 the least computationally expensive approach. Approach A3 is the most computationally expensive one because of the larger number of variables to be optimized at once. The cost of approach A1 is in-between. In approach A1, we solve 65 minimization problems, each of them having the same number of variables as the minimization problem in approach A2. It is thus more expensive than approach A2, but cheaper than approach A3. Moreover, the 65 minimization problems could be run in parallel since they are independent. The computational time will also depend on the input data since they have a direct impact on the cost function through the observation term. The cost will also vary depending on the size of the input data, i.e. on the number of stations. In this chapter, we used 65 stations, and the automatic registration ran in about 6s with approach A2, 15s with approach A1, and 86s with approach A3 for the synthetic case (6s, 10s and 39s for the southern Ghana case) on a personal computer. The computational time will increase with the number of stations, especially for approach A3. For approach A1, the compu-

tations can be decreased by removing the stations that do not record precipitation (by construction their mapping will be null), or by parallelizing the minimization problems. The chosen minimization method is not adapted to problems with a large number of variables, as would be needed for approach A3. A possibility would be to transform the constrained minimization problem into an unconstrained one by using a penalized cost function. It would then be possible to use a cheaper minimization method. This was done for the automatic registration for the spatial warping in the previous chapter (see description in Appendix 3.A.2).

The mappings are derived by the automatic registration that can be tuned by several parameters. These parameters are thus impacting the mappings. The background term of the cost function consists of several regulation terms corresponding to properties characterizing the “optimal” mapping. These terms are weighted by the regulation coefficients  $C_1$ ,  $C_2$  and  $c_s$  (for approach A3 only). We examined the impact of these coefficients on the mappings and the warped fields in Sections 4.3.3 and 4.3.3. They are mainly influencing the times with little or no rainfall, and so have a limited impact on the warped fields in terms of timing error and continuous statistics. Very large regulation coefficients are needed for them to have an effect on periods with more rain (e.g. with more than 5mm/h). Nevertheless, they have a visible and valuable effect on the mappings. The second regulation term ( $C_2$ ) prevents sharp discontinuities in the mapping, the first one tries to keep it as “small” as possible. The third term in approach A3 prevents unphysical discontinuity in space as was observed for approach A1. This term links the mappings of neighbouring stations together in order to avoid differences between them that are too large.

It is possible to modify the resolution of the mappings by changing the number of steps  $I$  in the automatic registration. The number  $I$  controls two things: the smoothing of the input data and the resolution of the mapping (i.e. the number of nodes of the warping grid). We examined the sensitivity of the warped field with respect to  $I$  in Section 4.3.3. It actually has a small impact on the warped field both in terms of timing error and continuous statistics. This could be partially due to the construction of the synthetic case in which all time series have a clearly defined rainfall peak. The number of steps  $I$  also has an impact on the computational time since the number of variables of the minimization problem increases with  $I$ . For example, with approach A3, the first step runs in less than 6s while the third one needs almost a minute. In our cases, with 65 stations, the computational aspect is not a problem, but could become one for larger cases with more stations.

For approaches A1 and A3, there is another step that has an important impact on the warping: the kriging of the mappings provided by the automatic registration. This step is necessary to be able to warp the entire domain. We chose ordinary kriging to interpolate the mappings onto the 2D-grid, however other interpolation method could have been used. The choice of the method has an influence on the warped field. We chose kriging because it can be used for interpolation and extrapolation, and could be linked to the assumption we made in approach A3. The same variogram is used to define the influence function in A3 and for the kriging. In section 4.3.3, we modified the range of the variogram for the kriging step. We observed that the kriging range could influence the warped field as much as the choice between approach A1 and A3 in terms of timing



error and statistics. The impact of the interpolation step might even be larger if we would use a completely different interpolation method.

The automatic registration has the advantage of not needing any manual selection, however this means that the inputs have to be similar enough for it to perform correctly. In both cases we studied here, the rainfall events are relatively well-defined in time, with a single rainfall peak in each time series. Approach A1 is the most sensitive to the input data. For example, in the southern Ghana case, at station TA00312, it stretches the event unnaturally because of the difference in intensity and timespan of the rain between TAHMO and IMERG time series (Figure 4.D.1). This problem is less apparent for approaches A2 and A3 because the mapping is constrained by the ones of the other stations. Similarly, the normalization step before the registration is mostly beneficial for approach A1. Without the normalization, the automatic registration with approach A1 gives illogical mappings at stations where IMERG's peak is much higher than TAHMO's. Another important point when using point measurements, especially when your measurement network is sparse, is that they need to cover the event. That is, if the rainfall event is not detected by enough stations, the mappings will not be representative or adapted enough to warp the time series on the whole IMERG's grid.

## 4.6. CONCLUSION

In this chapter, we investigated the use of a warping method for the gauge-adjustment of a satellite-based rainfall estimate with respect to the timing error. The warping method has been applied to two cases. We used a synthetic rainfall event, represented by an ellipse, to test the feasibility and accuracy of the method. This case also allowed us to study the sensitivity of the method to several parameters. We investigated the impact of the number of steps  $I$  and of the regulation coefficients in the automatic registration, as well as the impact of the kriging of the mappings after the registration. The second case was a convective rainfall event in southern Ghana. The time warping was applied in such a way that the rainfall estimates from IMERG-Late were shifted in time to match the gauge data from TAHMO. This case showed the potential of the method when applied to real and noisy precipitation data.

The automatic registration can process time series from several stations at the same time. Three approaches with different assumptions regarding the spatial dimensions were tested. The first approach assumes that all the mappings are independent, while the second one assumes that all stations have the same mapping. In the third approach, the mappings could vary from one station to the other but were linked through space based on their distance. All three approaches improves the continuous statistics and the timing error of the peak, but have a more limited and mixed impact on the position error. In general, the second approach shows a more limited improvement, but is more stable and spatially consistent than the two others. The results of the first and third approaches are similar, most of the differences are observed for the lower precipitation values. The independence of the mappings in the first approach can lead to unnatural distortions.

## 4.7. FUTURE WORK

This chapter investigated the use of time warping method to correct timing errors in precipitation estimates. Although the time warping would need to be tested on more rainfall events, it shows a good potential for gauge-adjusting rainfall estimates with respect to the timing errors. Extending the study to other events with different rainfall regimes would allow us to determine more precisely the limitations of the method. More cases would also allow us to investigate further the sensitivity of the method to the different parameters, and so to better tune the automatic registration.

Another possible next step would be to combine the time correction with a bias adjustment method. In this chapter, we focus on the timing error. The warping method is used to adjust the rainfall estimate with respect to the time, it does not act directly on the intensity. The easier option would be to apply an existing bias adjustment method after the warping, e.g. an additive or multiplicative adjustment or a PDF matching method. The warping and the bias adjustment would be two separate steps. The second option would be to adapt the morphing method described in [Mandel \*et al.\* \(2010\)](#) and [Beezley and Mandel \(2008\)](#) for the spatial warping. Morphing modifies both the spatial coordinates (or in the present case, the time coordinates) and the intensity by combining warping with cross-dissolving. However, the morphing cannot be used directly in the case of irregularly spaced measurements such as gauge observations. The morphing and the warping formulas are similar, but an extra term  $r$  is present for the morphing :

$$u_{morph} = (u + r) \circ (I + T) = u_{warp} + r \circ (I + T)$$

where  $r = v \circ (I + T)^{-1} - u$  is the residual. This term permits to correct the intensity, but requires knowledge of the target or truth  $v$ . Thus, we can compute the residual only at the gauge locations where  $v$  is known. At the other grid points,  $v$  and the residual are unknown. A solution could be to interpolate the gauge measurements or the residuals at the corresponding locations. However, the interpolation would also add some uncertainty.

As for the spatial warping (in Chapter 3), the time warping method described in this chapter assumes that the gauge measurements have no error. They are used as the “truth” by the automatic registration. The uncertainty on the gauge measurements could be taken into account by modifying the cost function, and more specifically the observation term as follow:  $J_o = (v - u \circ (I + T))^T R^{-1} (v - u \circ (I + T))$ , where  $R$  is covariance matrix of the observation error.



# APPENDIX

## 4.A. TAHMO STATIONS

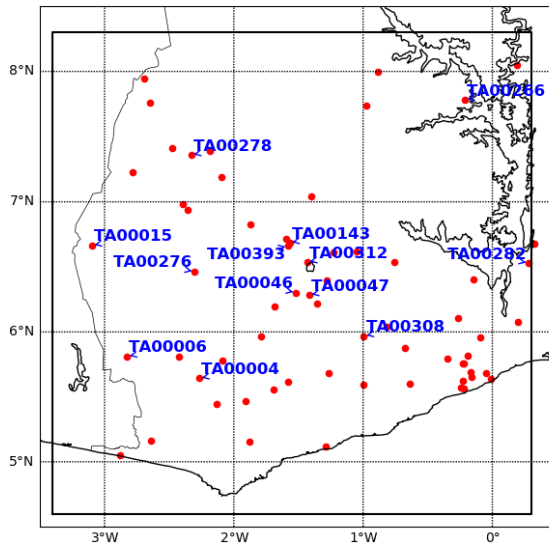


Figure 4.A.1: Position of all the TAHMO stations mentioned in this chapter.

## 4.B. MAPPINGS FROM THE SYNTHETIC CASE

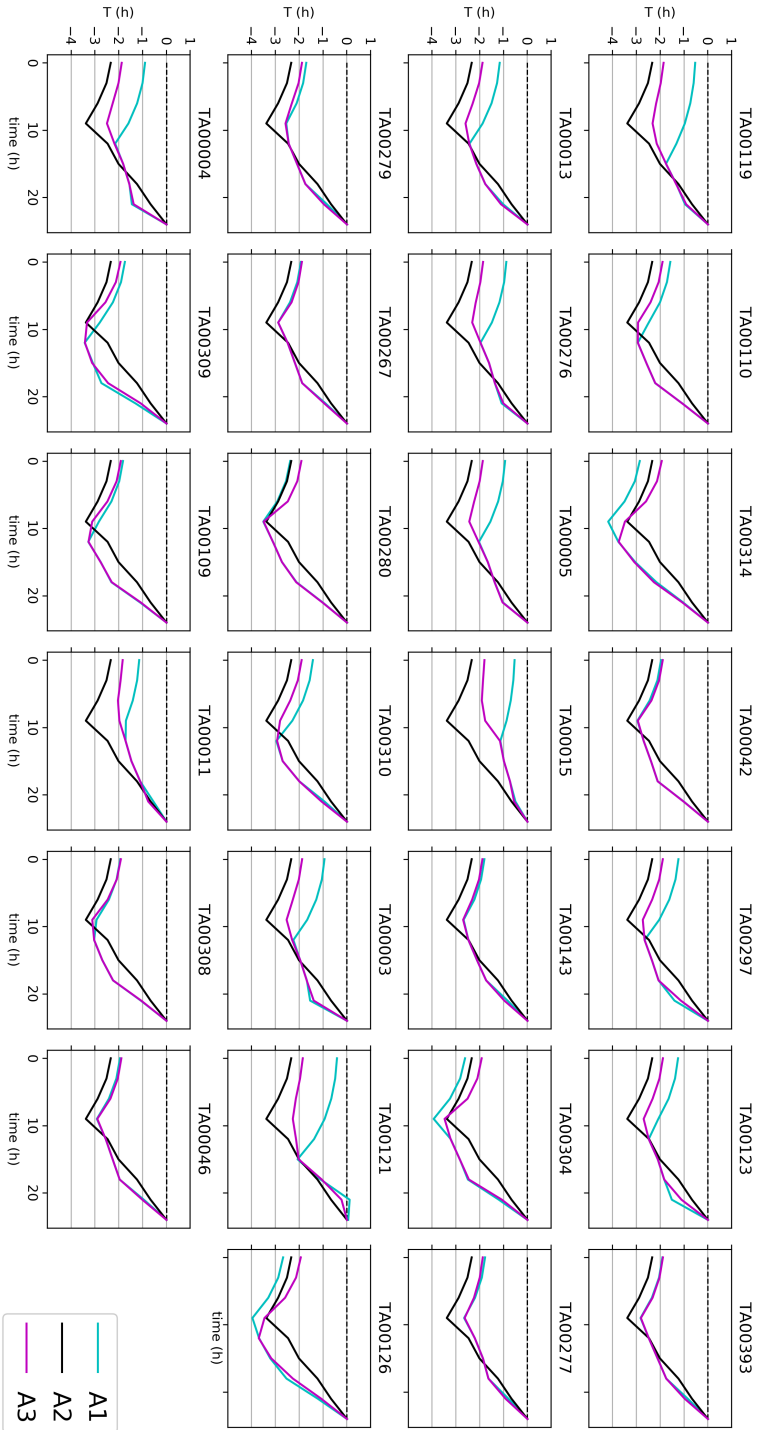


Figure 4.B.1: Mappings at the station locations for the three approaches A1, A2 and A3. Only the stations with more than 1mm/h rainfall in both inputs  $u$  and  $v$  are shown.

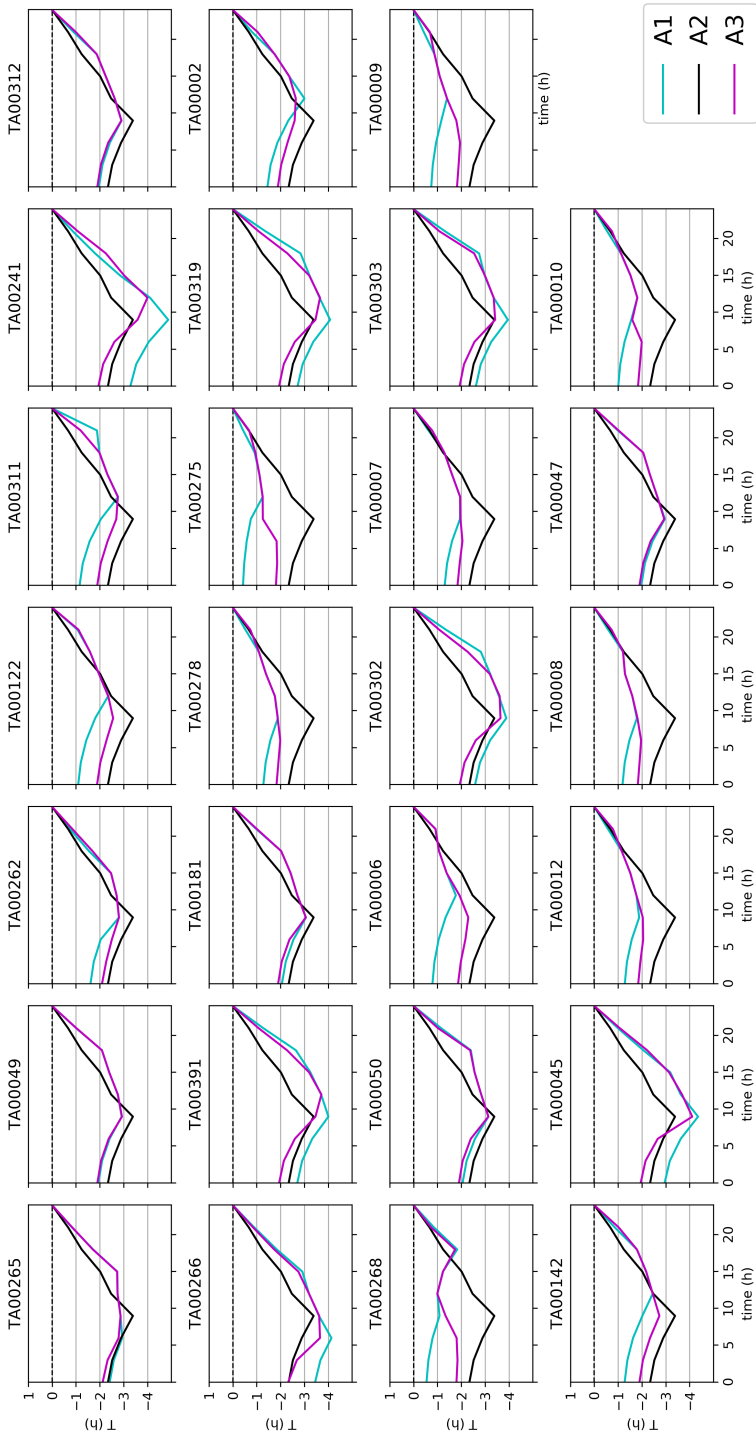


Figure 4.B.2: Figure 4.B.1 continuing ..

### 4.C. WARPED FIELDS FROM THE SYNTHETIC CASE

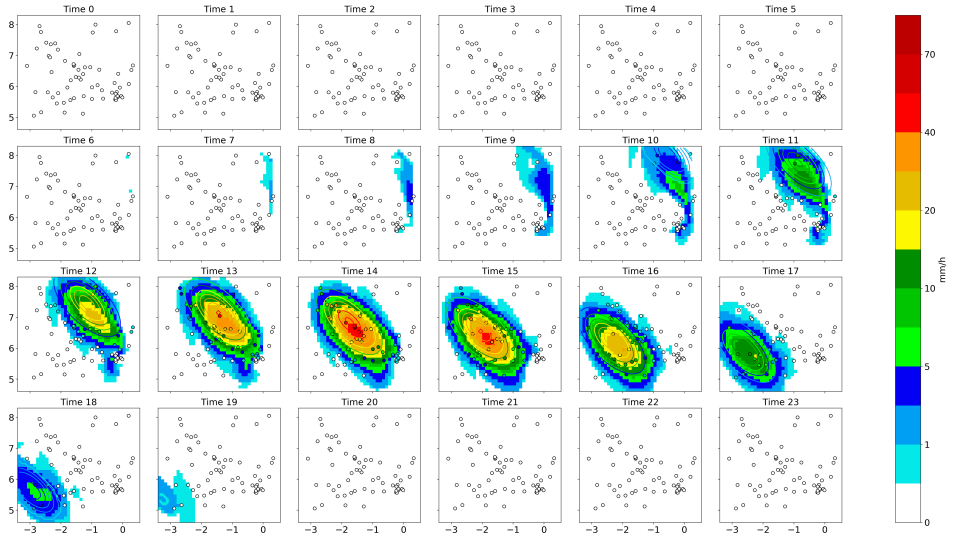


Figure 4.C.1: Warped precipitation field obtained with approach A1 (background), and the “true” precipitation field (contour lines) for the synthetic case. The fictive stations are represented by circles.

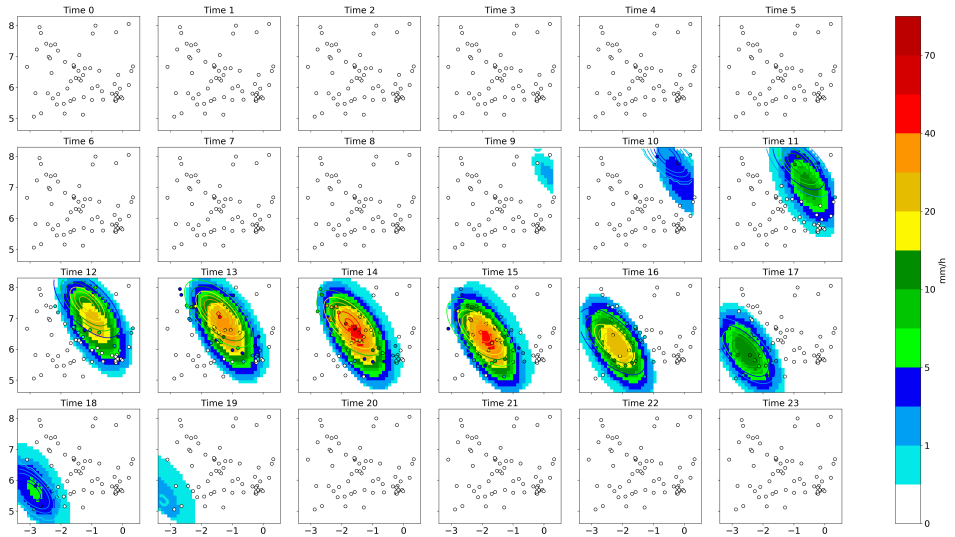


Figure 4.C.2: Warped precipitation field obtained with approach A2 (background), and the “true” precipitation field (contour lines) for the synthetic case. The fictive stations are represented by circles.

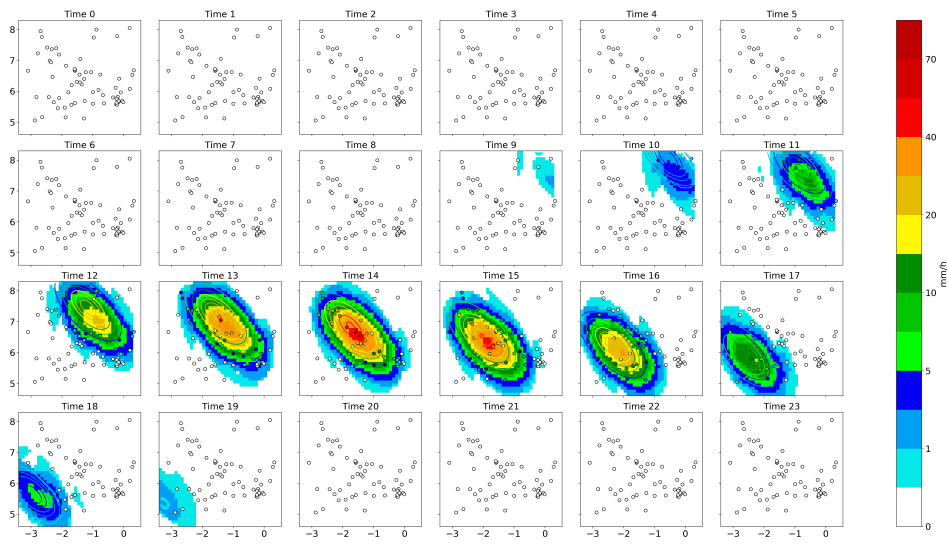


Figure 4.C.3: Warped precipitation field obtained with approach A3 (background), and the “true” precipitation field (contour lines) for the synthetic case. The fictive stations are represented by circles.



### 4.D. WARPED FIELDS FROM THE SOUTHERN GHANA CASE

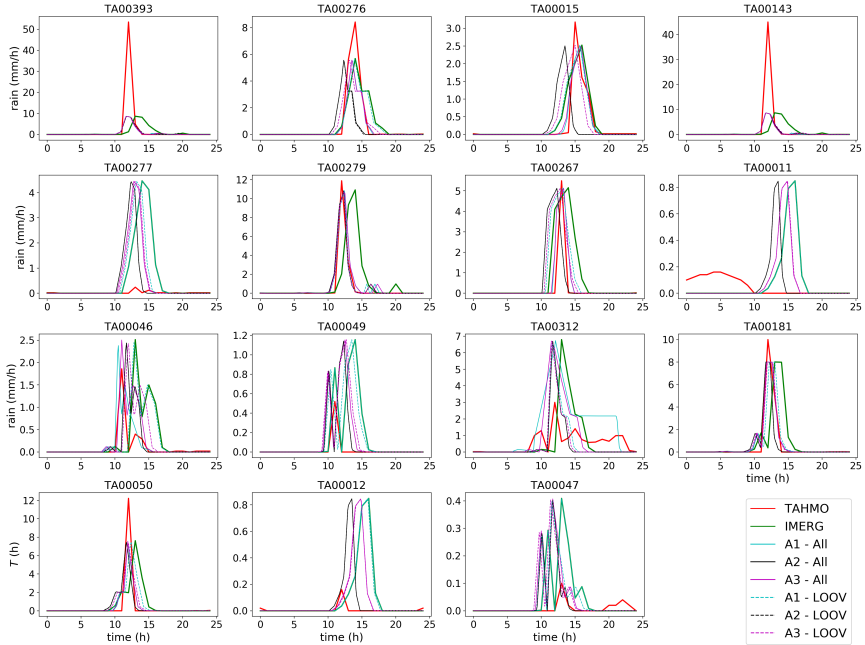


Figure 4.D.1: Warped time series compared to IMERG’s first guess and TAHMO. Only the stations with more than 0.1mm/h rainfall according to both TAHMO and IMERG are shown.

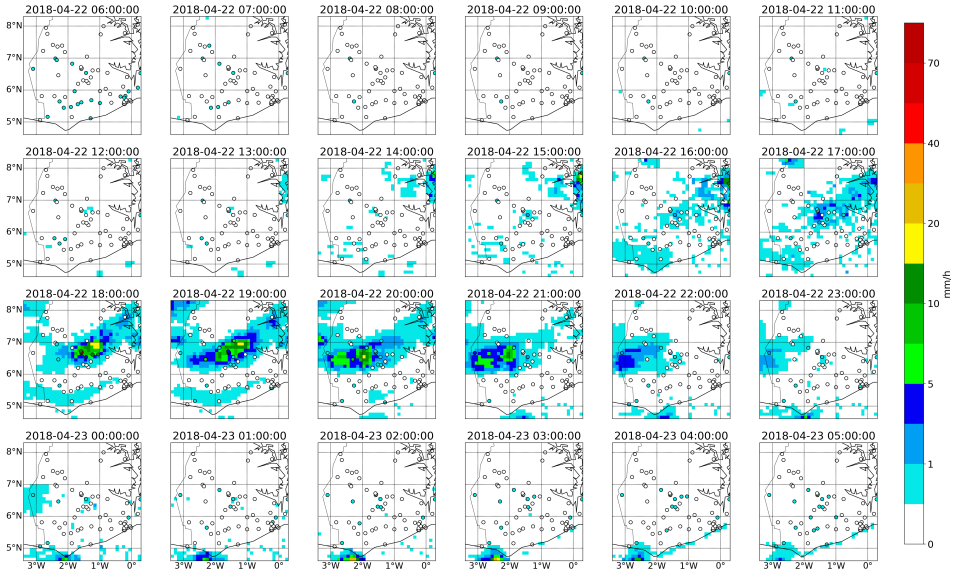


Figure 4.D.2: Warped precipitation field obtained with approach A1 (background), and gauge measurements (circles) for the southern Ghana case.

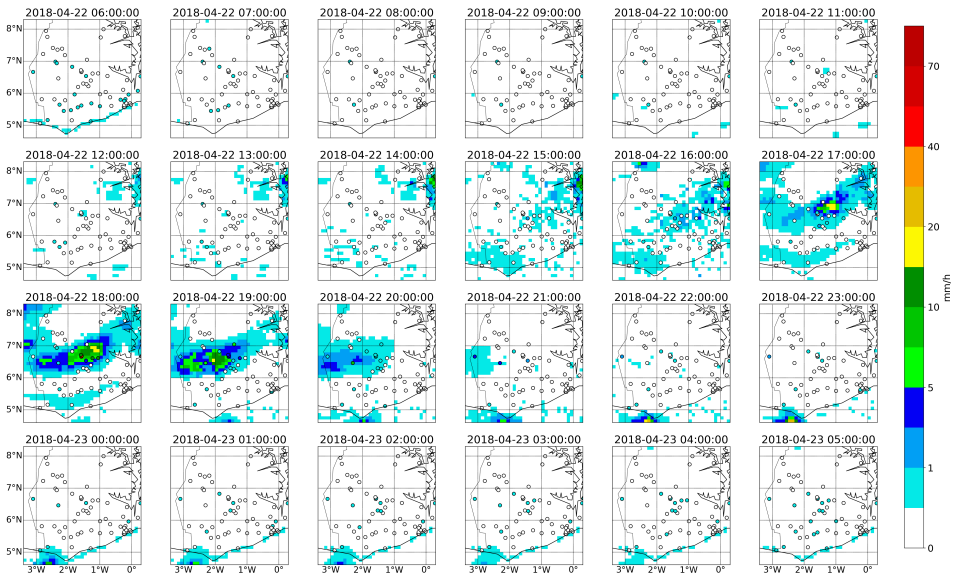


Figure 4.D.3: Warped precipitation field obtained with approach A2 (background), and gauge measurements (circles) for the southern Ghana case.

4

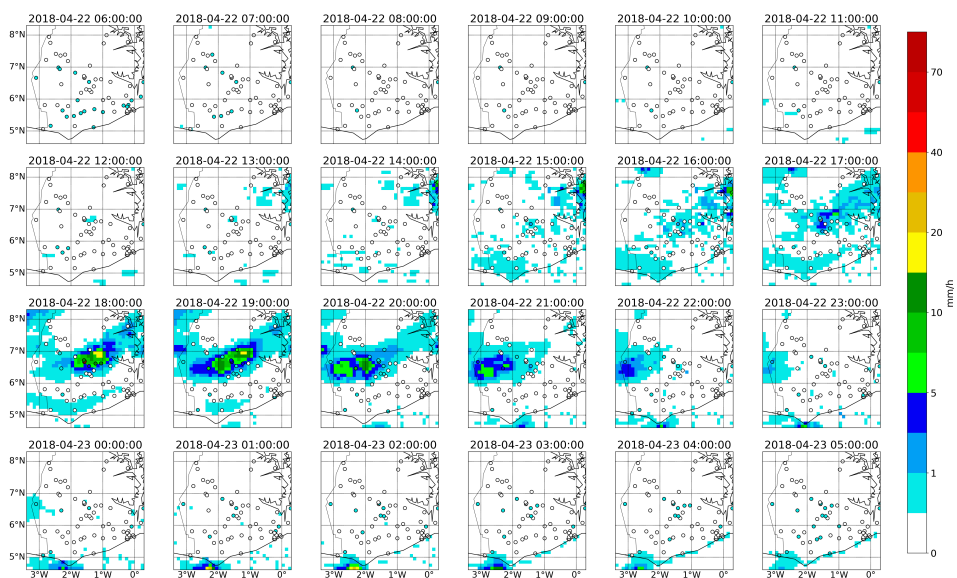


Figure 4.D.4: Warped precipitation field obtained with approach A3 (background), and gauge measurements (circles) for the southern Ghana case.

## REFERENCES

- J. E. Ball, *The influence of storm temporal patterns on catchment response*, *Journal of Hydrology* **158**, 285 (1994).
- V. P. Singh, *Effect of spatial and temporal variability in rainfall and watershed characteristics on stream flow hydrograph*, *Hydrological Processes* **11**, 1649 (1997).
- P. Máca and P. Torfs, *The influence of temporal rainfall distribution in the flood runoff modelling*, *Soil and Water Research* **4**, S102 (2009).
- U. Pfeifroth, J. Trentmann, A. H. Fink, and B. Ahrens, *Evaluating satellite-based diurnal cycles of precipitation in the african tropics*, *Journal of Applied Meteorology and Climatology* **55**, 23 (2016).
- V. Velichko and N. Zagoruyko, *Automatic recognition of 200 words*, *International Journal of Man-Machine Studies* **2**, 223 (1970).
- H. Sakoe and S. Chiba, *Dynamic programming algorithm optimization for spoken word recognition*, *IEEE Transactions on Acoustics, Speech, and Signal Processing* **26**, 159 (1978).
- E. J. Keogh and M. J. Pazzani, *Derivative dynamic time warping*, in *Proceedings of the 2001 SIAM International Conference on Data Mining (SDM)*, pp. 1–11.
- J. McIntosh and M. Yuan, *Assessing similarity of geographic processes and events*, *Transactions in GIS* **9**, 223 (2005).
- S. Lu, M.-c. ten Veldhuis, N. van de Giesen, A. Heemink, and M. Verlaan, *Precipitation regime classification based on cloud-top temperature time series for spatially-varied parameterization of precipitation models*, *Remote Sensing* **12**, (2020).
- V. Mantas, Z. Liu, C. Caro, and A. Pereira, *Validation of TRMM multi-satellite precipitation analysis (TMPA) products in the Peruvian Andes*, *Atmospheric Research* **163**, 132 (2015), 6th Workshop of the International Precipitation Working Group.
- M. D. Dilmi, L. Barthès, C. Mallet, and A. Chazottes, *Iterative multiscale dynamic time warping (IMs-DTW): a tool for rainfall time series comparison*, *International Journal of Data Science and Analytics* **10**, 65 (2020).
- D. Dilmi, L. Barthès, C. Mallet, and A. Chazottes, *Study of the impact of climate change on precipitation in Paris area using method based on iterative multiscale dynamic time warping (IMS-DTW)*, in *Proceedings of the 9th International Workshop on Climate Informatics* (Ecole Normale Supérieure, Paris, France, 2019).
- J. Mandel, J. D. Beezley, K. Eben, P. Jurus, V. Y. Kondratenko, and J. Resler, *Data assimilation by morphing fast fourier transform ensemble Kalman filter for precipitation forecasts using radar images*, (2010) UCD/CCM Report 289.
- J. D. Beezley and J. Mandel, *Morphing ensemble Kalman filters*, *Tellus A* **60**, 131 (2008).



# 5

## CONCLUSIONS AND RECOMMENDATIONS

*Gortosit an nos ewid lavared eo bet kàer an deiz.*

Breton proverb

## 5.1. CONCLUSIONS

There are many rainfall products available over sub-Saharan Africa, but also meaningful differences between them. Part of these discrepancies can be due to position and timing mismatches. In this thesis, we investigated a method to gauge-adjust rainfall estimates with respect to the position and timing of the rainfall events, instead of the usual bias correction. This is done by answering the following research questions:

1. What is the state of the art of rainfall estimates over Africa?
2. What is the best way to use warping to correct position errors in rainfall estimates?
3. What is the best way to use warping to correct timing errors in rainfall estimates?

The first part of this thesis (Chapter 2) answered the first research question by reviewing the different types of rainfall estimates: numerical models and reanalyses, satellite-based products and gauges-only products. The main conclusions of this review are summarized in Section 5.1.1. From the review, we noticed that the validations or comparisons of the rainfall estimates were in general focused on the occurrence or intensity of the rainfall. Less attention is given to the possible position and timing errors in the rainfall estimates, even though they can cause or increase the intensity error (e.g. double-penalty) and are of crucial importance for some applications.

The second part of this thesis focused on the second and third research questions (Chapters 3 and 4). It examined the use of warping to correct the position or the timing error. This is investigated by gauge-adjusting a satellite based estimate with respect to the position or the time (instead of the usual bias-adjustment). Section 5.1.4 summarizes the main observations and compares spatial and time warping.

### 5.1.1. STATE OF THE ART OF RAINFALL ESTIMATES OVER SUB-SAHARAN AFRICA

We started this thesis by reviewing the rainfall estimates available over Africa, our region of interest. Choosing which one to use for a specific application can be difficult because of their large number and their diversity. There are some common factors that influence the performance of the rainfall estimates. We examined five such factors and their impact on the estimates, namely the rainfall regime, the orography, the gauge density and the temporal and spatial resolutions. Since the method/algorithm used to derive an estimate also helps to understand its strengths and limitations, we also give a unified description for the most well-known satellite-based estimates. However, in the end, the choice of the “best” rainfall estimate depends mostly on the intended application. The requirements of the application on the resolution or coverage can reduce the number of choices. Moreover, depending on the application, some characteristics are more important than others. The rainfall estimates should be evaluated with respect to the characteristics meaningful for their intended use.

### 5.1.2. SPACE WARPING AS A WAY TO GAUGE-ADJUST SATELLITE-BASED ESTIMATES WITH RESPECT TO POSITION

From the review on rainfall products, we noticed that most studies focussed on intensity and occurrence and rarely on possible position and timing errors. Position errors

are more studied in the field of forecast verification. One particularly interesting type of spatial verifications are the field deformation methods. They are based on a spatial mapping that can be applied to the first guess field to correct it. We investigate the use of one of these methods, referred as warping in this thesis, to correct position errors in satellite-based rainfall estimates. The spatial warping method was tested on two case studies. The first one was a synthetic rainfall event represented by ellipses. It was used to evaluate the warping in a case for which the “truth” was known, and to explore its sensitivity to several parameters. The second case was a convective rainfall event over southern Ghana, with a rainfall peak of 53.45mm/h according to the gauge measurements. This case allowed us to test the warping method on real datasets, namely the IMERG-Late satellite-based estimate (with a  $0.1^\circ$ lat/lon resolution) and the TAHMO gauge-network. In both cases, we considered a time-window of 25 hours and the same network of 65 stations.

We examined three different approaches for the spatial warping method. All three approaches only modify the spatial coordinates, but they make different assumptions about the temporal dimension. The first one assumes that all time steps are independent. In the second approach we assume the opposite: all time steps have the same mapping. The third approach is a compromise between the first two approaches. The time steps can have different mappings, as in the first approach, but they are assumed to be linked through time.

The three approaches significantly decreased the position error of the rainfall peak in both case studies. They also improved the peak’s timing error and the continuous statistics on the intensity. In general, the second approach led to a more limited improvement due to the rigidity of its assumption of a unique mapping that is applied to all time steps. The first and second approach have similar effects on the position, timing and intensity error. They mainly differ in areas or time steps with no or low rainfall. With the first approach, the mappings can be very different from one time step to the other and cause some discontinuity in time. The third approach is the most computationally expensive but combines the advantages of both approaches.

### 5.1.3. TIME WARPING AS A WAY TO GAUGE-ADJUST SATELLITE-BASED ESTIMATES WITH RESPECT TO TIMING

The time warping method was adapted from the spatial one. As opposed to the spatial warping, here only the time coordinates were modified. We investigated three alternative approaches with different assumptions on the spatial relationship between time series. The first approach neglects the spatial dimension and treats the time series at each station independently. The second one assumes that the timing error is constant in space and so that all stations have the same mapping. In the third approach, the stations can have different mappings but they are linked through space. That is, two stations next to each others should have similar mappings. The time warping is applied to the same two case studies as the spatial warping.

In both case studies, the three approaches significantly decreased the timing error of the rainfall peak. The time warping also improved the continuous statistics but has a more mixed impact on the position error. The first and third approaches had similar results in terms of timing and intensity, they mostly differ for low rainfall values. In general, the second approach led to a more modest improvement, but was spatially more



consistent. In contrast, the independence of the mappings in the first approach led to some spatial discontinuity. The third approach turned out to be a good compromise. Its spatial consistency assumption reduced the risk of discontinuity, observed with the first approach. At the same time, it is less rigid than the unique mapping assumption of the second approach and so permits a more adapted correction of the rainfall estimates.

#### 5.1.4. GENERAL CONCLUSIONS ON WARPING

Both the spatial and the time warping have a positive impact on the rainfall estimates. The continuous statistics were significantly improved after the warping either in time or in space. The timing error was considerably decreased by both types of warping, sometimes more by the spatial one than by the time one. The same does not hold for the position error. As expected, it is decreased significantly by the spatial warping, however the time warping only has a limited impact on it. For the southern Ghana case, the time warping even increases the position error when considering the time steps with low amounts of rainfall. Hence, if both spatial and time warping are able to improve the rainfall estimates (in term of statistics), the spatial warping is more interesting because of its positive impact on both the position and timing errors.

The computational cost of applying the mapping (the warping itself) is negligible compared to the cost of finding the mapping (the automatic registration). The parameters that influence the latter cost are different for spatial and time warping. For the two cases studied here (with 65 stations and 25 hours), the time registration is faster than the spatial one, especially for the approach with the spatial or temporal consistency (A3). The cost increases with the number of time steps for the spatial registration. The number of stations does not influence it since the registration uses the interpolated field as input (and not directly the gauge measurements). On the other hand, the cost of the time registration increases with the number of stations, but does not depend on the number of time steps. The time registration is fast for the cases with 65 stations we studied, however it could encounter a bottleneck if this number increases. Then, the use of a penalized cost function would become necessary (as we did for the spatial registration). The temporal resolution of the time registration is governed by the number of steps  $I$ . Similarly, this number of steps  $I$  defines the spatial resolution for the spatial registration. That is, it determines the amount of details taken into account by the registration. It also impacts the computational time, and so can be tuned to decrease it if necessary. The choice of the number of steps is a trade-off between the resolution and the computational cost.

The main drawback of the warping method comes from the automatic registration method. The first guess and the target (or truth) have to be similar enough for the automatic registration to produce meaningful mappings. In the two cases we studied, the rainfall events were clearly defined and have a unique peak, which make them very suitable for the automatic registration. However, the registration can fail if the rainfall event from the satellite-based estimate and the one from the measurements are too dissimilar. For example, this happens if they have a different number of peaks. Moreover, the events have to be well captured by the gauge networks. This is particularly important for the spatial warping which relies on the interpolated field. If the peak of the event is not captured by the gauges, the interpolated field will not be able to represent the event

accurately (e.g. the center not at the correct position). In turn, the registration assumes that the interpolated field is the truth, which can lead to error.

The warping methods used in this thesis are based on the spatial morphing described in Mandel *et al.* (2010) and Beezley and Mandel (2008). Mandel *et al.* (2010) described a data assimilation method based on morphing in order to do that use both the intensity and position information from the radar precipitation data. However they did not implement it or apply to actual rainfall data. Grassotti *et al.* (1999) actually applied a field deformation method to rainfall data. They used ground-based radar observations to adjust satellite-based rainfall estimates with respect to the intensity and position of the rainfall. They showed that the adjusted satellite-based estimates were closer to the radar observations, and that it was beneficial to applied such position correction before blending the two types of rainfall estimates. One noticeable difference between these previous work and this thesis is the nature of the observation data. We used gauge measurements which are irregularly spaced, while they used gridded radar data. Using non-gridded data is introducing additional uncertainties since we have to interpolate. We modified the method accordingly so that it is not too influenced by areas without gauges. In Grassotti *et al.* (1999) and Mandel *et al.* (2010), the field deformation method is used to correct both the intensity and the position. The spatial warping method used in Chapter 3 only corrects the position. Another difference between their methods and ours is the way we deal with consecutive time steps. They processed each time step individually, while we processed all the time steps in the time window at once. This allowed us to take into account the temporal relationship between the displacement fields of the different time steps. In Chapter 4, we focussed on time distortions and modified the warping method to correct the timing of the rainfall event instead of the position.

## 5.2. RECOMMENDATIONS

Space and time warping have shown a promising potential. They succeeded in using the gauge data to improve the satellite-based estimate in the two cases we studied. However, some improvements are possible. They will be discussed in Section 5.2.1, as well as possible next steps.

In addition, before the end of this chapter and of the thesis, I would like to discuss briefly the the African Rainfall Project of the World Community Grid. Due to a delay in the launch of this project, I have not been able to include it in this thesis. I am thus seizing the opportunity to discuss it briefly in this chapter (see Section 5.2.2).

### 5.2.1. SPATIAL AND TIME WARPING

#### POSSIBLE IMPROVEMENTS FOR THE SPATIAL AND TIME WARPINGS

The space and time warping have been tested for two rainfall events. The synthetic event was used to investigate the accuracy of the methods when the “true” rainfall field was known. The second event was selected during the monsoon season of 2018 in southern Ghana. This case shows the applicability of warping to real noisy data. In both cases, space and time warping improved the rainfall estimates. However, more cases are needed to better assess the performance of space and time warping, and their limits. Warping should be tested for more cases with different rainfall regimes. This will

allow us to better determine the limits of the method and to derive feasibility criteria. As mentioned above, the main limitation of the warping is that the first guess and the observation fields have to be similar enough. The goal of the feasibility criteria is to quantify this similarity in order to know beforehand if the automatic registration would succeed or not. Studying more cases will also allow us to investigate further the sensitivity of the automatic registration (with respect to the regulation coefficient or the number of steps  $D$ ).

The space and time warping methods presented in this thesis are not taking into account the gauge measurements uncertainties. They consider the measurements as the “truth”. In the space warping, the automatic registration also assumes the kriged field (used as input) to be the “truth”. A possible way to take into account both the gauge uncertainties and the kriging error is to modify the cost function of the automatic registration. An observation error covariance matrix can be added in the observation term in a similar way as in variational data assimilation.

Space and time warping focus respectively on the position and timing error. They do not act directly on the intensity of the rainfall event. A possible next step is to combine the warping methods with a bias adjustment method. An existing bias adjustment method can be applied after the warping as second step, for example the additive or multiplicative adjustment or the PDF matching method. Another possibility is to use morphing. The space warping used in Chapter 3 is based on the morphing method described in [Mandel \*et al.\* \(2010\)](#) and [Beezley and Mandel \(2008\)](#). Morphing is based on warping, which modifies the spatial coordinates, and cross-dissolving, which modifies the amplitude or intensity. Thus, morphing impacts both the position and the intensity. However, the morphing cannot be applied directly in the case of point measurements, such as gauge observations. We will first need to adapt it to work with irregularly spaced observations.

#### COMBINING TIME AND SPACE WARPING TO CORRECT BOTH THE POSITION AND THE TIMING ERRORS

In this thesis, we investigate separately space and time warping. The time and position errors were considered independently, while they are in fact linked. A position error can be interpreted as a timing error and vice versa. The spatial warping approach with the time consistency permits to take into account the time dimension even if it does not allow movement in it. Similarly, the time warping with the spatial consistency only warps in the time dimension but takes into account the spatial dimensions. They are thus a good first step towards a 3D space-time warping. They can be applied one after the other in an iterative way to obtain a quasi-3D warping. This can easily be implemented from the existing algorithms. An interesting direction for future research will be to develop a fully 3D warping. This will permit to warp in space and time simultaneously, and so to fully take into account the relationship between the time and space dimensions. When the timing and position errors are treated separately, there is a risk of over correction. For example, the spatial warping can interpret part of the timing error as a position error and try to correct for it. In such a case, applying iteratively the time and the spatial warping would not lead to an optimal correction.

Developing such 3D warping method will have some challenges. The first one will be the computational cost. There are more variables to optimize over during the automatic

registration (three at each grid point compared to two for the spatial warping and one for the time warping), and so the computational cost will be more important than for the spatial or time warping methods. Besides the computational cost, another potential concern is that adding a dimension might make the automatic registration more sensitive to the issue of the similarity of the inputs. As mentioned earlier, the main drawback of the automatic registration is that the inputs need to be similar enough. In the case of the spatial warping with a unique mapping for all time steps (approach A2 in Chapter 3) or with the time consistency (approach A3), the time steps with too dissimilar rain fields were compensated by the others allowing the registration to succeed. Similarly, for the time warping (approaches A2 and A3 in Chapter 4), stations with very different time series were compensated by other stations. This compensation is not possible in the 3D case since the 3D rainfall data is considered as a whole. Thus, a fully 3D warping will be an interesting but challenging next step.

### WARPING AND DATA ASSIMILATION

In this thesis, we only used the warping to gauge-adjust satellite estimate with respect to the position or to the timing. However, warping can be used on different types of data. For example, it can be used for data assimilation into a numerical model. In fact, [Mandel \*et al.\* \(2010\)](#), on which our spatial warping is based, derived a framework to assimilate radar rainfall into a numerical model by combining morphing with an Ensemble Kalman Filter. Other field deformation methods have been used in combination with data assimilation methods for weather models. They were applied for various observation data, such as integrated water vapour ([Hoffman and Grassotti \(1996\)](#), [Alexander \*et al.\* \(1998\)](#), [Nehrkorn \*et al.\* \(2015\)](#)), satellite brightness temperature ([Aonashi and Eito \(2011\)](#), [Nehrkorn \*et al.\* \(2014\)](#)) or radar observation ([Brewster \(2003\)](#), [Nehrkorn \*et al.\* \(2014\)](#)). [Mandel \*et al.\* \(2010\)](#) developed a framework for the data assimilation of rainfall observation (from radar) into a numerical model, but do not apply it. In [Grassotti \*et al.\* \(1999\)](#), a field deformation method is applied to rainfall data, but not in the context of data assimilation. It is used to correct satellite-based estimates using ground-based radar data. Thus, field deformation methods have already been applied in combination with data assimilation, and they already have been applied to rainfall data. However, never at the same time. This will be an interesting subject to investigate. A challenge of such approach is the dynamical imbalance that can result from spatially displacing the forecast fields. This is a known problem and some methods to reduce such imbalance have been developed ([Nehrkorn \*et al.\*, 2014](#); [Hsiao \*et al.\*, 2010](#)).

The data assimilation of rainfall rate has been studied in the past decades and is now operational in several weather services ([Jones and Macpherson \(1997\)](#), [Lopez \(2011\)](#), [Tsuyuki \*et al.\* \(2003\)](#)). A challenge of the assimilation of rainfall data is the “zero-rain” problem. This problem arises when the model has no rainfall but the observation does or vice-versa ([Lopez \(2011\)](#)). Position mismatches can lead to such situation. Moreover, for any assimilated variable, position mismatches between the first guess and the observations can lead to important non-Gaussian background errors. Both variational and ensemble-based data assimilation methods are based on the assumption that the background errors are Gaussian. Deviating from that assumption leads to suboptimal results. Thus, correcting position mismatches before hand or assimilating the rainfall position at the same time as the rainfall rate can reduce these two problems.

### 5.2.2. HIGH-RESOLUTION WEATHER SIMULATION FOR SUB-SAHARAN AFRICA ON THE WORLD COMMUNITY GRID

In the second part of this thesis, we worked with gauges from TAHMO and a satellite-based product (IMERG). However, as mentioned above, there is a third type of estimate: NWP models and reanalyses. There is no regional reanalysis available for Africa. The global reanalyses are able to represent the main features of the monsoon, but they have a limited performance for more local scales. Moreover, they are too coarse for many applications. A possibility is to dynamically downscale a global reanalysis using a regional numerical model. There are several projects investigating and comparing numerical reanalysis over (parts of) Africa. However, they are generally using a relatively coarse resolution ( $\geq 10\text{km}$ ). Convection-permitting resolution ( $\leq 4\text{km}$ ) allows for a better representation of the rainfall, and in particular of convective rainstorms (Prein *et al.*, 2015; Fosser *et al.*, 2015). In most cases, dynamic downscaling at convection-permitting resolution is done over a limited area and/or for short periods (for example Pearson *et al.* (2010), Chamberlain *et al.* (2014), Zhang *et al.* (2016), Crook *et al.* (2019), Maurer *et al.* (2017), and Reinares Martínez and Chaboureau (2018)). An exception, is the CP4-Africa model (Pan-African Convection-Permitting Regional Climate Simulation with the Met Office UM) which will be run for 10 years for the whole continent at 4.5km resolution as part of the Future Climate for Africa (FCFA) Improving Model Processes for African Climate (IMPALA) project (Stratton *et al.*, 2018).

A special project in which the author was strongly involved, is the African Rainfall Project. The goal of the African Rainfall Project is to run the Weather Research and Forecasting (WRF) model for the whole sub-Saharan Africa at the high resolution of 1km for a year. However, running WRF (or another numerical model) at such resolution for such a large area is computationally expensive. It was made possible by IBM's World Community Grid. The World Community Grid (WCG) is part of the Social Corporate Responsibility program of IBM that crowdsources unused computing power from volunteers' devices and donates it to scientific projects. The author participated in the writing of the WCG grant proposal. Within this project, her role was the preparation of the inputs that were sent to the WCG, and the analyse of the outputs for the alpha and beta testing.

The simulation was adapted to the WCG by dividing the one year simulation over sub-Saharan Africa in many smaller ones of 48h over 52 km by 52 km domains. These simulations are small enough to be calculated on a single computer of a volunteer at the required resolution. In total, 35609 overlapping domains are covering the whole sub-Saharan Africa. The WRF model calculated all the atmospheric variables, but only about 15 variables of direct interest are stored. They are stored every 15 of simulation minutes, and represent 0.5PB data.

Future work includes the post-processing and the validation of the model outputs. During the post-processing phase, the smaller simulations will be merged back together to obtain one consistent simulation over the whole sub-Saharan Africa. The validation will consist of two parts: the validation of the settings (i.e. division in smaller domains) and the validation of the variables. Dividing a large domain in several smaller ones and running them independently was necessary to adapt to the WCG setting, but it is new. The first part of the validation will compare the simulation of the small domains to a simulation on a larger domain (e.g. 1000km by 500km). This simulation will be identical

to the smaller ones in terms of input data and parameterization, and will only differ by the dimension of the domain. It will be run on Cartesius, the Dutch national supercomputer. In the second part of the validation, the variables will be compared to satellite data and in-situ measurements from the TAHMO network. After the post-processing and validation are complete, the data will be made publicly available.

**Final remark:** Rainfall is an important component of the water cycle. It is at the same time vital for agriculture and ecology, and a potential danger. Too much or too little rainfall can lead to floods and droughts, which have large socio-economic impacts. That makes accurate rainfall estimates essential. With this thesis, we hope to have contributed to this vast topic.

## REFERENCES

- J. Mandel, J. D. Beezley, K. Eben, P. Jurus, V. Y. Kondratenko, and J. Resler, *Data assimilation by morphing fast fourier transform ensemble Kalman filter for precipitation forecasts using radar images*, (2010) UCD/CCM Report 289.
- J. D. Beezley and J. Mandel, *Morphing ensemble Kalman filters*, *Tellus A* **60**, 131 (2008).
- C. Grassotti, H. Iskenderian, and R. N. Hoffman, *Calibration and alignment*, *Journal of Applied Meteorology* **38**, 677 (1999).
- R. N. Hoffman and C. Grassotti, *A technique for assimilating SSM/I observations of marine atmospheric storms: Tests with ECMWF analyses*, *Journal of Applied Meteorology* **35**, 1177 (1996).
- G. D. Alexander, J. A. Weinman, and J. L. Schols, *The use of digital warping of microwave integrated water vapor imagery to improve forecasts of marine extratropical cyclones*, *Monthly Weather Review* **126**, 1469 (1998).
- T. Nehr Korn, B. K. Woods, R. N. Hoffman, and T. Auligné, *Correcting for position errors in variational data assimilation*, *Monthly Weather Review* **143**, 1368 (2015).
- K. Aonashi and H. Eito, *Displaced ensemble variational assimilation method to incorporate microwave imager brightness temperatures into a cloud-resolving model*, *Journal of the Meteorological Society of Japan. Ser. II* **89**, 175 (2011).
- T. Nehr Korn, B. Woods, T. Auligné, and R. N. Hoffman, *Application of feature calibration and alignment to high-resolution analysis: Examples using observations sensitive to cloud and water vapor*, *Monthly Weather Review* **142**, 686 (2014).
- K. A. Brewster, *Phase-correcting data assimilation and application to storm-scale numerical weather prediction. Part I: Method description and simulation testing*, *Monthly Weather Review* **131**, 480 (2003).
- L.-F. Hsiao, C.-S. Liou, T.-C. Yeh, Y.-R. Guo, D.-S. Chen, K.-N. Huang, C.-T. Terng, and J.-H. Chen, *A vortex relocation scheme for tropical cyclone initialization in advanced research WRF*, *Monthly Weather Review* **138**, 3298 (2010).

- C. D. Jones and B. Macpherson, *A latent heat nudging scheme for the assimilation of precipitation data into an operational mesoscale model*, *Meteorological Applications* **4**, 269 (1997).
- P. Lopez, *Direct 4D-Var assimilation of NCEP Stage IV radar and gauge precipitation data at ECMWF*, *Monthly Weather Review* **139**, 2098 (2011).
- T. Tsuyuki, K. Koizumi, and Y. Ishikawa, *The JMA mesoscale 4D-Var system and assimilation of precipitation and moisture data*, in *ECMWF/GEWEX Workshop on Humidity Analysis, 8-11 July 2002*, ECMWF (ECMWF, Shinfield Park, Reading, 2003) pp. 59–68.
- A. F. Prein, W. Langhans, G. Fosser, A. Ferrone, N. Ban, K. Goergen, M. Keller, M. Tölle, O. Gutjahr, F. Feser, E. Brisson, S. Kollet, J. Schmidli, N. P. M. van Lipzig, and R. Leung, *A review on regional convection-permitting climate modeling: Demonstrations, prospects, and challenges*, *Reviews of Geophysics* **53**, 323 (2015).
- G. Fosser, S. Khodayar, and P. Berg, *Benefit of convection permitting climate model simulations in the representation of convective precipitation*, **44**, 45 (2015).
- K. J. Pearson, R. J. Hogan, R. P. Allan, G. M. S. Lister, and C. E. Holloway, *Evaluation of the model representation of the evolution of convective systems using satellite observations of outgoing longwave radiation*, *Journal of Geophysical Research: Atmospheres* **115**, (2010).
- J. M. Chamberlain, C. L. Bain, D. F. A. Boyd, K. McCourt, T. Butcher, and S. Palmer, *Forecasting storms over Lake Victoria using a high resolution model*, *Meteorological Applications* **21**, 419 (2014).
- G. Zhang, K. H. Cook, and E. K. Vizy, *The diurnal cycle of warm season rainfall over West Africa. Part II: Convection-permitting simulation*, *Journal of Climate* **29**, 8439 (2016).
- J. Crook, C. Klein, S. Folwell, C. M. Taylor, D. J. Parker, R. Stratton, and T. Stein, *Assessment of the representation of west african storm lifecycles in convection-permitting simulations*, *Earth and Space Science* **6**, 818 (2019).
- V. Maurer, I. Bischoff-Gauß, N. Kalthoff, L. Gantner, R. Roca, and H.-J. Panitz, *Initiation of deep convection in the Sahel in a convection-permitting climate simulation for northern Africa*, *Quarterly Journal of the Royal Meteorological Society* **143**, 806 (2017).
- I. Reinares Martínez and J.-P. Chaboureaud, *Precipitation and Mesoscale Convective Systems: Explicit versus Parameterized Convection over Northern Africa*, *Monthly Weather Review* **146**, 797 (2018).
- R. A. Stratton, C. A. Senior, S. B. Vosper, S. S. Folwell, I. A. Boutle, P. D. Earnshaw, E. Kendon, A. P. Lock, A. Malcolm, J. Manners, C. J. Morcrette, C. Short, A. J. Stirling, C. M. Taylor, S. Tucker, S. Webster, and J. M. Wilkinson, *A Pan-African Convection-Permitting Regional Climate Simulation with the Met Office Unified Model: CP4-Africa*, *Journal of Climate* **31**, 3485 (2018).

# ACKNOWLEDGEMENTS

Firstly, I would like to thank my promotors Nick van de Giesen and Arnold Heemink for giving me the opportunity to do research/my PhD on this interesting topic.

Nick, thank you for your supervision and guidance. You always found the time for supervising me despite your busy schedule. You helped me to see beyond the current step towards the bigger picture.

Arnold Heemink and Martin Verlaan, I would like to thank you for many interesting discussions and the valuable inputs. Without you, Chapters 3 and 4 would have been different.

Marie-Claire ten Veldhuis, thank you for taking interest in my work and all your useful advice. I would also like to thank you for inviting me to your score meeting.

My thesis was possible thanks to the funding of Delft Global Initiative. I would like to thank them for their funding and support as well as for the community they built. I would also like to thank my Delft Global fellows for their support and inspiring stories of science.

I would also like to thank all the people from the World Community Grid (from IBM) for making the African Rainfall project possible. It was an exciting experience.

I would also like to thank my friends and colleagues who made my PhD life much more enjoyable/fun.

To my office mates: I enjoyed our lunches, coffee breaks and spontaneous discussions. Petra and Andreas, I am already missing our bouldering session. A special thanks to Andreas for his help with my computer issues.

Héloïse: Thank you for our “french” coffee breaks and for introducing me to bouldering.

To the score meeting group (Andreas, Monica, David, and Cynthia): I enjoyed our weekly meeting and sharing progress and stories with you. This group helped me feel part of the water management group.

Lydia and Betty, I would like to thank you for your help with the administrative tasks and for the supply of candies.

Last but not least, I would like to thank my family, and especially Sander, for their support during these years.





# CURRICULUM VITÆ

## Camille Marie-Jeanne Laurence LE COZ

23-09-1991      Born in Sèvres, France.

### EDUCATION

- 2009–2012      Bachelor of Science in Engineering  
Classe préparatoire aux grandes écoles, Lycée Chateaubriand, Rennes, France  
Ecole Centrale Marseille, Marseille, France
- 2011–2016      Diplôme d'ingénieur (equivalent to Master of Engineering)  
Ecole Centrale Marseille, Marseille, France
- 2013–2015      Master of Science in Applied Mathematics (cum laude)  
Delft University of Technology, Delft, the Netherland  
*Thesis:*      A modified Proper Orthogonal Decomposition procedure with patterns in time for parameter estimation.
- 2016–2020      PhD Doctoral Education  
Delft University of Technology, Delft, the Netherlands  
*Thesis:*      Straight as rain: Africa's rainfall measured, modeled, mapped, and analyzed.  
*Promotors:* Prof. dr. ir. N. van de Giesen  
Prof. dr. ir. A. Heemink

## WORK EXPERIENCES & INTERNSHIPS

- Jun–Jul 2013      Internship  
M2P2 laboratory (Mécanique, Modélisation et Procédés Propres)  
*Topic:*          Calcul numérique d'équilibre dans les réacteurs à fusion.
- May–Oc. 2014    Student assistant  
Delft University of Technology, Delft, the Netherlands
- Sep–Dec 2014    Internship  
Deltares, Delft, the Netherlands  
*Topic:*          Computation of the self-attraction and loading term  
in a global time model.

# LIST OF PUBLICATIONS

## PEER-REVIEWED JOURNAL ARTICLES

3. **C. Le Coz**, and N. van de Giesen, *Comparison of Rainfall Products over Sub-Saharan Africa*, *Journal of Hydrometeorology* **21**, 553–596 (2020).
2. **C. Le Coz**, A. Heemink, M. Verlaan, M.-C. ten Veldhuis, and N. van de Giesen, *Correcting Position Error in Precipitation Data Using Image Morphing*, *Remote Sensing* **11**, 2557 (2019).
1. M. Irazoqui Apecechea, M. Verlaan, F. Zijl, **C. Le Coz**, and H. Kernkamp, *Effects of self-attraction and loading at a regional scale: a test case for the Northwest European Shelf*, *Ocean Dynamics* **67**, 729–749 (2017).

## ORAL AND POSTER PRESENTATIONS

9. N. van de Giesen, **C. Le Coz** and L. A. Treinish, *The African Rainfall Project: High resolution (1km) weather modeling at continental scale thanks to the World Community Grid*, AGU Fall Meeting, Online, 1-17 December 2020. (Display)
8. **C. Le Coz**, A. Heemink, M. Verlaan, M.-C. ten Veldhuis, and N. van de Giesen, *Correcting position error in rainfall estimates using temporal and spatial warping*, EGU General Assembly 2020, Online, 4-8 May 2020. (Display)
7. **C. Le Coz**, A. Heemink, M. Verlaan, M.-C. ten Veldhuis, and N. van de Giesen, *Applying image morphing to precipitation data, a case study in Southern Ghana*, EMS Annual Meeting 2019, Copenhagen (Denmark), 9-13 September 2019. (Poster)
6. **C. Le Coz**, A. Heemink, M. Verlaan, and N. van de Giesen, *Gauge-adjustment of satellite-based rainfall estimates using morphing*, EGU General Assembly 2019, Vienna, 7–12 April 2019. (Poster)
5. **C. Le Coz**, A. Heemink, M. Verlaan, M.-C. ten Veldhuis, and N. van de Giesen, *Precipitation morphing: TAHMO-adjusted satellite products over the Volta Basin region*, EMS Annual Meeting 2018, Budapest (Hungary), 3-7 September 2018. (Poster)
4. **C. Le Coz**, M.-C. ten Veldhuis, and N. van de Giesen, *Comprehensive review of rainfall products over Africa*, EGU General Assembly 2018, Vienna, 8–13 April 2018. (Poster)
3. **C. Le Coz**, *An overview of rainfall products over Africa*, Boussinesq Lecture 2017, Delft (the Netherlands), 26 October 2017. (Oral)
2. **C. Le Coz**, M.-C. ten Veldhuis, and N. van de Giesen, *Africa's rainfall: Systematic literature comparison of rainfall products*, EMS Annual Meeting 2017, Dublin (Ireland), 4-8 September 2017. (Poster)
1. **C. Le Coz**, and N. van de Giesen, *Comparison of rainfall products over Africa*, EGU General Assembly 2017, Vienna, 23–28 April 2017. (Poster)

## CODE

Part of the Python code used for this thesis is available on github:

2. C. Le Coz (2021) spatial-warping\_thesis [Source code]. [https://github.com/clecoz/spatial-warping\\_thesis](https://github.com/clecoz/spatial-warping_thesis)
1. C. Le Coz (2021) time-warping\_thesis [Source code]. [https://github.com/clecoz/time-warping\\_thesis](https://github.com/clecoz/time-warping_thesis)